Design Principles and Field Performance of Software-Augmented Solar Sensors for Resolving Spectral Irradiance and Atmospheric Parameters

by

Viktar Tatsiankou

Thesis submitted in partial fulfilment of the requirements for the PhD degree in Electrical and Computer Engineering

School of Electrical Engineering and Computer Science
Faculty of Engineering
University of Ottawa

“Загляне сонца і ў наша ваконца”

“The sun will peek in our window”

– Belarussian proverb

Table of Contents

Abstract

The present work details the design principles and field performance of software-augmented, multi-functional sensors capable of resolving solar spectral irradiance and atmospheric parameters, such as aerosol optical depth, total column ozone and precipitable water vapour. The primary motivation behind this research and development work is the solar industry's increasing need for spectral and atmospheric data, the acquisition of which, prior to this work, was not commercially practical or cost-effective.

This thesis presents the direct solar spectral irradiance meter (SolarSIM-D2), which was designed for photovoltaic and atmospheric science applications. The instrument measures the direct normal irradiance (DNI) in six narrow wavelength bands. These measurements are combined with radiative transfer models to determine the spectral transmittance profiles of key atmospheric components, such as spectral aerosols, total column ozone and precipitable water vapour, and subsequently resolve the spectral DNI over the complete 280–4000 nm range. Multiple SolarSIM-D2s were calibrated and validated at the National Renewable Energy Laboratory (NREL) in the United States and at the World Radiation Center in Switzerland against reference instrumentation. In addition, a comprehensive uncertainty analysis was performed for all of the SolarSIM-D2's measurands.

This work also describes the global solar spectral irradiance meter (SolarSIM-G), which was designed to resolve the spectral and broadband global irradiances over the complete 280–4000 nm spectral range, primarily for use in the photovoltaic industry. The all-sky parameterized transmittance model was developed, capable of deriving the spectral and broadband global irradiances from the SolarSIM-G's nine optical measurements under clear and cloudy conditions. This model uses radiative transfer algorithms to resolve in real-time the combined contribution of the direct and diffuse irradiance components, including the effects of atmospheric and cloud scattering. Multiple SolarSIM-Gs were calibrated and validated at NREL against reference instrumentation.

The SolarSIM sensors represent a significant advancement in the field of solar measurements by providing a wealth of detailed spectral and atmospheric data in a compact, affordable system as compared to traditional alternatives. A notable impact of this work is the commissioning of the Canadian Solar Spectral Irradiance Meter (CanSIM) network, consisting of seven stations across Canada, each containing a SolarSIM-D2 and a SolarSIM-G. CanSIM data was used to develop a novel global irradiance decomposition algorithm to derive the direct and diffuse irradiance components from the SolarSIM-G's measurements. This method has a factor of two to three improvement in the root-mean-square error for the DNI retrieval as compared to the existing state-of-the-art decomposition algorithms.

Acknowledgements

Funding for the research work performed in this thesis has been provided in part by the National Sciences and Engineering Research Council of Canada (NSERC) through the Alexander Graham Bell Scholarship, and from the Ontario Ministry of Training, Colleges and Universities through Ontario Graduate Scholarship (OGS).

Thank you Dr. Karin Hinzer for your never-ending support throughout my graduate studies which began nearly eight years ago. Your warm personality and addictive enthusiasm have encouraged my research and have driven me to move forward.

Thank you Dr. Henry Schriemer for always being there when I needed your help. Your astute guidance and thorough review of my work were a big part in advancing this research.

Thank you Dr. Richard Beal for guiding my research and challenging me to be better. Your methodical and careful approach to solving problems has made me more organized and patient in doing my research.

Thank you Marjorie and Alex Dow for giving me the opportunity to come to this great country and to provide me with everything that I needed to succeed. I am forever grateful for the sacrifices that you have made to make my future brighter. ♡

A special thank you goes to my wife, Roxanne Bouvier, for her unconditional love, mental support, and constant encouragement. Thank you for believing in me, for always being so understanding, and for bringing into this world our precious daughters, Katya and Natalie. Our children are our strength that fans the flame of our success. ♡

Thank you my dear sister Veronika for always cheering me on and supporting my endeavours. Your perseverance and hard work is admirable and inspiring. ♡

Я также хотел бы поблагодарить мою любимую бабушку Машу за её любовь и постоянную поддержку на протежении всех этих лет. ♡

И наконец, хотелось бы поблагодарить моих уважаемых родителей. Огромное вам спасибо за вашу поддержку и веру в меня. Спасибо вам за то, что позволили мне осуществить мои мечты, даже если это означало не видеться с вами на протяжении более десяти лет. Как отец двоих прекрасных дочерей, я только сейчас понимаю, как тяжело было решиться на такой шаг и отпустить меня в Канаду, и я всегда буду благодарен вам за это. Вы мне доказали этим самым, что тяжелая работа и самоотдача всегда окупаются в жизни. Вы научили меня, что семья превыше всего и всегда стоит на первом месте. Я буду следовать этими мудрыми наставлениями в жизни и сделаю все возможное, чтобы передать их вашим внучкам. Я люблю вас, Мама и Папа. ♡

Dedication

Эта диссертация посвящается моим дорогим и уважаемым дедушкам: Богачёву Михаилу Антоновичу и Татенкову Олегу Герасимовичу, которые служили мне примером для достижения поставленных целей.

Statement of originality

Unless otherwise noted, the research work presented in this thesis was carried out solely by the author under the supervision of Dr. Karin Hinzer during the period of his PhD studies. To the best of his knowledge, the results contained in this thesis are original.

Publications

The following publications resulted from my thesis work:

1. **V. Tatsiankou**, K. Hinzer, H. Schriemer, and R. Beal, "Improved global irradiance decomposition by sky condition classification from measured spectral clearness indices". *47th IEEE Photovoltaic Specialists Conference (PVSC)*, 2020.

2. **V. Tatsiankou**, K. Hinzer, H. Schriemer, and R. Beal, "Toward routine measurement and calculation of spectrally corrected DNI for CPV systems". *AIP Conference Proceedings (CPV-15)*, 2019.

3. **V. Tatsiankou**, K. Hinzer, H. Schriemer, S. Kazadzis, N. Kouremeti, J. Gröbner and R. Beal, "Extensive validation of solar spectral irradiance meters at the World Radiation Center". *Journal of Solar Energy*, vol. 166, pp. 80-89, 2018.

4. S. Kazadsis, N. Kouremeti, J. Gröbner, **V. Tatsiankou**, *et al.* "Results from the 4th WMO Filter Radiometer Comparison for aerosol optical depth measurements". *Journal of Atmospheric Chemistry and Physics*, vol. 18, pp. 3185-3201, 2018.

5. **V. Tatsiankou**, K. Hinzer, H. Schriemer, P. McVey-White, and R. Beal, "Efficient, real-time global spectral and broadband irradiance acquisition". *45th IEEE Photovoltaic Specialists Conference (PVSC)*, 2018.

6. **V. Tatsiankou**, K. Hinzer, H. Schriemer, P. McVey-White, and R. Beal, "Deployment and early results from the CanSIM network". *AIP Conference Proceedings (CPV-13)*, 2017.

7. **V. Tatsiankou**, K. Hinzer, H. Schriemer, K. Emery, and R. Beal, "Design principles and field performance of a solar spectral irradiance meter". *Journal of Solar Energy*, vol. 133, pp. 94-102, 2016.

8. **V. Tatsiankou**, K. Hinzer, H. Schriemer, J. E. Haysom, and R. Beal, "Long term performance analysis of solar spectral irradiance meters". *AIP Conference Proceedings (CPV-12)*, 2016.

9. **V. Tatsiankou**, K. Hinzer, H. Schriemer, J. E. Haysom, and R. Beal, "A novel instrument for cost-effective and reliable measurement of solar spectral irradiance". *42nd IEEE Photovoltaic Specialists Conference (PVSC)*, 2015.

Patents

The following patents were granted during the course of my PhD work:

1. **V. Tatsiankou**, R. Beal, "Global solar spectrum devices and methods". U.S. Patent 10,209,132 B2 issued February 19, 2019.
2. **V. Tatsiankou**, R. Beal, "Global solar spectrum devices and methods". U.S. Patent 10,359,314 B2 issued July 23, 2019.

List of Figures

List of Symbols and Acronyms

Roman Symbols

F_s	Downward aerosol scattering fraction
m	Geometric air mass
m_i	Optical air mass of an atmospheric constituent, i
r	Ratio of the average to actual sun-earth distance
R_g	Spectral ground albedo
R_s	Spectral sky reflectivity
S_0	Extraterrestrial spectral irradiance
S_a	Spectral aerosol scattering from multiple ground-sky reflections
S_DHI	Spectral diffuse horizontal irradiance
S_DNI	Spectral direct normal irradiance
S_GHI	Spectral global horizontal irradiance
S_m	Spectral irradiance due to scattering
S_R	Spectral Rayleigh scattering
T_i	Transmittance of an atmospheric constituent, i
T_aa	Transmittance of aerosol absorption
T_as	Transmittance of aerosol scattering
T_a	Transmittance of aerosol extinction
T_g	Transmittance of uniformly mixed gases
T_o	Transmittance of total column ozone
T_R	Transmittance of Rayleigh scattering
T_w	Transmittance of precipitable water vapour
Z	Solar zenith angle

Greek Symbols

λ	Wavelength
ϕ	Solar azimuth angle
τ	Optical depth
τ_i	Optical depth of an atmospheric constituent, i
θ	Solar elevation angle

Acronyms

AERONET	Aerosol Robotic Network
AM	Air mass
AM0	Air mass "zero" or extraterrestrial solar spectrum
AU	Astronomical unit
CanSIM	Canadian Solar Spectral Irradiance Meter (network)
CPV	Concentrating photovoltaic(s)
DHI	Diffuse horizontal irradiance
DNI	Direct normal irradiance
DU	Dobson unit
GHI	Global horizontal irradiance
ISO	International Organization for Standardization
NIST	National Institute of Standards and Technology
NREL	National Renewable Energy Laboratory
PMOD	Physikalisch-Meteorologisches Observatorium Davos
PV	Photovoltaic(s)
SCF	Spectral correction factor
SMARTS	Simple Model of the Atmospheric Radiative Transfer of Sunshine
SolarSIM	Solar spectral irradiance meter
SolarSIM-D2	Direct irradiance version of a SolarSIM
SolarSIM-G	Global irradiance version of a SolarSIM
SPA	Solar position algorithm
TEC	Thermo-electric cooler
TSI	Total solar irradiance
WRC	World Radiation Center
WRR	World Radiometric Reference

Chapter 1

Introduction

Solar irradiance measurements are essential for understanding our planet's primary energy source. Since the dawn of civilization, humans understood the importance of the sun and used it to better their lives. Thousands of years ago, buildings were designed to take advantage of sunlight for improved heating and illumination. Today, thousands of solar farms are in operation worldwide with over 500 GW of installed capacity - enough to power millions of homes [1]. DNV GL, a global risk management and quality assurance group, predicts that by 2050 solar power will become the primary energy source on the planet, making up 40% of the total electricity generation [2]. On route toward achieving this ambitious goal, the solar industry must further drive down its levelized cost of electricity. With the impressive reductions realized in photovoltaic (PV) module prices thus far, the cost of financing is now becoming a dominant factor in solar farm economics. This cost is directly linked to the uncertainty associated with the amount of electricity that a proposed PV power plant is projected to produce. It has long been known that including spectral irradiance and atmospheric data in PV performance models can significantly reduce this prediction uncertainty [3]–[5]. However, the instruments used to provide the aforementioned data, namely spectroradiometers and sun photometers, are too expensive and difficult to maintain, making them impractical for routine industrial deployment. This example is one of many reasons why my research work has focused on the design and field performance of software-augmented and multi-functional sensors, which provide detailed spectral and atmospheric data that is critical for many applications, including solar energy research, atmospheric sciences and solar power forecasting.

The first part of my research involved finding a better solution for obtaining the spectral direct normal irradiance (DNI), as often desired for the concentrating photovoltaic (CPV) applications. At the heart of the CPV technology are high-efficiency multi-junction solar cells, which due to their architecture are more sensitive to solar spectral variations than the single junction devices used in the traditional PV industry. Thus, knowledge of the local solar spectrum is critical for a complete performance analysis of CPV systems [6]–[9]. Performing measurements of solar spectral irradiance has historically been a daunting task. The traditional way to measure the local solar spectrum is to deploy a field spectroradiometer, which disperses the incoming light into its constituent wavelengths using a complex, temperature-controlled optical system. The dispersed light is then measured by a diode array or a charge-coupled device. As a result, field spectroradiometers are expensive, bulky and power hungry instruments, with deployments historically being limited to well-funded research institutions and government laboratories [10]–[12]. Instead of working directly with spectral data, one can also use a spectroheliometer - a device based on triple-junction isotype reference cells [13]. Although spectroheliometers can be more affordable and reliable than spectroradiometers, they are also less flexible, being restricted to a particular multi-junction solar cell architecture. In lieu of actual measurements, the local solar spectrum may be simulated using modelling tools, such as the Simple Model of the Atmospheric Radiative Transfer of Sunshine (SMARTS), but the accuracy of this approach relies on rarely available atmospheric data inputs, such as the aerosol optical depth at 500 nm, the total column ozone amount and the precipitable water vapour content[1]. One can use the aforementioned atmospheric data from the Aerosol Robotic Network (AERONET) [15], [16] or interpolate the necessary data from nearby sites [17]. However, the geographic sparsity AERONET sites remains a big impediment to the general applicability of this technique.

It is known that sunlight is an inherently constrained light source and it is therefore possible to reconstruct the solar spectrum from a select few spectral measurements [18]–[21]. Through decades of observations, the extraterrestrial solar spectrum has become known to a high level of accuracy [22] and there are only a handful of major phenomena that impact the clear-sky sun spectrum as it propagates through the atmosphere, namely

- Rayleigh scattering,
- precipitable water vapour absorption,
- aerosol absorption,
- ozone absorption and
- atmospheric gases absorptions.

Using atmospheric radiative transfer modelling, I determined that, by measuring the spectral irradiance in only six specific, narrow wavelength bands, one can accurately resolve the spectral aerosol, ozone and precipitable water vapour absorptions, and subsequently the direct normal terrestrial solar spectrum in the entire 280–4000 nm range. Based on these results, I designed, built, validated and commercialized a direct solar spectral irradiance meter (SolarSIM-D2), that reduces the cost, by tenfold, of accurately resolving the direct solar spectrum, aerosols, total column ozone and atmospheric precipitable water vapour amounts, as shown in Figure 1.1a. The design, calibration procedure and field performance of this instrument at National Renewable Energy Laboratory (NREL) in the US against co-located pyrheliometers and spectroradiometers was published in the Journal of Solar Energy, as included in Section 3.1.1.

Although the instrument's spectral and broadband DNI capabilities have been assessed at NREL, additional analysis was needed to determine the SolarSIM-D2's derivation accuracy for its other measurands, such as the spectral aerosol optical depth, total column

[1] For background information the reader may examine Chapter 2 of my MASc thesis [14].

(a)

(b)

Figure 1.1: a) SolarSIM-D2: Solar spectral irradiance meter for resolving the direct normal spectral irradiance and atmospheric constituents b) SolarSIM-G: Solar spectral irradiance meter for resolving the global spectral irradiance.

ozone and precipitable water vapour. As such, I have performed a comprehensive uncertainty analysis for all of the SolarSIM-D2's measurands using the Guide to the Expression of Uncertainty Measurements [23]. This analysis was used to evaluate the field deployment of four SolarSIMs at Physikalisch-Meteorologisches Observatorium Davos and World Radiation Center (PMOD/WRC) in Davos, Switzerland, where I further assessed the SolarSIM-D2's derivation accuracy for spectral and broadband DNI, in addition to spectral aerosol optical depth, total column ozone amount and atmospheric precipitable water vapour content, against the state-of-the art reference instruments. Details of this work, including the aforementioned uncertainty analysis, were published in the Journal of Solar Energy and can be found in Section 3.1.2.

Through further research, I discovered that the six-channel model is only sufficient when resolving the direct solar spectrum, which is typically useful for CPV-based applications. The vast majority of the PV industry use flat panels which absorb a combination of direct and diffuse sunlight, or a global irradiance. By using atmospheric radiative transfer modelling, I determined that to accurately resolve the global solar spectrum under clear and cloudy conditions, one must add at least three additional measurement channels as compared to the SolarSIM-D2, one in the ultraviolet and two in the infrared spectral ranges. Based on these findings, I designed, built, validated and commercialized a global SolarSIM (SolarSIM-G), which resolves the global spectral and broadband irradiance over the full 280–4000 nm range in one compact, rugged and cost-effective instrument, as pictured in Figure 1.1b. The innovations underpinning the SolarSIM-G are encapsulated in two US patents, one of which is included in Appendix for reference. The SolarSIM-G's calibration procedure and field performance at NREL is presented in Section 3.2.1.

Throughout the development of the SolarSIM technology, I created numerous programming scripts, test jigs and control systems to assess various aspects of instrument's design. Section 3.3 describes critical characterization methods that are necessary to ensure the high accuracy of SolarSIM measurements, namely the thermal test, the directional response test and the optical calibration. The results from a thermal test are used to automatically "correct" for the temperature dependence of the SolarSIM photodiodes, thus reducing the instrument's measurement uncertainty. On the other hand, the directional response test verifies the SolarSIM-G's compliance to the international standard for global irradiance measurements. In addition, the optical calibration ensures the traceability of SolarSIM measurements to the International System of Units via a reference lamp from the National Institute of Standards and Technology.

The SolarSIM technology represents a significant advancement over existing state-of-the art measurement methods, as it enables the acquisition of detailed spectral and atmospheric data from rugged, compact sensors which have no moving parts. One of the notable impacts of this thesis work is the commissioning of the Canadian Solar Spectral Irradiance Meter (CanSIM) network, consisting of seven stations, each containing a SolarSIM-D2 and a SolarSIM-G. As described in Section 4.1, the CanSIM network is the world's first real-time solar spectral irradiance network enabling many applications in solar energy research and atmospheric sciences. For example, the CanSIM data can be used to calculate the spectral correction factors (SCFs), which quantify the effect of local spectral conditions on a specific PV or CPV module, and, as simple time series data, have the added benefit of being easily implemented within existing PV or CPV performance models. As such, in Section 4.2, I have used CanSIM data to demonstrate the use of spectrally corrected DNI, i.e. the product of DNI and the SCF, as a metric to quantify annual, local atmospheric effects on the energy yield of a hypothetical CPV mono-module. Furthermore, in Section 4.3, I have used the equivalent of seven years' worth of station data from four CanSIM stations and one station in China to develop, calibrate and validate a novel global irradiance decomposition algorithm to derive the broadband DNI and DHI with much lower uncertainty compared to other state-of-the-art decomposition models. More importantly, the commercialization of the SolarSIM technology has provided the research community with a tool to obtain detailed spectral and atmospheric data, which, at the time of writing, has resulted in twelve third-party publications, as listed in Section 4.4. Overall, these examples highlight a substantial contribution made by this thesis work to the field of solar measurements.

1.1 Thesis Outline

This thesis is presented as an assembly of journal articles and select, most-relevant, conference proceedings. Each paper is stand-alone and therefore contains its own background theory, methodology, results, discussion and reference sections. As a result, some papers may exhibit a small degree of overlap, predominantly in the introductory sections. The references for non-article materials are shown at the end of this thesis in the References section.

Chapter 2 introduces the basic concepts that are necessary to understand and model the distribution of the solar spectral resource at the earth's surface. This chapter demonstrates how the parameterized effects of the atmosphere and clouds give rise to three sunshine components, namely the direct normal, diffuse horizontal, and global horizontal spectral irradiances. General equations and theory are given to express the spectral irradiance on the horizontal surface under all sky conditions at any location.

Chapter 3 presents this thesis' main body of work by detailing the direct and global SolarSIM sensors. More specifically, Section 3.1.1 describes the parameterized transmittance model and the algorithm used to derive the spectral DNI and atmospheric parameters from the SolarSIM-D2's calibrated irradiance measurements. Section 3.1.2 derives a comprehensive uncertainty analysis for all SolarSIM-D2 measurands, and then presents the field performance of four SolarSIMs at the WRC as compared against reference instrumentation. Section 3.2.1 details the design, calibration procedure and field performance of the SolarSIM-G for deriving the spectral and broadband GHI under all sky conditions. The additional optical and mechanical design details of the SolarSIM-G are presented in the U.S. patent 10,359,314 B2, which is included in the Appendix. Finally, Section 3.3 describes the characterization methods developed for both direct and global SolarSIMs, including the thermal test, directional response setup and optical calibration.

Chapter 4 presents the manuscripts that demonstrate the use of SolarSIM instruments in solar research applications. Section 4.1 describes the commissioning of the CanSIM network - consisting of seven measurement stations that are capable of retrieving in real-time all three spectral irradiance components over the full solar spectral range, in addition to the spectral aerosol optical depth, total column ozone and precipitable water vapour. Section 4.2 demonstrates the use of CanSIM data in calculating SCFs for a hypothetical CPV module. The SCF is a convenient metric that encapsulates the effect of local atmospheric conditions on the performance of a specific solar module and can be expressed as a time series, thus removing the complexity of working with vast spectral data sets. Section 4.3 presents a novel global irradiance decomposition algorithm, which derives the broadband DNI and DHI from the SolarSIM-G's spectral GHI measurements. This is accomplished through a quantitative approach of classifying atmospheric conditions via spectral clearness indices, which are also used as predictors in the irradiance decomposition algorithm. Finally, Section 4.4 lists a number of third party publications that have used local SolarSIM measurements in their respective research.

Chapter 5 presents the conclusion of this work by summarizing its main contributions to the field of solar measurements and photovoltaics as a whole. Lastly, possible next steps and applications to further advance this research are suggested.

1.2 Copyright Permissions

The journal articles in Sections 3.1.1 and 3.1.2 are presented in full and are reprinted with the permission from the Journal of Solar Energy.

- V. Tatsiankou, K. Hinzer, H. Schriemer, K. Emery, and R. Beal, "Design principles and field performance of a solar spectral irradiance meter". *Journal of Solar Energy*, vol. 133, pp. 94-102, 2016.

- V. Tatsiankou, K. Hinzer, H. Schriemer, S. Kazadzis, N. Kouremeti, J. Gröbner and R. Beal, "Extensive validation of solar spectral irradiance meters at the World Radiation Center". *Journal of Solar Energy*, vol. 166, pp. 80-89, 2018.

The manuscripts in Sections 3.2.1 and 4.3 are presented in full and are reprinted with the permission from Institute of Electrical and Electronics Engineers (IEEE).

- V. Tatsiankou, K. Hinzer, H. Schriemer, P. McVey-White, and R. Beal, "Efficient, real-time global spectral and broadband irradiance acquisition". *45th IEEE Photovoltaic Specialists Conference (PVSC)*, 2018.
- V. Tatsiankou, K. Hinzer, H. Schriemer, P. McVey-White, and R. Beal, "Improved global irradiance decomposition by sky condition classification from measured spectral clearness indices". *47th IEEE Photovoltaic Specialists Conference (PVSC)*, 2020.

The manuscripts in Sections 4.1 and 4.2 are presented in full and are reprinted with the permission from AIP Publishing.

- V. Tatsiankou, K. Hinzer, H. Schriemer, P. McVey-White, and R. Beal, "Deployment and early results from the CanSIM network". *AIP Conference Proceedings (CPV-13)*, 2017
- V. Tatsiankou, K. Hinzer, H. Schriemer, and R. Beal, "Toward routine measurement and calculation of spectrally corrected DNI for CPV systems". *AIP Conference Proceedings (CPV-15)*, 2019.

Chapter 2

Solar Spectral Resource

The sun emits spectrally non-uniform electromagnetic radiation, which can be approximated as an isotropic blackbody radiator with a surface temperature of 5800 K. A small amount of the sun's total irradiance, about 1361 W/m^2, reaches the top of the earth's atmosphere, where it is referred to as the air mass zero (AM0) extraterrestrial solar spectral irradiance. On its way to the earth's surface, portions of the AM0 spectrum are scattered and absorbed by various atmospheric constituents, such as aerosols, cloud droplets, water vapour and ozone molecules, and these complex interactions give rise to the direct, diffuse and global spectral irradiance components observed at ground level. This chapter takes a detailed look at the parameterized effects of the atmosphere on the spectral distribution of solar irradiance.

2.1 Extraterrestrial Irradiance

The sun emits electromagnetic radiation at different intensities in a wide wavelength range and its spectral distribution generally approximates the spectrum of an ideal blackbody radiator at around 5800 K. Over the last several decades numerous measurement campaigns have been conducted to quantify the sun's spectral distribution in space, otherwise known as the air mass zero or AM0 extraterrestrial solar spectrum, as it has considerable importance in many applications, including solar energy, atmospheric physics and climate studies to name a few. Historically, two methods have been used to measure the extraterrestrial spectral irradiance; ground-based telescopes pointing at the sun and spectrometers deployed in space. These experiments all focused on measuring specific parts of the solar spectrum, because all spectral instruments involved had detectors with limited spectral ranges. However, for many practical applications the knowledge of the "full" wavelength range (280–4000 nm) is desired, because virtually all of the sun's energy reaching the earth's surface lies within it. As a result, the full wavelength range of the AM0 spectrum must be assembled synthetically from multiple data sources, such as Gueymard's AM0 spectrum [22], which is widely used in solar energy applications. Figure 2.1 presents this synthetic spectrum in the 280–4000 nm spectral range. Over 75% of the AM0 irradi-

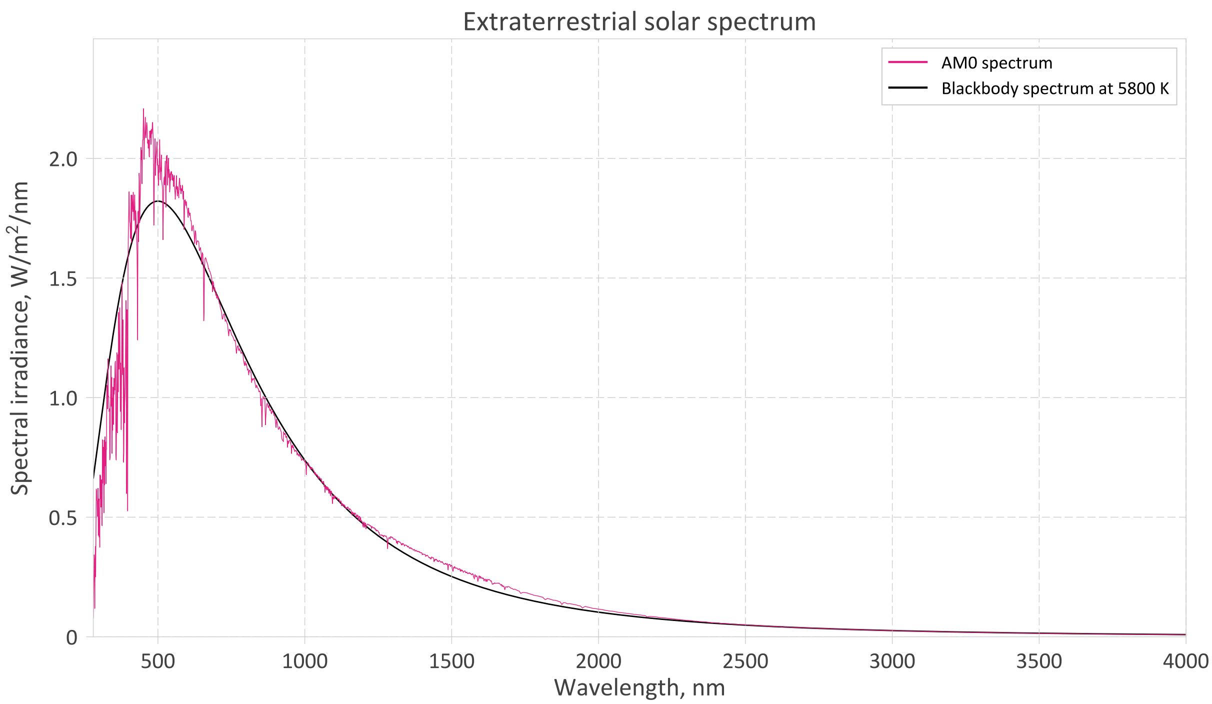

Figure 2.1: Synthetic AM0 extraterrestrial solar spectrum in the 280-4000 nm range at the mean sun-earth distance from [22]. This spectrum can be approximated as an ideal blackbody radiator with a surface temperature of 5800 K.

ance is contained within the 280–1100 nm range, with a peak irradiance of approximately 2.2 W/m^2/nm occurring at 451 nm.

The integral of the AM0 spectrum defines the total solar irradiance (TSI) which is currently accepted as 1360.8 $\pm$0.5 W/m^2 [24], but is known to slightly fluctuate by about $\pm$3 W/m^2 due sun spot activity [22]. Furthermore, because of the elliptical nature of the earth's orbit around the sun, the varying distance between two bodies causes the TSI to deviate from the solar constant by about $\pm$3% throughout the year. The latter variability can be accurately predicted and taken into account by most solar position algorithms.

2.2 Solar Coordinates

Knowing the relative position of the sun is important for many engineering applications, particularly in the field of solar energy. Two parameters, namely the azimuth and elevation angles, are typically used to define the sun's position within the observer's hemisphere, as shown in Figure 2.2. The elevation angle, θ, is measured from the horizontal plane up, with the maximum range of values from 0° (the sun is at horizon) to 90° (the sun is directly overhead). Often, the zenith angle, Z, is used in place of the elevation angle. It is measured from the zenith axis down to the solar position, such that $Z = 90° - \theta$. Meanwhile, the azimuth angle, ϕ, ranges from 0° to 360°, where 0° corresponds to true north.

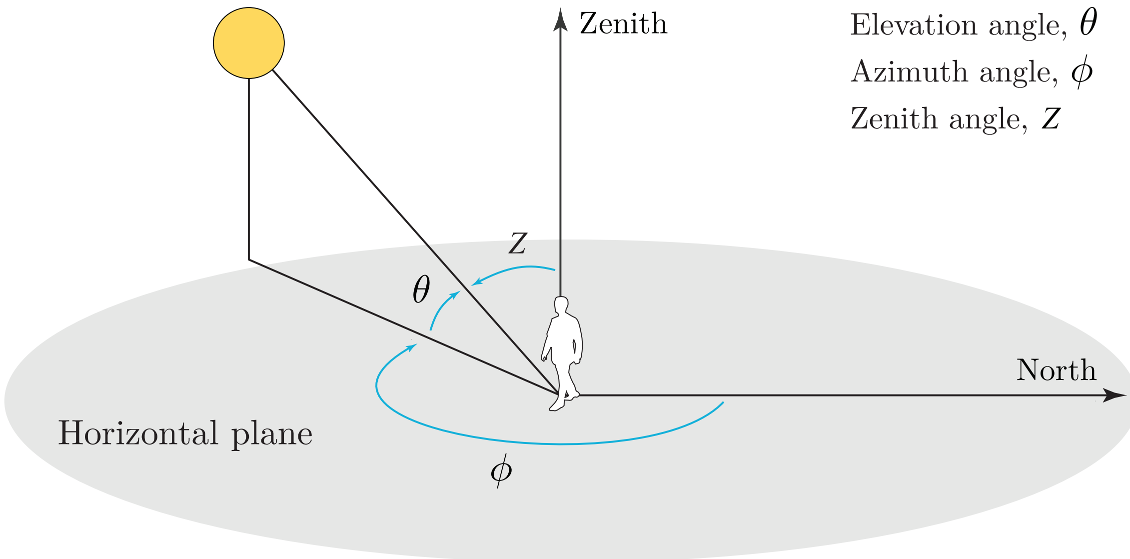

Figure 2.2: Local coordinate system defining the sun's position through the elevation and azimuth angles. The elevation angle is measured from the horizontal plane up, while the azimuth angle is measured clockwise from the north axis to the projection of the sun's position onto the horizontal plane.

Accurate computation of the solar elevation and azimuth angles can be an involved process due to the complex geometry between the sun and the observer on the earth, and, as a result, numerous solar position algorithms (SPA) exist to simplify this task. The National Renewable Energy Laboratory in the US has developed one of the most accurate SPAs currently available, with a stated error of $\pm 0.0003°$ from 2000 BC to AD 6000 [25]. This SPA requires several basic inputs from the user, namely the geographic latitude, longitude, altitude, local standard time and timezone, ambient pressure and air temperature. Amongst many output parameters, this algorithm provides the computed azimuth and elevation angles, and the sun-earth distance, which are essential for modelling the incident solar spectral resource.

2.3 Direct, Diffuse and Global Irradiances

On a clear-sky day the AM0 spectrum passes through the atmosphere largely unaffected and strikes the local horizontal plane at some elevation angle. This type of sunlight is termed the direct normal irradiance (DNI), consisting of near-collimated rays with a $\pm 0.267°$ divergence due to sun-earth geometry. Because of historical limitations in solar tracker accuracy, the technical definition of DNI was originally defined and is now accepted to be within a much wider $\pm 2.5°$ angular cone surrounding the sun disk [23]. The DNI that is outside of the sun's photosphere but still within the $\pm 2.5°$ technical limit is known as the circumsolar radiation. The remainder of the solar irradiance is scattered in all directions by the atmosphere and clouds, as shown in Figure 2.3. The scattered irradiance reaching the earth's surface is termed the diffuse horizontal irradiance (DHI), which also includes

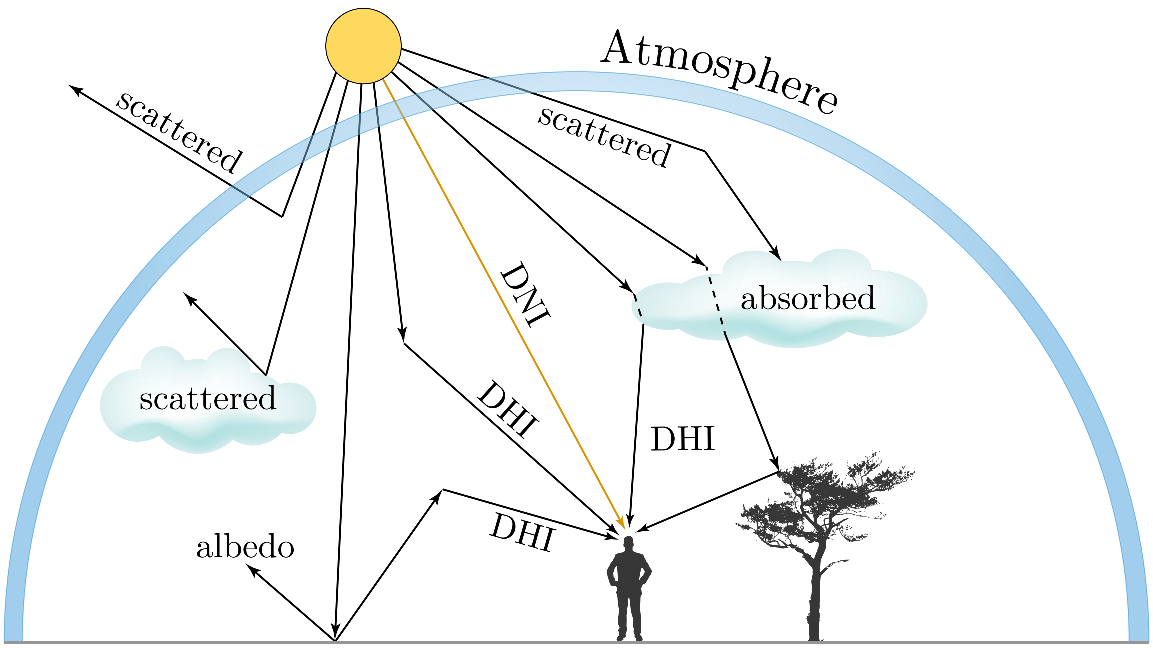

Figure 2.3: Atmospheric scattering and absorption of sunlight give rise to direct normal irradiance (DNI) and diffuse horizontal irradiance (DHI), which in combination are known as the global horizontal irradiance (GHI).

a small portion of the irradiance arising from multi-scattering effects between the ground albedo and the sky. The horizontal contribution of the DNI plus the DHI combine to yield the global horizontal irradiance (GHI).

GHI is the most common metric used to quantify the amount of sunlight in a given location and it is defined as

$$\mathrm{GHI} = \mathrm{DNI} \cdot \sin(\theta) + \mathrm{DHI}, \tag{2.1}$$

where θ is the sun's elevation angle. Equation 2.1 is a fundamental expression for many solar energy applications, and can also be written as

$$\int_{280}^{4000} S_{\mathrm{GHI}}(\lambda) \cdot \mathrm{d}\lambda = \Big(\int_{280}^{4000} S_{\mathrm{DNI}}(\lambda) \cdot \mathrm{d}\lambda \Big) \cdot \sin(\theta) + \int_{280}^{4000} S_{\mathrm{DHI}}(\lambda) \cdot \mathrm{d}\lambda, \tag{2.2}$$

where $S_{\mathrm{GHI}}(\lambda)$, $S_{\mathrm{DNI}}(\lambda)$, and $S_{\mathrm{DHI}}(\lambda)$ are the spectral GHI, DNI, and DHI, respectively, within the 280–4000 nm range. The clear-sky spectral DNI is defined as

$$\mathrm{S}_{\mathrm{DNI}}(\lambda) = S_0(\lambda) \cdot r^2 \cdot T_{\mathrm{a}}(\lambda) \cdot T_{\mathrm{g}}(\lambda) \cdot T_{\mathrm{o}}(\lambda) \cdot T_{\mathrm{R}}(\lambda) \cdot T_{\mathrm{w}}(\lambda), \tag{2.3}$$

where $S_0(\lambda)$ is the extraterrestrial irradiance, r is the ratio of the average to actual sun-earth distance, and $T_{\mathrm{i}}(\lambda)$ is the transmittance of each atmospheric constituent, with the subscripts "a", "g", "o", "R", and "w" referring to aerosol absorption and scattering,

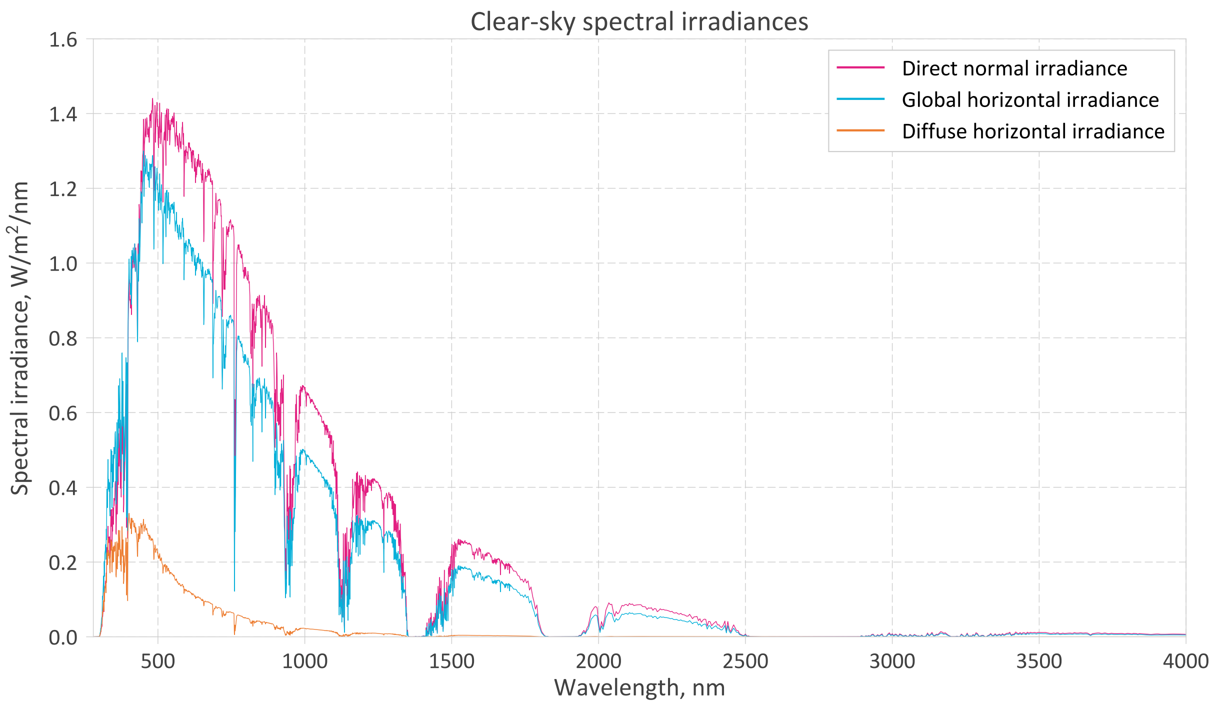

Figure 2.4: Modelled clear-sky spectral distribution of direct normal, global and diffuse horizontal irradiances for the solar elevation angle of 45°.

uniformly mixed gas absorption, ozone absorption, Rayleigh scattering, and water vapour absorption, respectively. The transmittance of atmospheric constituent, T_i, is given by

$$T_i(\lambda) = \exp\big(-\tau_i(\lambda) \cdot m_i\big), \tag{2.4}$$

where $\tau_i(\lambda)$ and m_i is the optical depth and the optical air mass associated with each atmospheric constituent, respectively. The geometric air mass, m, is defined as

$$m = \frac{1}{\sin(\theta)}. \tag{2.5}$$

The described parameterization of the spectral DNI is the basic working principle behind the SolarSIM-D2. The instrument's six optical measurements are combined with radiative transfer models to derive key atmospheric transmittances, namely due to aerosols, ozone and water vapour. The other transmittances from Equation 2.3 can be directly computed as they are generally functions of air temperature and ambient pressure. The expanded methodology for doing so is described more specifically in Section 3.1.1.

The expression for the clear-sky spectral DHI is more involved as compared to the direct beam irradiance, but it can be generally described as

$$S_{\mathrm{DHI}}(\lambda) = S_{\mathrm{R}}(\lambda) + S_{\mathrm{a}}(\lambda) + S_{\mathrm{m}}(\lambda), \tag{2.6}$$

where $S_{\mathrm{R}}(\lambda)$ and $S_{\mathrm{a}}(\lambda)$ are Rayleigh and aerosol scattering components, respectively, and $S_{\mathrm{m}}(\lambda)$ is the component that accounts for multiple reflections between the ground and the atmosphere. The analytical computation of $S_{\mathrm{R}}(\lambda)$ and $S_{\mathrm{a}}(\lambda)$ is very involved, but these functions can be approximated by the following expressions [26]

$$S_{\mathrm{R}}(\lambda) = \frac{S_{\mathrm{DNI}}(\lambda)}{T_{\mathrm{R}}(\lambda)} \cdot \sin(\theta) \cdot \left[1 - T_{\mathrm{R}}(\lambda)\right] \cdot 0.5, \tag{2.7}$$

$$S_{\mathrm{a}}(\lambda) = \frac{S_{\mathrm{DNI}}(\lambda)}{T_{\mathrm{a}}(\lambda)} \cdot \sin(\theta) \cdot T_{\mathrm{aa}}(\lambda) \cdot \left[1 - T_{\mathrm{as}}(\lambda)\right] \cdot F_{\mathrm{s}}(\lambda), \tag{2.8}$$

where $T_{\mathrm{aa}}(\lambda)$ and $T_{\mathrm{as}}(\lambda)$ are the transmittances of the aerosol absorption and aerosol scattering, respectively, and $F_{\mathrm{s}}(\lambda)$ is the downward aerosol scattering fraction, which are all involved functions that are strongly dependent on the aerosol particle shape, size, and concentration, as well as the atmospheric conditions. The spectral DNI, Rayleigh and aerosol scattering give rise to multiple reflections between the ground and the atmosphere. This contribution to the spectral DHI can be modelled as [26]

$$S_{\mathrm{m}}(\lambda) = \left[S_{\mathrm{DNI}}(\lambda) \cdot \sin(\theta) + S_{\mathrm{R}}(\lambda) + S_{\mathrm{a}}(\lambda)\right] \cdot \frac{R_{\mathrm{g}}(\lambda) \cdot R_{\mathrm{s}}(\lambda)}{1 - R_{\mathrm{g}}(\lambda) \cdot R_{\mathrm{s}}(\lambda)}, \tag{2.9}$$

where $R_{\mathrm{g}}(\lambda)$ is the spectral ground albedo and $R_{\mathrm{s}}(\lambda)$ is the sky reflectivity.

Figure 2.4 exhibits the modelled spectral distributions of direct normal, global and diffuse horizontal irradiances on a clear-sky day at solar elevation angle of 45°. These simulations were performed using a Simple Model of the Atmospheric Radiative Transfer of Sunshine (SMARTS), version 2.9.5 [27], [28]. As shown, the shapes of spectral DNI and GHI resemble one another under clear-sky conditions, as the latter arises mostly from the horizontal contribution of the direct normal beam irradiance throughout the 280–4000 nm range. The spectral DHI is virtually zero in the infrared region beyond 1100 nm, as the atmosphere mostly scatters the AM0 irradiance at shorter wavelengths. Consequently, most of the diffuse irradiance contribution to the spectral GHI, by proportion, occurs at wavelengths below 400 nm.

2.4 Impact of Atmospheric Constituents

Figure 2.5 shows the impact of the main atmospheric constituents on the direct beam spectral irradiance in the 280–4000 nm range under clear sky conditions. The transmittances due to each parameter can either be characterized as a smooth function of wavelength, such as Rayleigh scattering and aerosol extinction, or consisting of sharp spectral absorption bands, such as the case for the uniformly mixed gases (oxygen, carbon dioxide, methane), ozone and water vapour. The biggest difference between Rayleigh and aerosol scattering is the size of the particles involved. The first process arises mostly from scattering of sunlight by nitrogen and oxygen molecules, with the effective radii of approximately 0.3 nm, while the latter arises due to colloids of solid or liquid particles (aerosols) ranging in radii from 1–100,000 nm. Because of their relatively large particle size and radii variability, aerosols not only scatter the solar radiation but also absorb it. Consequently, the aerosol absorption must be measured locally to be accurately quantified.

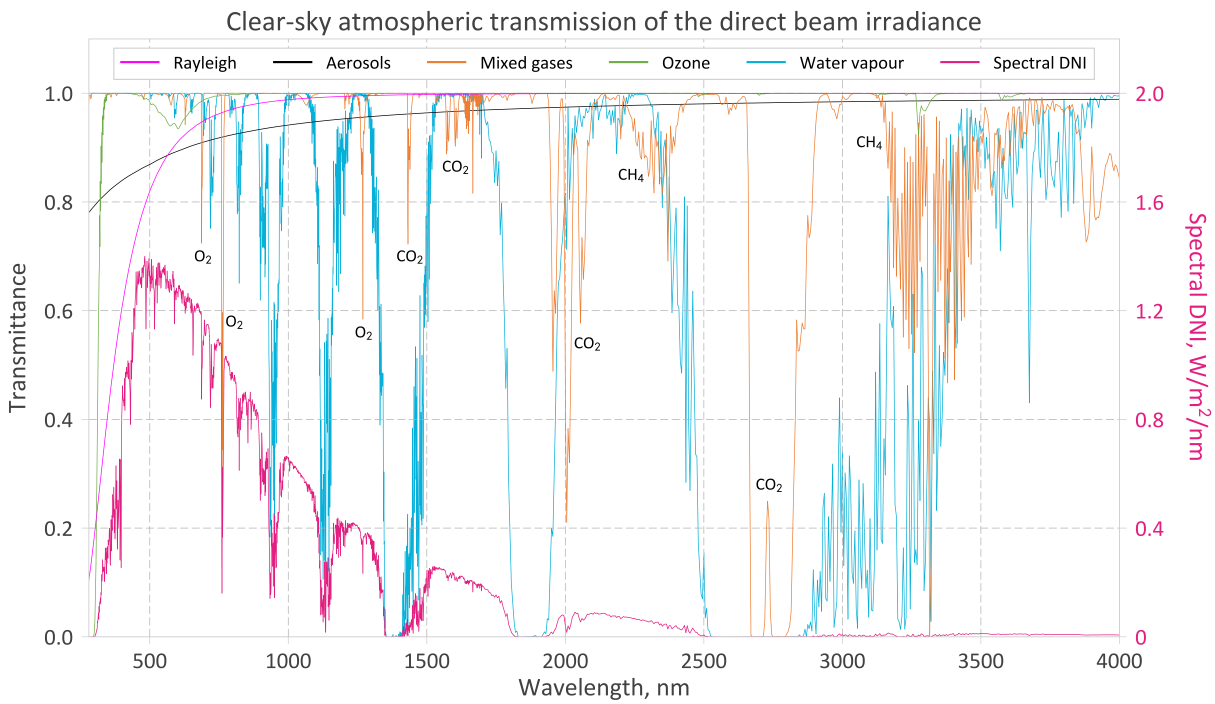

Figure 2.5: The impact of main atmospheric constituents on the direct beam irradiance under clear-sky conditions. This spectral DNI simulation is performed with an aerosol optical depth of 0.1 at 500 nm, a total column ozone of 340 DU, a precipitable water vapour amount of 14 mm, and a solar elevation angle of 45°.

The remaining atmospheric processes are molecular thus resulting in distinct spectral absorption profiles within the solar spectrum. Oxygen (O_2) molecules have a few sharp but very narrow absorption peaks centered at about 687, 761 and 1269 nm, while carbon dioxide (CO_2) and methane (CH_4) gases have wider absorption bands in the infrared region, as indicated in Figure 2.5. Ozone absorbs most of the harmful ultraviolet radiation below 300 nm, while having a moderate absorption in the Chappuis band centered at 610 nm. Lastly, water vapour has a very large effect on the direct beam irradiance, with numerous absorption bands, most notably centered around 940, 1130, 1370, 1875, and 2670 nm. The remaining spectral features in Figure 2.5 are due to absorption processes within the sun's atmosphere.

2.5 Effect of Clouds

Clouds have a profound effect on the solar spectral irradiance, mostly resulting in its attenuation but can also lead to irradiance enhancement under lensing conditions, i.e. when the unobstructed sun disk is surrounded by the clouds [29]. Most engineering models of solar irradiance do not account for the cloud spectral transmission due to the complexity associated with defining parameters, such as the cloud type, liquid water content, and the effective particle radius [30]. As a result, more involved models, such as the radia-

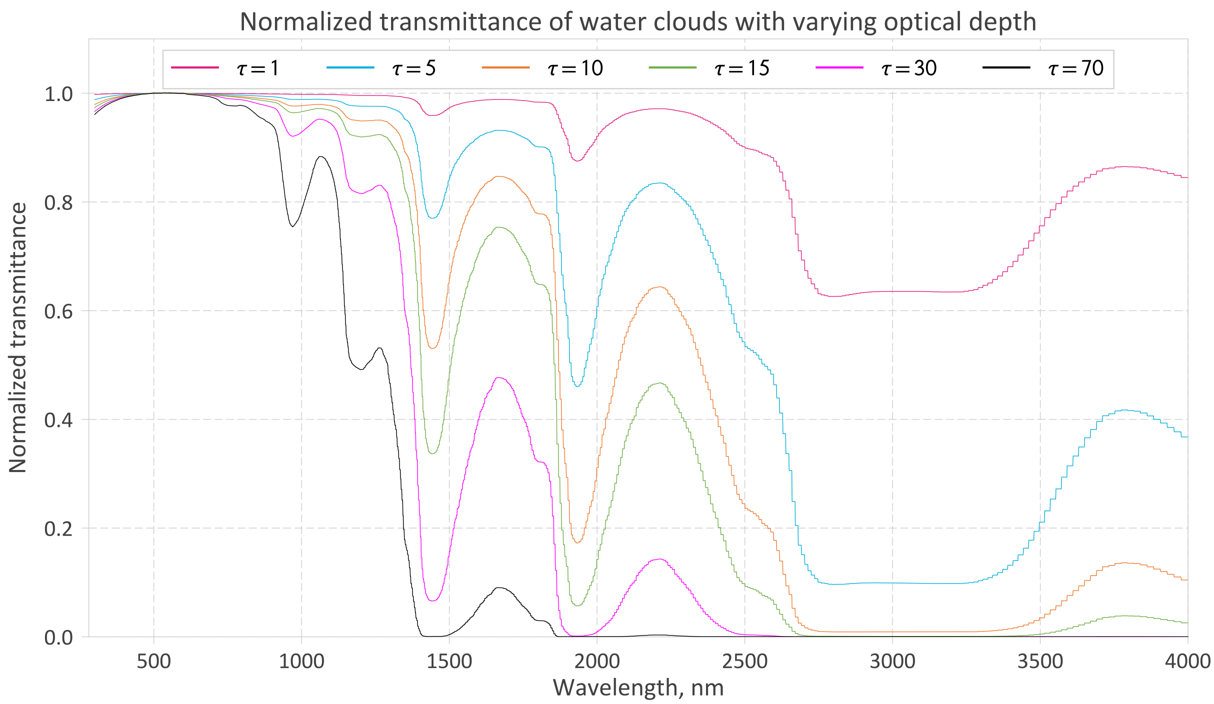

Figure 2.6: Simulation of water cloud transmittances for effective droplets' radii of 15μm at different cloud optical depths, τ. All transmittances are normalized at 500 nm.

tive transfer code libRadtran [31], must be used to perform this task. Figure 2.6 shows the libRadtran simulations for a one-kilometre thick layer of a water cloud with effective droplet's radii of 15 μm with total cloud optical depth, τ, varying from 1 to 70. The transmittances were normalized to 500 nm. Generally, below 900 nm clouds absorb and scatter the spectral irradiance almost uniformly, which explains why they look generally grayish-white to the human eye. However, further in the infrared region the cloud transmittance has distinct absorption bands, which generally coincide with the precipitable water vapour absorption bands. Under very overcast conditions ($\tau > 70$), clouds completely remove the spectral irradiance with wavelengths greater than 2000 nm, as demonstrated in Figure 2.6, while still allowing some of the visible light to pass through.

The aforementioned insights are employed as part of the SolarSIM-G's all-sky parameterized model to derive the cloud transmittance in the 1000-4000 nm range. The measurements from the SolarSIM-G's two furthest infrared channels are used to classify the clouds as either consisting of water droplets, ice crystals, or both. Subsequently, the model estimates the corresponding cloud optical depth for a one-kilometre thick, uniform cloud layer. Once the cloud type and its optical depth are known, the model computes the corresponding cloud transmittance in the 1000-4000 nm range. This methodology is essential for accurately determining the spectral and broadband global irradiances from the SolarSIM-G measurements. The efficacy of this approach has been validated by conducting definitive field studies comparing the measurements between the SolarSIM-G and reference instruments under all sky conditions, as demonstrated in Section 3.2.1 and Section 4.3.

Chapter 3

Solar Spectral Irradiance Meters

3.1 Direct SolarSIM

3.1.1 Design Principles and Field Performance

3.1.1.1 Scope and Impact

The following publication describes a direct solar spectral irradiance meter (SolarSIM-D2) that I designed for measuring the spectral DNI in six narrow wavelength bands. These measurements are combined with radiative transfer models to determine key atmospheric transmittances and the resulting spectral DNI under all sky conditions. This paper presents the design principles of the SolarSIM-D2 and the implementation of a parameterized transmittance model. Two SolarSIMs were calibrated at the National Renewable Energy Laboratory (NREL) and their short-term field performance was evaluated against reference spectroradiometers' and absolute cavity radiometer's measurements. A follow up longer-term study was performed at the University of Ottawa Outdoor Test Facility against a reference spectroradiometer and a pyrheliometer.

The SolarSIM-D2 represents a bold new approach to the measurement of spectral DNI and atmospheric constituents, which is critical for many applications, including solar research, atmospheric science, and weather forecasting. Prior to this development, spectral field measurements were predominantly reserved for national labs and well-funded institutions, primarily due to the high cost of spectroradiometers. With the advent of this novel sensor, the real-time spectral DNI data in the 280–4000 nm has become more readily available to researchers and other interested parties. Its relatively small size, low cost, and rugged design featuring no internal moving components, make the SolarSIM-D2 a very strong candidate for routine and dependable monitoring of solar spectral irradiance and atmospheric parameters.

3.1.1.2 Author Contributions

Viktar Tatsiankou: All research and scientific contributions in this article are my own but were sometimes guided and supported by other co-authors. The presented manuscript is a significant extension of my Master's work, where I previously designed, built, and field tested a direct SolarSIM prototype coupled with a parameterized transmittance model to derive the spectral and broadband DNI in the 280-4000 nm spectral range. The device functioned properly for a few weeks before moisture ingress led to the degradation of its soft-coated, bandpass interference filters and thus no useful irradiance data was obtained beyond that point. The relatively small data set however was sufficient to demonstrate that the developed methodology had the potential to be a viable alternative to expensive field spectroradiometers.

The first stage of my PhD work has focused on optimizing the approach developed during my Master's work, so that it could become the default instrument for performing spectral and broadband DNI measurements for both research and commercial applications. To accomplish this goal, the mechanical, optical, electrical and algorithmic designs had to be overhauled and optimized. These changes occurred incrementally through continuous research and development efforts, and culminated in two successive, commercialized SolarSIM versions, namely the D and the D2. The publication in this section describes the design, calibration, and field testing of the SolarSIM-D. Compared to the Master's prototype, the SolarSIM-D's mechanical design was completely overhauled by designing a sealed, custom aluminum enclosure with a pressure equalization vent to allow accurate operation of the ambient pressure and temperature sensor. The optical system was substantially improved by re-designing the optical train. First, the soft-coated bandpass filters were replaced with the hard-coated filters for increased environmental durability, improved transmittance, and better out of band rejection. Next, the photodiodes' field of view was redesigned to be 5°, instead of 5.8°, as per the WMO's standard for radiometric measurements of DNI. Furthermore, the collimation tube between the optical filters and the photodiodes was redesigned to minimize unwanted off-axis direct beam and/or diffuse irradiance contributions. The electrical design was modified by consolidating all components, including the photodiodes, onto a single printed circuit board, and adding an on-board temperature sensor to enable the automated thermal correction of the photodiodes' responsivities. The communication interface was changed from RS-232 to RS-485 to improve noise immunity and increase the transmission distance. As a result, a new communication protocol was developed between a host and the SolarSIM to send and write data.

The aforementioned changes were embodied in the SolarSIM-D, two of which were built, then optically calibrated and field tested at NREL, which is the subject of this section's publication. The comparative analysis against the reference instrumentation at NREL gave me the additional insight to improve the spectral reconstruction algorithm by swapping the bandpass filters centred at 780 nm and 1030 nm with the filters centred at 675 nm and 880 nm, respectively. These new optical channels were carefully chosen after performing optimization studies based on the field performance of the SolarSIMs at NREL. As a result, the reconstruction algorithm for retrieving the spectral aerosol optical depth and total column ozone amount was then optimized to reflect this new optical channel configuration.

Furthermore, the water vapour content retrieval algorithm was improved to be more stable at lower elevation angles. The described optical and algorithmic changes were implemented in the next design iteration, which resulted in the development of the SolarSIM-D2, whose uncertainty analysis and field performance are described in Section 3.1.2.

Dr. Karin Hinzer: As my supervisor and the director of the SUNLAB at the University of Ottawa, Karin oversaw my research and assisted with preparing the final manuscript.

Dr. Henry Schriemer: As the associate director of the SUNLAB at the University of Ottawa, Henry oversaw my research and helped to review and edit the manuscript.

Keith Emery: Keith has set up reference instruments at NREL's Optical Test Facility and provided me with their measurements, which were used in my comparative analysis. He also helped to review the final manuscript.

Dr. Richard Beal: As a collaborator from Spectrafy, Richard guided my research and aided in reviewing the final manuscript.

3.1.1.3 Publication

The publication follows on next page.

V. Tatsiankou, K. Hinzer, H. Schriemer, K. Emery, and R. Beal, "Design principles and field performance of a solar spectral irradiance meter". *Journal of Solar Energy*, vol. 133, pp. 94-102, 2016.

Available online at www.sciencedirect.com

ScienceDirect

Solar Energy 133 (2016) 94–102

SOLAR ENERGY

www.elsevier.com/locate/solener

Design principles and field performance of a solar spectral irradiance meter

V. Tatsiankou [a,*], K. Hinzer [a], J. Haysom [a], H. Schriemer [a], K. Emery [b], R. Beal [c]

[redacted]

Received 8 September 2015; received in revised form 29 February 2016; accepted 25 March 2016

Communicated by: Associate Editor David Renne

Abstract

A solar spectral irradiance meter (SSIM), designed for measuring the direct normal irradiance (DNI) in six wavelength bands, has been combined with models to determine key atmospheric transmittances and the resulting spectral irradiance distribution of DNI under all sky conditions. The design principles of the SSIM, implementation of a parameterized transmittance model, and field performance comparisons of modeled solar spectra with reference radiometer measurements are presented. Two SSIMs were tested and calibrated at the National Renewable Energy Laboratory (NREL) against four spectroradiometers and an absolute cavity radiometer. The SSIMs' DNI was on average within 1% of the DNI values reported by one of NREL's primary absolute cavity radiometers. An additional SSIM was installed at the SUNLAB Outdoor Test Facility in September 2014, with ongoing collection of environmental and spectral data. The SSIM's performance in Ottawa was compared against a commercial pyrheliometer and a spectroradiometer over an eight month study. The difference in integrated daily spectral irradiance between the SSIM and the ASD spectroradiometer was found to be less than 1%. The cumulative energy density collected by the SSIM over this duration agreed with that measured by an Eppley model NIP pyrheliometer to within 0.5%. No degradation was observed.

Keywords: Solar spectral irradiance meter; SSIM; Direct normal spectral irradiance; Solar resource assessment; Atmospheric parameterization; Solar spectrum

1. Introduction

Photovoltaic (PV) system performance fundamentally depends on the incident solar spectrum, which fluctuates both temporally and geographically. Different solar technologies respond to such fluctuations in varying degree, with single junction devices typically less influenced by spectral changes than are multi-junction solar cells (MJSC). A MJSC, used terrestrially in concentrator photovoltaic systems, consists of series-connected subcells with different bandgaps for more efficient use of the solar spectrum than is possible with a single junction because thermalization and transmission losses are reduced. In such a structure, the lowest current-generating subcell limits the performance of other subcells, so for optimal performance a MJSC is designed to be near current matched for a specific spectrum, such as the AM1.5D from the ASTM G173 standard (McMathon et al., 2002; Guter et al., 2009; Wiemer et al., 2011). But under outdoor conditions the solar spectrum deviates from the reference due to varying meteorological conditions, resulting in subcell current mismatch and thus reduced concentrator photovoltaic system performance

* Corresponding author. Tel.: [redacted]
E-mail address: [redacted]

http://dx.doi.org/10.1016/j.solener.2016.03.054
0038-092X/

(Muller et al., 2010; Chan et al., 2014; García-Domingo et al., 2014). Quantification of the solar spectrum is thus required for a complete performance analysis of these systems.

A field spectroradiometer is typically the most accurate way to determine a local solar spectrum. However, these measurements are rarely performed due to prohibitive instrumentation costs, which can approach \$100 K (depending on spectral range and manufacturer). The more cost-effective pyrheliometer, which measures the broadband direct normal irradiance (DNI) with an estimated uncertainty of $\pm 2\%$ (Sengupta et al., 2015), is typically used instead, but it does not provide the desired spectral information.

The solar spectrum may be reconstructed using modeling tools if sufficient local data exists. The Simple Model of the Atmospheric Radiative Transfer of Sunshine (SMARTS) has become the standard modeling tool (Gueymard, 1995, 2001). However, SMARTS requires inputs, such as the aerosol optical depth (at 500 nm), precipitable water vapor content, and ozone column amount, that are not often known locally. The Aerosol Robotic Network (AERONET), with over 300 stations worldwide, can provide these parameters to nearby sites (Holben et al., 1998, 2001) or can be used to interpolate necessary local parameters (Chan et al., 2013), but the AERONET site sparsity remains a severe constraint on the general applicability and accuracy of this technique. By contrast, we use an instrumentation-based approach for local spectral reconstruction via limited spectral sampling that retains the accuracy of the spectroradiometer but at a far lower price point. Historically, this technique for derivation of the continuous spectral distribution of sunlight was attempted before (Michalsky and Kleckner, 1984; Osterwald et al., 1988). More specifically, NREL developed the Atmospheric Optical Calibration System (Cannon and Hulstrom, 1993) as a low-cost measurement for spectral solar irradiance based on a SPCTRL2 model (Bird and Riordan, 1986) and a four-channel sun photometer.

Our solar spectral irradiance meter (SSIM), shown in Fig. 1a, uses ground-based measurements to inform software algorithm for rapid resolution of the location-specific solar spectrum across the entire 280–4000 nm range. The numerical integration of the SSIM's spectrum yields the DNI as typically measured by a pyrheliometer. It is a cost-effective alternative to purchasing a spectroradiometer and a pyrheliometer. The irradiance is measured in six carefully chosen wavelength bands, using low-cost silicon photodiodes with bandpass filters, to allow spectral reconstruction through parametrization of the major atmospheric processes (Tatsiankou et al., 2013).

In 2013, a two month deployment at the SUNLAB Outdoor Test Facility showed encouraging results, with the SSIM and Eppley pyrheliometer DNI agreeing within $\pm 1.5\%$, on average (Tatsiankou et al., 2014; Tatsiankou, 2014). Good spectral agreement between the SSIM and a commercial spectroradiometer was also observed.

Below we describe the design features of our commercially packaged SSIMs, and the parameterized transmittance model which the spectral reconstruction algorithm implements. Calibration and comparison results against National Renewable Energy Laboratory (NREL) multiple spectroradiometers and one of their primary absolute cavity radiometers are presented, followed by an eight month comparative study at the SUNLAB Outdoor Test Facility with an Eppley model NIP pyrheliometer and an ASD FieldSpec 3 spectroradiometer.

2. SSIM design features

The SSIM uses silicon photodiodes coupled with six bandpass filters to measure the spectral DNI in six wavelength bands with 10 nm full widths at half maximum (FWHM). By sampling the solar spectrum in these carefully selected wavelength channels, we are able to quantify aerosol absorption and scattering, ozone absorption, and water vapor absorption – three of the six dominant atmospheric processes that parameterize the spectrum. Table 1 shows which wavelength channels target each parameter. This is possible because the SSIM's channels are chosen in spectral regions where only one unknown atmospheric constituent dominates. For example, channels centered at

(a) (b)

Fig. 1. (a) SSIM installed at the University of Ottawa solar test site. (b) Two SSIMs tested at the NREL's Outdoor Test Facility.

Table 1
SSIM's channel specifications and target atmospheric constituents (Tatsiankou et al., 2013).

Channel center (nm)	Target parameter	FWHM (nm)
420, 500, 780, 1020	Aerosols	10
610	Ozone	10
940	Water vapor	10

500 and 780 nm can be used to deduce aerosol extinction for every wavelength in between these bands, since they are not significantly affected by either ozone or water vapor absorptions (Tatsiankou et al., 2013). The impact of the three remaining processes – mixed gas (O_2, CO_2, and CH_4) absorption, NO_2 absorption, and Rayleigh scattering – on spectral composition are primarily determined from local temperature and air pressure.

Each photodiode is situated within a collimation tube whose aperture and field stop geometries conform to the World Meteorological Organization standard for radiometric measurements of DNI (WMO, 2008). The 5° field of view is achieved by the geometric design of the SSIM's collimation tubes, which are concentric with the photodiodes. The aperture of each collimation tube is covered by a bandpass filter and is protected from the ambient environment by a BK-7 front window. The instrument does not require temperature control, because it applies an automated temperature calibration for each photodiode. The internal humidity is kept at a low level with a desiccant. The anodized aluminum housing encloses a data acquisition printed circuit that sequentially measures photodiode current from each channel, as well as ambient temperature and pressure. The photodiode current measuring circuit features a 0.1 pA input bias and 0.01 mV input offset transimpedance amplifier coupled with a 22-bit delta-sigma analog-to-digital converter. The total power consumption of the circuit is approximately 0.7 W. The photodiode current, ambient temperature and pressure data are sent via RS-485 communication protocol to a remote computer where specialized software driven by a graphical user interface implements spectral reconstruction over the 280–4000 nm range in real time (Tatsiankou et al., 2015). The reconstruction algorithm is based on the parameterized transmittance model discussed below.

3. Parameterized transmittance model

On a clear day the spectral DNI can be written as

$$S(\lambda) = S_0(\lambda) \cdot r^2 \cdot T_a(\lambda) \cdot T_g(\lambda) \cdot T_n(\lambda) \cdot T_o(\lambda) \cdot T_R(\lambda) \cdot T_w(\lambda), \tag{1}$$

where $S_0(\lambda)$ is the extraterrestrial irradiance (known as AM0), r is the ratio of the average to actual Sun to Earth distance, and $T_i(\lambda)$ is the transmittance of each atmospheric constituent, where the subscripts "a", "g", "n", "o", "R", and "w" referring to aerosol absorption and scattering, mixed gas absorption (O_2, CO_2, and CH_4), NO_2 absorption, ozone absorption, Rayleigh scattering, and water vapor absorption, respectively. The AM0 spectrum, with an integrated irradiance value of 1366.1 W/m^2, is adopted from the most recent measurements (Gueymard, 2004).

Eq. (1) can be expressed equivalently by Beer's law as

$$S(\lambda) = S_0(\lambda) \cdot r^2 \cdot \exp\left[-\tau_a(\lambda) \cdot m_a - \tau_g(\lambda) \cdot m_g - \tau_n(\lambda) \cdot m_n - \tau_o(\lambda) \cdot m_o - \tau_R(\lambda) \cdot m_R - \tau_w(\lambda) \cdot m_w^*\right], \tag{2}$$

where τ_i and m_i are the optical depth and the air mass associated with each atmospheric component, respectively, and each transmittance is given by

$$T_i(\lambda) = \exp(-\tau_i \cdot m_i). \tag{3}$$

The optical depth is a dimensionless measure of atmospheric transparency, as influenced by absorption and scattering. The air mass values are functions of the zenith angle of the sun. The air mass of each component can be written as (Gueymard, 2006)

$$m_i = \left[\cos(Z) + \kappa_{i1} \cdot Z^{\kappa_{i2}} \cdot (\kappa_{i3} - Z)^{\kappa_{i4}}\right]^{-1}, \tag{4}$$

where Z, zenith angle (in degrees) of the sun, calculated with the NREL solar position algorithm with an accuracy of $\pm 0.0003°$ (Reda and Andreas, 2004). The κ_{ij} parameters are given in Table 2 (Gueymard, 2006).

The optical depths for each parameter depend uniquely on wavelength, thus allowing unambiguous spectral reconstruction from a very limited data set. Aerosol extinction can be modeled empirically within each region y by Ångström's power law as (Ångström, 1929)

$$\tau_a(\lambda) = \beta_y \cdot \lambda^{-\alpha_y}, \tag{5}$$

where β_y and α_y are coefficients that are determined experimentally. The SSIM has four aerosol channels, with each set of β_y and α_y coefficients found and applied to the entire spectral region y between two adjacent aerosol channels.

Optical depth due to mixed gases is caused by the cumulative effect of multiple gases that are assumed to be uniformly distributed in the atmosphere and is represented as

$$\tau_g(\lambda) = p_{CH_4} \cdot A_{CH_4}(\lambda) + p_{CO_2} \cdot A_{CO_2}(\lambda) + p_{O_2} \cdot A_{O_2}(\lambda), \tag{6}$$

where p_i is the path length (or the total column abundance) of the constituent gas (in atm-cm), and $A_i(\lambda)$ is its wavelength-dependent absorption coefficient (in cm^{-1}).

Table 2
Optical air mass coefficients for Eq. (3).

Air mass	i	κ_{i1}	κ_{i2}	κ_{i3}	κ_{i4}
m_a	1	0.169	0.182	95.318	−1.954
m_g	2	0.484	0.0959	96.741	−1.754
m_n	3	1.121	1.613	111.55	−3.263
m_o	4	1.065	0.638	101.8	−2.269
m_R	5	0.484	0.0959	96.741	−1.754
m_w^*	6	0.107	0.114	93.781	−1.920

Note: $m_w^* = m_w^{0.943}$.

Each total column abundance depends on temperature and pressure as (Gueymard, 2006)

$$p_i = \chi_g \cdot H \cdot P_r^{\gamma} \cdot T_r^{\varphi}, \quad (7)$$

where χ_g is the known volume mixing ratio of gas (in parts per million by volume), $H = 8.429 \times 10^5$ cm is the scale height of the isothermal atmosphere, whose reference temperature and pressure are 288 K and 101.325 kPa, respectively; P_r and T_r are ratios of actual to reference pressure and temperature, respectively; and γ, φ are pressure and temperature correction coefficients, respectively. Table 3 presents the volume mixing ratios along with pressure and temperature correction coefficients for mixed gases. This optical depth may therefore be calculated directly from the measured ambient temperature and pressure.

Ozone and nitrogen dioxide optical depths τ_i, where i = "o" or "n", can both be expressed as (Gueymard, 2006)

$$\tau_i(\lambda) = p_i \cdot A_i(\lambda) \cdot C_i(\lambda), \quad (8)$$

where $A_i(\lambda)$ is an absorption coefficient in (cm^{-1}), $C_i(\lambda)$ is a unitless temperature correction function, and p_i is a path length (in atm-cm). $A_i(\lambda)$ and $C_i(\lambda)$ are known quantities for both ozone and nitrogen dioxide. While the ozone optical depth may be extracted from the SSIM ozone channel measurement, the nitrogen dioxide optical depth may be calculated directly. A total column abundance $p_n = 0.00118$ atm-cm is used, which is the average concentration of nitrogen dioxide in Montreal, Canada in 2005 under the assumption that this pollution layer is 1 km thick (Gilbert et al., 2005).

Rayleigh scattering is a well-known phenomenon (Bucholtz, 1995; Bodhaine et al., 1999) that allow the optical depth to be calculated from (Gueymard, 2006)

$$\tau_R(\lambda) = \frac{P_r}{n_1 \cdot \lambda^4 + n_2 \cdot \lambda^2 + n_3 + n_4 \cdot \lambda^{-2}}, \quad (9)$$

where P_r is the ratio of site to sea level ambient pressure, and $n_1 = 117.341$ nm^{-4}, $n_2 = 1.511$ nm^{-2}, $n_3 = 0.0175$, and $n_4 = 8.774$ nm^2.

The expression for precipitable water vapor optical depth is (Gueymard, 2006)

$$\tau_w(\lambda) = p_w^{0.943} \cdot \varepsilon_1(\lambda) \cdot \varepsilon_2(\lambda) \cdot A_w(\lambda), \quad (10)$$

where $A_w(\lambda)$ is the known absorption coefficient (cm^{-1}), $\varepsilon_1(\lambda)$ is a pressure scaling factor that accounts for water vapor's inhomogeneity in the atmosphere, $\varepsilon_2(\lambda)$ is a correction factor that improves parameterization away from the band center under fluctuating humidity conditions, and p_w is the water vapor path length (in atm-cm). Absorption coefficients and correction factors for all atmospheric constituents are used as in SMARTS, except for some minor modifications. With the model definitely described, we now discuss its implementation in our spectral reconstruction algorithm.

Table 3
Mixed gases volume mixing ratios (Jacobson, 2005) with pressure and temperature correction coefficients (Gueymard, 2006).

Mixed gas	χ_g (ppmv)	γ	φ
CH_4	1.8	1.125	0.0473
CO_2	375	1	0
O_2	209500	1	0

4. Algorithm implementation

As seen in Section 3, parameters $T_g(\lambda)$, $T_n(\lambda)$, and $T_R(\lambda)$ in Eq. (1) are directly calculable if geographic parameters, time stamp, ambient temperature, and site pressure are known. We now describe the algorithm used by the SSIM software to determine the three remaining transmittances, focusing primarily on the aerosols.

The spectral irradiance measured by the SSIM aerosol channel centered at λ_c is given by Eq. (1), except that $T_o(\lambda)$ and $T_w(\lambda)$ are set to unity for $\lambda_1 \leqslant \lambda \leqslant \lambda_2$, where λ_1 and λ_2 delimit the 50 nm range of wavelengths for which the filter transmittance $F_i(\lambda)$ is nonzero. The manufacturer's generic filter transmittance data is used for each channel. Therefore, the simulated current of the photodiode for aerosol channel i can be expressed as

$$I_i = D \cdot r^2 \cdot \int_{\lambda_1}^{\lambda_2} T_a(\lambda) \cdot C_i(\lambda) \cdot d\lambda, \quad (11)$$

where D is the active area of the photodiode, r is the ratio of the average to actual Sun to Earth distance, $C_i(\lambda) = S_0(\lambda) \cdot T_g(\lambda) \cdot T_n(\lambda) \cdot T_R(\lambda) \cdot F_i(\lambda) \cdot R(\lambda)$, and $R(\lambda)$ is the manufacturer's responsivity of the photodiode. The uniform trapezoidal rule is used to do the integration in Eq. (11), once $T_a(\lambda)$ is known. Eqs. (2) and (5) in Eq. (3) gives

$$T_a(\lambda) = \exp\left[-\beta_y \cdot \lambda^{-\alpha_y} \cdot m_a\right], \quad (12)$$

and for a given aerosol extinction region y, the values of α_y and β_y are optimized such that the simulated photodiode current agrees with the measured current from the SSIM. A Golden section search algorithm is used to find the values of α_y and β_y that produce the smallest residual error (Press et al., 1992). This optimization routine is performed for each aerosol region y to determine the aerosol transmittance $T_a(\lambda)$. Calculation of the aerosol transmittance is a crucial step in deriving ozone and water vapor transmittances.

The spectral irradiance for ozone and water vapor channels is also given by Eq. (1). To determine $T_o(\lambda)$, one sets $T_w(\lambda)$ to unity, and vice versa, using equations of the same form as Eq. (11) to find anticipated photodiode currents. The same optimization process is followed. The unknown ozone and water vapor transmittances are each expressed in like manner to Eq. (12). Both ozone and water vapor total column abundances, p_o and p_w, are found with a Golden section search algorithm that minimizes the residual difference between the simulated and measured current values. Once all parameters are found, the final spectral distribution is calculated from Eq. (1) with a 1 nm resolution.

5. Calibration and initial evaluation

5.1. Calibration

A side-by-side on-sun comparison of the SSIM with a calibrated direct normal spectroradiometer was done. This test was performed at NREL's Outdoor Test Facility in Golden, Colorado, USA (39.74°N, 105.18°W) on 17 November 2014. Two SSIMs (serial numbers SN102 and SN103) were mounted on a SOLYS 2 sun tracker, as shown in Fig. 1b. Data were acquired and processed from both devices every five seconds. The reference spectroradiometer, a Prede PGS-100, was located at NREL's Solar Radiation Research Laboratory, 200 m west and 100 m higher than the SSIM location. It has a silicon CCD array with a 1 degree field of view, a spectral range from 350 to 1050 nm, a spectral bandwidth of 3.6 nm, and a 0.7 nm resolution. Last calibrated on 6 November 2014 (mere days before this work), the PGS-100 spectroradiometer has traceability to the NIST Spectral Irradiance Lamp Standard through a LICOR LI-1800 secondary standard spectroradiometer.

The calibration procedure ensured that the SSIM's spectral irradiance in its six optical channels matched the irradiance from the PGS-100 at the corresponding wavelengths. Upon completion, six calibration factors were obtained, one for each channel, to compensate for deviations from the generic manufacturer's filter transmittances and photodiode responsivities used in our model. Immediately after calibration, the solar spectra from both SSIMs, the PGS-100, and the extended range spectroradiometer combination EKO MS-710 and EKO MS-712 (WISER) were acquired, as shown in Fig. 2a. Both SSIMs are in excellent agreement with the PGS-100, which validates the SSIM design and parameterized transmittance model. As expected, the PGS-100 and WISER spectra agree to within the measurement uncertainties of both instruments.

5.2. Short term performance

Following the calibration procedure, the SSIM performance was extensively tested against NREL reference instrumentation. On 21 November 2014, four spectroradiometers, calibrated at NREL within the last 6 months

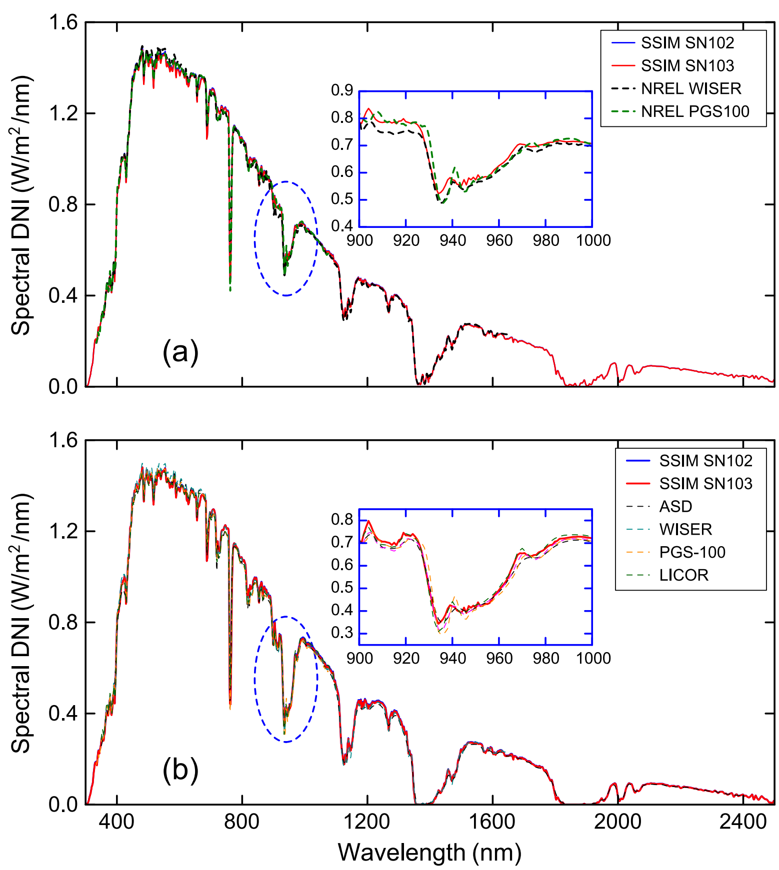

Fig. 2. (a) Solar spectra measured by the SSIMs as compared to that measured by PGS-100 and WISER spectroradiometers immediately after the calibration procedure on November 17, 2014 at 13:05 MST. (b) Solar spectra measured by the SSIMs as compared to that measured by PGS-100, WISER, ASD, and LICOR spectroradiometers four days after the calibration on November 21, 2014 at 10:00 MST. Insets are magnifications around the water vapor channel to facilitate comparisons.

using a calibrated standard lamp purchased from NIST, were used for a comparative analysis with the SSIMs. To the aforementioned PGS-100 and WISER, LICOR LI-1800 and ASDi FieldSpec 3 (ASD) spectroradiometers were added. The latter two instruments were mounted on a separate tracker within a few meters of the SSIMs. Excellent agreement was found between all instruments with their integral of spectral irradiance agreeing to within 1% as compared to the SSIMs' integral of spectral irradiance in corresponding wavelengths range, as shown in Fig. 2b. The ASD tends to slightly underestimate the solar irradiance for wavelengths below 450 nm as compared to the other reference instruments. The ASD's ability to measure the solar spectrum up to 2500 nm, however, validates the SSIM performance in the IR range.

An Eppley HF absolute cavity radiometer (ACR) with traceability to the World Radiometric Reference was used to infer SSIM performance across the solar spectral range through continuous measurement of the DNI (Fröhlich, 1991; Reda, 1996). To compare with ACR DNI, SSIM DNI was obtained every five seconds and the reconstructed solar spectra were integrated across the entire 280–4000 nm range; the results are presented in Fig. 3a. Gaps appear in the measurement record since data acquisition was done only under clear sky conditions during which the sun's disk was unobscured by visible clouds. The DNI from both SSIMs was found to be within ±1%, on average, of ACR DNI. Since the ACR has a field accuracy of 0.5% (Michalsky et al., 2011), this is an exceptionally good agreement. These two SSIMs are now used as SUNLAB tertiary calibration standards.

6. Seasonal field trials

SSIM with a serial number SN101 was installed at the SUNLAB Outdoor Test Facility (45.42°N, 75.68°W) in September 2014. The device was situated on the same mechanical plate assembly as an Eppley model NIP pyrheliometer and an ASD FieldSpec 3 spectroradiometer, which measures spectral DNI in the 350–1830 nm range. The assembly was mounted on a Golden Sun GS-3500 dual-axis tracking system to point these instruments directly at the sun to within accuracy of ±0.2° (Schriemer et al., 2015).

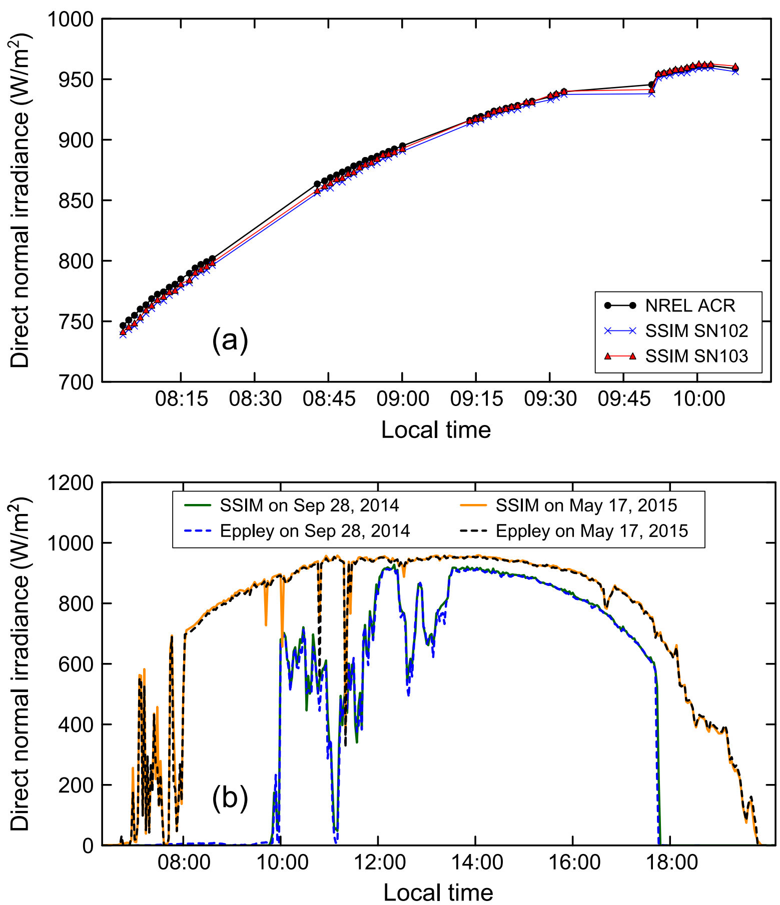

Fig. 3. (a) Comparison of the DNI from the SSIMs SN102 and SN103 and the Eppley absolute cavity radiometer (ACR) on 21 November 2014. Data were acquired only under optimal atmospheric conditions. (b) Comparison of the DNI between the Eppley pyrheliometer and SSIM on a partially cloudy and a mostly clear sky day, occurring on 28 September 2014 and 21 May 2015, respectively.

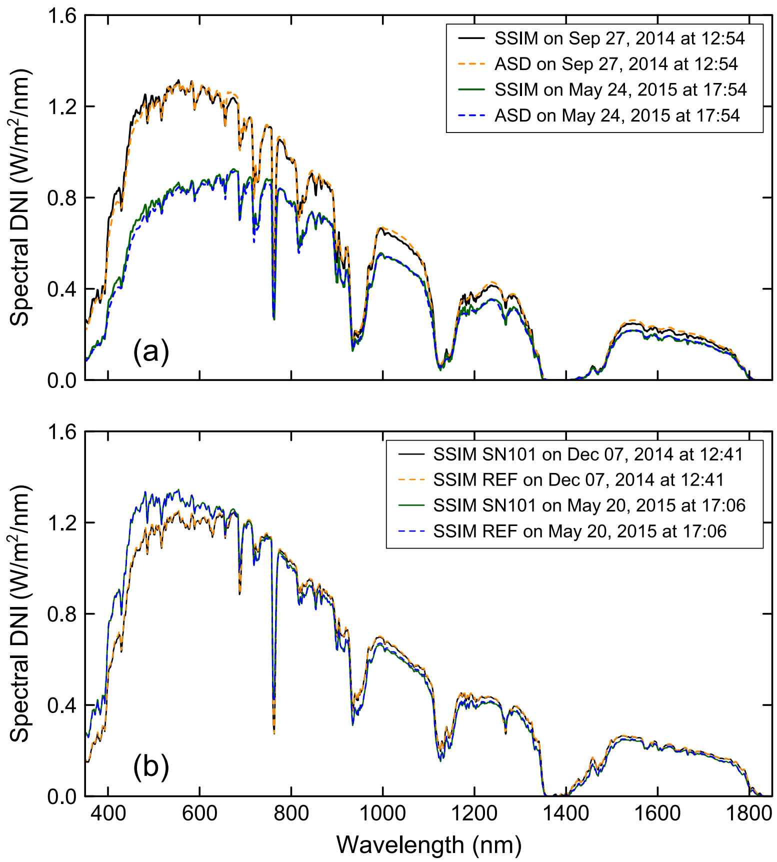

Fig. 4. (a) Comparison of ASD spectroradiometer and SSIM spectra for selected timestamps. (b) Comparison of spectra as measured by SSIM SN101 and reference SSIM SN102 on the calibration date of 7 December 2014 and four months later on May 3 2015.

SSIM SN101 was initially calibrated against the ASD spectroradiometer through direct on-sun comparison, using the same approach as at NREL. It was re-calibrated on 7 December 2014 against the NREL-calibrated reference SSIM SN102 and the new calibration file was also applied to all preceding data gathered by SSIM SN101.

The performance of the SSIM was evaluated against the Eppley pyrheliometer and the ASD spectroradiometer at the SUNLAB Outdoor Test Facility during the course of eight months. Representative comparisons of SSIM and pyrheliometer DNI profiles are shown in Fig. 3b for two separate days, a partially cloudy on 28 September 2014, and a mainly clear on 17 May 2015. SSIM and pyrheliometer DNI were found to agree within ±1% under clear sky conditions, on average. This exceptional agreement was only slightly degraded during times of rapid cloud transients due to the difference in detector response times. Similarly, representative comparisons of SSIM and ASD spectra shown in Fig. 4a for selected timestamps on 27 September 2014 and 24 May 2015, demonstrate a good spectral agreement between both instruments. The difference in the integrated spectral irradiance was found to be less than 1%, on average, although the ASD spectroradiometer again tended to systematically underestimate the solar spectrum below 500 nm. In service degradation of SSIM SN101 spectral channels was also periodically assessed over the eight month field trial by comparison with the SSIM calibration standard (SN102, stored indoors). SSIM spectra taken on 3 April 2015, about four months after the 7 December 2014 calibration date, show no appreciable difference between the in field unit and the reference standard, suggesting long term SSIM reliability.

To further validate SSIM longterm reliability, its cumulative and daily energy densities derived from the measured local solar spectra were compared to the corresponding measurements from the pyrheliometer across a continuous eight month period from 27 September 2014 to 28 May 2015. Data were acquired at two minute intervals and energy densities calculated for all values exceeding a DNI threshold of 50 W/m^2 and is summed up over the course of eight months with a two minute resolution. Several days where omitted due to snow coverage. The results are shown in Fig. 5. The daily energy densities (left axis), shown by the red[1] and green bars, for the SSIM and pyrheliometer,

[1] For interpretation of color in Fig. 5, the reader is referred to the web version of this article.

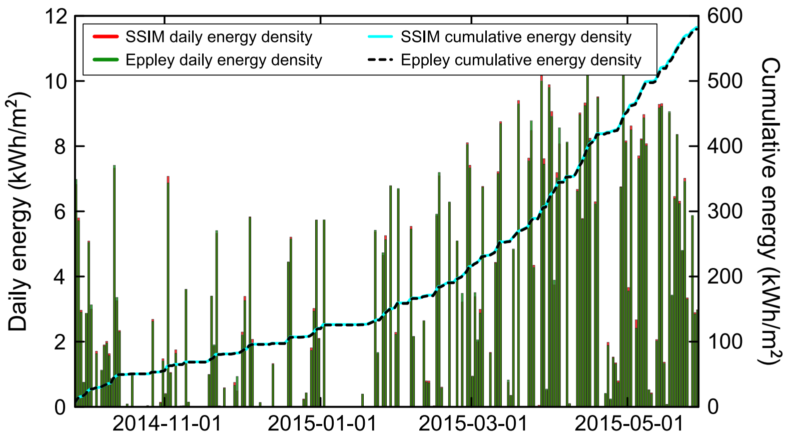

Fig. 5. The cumulative and daily energy densities comparison between the Eppley pyrheliometer and the SSIM over eight months. The cumulative energy density as measured by the SSIM agrees to less than 0.5% of the corresponding value as reported by the Eppley pyrheliometer.

respectively, are seen to be in excellent agreement across the entire eight month period, differing by only ±1% on average. Eppley pyrheliometer and SSIM cumulative energy densities for this period are 579.5 and 582.3 kW h/m^2, respectively. This difference, of less than 0.5%, indicates truly exceptional agreement, considering the pyrheliometer's measurement uncertainty of ±2%.

7. Conclusion

A SSIM has been presented as a reliable, accurate and cost-effective alternative to a spectroradiometer and a pyrheliometer. Two SSIMs were validated at NREL against secondary reference spectroradiometers and an Eppley ACR. The SSIMs showed an excellent performance against four spectroradiometers at NREL, with a near perfect matching in spectral irradiance under clear sky conditions. The DNI was found to be within ±1% of the ACR DNI, on average.

SSIM long term performance was validated against a Eppley model NIP pyrheliometer and an ASD spectroradiometer at the SUNLAB Outdoor Test Facility between 27 September 2014 and 28 May 2015. During this period the DNI determined by the SSIM was found to agree within ±1% of that measured directly by the pyrheliometer with over 20,000 data points used in the analysis. The SSIM was found to accurately reproduce the solar spectrum, with the integrated spectral irradiance agreeing with that of the ASD spectroradiometer and the reference SSIM to within ±1%. Furthermore, the integrated difference in the cumulative energy density between the SSIM and an Eppley pyrheliometer was within 0.5% over the course of eight months. No degradation of bandpass filter performances or detector sensitivities was observed.

These results demonstrate that the SSIM is an accurate and reliable instrument for measuring solar spectral irradiance in six wavelength bands, providing an accurate reconstruction of the solar spectrum and broadband DNI. The small size, low cost and rugged design with no internal moving components makes it a very strong candidate for routine and dependable monitoring of solar spectral irradiance in diverse environments.

Acknowledgments

The authors would like to acknowledge support from the National Sciences and Engineering Research Council of Canada, the Ontario Research Fund – Research Excellence program, the Ontario Centres of Excellence, Canada Research Chair program, and the Canadian Foundation for Innovation.

The NREL portion of this work was supported by the U.S. Department of Energy under Contract No. DE- AC36-08-GO28308 with the National Renewable Energy Laboratory.

References

Ångström, A., 1929. On the atmospheric transmission of sun radiation and on dust in the air. Geogr. Ann. 11, 156–166.
Bird, R.E., Riordan, C., 1986. Simple solar spectral model for direct and diffuse irradiance on horizontal and tilted planes at the earth's surface for cloudless atmospheres. J. Climate Appl. Meteorol. 25 (1), 87–97.
Bodhaine, B.A., Wood, N.B., Dutton, E.G., Slusser, J.R., 1999. On Rayleigh optical depth calculations. J. Atmos. Ocean. Technol. 16, 1854–1861.
Bucholtz, A., 1995. Rayleigh-scattering calculations for the terrestrial atmosphere. Appl. Opt. 34 (15), 2765–2773.
Cannon, T., Hulstrom, R., 1993. Atmospheric optical calibration system for outdoor testing of photovoltaic devices. Metrologia 30 (4), 409.
Chan, N.L.A., Brindley, H.E., Ekins-Daukes, N.J., 2014. Impact of individual atmospheric parameters on CPV system power, energy yield and cost of energy. Prog. Photovoltaics Res. Appl. 22 (10), 1080–1095.
Chan, N.L.A., Young, T.B., Brindley, H.E., Ekins-Daukes, N.J., Araki, K., Kemmoku, Y., Yamaguchi, M., 2013. Validation of energy prediction method for a concentrator photovoltaic module in Toyohashi, Japan. Prog. Photovoltaics Res. Appl. 21 (8), 1598–1610.
Fröhlich, C., 1991. History of solar radiometry and the world radiometric reference. Metrologia 28 (3), 111.
García-Domingo, B., Aguilera, J., de la Casa, J., Fuentes, M., 2014. Modelling the influence of atmospheric conditions on the outdoor real

performance of a CPV (concentrated photovoltaic) module. Energy 70, 239–250.

Gilbert, N.L., Goldberg, M.S., Beckerman, B., Brook, J.R., Jerrett, M., 2005. Assessing spatial variability of ambient nitrogen dioxide in Montreal, Canada, with a land-use regression model. J. Air Waste Manage. Assoc. 55 (8), 1059–1063.

Gueymard, C., 1995. SMARTS2: A Simple Model of the Atmospheric Radiative Transfer of Sunshine: Algorithms and Performance Assessment. Florida Solar Energy Center, Cocoa, FL.

Gueymard, C.A., 2001. Parameterized transmittance model for direct beam and circumsolar spectral irradiance. Sol. Energy 71, 325–346.

Gueymard, C.A., 2004. The sun's total and spectral irradiance for solar energy applications and solar radiation models. Sol. Energy 76, 423–453.

Gueymard, C.A., 2006. SMARTS2 Code, Version 2.9.5, User's Manual. Tech. Rep., Solar Consulting Services.

Guter, W., Schöne, J., Philipps, S.P., Steiner, M., Siefer, G., Wekkeli, A., Welser, E., Oliva, E., Bett, A.W., Dimroth, F., 2009. Current-matched triple-junction solar cell reaching 41.1% conversion efficiency under concentrated sunlight. Appl. Phys. Lett. 94 (22), 223504.

Holben, B., Eck, T., Slutsker, I., Tanre, D., 1998. AERONET – a federated instrument network and data archive for aerosol characterization. Remote Sens. Environ. 66 (1), 1–16.

Holben, B., Tanre, D., Smirnov, A., Eck, T., 2001. An emerging ground-based aerosol climatology: aerosol optical depth from AERONET. J. Geophys. Res.: Atmos. 106 (D11), 12067–12097.

Jacobson, M.Z., 2005. Fundamentals of Atmospheric Modeling. Cambridge University Press, New York, USA.

McMathon, W., Kurtz, S., Emery, K., Young, M., 2002. Criteria for the Design of GalnP/GaAs/Ge Triple Junction Cells to Optimize their Performance Outdoors. Tech. Rep. National Renewable Energy Laboratory.

Michalsky, J., Dutton, E.G., Nelson, D., Wendell, J., Wilcox, S., Andreas, A., Gotseff, P., Myers, D., Reda, I., Stoffel, T., 2011. An extensive comparison of commercial pyrheliometers under a wide range of routine observing conditions. J. Atmos. Ocean. Technol. 28 (6), 752–766.

Michalsky, J., Kleckner, E., 1984. Estimation of continuous solar spectral distributions from discrete filter measurements. Sol. Energy 33 (1), 57–64.

Muller, M., Marion, B., Kurtz, S., Rodriguez, J., 2010. An investigation into spectral parameters as they impact CPV module performance. In: AIP Conference Proceedings, vol. 1277, p. 307.

Osterwald, C., Emery, K., Myers, D., Riordan, C., 1988. Extending the spectral range of silicon-based direct-beam solar spectral radiometric measurements. Photovoltaic Specialists Conference, 1988. Conference Record of the Twentieth IEEE. IEEE, pp. 1246–1250.

Press, W.H., Teukolsky, S.A., Vetterling, W.T., Flannery, B.P., 1992. Golden section search in one dimension. Numer. Recipies C: Art Sci. Comput. 2.

Reda, I., 1996. Calibration of a Solar Absolute Cavity Radiometer with Traceability to the World Radiometric Reference. Tech. Rep. National Renewable Energy Lab., Golden, CO, USA.

Reda, I., Andreas, A., 2004. Solar position algorithm for solar radiation applications. Sol. Energy 76 (5), 577–589.

Schriemer, H., Cook, J.P., Sharma, P., De La Salle, L., Carle, F., White, P.M., Tatsiankou, V., Bosscher, N., Haysom, J.E., Dragomirescu, E., Hinzer, K., 2015. Refractive concentrator optics architectures, tracker precision, and cumulative energy harvest. 42nd IEEE Photovoltaic Specialists Conference (PVSC).

Sengupta, M., Habte, A., Kurtz, S., Dobos, A., Wilbert, S., Lorenz, E., Stoffel, T., Renné, D., Gueymard, C.A., Myers, D., et al., 2015. Best Practices Handbook for the Collection and use of Solar Resource Data for Solar Energy Applications. Tech. Rep. National Renewable Energy Laboratory.

Tatsiankou, V., 2014. Instrumentation Development for Site-specific Prediction of Spectral Effects on Concentrated Photovoltaic System Performance Master's Thesis. University of Ottawa.

Tatsiankou, V., Hinzer, K., Muron, A., Haysom, J., Schriemer, H., Myrskog, S., 2014. Solar resource assessment with the solar spectral irradiance meter. International Conference on Concentrating Photovoltaic Systems: CPV-10.

Tatsiankou, V., Hinzer, K., Muron, A., Mohammed, J., Wilkins, M., Haysom, J., Schriemer, H., Myrskog, S., 2013. Reconstruction of the solar spectral resource using limited spectral sampling for concentrating photovoltaic systems. In: Photonics North, vol. 891506. International Society for Optics and Photonics.

Tatsiankou, V., Hinzer, K., Schriemer, H., Haysom, J., Beal, R., 2015. A novel instrument for cost-effective and reliable measurement of solar spectral irradiance. Photovoltaic Specialist Conference (PVSC), 2015 IEEE 42nd. IEEE, pp. 1–4.

Wiemer, M., Sabnis, V., Yuen, H., 2011. 43.5% efficient lattice matched solar cells. SPIE Solar Energy+ Technology. International Society for Optics and Photonics, 810804–810804.

WMO, 2008. Guide to Meterological Instruments and Methods of Observation.

3.1.2 Measurement Uncertainty and Field Campaigns

3.1.2.1 Scope and Impact

The presented work shows a comprehensive uncertainty analysis for all SolarSIM-D2 measurands, including spectral and broadband DNIs, spectral aerosol optical depth, total column ozone and precipitable water vapour content. These findings were used to evaluate the measurements of four SolarSIMs deployed at the Physikalisch-Meteorologisches Observatorium Davos and World Radiation Center in Davos, Switzerland against reference instrumentation, which included spectroradiometers, absolute cavity radiometers, Brewer spectrophotometers and sun photometers.

Performing the uncertainty analysis for the SolarSIM-D2's measurands was an important step toward validating the instrument's multi-functionality with many possible applications in solar research, atmospheric sciences, and weather forecasting. The field deployment at the World Radiation Center further proved that the SolarSIM-D2 is capable of performing accurate and precise measurements of broadband and spectral DNI, spectral aerosol optical depth, total column ozone and precipitable water vapour.

3.1.2.2 Author Contributions

Viktar Tatsiankou: All research and scientific contributions in this article are my own but were sometimes guided and supported by other co-authors. The primary contribution is the completion of a comprehensive uncertainty analysis for all SolarSIM-D2's measurands. This work thus has contextualized the measurement uncertainty of different SolarSIM outputs as compared to the corresponding measurements from the state-of-the-art instruments. The supporting contribution is the performance analysis of four SolarSIM-D2s at the World Radiation Center compared against reference instruments for the measurement of the spectral and broadband DNI, spectral aerosol optical depth, total column ozone and precipitable water vapour.

Dr. Stelios Kazadzis: As a researcher at the World Radiation Center, Stelios has helped with structuring the uncertainty analysis of aerosols, and assisted in editing the manuscript.

Dr. Natalia Kouremeti: As a researcher at the World Radiation Center, Natalia provided the spectral data from the reference instruments which I used in the uncertainty analysis.

Dr. Julian Gröbner: As the co-head of the World Radiation Center, Julian guided the methodology of the uncertainty analysis for all SolarSIM measurands, and assisted in editing the manuscript.

Dr. Karin Hinzer: As my supervisor and the director of the SUNLAB at the University of Ottawa, Karin oversaw my research and assisted with preparing the final manuscript.

Dr. Henry Schriemer: As the associate director of the SUNLAB at the University of Ottawa, Henry oversaw my research and helped to review and edit the manuscript.

Dr. Richard Beal: As a collaborator from Spectrafy, Richard guided my research and aided in reviewing the final manuscript.

3.1.2.3 Publication

The following publication is presented on next page.

V. Tatsiankou, K. Hinzer, H. Schriemer, S. Kazadzis, N. Kouremeti, J. Gröbner and R. Beal, "Extensive validation of solar spectral irradiance meters at the World Radiation Center". *Journal of Solar Energy*, vol. 166, pp. 80-89, 2018.

The following publication is not shown in this section as it represents a more contextualized representation of my previous work related to the spectral aerosol optical depth retrieval.

S. Kazadsis, N. Kouremeti, J. Gröbner, V. Tatsiankou, *et al.* "Results from the 4th WMO Filter Radiometer Comparison for aerosol optical depth measurements". *Journal of Atmospheric Chemistry and Physics*, vol. 18, pp. 3185-3201, 2018.

Solar Energy 166 (2018) 80–89

Contents lists available at ScienceDirect

Solar Energy

journal homepage: www.elsevier.com/locate/solener

Extensive validation of solar spectral irradiance meters at the World Radiation Center

V. Tatsiankou[a,c,*], K. Hinzer[a], H. Schriemer[a], S. Kazadzis[b], N. Kouremeti[b], J. Gröbner[b], R. Beal[c]

[redacted]

ARTICLE INFO

Keywords:
Solar spectral irradiance meter
SolarSIM
Direct normal spectral irradiance
Aerosol optical depth
Total ozone column amount
Precipitable water vapor content
Solar resource assessment
Atmospheric parameterization

ABSTRACT

A comprehensive uncertainty analysis validates a Solar Spectral Irradiance Meter (SolarSIM) for accurately resolving the spectral and broadband direct normal irradiances (DNI), spectral aerosol optical depth (AOD), precipitable water vapour and atmospheric total column ozone amounts. The derivation of these parameters from four SolarSIMs were compared to reference instrumentation at the Physikalisch-Meteorologisches Observatorium Davos and World Radiation Center (PMOD/WRC) in Davos, Switzerland in September 2015. The SolarSIMs are the first instruments to ever simultaneously participate in the 12th WMO International Pyrheliometer Comparison, Fourth Filter Radiometer Comparison, and First Spectroradiometer Comparison. The SolarSIMs' DNI data were compared to the World Standard Group's PMO2 absolute cavity radiometer, with World Radiometric Reference factors ranging from 0.999674 to 0.994610 for the best and the worst performing devices, respectively. In addition, the SolarSIMs' spectral DNI data was compared against PMOD's Precision Spectral Radiometer. The mean difference of the spectral DNI was found to be less than 5% for wavelengths above 400 nm. The SolarSIMs' measurements of AOD data were compared against PMOD's Precision Filter Radiometer triad. The median AOD differences and their standard deviations were found to be 0.0046 ± 0.0044, 0.0016 ± 0.0034, 0.0018 ± 0.0026, and 0.0041 ± 0.0022 for 368 nm, 412 nm, 500 nm, and 865 nm, respectively. The SolarSIMs' measurements of precipitable water vapour were compared against PMOD's Cimel CE318 sun photometer. The median difference and the corresponding standard deviation averaged 1 ± 0.2 mm for all SolarSIMs. Furthermore, the SolarSIMs' measurements of total column atmospheric ozone were compared against PMOD's Brewer MkIII spectrophotometer. The median difference and the corresponding standard deviation averaged 6 ± 7 DU for all SolarSIMs.

1. Introduction

For decades now, measurements of sunlight have been vital for solar energy research, atmospheric science, and weather forecasting applications. Broadband direct normal irradiance (DNI) measurements, for example, have been extensively used for solar resource assessment and calibration of satellite-derived irradiance data sets (AlYahya and Irfan, 2016; Cebecauer and Suri, 2016). More recently, with the advent of concentrating photovoltaic technologies, spectral DNI measurements became critical for performance analysis of solar modules with high efficiency multi-junction solar cells (Núñez et al., 2016; Araki and Yamaguchi, 2003). Besides the spectral and broadband irradiance data, direct sun observations can quantify the aerosol optical depth (AOD), precipitable water vapor (PWV) and total column ozone contents of the atmosphere. The aerosols and water vapor impact earth's radiation budget and are key inputs into weather prediction models and climate studies (Holben et al., 2001; Liang et al., 2015; Karabatić et al., 2011), while the ozone layer is critical for protecting life on our planet, as it attenuates damaging ultraviolet radiation.

For over 50 years the Physikalisch-Meteorologisches Observatorium Davos and World Radiation Center (PMOD/WRC) in Davos, Switzerland has guaranteed the global homogenization of solar measurements by hosting quinquennial instrument inter-comparisons, such as the International Pyrheliometer Comparison (IPC) (Finsterle, 2016), the Filter Radiometer Comparison (FRC) (Kazadzis et al., 2016), and the Spectroradiometer Comparison (SRC) (Schmutz et al., 2016). A group of absolute cavity radiometers, known as the World Standard Group (WSG), is the manifestation of the World Radiometric Reference (WRR) with an estimated uncertainty to the International System of Units. The WRR is the world's primary standard for the DNI. During the IPC, the

* Corresponding author at: [redacted]
E-mail address: [redacted]

https://doi.org/10.1016/j.solener.2018.03.044
Received 13 November 2017; Received in revised form 2 March 2018; Accepted 15 March 2018

participating instruments are calibrated against the WSG and produce the new national or institutional DNI references with traceability to the WRR. Likewise, during the FRC, the measurements from a triad of Precision Filter Radiometers (PFRs) serve as the reference to the world's aerosol measuring community. More recently, the PMOD development of a Precision Solar Radiometer (PSR) has enabled spectral DNI comparisons to be performed (Gröbner et al., 2014). All these events at the WRC provide unique opportunities to assess the performance of novel devices against global references. Our solar spectral irradiance meter (SolarSIM) is a first instrument to participate in all three WRC comparisons.

The SolarSIM uses ground-based measurements to inform software algorithms for rapid resolution of the location-specific solar spectrum, total irradiance and atmospheric constituents. The SolarSIM works by measuring the solar spectral irradiance in six carefully chosen wavelength bands, using silicon photodiodes with rugged, hard coated bandpass filters,[1] to allow spectral reconstruction through parametrization of the major atmospheric processes, including aerosol extinction, ozone and water vapor absorptions (Tatsiankou et al., 2013; Tatsiankou et al., 2016). The direct sun version of the SolarSIM allows the user to resolve in the 280–4000 nm range the spectral AOD, PWV, atmospheric total column ozone, and ultimately compute the spectral and broadband DNI - thus providing data that typically requires five to seven commercial instruments. The ability to simultaneously obtain these solar and atmospheric parameters with only one instrument reduces cost, avoids diversity in data acquisition protocols and setup requirements, and so facilitates many research and commercial applications (Caballero et al., 2018; Rodrigo et al., 2017; Majumdar and Cunningham, 2017; Theristis et al., 2016; Fernández et al., 2016).

In this paper we perform a complete uncertainty analysis for all SolarSIM measurands. We first define the uncertainty of irradiance measurement for each of six SolarSIM channels, and then use these findings to derive the uncertainties of spectral and broadband DNI, spectral AOD, PWV and total column ozone. These results are compared to actual measurements from four SolarSIMs at the WRC during 28 September to 10 October 2015, which participated in the 12th IPC (DNI comparison), fourth FRC (AOD comparison), and first SRC (spectral DNI comparison). Additionally, the SolarSIMs' measurements of PWV content and total column ozone were compared against data from a co-located Cimel sun photometer and Brewer MkIII spectrophotometer, respectively.

2. Instrumentation setup

Four SolarSIMs with serial numbers SN102 and SN103 (D1 model), and SN112 and SN113 (D2 model), manufactured by Spectrafy Inc., were installed on the roof top of the WRC in Davos, Switzerland (46.81°N, 9.84°E) on 27 September 2015. The SolarSIM-D2 is a more rugged version of the SolarSIM-D1, designed to have an extended temperature range, lower power consumption, and improved internal humidity management. The SolarSIMs have a ± 2.5° field of view with a 1° slope angle, conforming to the World Meteorological Organization (WMO) standard for radiometric measurements of DNI (WMO, 2008). The instruments were mounted on a Brusag sun tracker with a custom aluminum plate and bracket, as shown in Fig. 1. They were aligned normal to the sun using a reference pinhole on each SolarSIM enclosure and a three point adjustment method. Each SolarSIM was interfaced to a laptop via Spectrafy's COMBOX accessory, which provides power and RS-485 communication to the instrument. A specialized graphical user interface on the laptop enables data acquisition from each instrument every five seconds. It takes 500 ms for a SolarSIM to acquire and send the current values, ambient temperature and pressure, and internal temperature and humidity to the host for analysis. Depending on the hardware specifications, it takes a typical laptop about 100 ms to process the raw data into spectral products. Throughout this paper, SolarSIMs SN102, SN103, SN112, and SN113 are referenced as SSIM 1, SSIM 2, SSIM 3, and SSIM 4, respectively.

Fig. 1. SolarSIMs, versions D1 and D2, installed on a Brusag tracker on the roof top at the World Radiation Center, Davos, Switzerland (white finish - SolarSIM-D1, silver finish - SolarSIM-D2). (For interpretation of the references to color in this figure legend, the reader is referred to the web version of this article.)

3. Measurement methodology overview

The SolarSIM measures the calibrated irradiance in six optical bands centered at 420, 500, 610, 675, 880, and 940 nm with full widths at half maxima of 10 nm. It also senses the ambient temperature, atmospheric pressure, and the device's internal temperature. These measurements are fed into our radiative transfer model to derive the spectral DNI and AOD in the 280–4000 nm range (with a 1 nm resolution), broadband DNI, total column ozone and PWV (Tatsiankou et al., 2016). The atmospheric parameterization follows a methodology similar to a Simple Model of the Atmospheric Radiative Transfer of Sunshine (SMARTS) (Gueymard, 1995, 2006). SMARTS methodology was chosen because it has been demonstrated to have robust performance and fast computational speed (Gueymard, 2008), and, hence, it was adapted in our architecture. The procedure for parameterizing the atmosphere from the SolarSIM measurements consists of the following steps:

1. Calibrate an instrument:
   a. Determine the temperature coefficients for each channel.
   b. Perform on-sun calibration against a reference spectroradiometer or a reference SolarSIM.
2. Acquire the current from six optical channels, ambient temperature and pressure, and the internal temperature.
3. Use our radiative transfer model to derive the spectral irradiance, the spectral AOD, DNI, total column ozone and PWV content:
   a. Compute the zenith angle and the sun-earth distance using National Renewable Energy Laboratory's (NREL) solar position algorithm (Reda and Andreas, 2008).
   b. Apply the sun-earth distance correction on the extraterrestrial solar spectrum from Gueymard (2004).
   c. Calculate Rayleigh scattering and the transmittances from various atmospheric gases (CO_2, CH_4, O_2, NO_2) (Gueymard, 2006).
   d. Determine the spectral AOD and its transmittance from the 420, 500, 675, and 880 nm channels (Tatsiankou et al., 2013).
   e. Compute the total column ozone and its spectral transmittance from the 610 nm channel (Tatsiankou et al., 2013).
   f. Calculate the PWV content and its spectral transmittance from the 940 nm channel (Tatsiankou et al., 2013).

[1] conform to MIL-C-48497A and MIL-STD-801F standards.

g. Determine the spectral irradiance by applying the derived atmospheric constituents' transmittances to the extraterrestrial spectrum (Tatsiankou et al., 2013).
h. Integrate the spectral irradiance to obtain the DNI.

The absorption coefficients and mixing ratios of the atmospheric gases used in our algorithm are taken from SMARTS under light pollution conditions (Gueymard, 2006), except for the carbon dioxide, whose mixing ratio is set to 400 ppmv.

4. Uncertainty analysis

We perform the uncertainty analysis for a SolarSIM by generally following the Guide to the Expression of Uncertainty Measurements (GUM) (JCGM, 2008). Our procedure can be summarized in five steps:

1. Determine the equation or functional relationship describing or approximating the measurand.
2. Identify the dominant sources of uncertainty associated with each variable in the measurement equation or functional relationship from step 1.
3. Determine standard uncertainty for each variable using either statistical methods (Type A uncertainty) or non-statistical methods (Type B uncertainty). Type A uncertainty is defined as the standard deviation of the data set as per Eq. (1)

$$\mu_A = \sqrt{\frac{\sum_{i=1}^{n}(X_i - \overline{X})^2}{n-1}}, \tag{1}$$

where μ_A is the Type A uncertainty, X_i are data points, $\overline{X}$ is the mean of a data set, and n is the number of data points.
All other uncertainties that cannot be statistically estimated are labeled as Type B uncertainties, and are assumed to have either a rectangular or a normal distribution. These relationships are defined in Eqs. (2a) and (2b), respectively, as

$$\mu_{B,\text{rectangular}} = \frac{u_e}{\sqrt{3}}, \tag{2a}$$

$$\mu_{B,\text{normal}} = \frac{u_e}{k}, \tag{2b}$$

where $\mu_{B,\text{rectangular}}$ and $\mu_{B,\text{normal}}$ are the Type B uncertainties with a rectangular and a normal distribution, respectively, u_e is the uncertainty estimate, and k is a desired coverage factor.
For variables with multiple sources of uncertainties, we combine them using the Root Sum Squared (RSS) method.
4. Calculate the combined standard uncertainty of the measurand by adding standard uncertainties from step 3 using the RSS method.
5. Calculate the expanded uncertainty by multiplying the combined standard uncertainty by a desired coverage factor, k. In our case, we chose $k = 1$ to give the confidence level of 68%, as our combined standard uncertainty estimates are believed to be conservative.

Using this general procedure, we first evaluate the uncertainty of SolarSIM irradiance measurement in the six optical channels. For this case, the most dominant processes are identified as the on-sun calibration against a reference spectroradiometer and the photodiodes' temperature dependence. We then use these findings to estimate the uncertainty for our spectral model in deriving the spectral and broadband DNI, the spectral AOD, the total column ozone and PWV. We view the approach taken in this section as a good starting point in quantifying the uncertainties of numerous SolarSIM measurands. As more comparison data is gathered against reference instruments with well-defined uncertainties, a more refined estimate of the SolarSIM outputs' uncertainties will be obtained.

Table 1
Summary of the two main contributors to SolarSIM channel irradiance uncertainty. α is the photodiode temperature coefficient, μ_α is its standard uncertainty, and μ_t is the uncertainty of the temperature correction; μ_s is the uncertainty in the reference spectroradiometer's irradiance measurements. μ_t and μ_s are combined to yield μ_{irad}, the combined standard uncertainty of irradiance measurement at each SolarSIM channel.

	Bandpass filter central wavelength, λ_c (nm)					
	420	500	610	675	880	940
	Photodiode temperature response					
α (%/°C)	0.11	0.01	0.00	0.00	0.02	0.05
μ_α (%/°C)	0.019	0.008	0.011	0.012	0.009	0.017
μ_t (%)	0.44	0.20	0.25	0.28	0.21	0.39
	Calibration uncertainties					
μ_s (%)	1.95	1.15	0.9	1.00	1.15	1.45
	Combined irradiance uncertainties					
μ_{irad} (%)	1.99	1.17	0.93	1.04	1.17	1.50

4.1. Temperature dependence

The spectral responsivity of silicon photodiodes varies as a function of temperature. The magnitude of this change is typically linear with temperature, and primarily depends on the silicon's crystal growth process, material quality, and packaging. Table 1 shows typical temperature coefficients for SolarSIM channels denoted by α, where %/°C is the percentage change of the photodiode responsivity per degree Celsius for the specific channel with a center wavelength, λ_c. The 500, 610, 675, and 880 nm channels exhibit negligible temperature dependence, while the 420 nm and 940 nm channels have a moderate temperature sensitivity of 0.11 and 0.05%/°C, respectively. We determine these coefficients by monitoring the photodiode outputs, during a temperature sweep under a 250 W quartz tungsten halogen light source. The spectral stability of the lamp is monitored by external silicon photodiodes with bandpass filters, whose center wavelengths and full-width at half-maxima are matched to the six SolarSIM channels. The SolarSIM's internal temperature is first cooled to 20 °C, then the device is placed on the thermo-electric cooler stage, which is pre-heated to 35 °C. We then gradually raise the temperature set point of the stage to 60 °C. As the internal temperature of the SolarSIM increases, we record the photodiode current from each channel versus the internal temperature. Once the internal temperature reaches 40 °C, we stop the test and compute the best line of fit slopes for each of the six channels, thereby yielding the temperature coefficients. We estimate the uncertainty of the temperature coefficient for each channel, μ_α, by computing the standard deviation, as per Eq. (1), of the derived temperature coefficients from ten experiments for the same device. We then define μ_t, the uncertainty in the temperature correction of the photodiode's responsivity

$$\mu_t = \frac{\mu_\alpha \cdot \Delta T}{\sqrt{3}}, \tag{3}$$

where ΔT is the maximum delta in C° the SolarSIM's internal temperature is assumed to undergo in the field as compared to the corresponding temperature during the optical calibration. We set ΔT as 40 °C. Eq. (3) has the square root of three in the denominator because we assume μ_t is a Type B uncertainty with a rectangular distribution. The computed values of μ_t for each channel are presented in Table 1.

4.2. On-sun optical calibration

The SolarSIM's optical channels have been calibrated for absolute irradiance, on-sun, against a LI-1800 secondary standard spectroradiometer at NREL. The calibration procedure ensures that the absolute irradiance measured by the SolarSIM in its six optical channels matches the irradiance as measured by the reference spectroradiometer at the corresponding wavelengths. By doing so, we largely compensate for deviations from the filter transmittances and photodiode responsivities assumed in our spectral model, except for filter's center-wavelength and full width at half maxima variations from the nominal values. The dominant source of uncertainty in performing this procedure is the LI-1800's irradiance measurement uncertainty, μ_s, which has been quantified by NREL's researchers (personal communication with Afshin Andreas, September 2017). We combine μ_t and μ_s to yield

$$\mu_{\text{irad}} = \sqrt{\mu_t^2 + \mu_s^2}, \tag{4}$$

where μ_{irad} is the combined standard uncertainty of the SolarSIM irradiance measurement, as summarized in Table 1. Evidently, the measurement uncertainty of the reference spectroradiometer is a limiting component of the SolarSIM accuracy.

4.3. Spectral DNI uncertainty

We have estimated the combined standard percent uncertainty in deriving the spectral irradiance from the SolarSIM's radiative transfer model, $\mu(\lambda)_{\text{spec}}$, by comparing the spectral DNI as measured by the EKO's WISER spectroradiometer in the 350–1633 nm range against the corresponding spectra simulated by the SolarSIM's model. We define this uncertainty

$$\mu(\lambda)_{\text{spec}} = \sqrt{\mu_{\text{model}}(\lambda)^2 + \mu_{\text{wiser}}(\lambda)^2}, \tag{5}$$

where μ_{model} is the standard uncertainty of our model with respect to the WISER data and $\mu_{\text{wiser}}(\lambda)$ is the WISER's combined standard uncertainty, which we assumed as 2.5% across the entire spectral range. We calculate $\mu_{\text{model}}(\lambda)$ as

$$\mu(\lambda)_{\text{model}} = \sqrt{\frac{\sum_{t=1}^{n}[D_t(\lambda) - \overline{D}(\lambda)]^2}{n-1}} + \frac{\overline{D}(\lambda)}{\sqrt{3}}, \tag{6}$$

where $D_t(\lambda)$ is the percent spectral difference between simulated and measured spectra for timestamp t,$\overline{D}(\lambda)$ is the mean percent spectral difference of the entire data set, and n is the number of measured spectra. The first part of Eq. (6) is the standard deviation of the percent spectral difference between the measured and simulated spectra data set, while the second part is $\overline{D}(\lambda)$ which we treated as a Type B component with a rectangular distribution. We included the latter component in the uncertainty calculation because it cannot be compensated for during the optical calibration.

Over 10,000 WISER spectra were gathered from 19 September 2014 to 17 March 2015, when the WISER was in spectral DNI mode at the Solar Radiation Research Facility (SRRL) (Andreas and Stoffel, 1981). The data set was filtered to exclude cloudy periods by only accepting spectra when the DNI is over 300 W/m^2. We simulated the variability in bandpass filter transmittances by applying the center-wavelength's manufacturing tolerance of ± 2 nm to the nominal filter transmittance using a rectangular distribution. The corresponding filter profiles and photodiode responsivities were superimposed with the measured spectral DNI from the WISER spectroradiometer to simulate a distribution of theoretical currents from each SolarSIM channel, similar to the technique used in our previous work (Tatsiankou et al., 2013). In addition, we applied the combined standard uncertainty, μ_{irad}, with normal distribution from Table 1 to the simulated current values to mimic realistic in-field operation. Local ambient temperatures and atmospheric pressures were also extracted from the SRRL database and fed into the SolarSIM model for each five minute interval. Fig. 2 shows the computed mean percent spectral difference and the percent spectral standard deviation of the analyzed data set, as well as, μ_{spec}, the combined standard uncertainty of our model in deriving the spectral DNI. Based on this analysis, we then split the spectral uncertainty into three ranges: < 420 nm, 420–880 nm, > 880 nm, and assign conservative combined standard uncertainties of < 10%, < 3%, and < 5%, respectively, as per Fig. 2. Note that we have not included data corresponding to the oxygen absorption peaks centered at 687 and 761 nm, and water

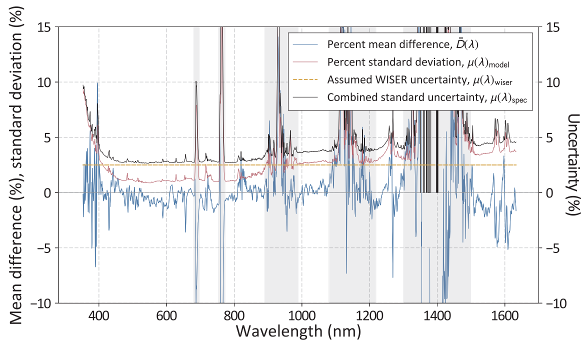

Fig. 2. The estimated spectral uncertainty of our model as compared to the spectral DNI measurements from NREL's EKO WISER spectroradiometer. Over 10,000 measured spectra was used in this analysis. We assume the WISER has a flat 2.5% spectral measurement uncertainty across its 350–1633 nm range. The mean percent difference, the percent standard deviation, and the estimated combined uncertainty of our spectral DNI model was derived by comparing the simulated and measured spectra. The gray areas denote the oxygen absorption peaks centered at 687 and 761 nm, and water vapor absorption bands centered at 934, 1130, and 1400 nm, where increased uncertainty is expected.

vapor absorption bands centered at 934, 1130, and 1400 nm. In those areas we expect increased uncertainty due to the extreme gradients of numerous oxygen and water vapour absorption lines. We have applied the computed uncertainties from the three ranges to the AM1.5D spectrum and computed the absolute spectral DNI uncertainty in units of W/m^2/nm for each range, as shown in Table 3.

4.4. DNI uncertainty

We have estimated the combined standard uncertainty, in units of W/m^2, for the SolarSIM's DNI measurement, μ_{DNI}, by performing a comparison of the DNI data generated by the SolarSIM-D2 SN107[2] against the two first class CHP-1 pyrheliometers from Kipp and Zonen at the SRRL. We define this uncertainty through the following expression

$$\mu_{\text{DNI}} = \sqrt{\mu_d^2 + \mu_{\text{chp}}^2}, \tag{7}$$

where μ_{chp} is the combined standard uncertainty of the CHP-1 pyrheliometers, assumed as 10 W/m^2, and μ_d is the uncertainty of the SolarSIM SN107 DNI data versus reference DNI data. We express μ_d as

$$\mu_d = \sqrt{\frac{\sum_{i=1}^{n}(d_i - \overline{d})^2}{n-1}} + \frac{\overline{d}}{\sqrt{3}}, \tag{8}$$

where d_i is the DNI difference in W/m^2 between the SolarSIM and pyrheliometers for data point i,$\overline{d}$ is the mean difference of the SolarSIM versus the reference DNI data set, and n is the number of analyzed data points per instrument. The first part of Eq. (8) is the standard deviation of the DNI difference between the SolarSIM's and reference instrument's data sets, while the second part is $\overline{d}$, which we treated as a Type B component with a rectangular distribution. We included the latter component in the uncertainty calculation because it cannot be compensated for during the optical calibration.

The comparison spanned the entire year from 2 September 2016 to 2 September 2017, with data being filtered to exclude cloudy periods as in previous section. Over 100,000 cloud-free data points per instrument are used in the analysis with a one minute resolution. The reference DNI data was obtained by averaging the values from both CHP-1 pyreliometers. The mean difference and the standard deviation of the SolarSIM's DNI values as compared to the CHP-1 pyrheliometers' data are −1.6 W/m^2 and 8.3 W/m^2, respectively. We then computed the

[2] SolarSIM-D2 SN107 data is publicly available at http://midcdmz.nrel.gov/srrl_ssim/.

combined standard uncertainty of the SolarSIM SN107 DNI measurement to be 13.0 W/m^2 as per Eq. (7), or 1.5%, as the mean reference DNI was 869.9 W/m^2. We assume the estimated DNI uncertainty is valid for all SolarSIMs.

4.5. AOD uncertainty

The SolarSIM determines the spectral AOD in the 280–4000 nm range using four wavelength bands: 420, 500, 675, and 880 nm. These four channels create three aerosol regimes (below 500 nm, between 500 and 675 nm, and above 675 nm) within which the SolarSIM algorithm assumes that AOD behaves according to the Ångström power law. We assume the standard uncertainty in the AOD derivation, μ_{AOD}, depends primarily on the uncertainties of the spectral irradiance measurement, μ_{irad}, and the assumed irradiance of the AM0 spectrum in each aerosol channel, μ_{AM0}, and can be expressed as

$$\mu_{AOD} = \sqrt{\mu_{irad}^2 + \mu_{AM0}^2} \quad (9)$$

We assume that other uncertainties, such as calculation of the total ozone column, Rayleigh scattering, and optical air masses, are much smaller compared to the aforementioned ones. The uncertainty of irradiance measurement in the four aerosol channels is detailed in Table 1. The uncertainty of the AM0 irradiance in the four aerosol channels is estimated from Gueymard (2004). In that work the standard deviation of the integrated irradiance for the 400–700 nm and 700–1000 nm bands was found to be 1.2% and 0.8%, respectively. We then combine μ_{irad} and μ_{AM0} as per Eq. (9) and summarize the results in Table 2. We extend the analysis to the 280–4000 nm range from the computed AOD channel uncertainties. For wavelengths below 420 nm and above 880 nm, we estimate the uncertainties by combining the AOD uncertainties at 420 and 500 nm, and 675 and 880 nm channels, respectively, using the RSS method. For the 420–500 nm, 500–675 nm, and 675–880 nm ranges, the AOD uncertainty is conservatively estimated to be the largest uncertainty of the two channels bounding the spectral region, as shown in Table 3. We find the lowest AOD uncertainty of 0.014, for an air mass of 1, to be in the 675–880 nm region.

4.6. Precipitable water vapour uncertainty

We have estimated the combined standard uncertainty, in units of mm, for the SolarSIM's PWV measurement, μ_{H2O}, similar to Section 4.4. We compared the PWV data derived by SolarSIM-D2 SN107 against the co-located PWV reference at the SRRL - Zephyr Geodetic Global Position System (GPS) Antenna and a Trimble Net9R Data Acquisition system. We express μ_{H2O} as

$$\mu_{H2O} = \sqrt{\mu_h^2 + \mu_{gps}^2}, \quad (10)$$

where μ_h is the uncertainty of the SolarSIM's PWV data with respect to the reference PWV data, with the latter having an estimated combined standard uncertainty, μ_{gps}, of 1 mm (Andreas and Stoffel, 1981). The expression for μ_h is defined by Eq. (8), where d_i is the PWV difference, in units of mm, between the SolarSIM and the reference instrument for data point i,$\bar{d}$ is the mean PWV difference of the SolarSIM versus the reference PWV data set.

Table 2
The combined standard uncertainty of retrieving the AOD, μ_{AOD}, at four SolarSIM's aerosol channels, λ_i. μ_{AOD} primarily depends on the uncertainties in irradiance measurement and the AM0 spectrum, μ_{irad} and μ_{AM0}, respectively.

λ_i (nm)	μ_{irad} (%)	μ_{AM0} (%)	μ_{AOD} (%)	μ_{AOD} [a]
420	1.99	1.2	2.32	0.023
500	1.17	1.2	1.68	0.017
675	1.04	0.8	1.31	0.013
880	1.17	0.8	1.41	0.014

[a] For an air mass of 1.

Table 3
The summary of relative and absolute combined standard uncertainties for SolarSIM outputs, which include the spectral DNI and the AOD in the 280–4000 nm range, the broadband DNI, the ozone and PWV amounts.

Parameter	Range (nm)	Uncertainty (%)	Absolute uncertainty
Spectral DNI	<420	<10	<0.099 $W/m^2/nm$ [*]
	420–880	<3	<0.043 $W/m^2/nm$ [*]
	>880	<5	<0.044 $W/m^2/nm$ [*]
	280–4000	1.5	13.0 W/m^2
AOD [**]	<420	2.9	0.029
	420–499	2.3	0.023
	500–675	1.7	0.017
	675–880	1.4	0.014
	>880	1.9	0.019
PWV	N/A	14.6	1.6 mm
Ozone	N/A	18.8	64 DU [*]

[*] At AM1.5D conditions.
[**] For an air mass of 1.

Analogously to Section 4.4, the PWV comparison spanned the entire year from 2 September 2016 to 2 September 2017. Over 100,000 cloud-free data points per instrument are used in the analysis with a one minute resolution. The mean difference and the standard deviation of the SolarSIM's PWV values as compared to the reference instrument's data are −0.94 mm and 1.08 mm, respectively. We then compute the combined standard uncertainty of the SolarSIM-D2 SN107's PWV measurement to be 1.57 mm as per Eq. (10), or 14.6%, as the mean PWV reference value was 10.76 mm. We assume the computed PWV uncertainty is valid for all SolarSIMs.

4.7. Ozone column retrieval uncertainties

At the time of writing, there was no available long term data comparing the total column ozone derived from a SolarSIM-D2 and a reference ozone instrument, such as the Brewer spectrophotometer. As such, we use a non-standard technique of estimating the ozone retrieval uncertainty of the SolarSIM. We simulate the spectral DNI with SMARTS under AM1.5D conditions (using an ambient pressure of 101.325 kPa, an airmass of 1.5, an AOD at 500 nm of 0.084, an ozone content of 340 DU, and a PWV of 14.2 mm). We then reconstruct the SMARTS spectrum using our six channel spectral model by applying the irradiance uncertainty to the optical channels as per Table 1 and AM0 uncertainties from Table 2, assuming a normal distribution. In addition, we simulate the variability in bandpass filter transmittances by applying the manufacturer's center wavelength tolerance of ± 2 nm to the nominal filter profile using a rectangular distribution. The retrieved ozone values are compared to SMARTS's nominal ozone input of 340 DU. Consistent results are achieved by analyzing 10,000 spectra, and we obtain a mean difference of 2 DU and a standard deviation of 64 DU. We combine these quantities as per Eq. (8), where d_i is the total ozone column difference in units of DU between the SolarSIM's derived ozone content and the SMARTS's input of 340 DU for iteration i and $\bar{d}$ is the mean total ozone column difference of the data set. The results yield the SolarSIM's combined standard uncertainty for total column ozone as 64 DU or 18.8%.

5. Performance at the World Radiation Center

5.1. WMO International Pyrheliometer Intercomparison XII

The WMO International Pyrheliometer Intercomparison (IPC) was first held in 1959 and now takes place every five years at the WRC in Davos, Switzerland. The IPC ensures traceability of the solar radiation measurements through the World Radiometric Reference (WRR), which

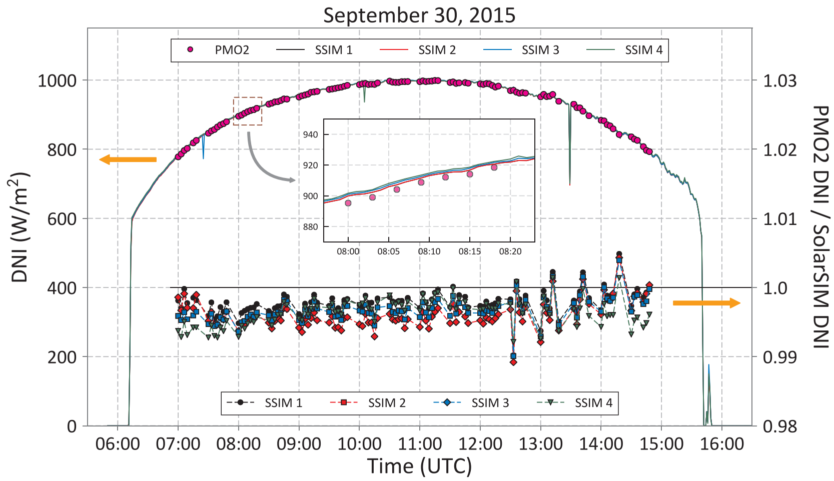

Fig. 3. A comparison of the daily DNI (left axis) and the ratio of the DNI (right axis) as measured by the IPC reference instrument (PMO2) and the SolarSIMs on September 30, 2015. The inset is the DNI profile magnification from 07:55 to 08:25 UTC.

is the world standard for total solar irradiance. The WRR is determined from the irradiance average of six absolute cavity radiometers: CROM2L, MK67814, HF18748, PAC3, PMO2, and PMO5, otherwise known as the World Standard Group (WSG).

The IPC-XII (2015) attracted 111 attendees from 33 countries and 134 new WRR factors were determined for participating radiometers, including the four SolarSIMs previously described (Finsterle, 2016). PMO2 absolute cavity radiometer with the correction factor to the WRR served as the DNI reference during the event. DNI measurements were conducted in periods of 19.5 min duration, re-starting every 30 min. The base cadence was one irradiance measurement every 90 s, which resulted in a maximum of 14 irradiance readings per series from the PMO2, assuming acceptable atmospheric conditions (data were discarded if the AOD at 500 nm exceeded 0.12). DNI data from each SolarSIM were submitted daily to the WRC for evaluation.

Fig. 3 shows the daily DNI profiles as resolved by the SolarSIMs and the reference absolute cavity radiometer on 30 September 2015. The latter is represented by the solid (magenta) dots, and the former are shown by the four lines; the inset provides a magnified comparison of the absolute DNI values. Note the SolarSIM's DNI data was averaged over ±15 s from a minute mark, and then this value was assigned to that minute. The ratios of the IPC reference DNI and the SolarSIMs' DNI fall within ± 1%. The average ratio between the IPC reference and the test instrument define the WRR factor for the latter. The WRR factors for the SolarSIMs as computed by the WRC are 0.999674, 0.998951, 0.994610, and 0.99949, with standard deviations of 0.14%, 0.22%, 0.2%, and 0.25% for SSIM 1, SSIM 2, SSIM 3, and SSIM 4, respectively (Finsterle, 2016).[3] These results are consistent with the DNI uncertainty analysis conducted in Section 4.4.

5.2. Spectroradiometer comparison

The First Spectroradiometer Comparison at the WRC included three types of spectral measurement equipment: one EKO MS711/MS712 (WISER) spectroradiometer, two Precision Solar Radiometers (PSRs) (Gröbner et al., 2014), and four SolarSIMs. The main specifications of these instruments are presented in Table 4. Due to the limited spectral range of the PSRs and the WISER, the spectral comparison was restricted to the 300–1700 nm range. October 1, 2015 was selected for the analysis because data from all participating instruments were available.

[3] The IPC-XII report mentions COFOVO Energy as the manufacturer of the SolarSIMs. Since then, the SolarSIM business has been transferred to Spectrafy Inc.

Table 4
Specifications of the three types of instruments participating in the First Spectroradiometer Comparison.

Manufacturer	Instrument	Resolution	Step	Range
WRC	PSR	1–6 nm	0.7 nm	302–1020 nm
EKO	WISER	7 nm	1 nm	300–1700 nm
Spectrafy	SolarSIM-D2	1 nm*	1 nm*	280–4000 nm*

* Based on a spectral reconstruction model.

The timestamps from every instrument were synchronized to the nearest minute, resulting in 66 matching spectra between 09:00 and 15:00 UTC. The average DNI spectra for all seven instruments are presented in Fig. 4a. The spectral irradiance data from the SolarSIMs have been smoothed using a 5 nm central averaging technique, to better match the lower spectral resolution of the spectroradiometers. Fig. 4b shows the mean spectral difference and spectral standard deviation for the SSIM 1 versus the PSR-004 over the 302–1020 nm range, and versus the EKO WISER over the 1021–1700 nm range. The standard deviation mainly falls within the uncertainties for spectral DNI as presented in Table 3, except for areas below 315 nm and above 1650 nm. For the first range, the SolarSIM's short wavelength extrapolation of the AOD from 420 nm and 500 nm channels is the most likely cause. For the latter range, the WISER is known to have problems with order sorting filters (Andreas, 2016). Nonetheless, the mean difference of the spectral DNI between the SolarSIMs and the reference spectroradiometers was < 5%, excluding the oxygen and PWV bands. The statistical performance of SSIM 1 is representative of the other three SolarSIMs.

5.3. Filter Radiometer Comparison IV

The Filter Radiometer Comparison (FRC) is held with the same regularity as the IPC. The FRC-IV attracted over 30 AOD-resolving instruments belonging to AERONET, GAW-PFR, Skynet, SURFRAD and other measurements networks. The instruments included Spectrafy's SolarSIM, WRC's Precision Filter Radiometer (PFR) and Precision Solar Radiometer (PSR), Middleton Solar's SP02, Cimel's CE318, Yankee Environmental System's Multi-Filter Rotating Shadow-band Radiometer, Prede's POM-2, and Microtops' model II hand-held sun photometer (Schmutz et al., 2016).

One of the main goals of the FRC is to homogenize the global AOD measurements through traceability to the world's aerosol standard group of spectral radiometers. This standard is defined as a triad of

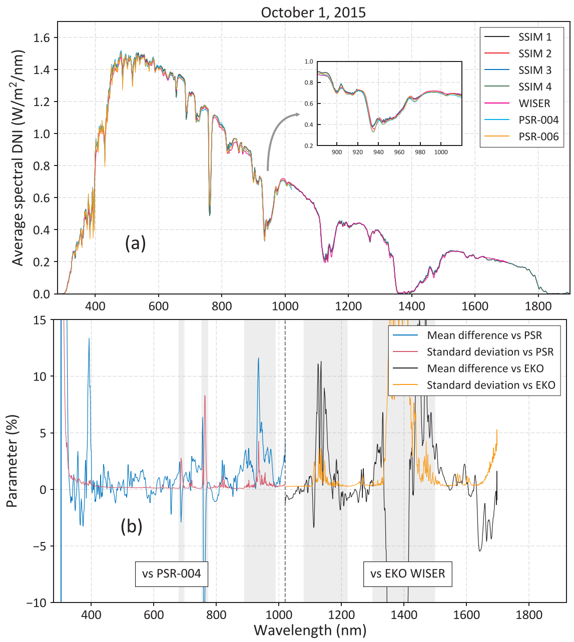

Fig. 4. (a) The average spectral DNI of 66 time-synchronous spectra from each of four SolarSIMs, two PSRs, and the EKO WISER spectroradiometer at the WRC from 09:00 to 15:00 UTC on October 1, 2015. The inset is the magnification for the 881–1020 nm spectral range. (b) The mean difference, standard deviation, and the combined uncertainty of the spectral DNI between the SolarSIM SN102 and PSR-004, EKO WISER spectroradiometers on October 1, 2015. The analysis spanned the 302–1020 nm and 1021–1700 nm ranges for the PSR-004 and EKO WISER, respectively. The gray areas denote the oxygen absorption peaks centered at 687 and 761 nm, and water vapour absorption bands centered at 934, 1130, and 1400 nm, where increased standard deviation is expected. Note that SolarSIM data were smoothed with 5 nm central averaging to aid comparison.

reference PFR instruments, which is established by the World Optical Depth Research and Calibration Center at the WRC, and is based on the recommendation from the WMO (Kazadzis et al., 2017). Each PFR measures the AOD at 368 nm, 412 nm, 500 nm, and 862 nm with a ± 1.25° field of view and a 0.7° slope angle.

Since the SolarSIM resolves in real time the complete AOD spectrum across the 280–4000 nm range, comparisons were made against all four PFR channels. Fig. 5 shows a full day of time-synchronous AOD differences between the SolarSIMs and PFR triad data obtained on 30

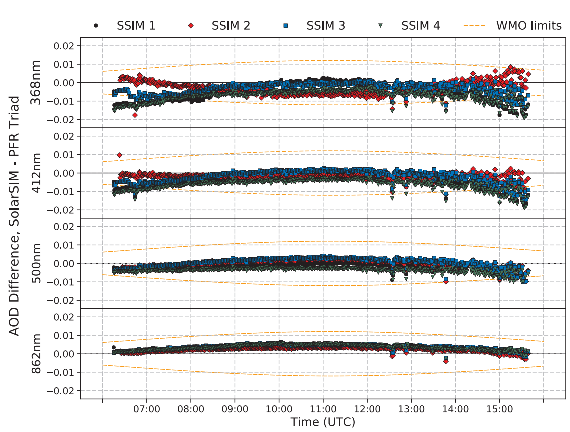

Fig. 5. AOD difference comparison between the SolarSIMs and the PFR triad for data acquired on 30 September 2015.

September 2015. The dashed orange lines delimit the AOD differences according to the WMO recommended $U95$ criterion, defined as (WMO, 2005)

$$U95 < \pm [0.005 + 0.01/m], \quad (11)$$

where m is the optical air mass. The first term accounts for instrumental and algorithmic uncertainties, while the second term addresses the relative uncertainty in instrument calibration. The $U95$ criterion stipulates that the AOD measured by high quality instruments should be within the specified limits 95% of the time.

As is evident from Fig. 5, the AOD differences between the SolarSIMs and the PFR triad at 500 nm and 862 nm are consistently within the $U95$ limits for most of the day. At 368 nm and 412 nm, however, the AOD differences tends to be lower than the $U95$ limit at air masses of greater than 3.5 or at sun elevation angles less than 16°, which correspond to measurement times before 07:00 UTC and after 15:20 UTC. Most likely, the differences in the AOD retrieval algorithms, such as the calculation of air mass, Rayleigh scattering, and ozone absorption, and differences in calibration methods between the instruments are responsible for these AOD discrepancies. The PFR triad has maintained a stability of under 1% since 2005. This is achieved by continuous monitoring of the differences of the three instruments and six month periodic checks using transferable instruments that are calibrated by the Langley technique at Izaña Atmospheric Observatory in Spain and Mauna Loa Observatory in USA. SSIM 1 and SSIM 2 were calibrated against a Licor LI-1800 secondary standard spectroradiometer at the NREL in Golden, US, while SSIM 3 and SSIM 4 were calibrated against SSIM 1 at the SUNLAB Solar Test Site in Ottawa, Canada (Tatsiankou et al., 2016). The latter method is expected to have higher uncertainty in the AOD measurement as compared to the Langley plot method.

The aggregate AOD performance of all SolarSIMs from 28 September to 1 October 2015 is summarized in Table 5, where λ, $\Delta\widetilde{\mu}$, σ, and N_{U95} denote the AOD wavelength, the median AOD difference, the standard deviation of the AOD difference, and the percentage of data points that fall within the $U95$ criterion, respectively. The data statistics are generated for two SolarSIMs' calibrations performed against the PGS-100 and LI-1800 spectroradiometers, respectively, at NREL. PGS-

Table 5
Summary of the SolarSIMs' AOD performance against the PFR triad from September 28 to October 1, 2015, where λ, $\Delta\widetilde{\mu}$, σ, and N_{U95} denote the AOD wavelength, the median AOD difference, the standard deviation of the AOD difference, and the percentage of data points that fall within the WMO's $U95$ criterion, respectively. Data are presented for two different calibrations - against the PSG-100 and LI-1800 spectroradiometers deployed by the National Renewable Energy Laboratory. Note, the italicised values denote the SolarSIM's AOD wavelengths for which less than 95% of data points fall within the WMO criterion from Eq. (11).

		Calibration vs. PGS-100		Calibration vs. LI-1800	
λ	Device	$\Delta\widetilde{\mu} \pm \sigma$	N_{U95}(%)	$\Delta\widetilde{\mu} \pm \sigma$	N_{U95}(%)
368 nm	SSIM 1	+ 0.027 ± 0.010	*8.6*	−0.001 ± 0.006	*85.7*
	SSIM 2	+ 0.020 ± 0.005	*0*	−0.002 ± 0.004	97.8
	SSIM 3	+ 0.018 ± 0.007	*13.3*	−0.002 ± 0.003	95.1
	SSIM 4	+ 0.026 ± 0.010	*8.8*	−0.006 ± 0.005	*79.5*
412 nm	SSIM 1	+ 0.014 ± 0.006	*32.9*	−0.001 ± 0.004	*92.9*
	SSIM 2	+ 0.011 ± 0.005	*38.1*	−0.000 ± 0.002	99.1
	SSIM 3	+ 0.010 ± 0.005	*66.6*	−0.000 ± 0.003	97.1
	SSIM 4	+ 0.011 ± 0.006	*46.8*	−0.005 ± 0.004	*85.2*
500 nm	SSIM 1	−0.000 ± 0.003	100.0	−0.001 ± 0.002	98.9
	SSIM 2	+ 0.001 ± 0.005	99.9	+ 0.002 ± 0.003	99.2
	SSIM 3	+ 0.000 ± 0.004	100.0	+ 0.002 ± 0.003	99.3
	SSIM 4	−0.004 ± 0.005	100.0	−0.003 ± 0.002	97.9
862 nm	SSIM 1	−0.005 ± 0.003	100.0	+ 0.004 ± 0.002	99.6
	SSIM 2	−0.004 ± 0.005	100.0	+ 0.003 ± 0.002	99.4
	SSIM 3	−0.004 ± 0.004	100.0	+ 0.005 ± 0.002	99.4
	SSIM 4	−0.003 ± 0.004	100.0	+ 0.004 ± 0.003	99.2

100 has a non-removable collimation tube and hence cannot be directly calibrated using a standard lamp method. Instead, it is calibrated outdoors in the direct normal mode against the LI-1800 spectroradiometer, which results in higher measurement uncertainty for the PGS-100 as compared to the LI-1800. As a result, the AOD performance of the SolarSIMs is poorer when the PGS-100 calibration is applied as compared to a LI-1800 calibration, especially for < 420 nm. Nonetheless, the performance of all SolarSIMs for both calibration methods fall within the calculated uncertainties from Table 2. Furthermore, using the LI-1800 calibration for 500 nm and 862 nm all four SolarSIMs comply with the WMO *U*95 criterion, while for 368 nm and 412 nm two out four SolarSIMs meet this criterion[4]. The short wavelength extrapolation, especially at 368 nm, is understandably slightly less accurate than the longer wavelength interpolations.

5.4. Precipitable water vapor content comparison

Precipitable water vapor (PWV) is a highly-variable trace gas in the atmosphere that serves as a key input parameter in weather predictions models and climate studies (Liang et al., 2015; Karabatić et al., 2011). During the IPC-XII, PWV data acquired by a co-located Cimel CE318 sun photometer from the Aerosol Robotic Network (AERONET) was compared against PWV data derived by the SolarSIMs (Holben et al., 1998). Both instruments measure the solar irradiance near 940 nm, which is well suited for analyzing the atmospheric PWV content according to Halthore et al. (1997).

Fig. 6 shows the daily profile of PWV content on 30 September 2015, as measured by the SolarSIMs and the Cimel CE318 sun photometer. The SolarSIMs, on average, report PWV values that are approximately 1 mm higher than the Cimel CE318. Extending the evaluation over a 13 day period, a comparison of the daily average PWV content is shown in Fig. 7. Over this time period 248 time-synchronous data points were gathered for the SolarSIMs and the Cimel, allowing the calculation of the mean differences and standard deviations of 0.96 ± 0.21 mm, 1.02 ± 0.23 mm, 0.71 ± 0.15 mm, and 0.84 ± 0.23 mm for SSIM 1, SSIM 2, SSIM 3, and SSIM 4, respectively; the average Cimel PWV was 5.72 mm. These results are in line with measurement uncertainties of both the SolarSIMs and the Cimel, considering the Cimel can have a measurement bias of −25% or −1.43 mm under these PWV conditions (Schneider et al., 2010). We view these comparative results as a good starting point in quantifying the PWV measurement accuracy of the SolarSIM. Future research will include a long-term, comparative study between a SolarSIM and a Fourier Transform Infrared Spectrometer to gain a further insight into the PWV retrieval capability of the SolarSIM.

5.5. Total column atmospheric ozone comparison

Ozone is an atmospheric gas critically necessary to attenuate solar UV radiation, which has been linked to skin cancer, immune system suppression, and eye damage (WHO, 1994). As a result, it is crucial to monitor the total column ozone in the atmosphere. At present, Brewer spectrophotometers comprise the largest ground-based ozone measurement network in the world, spanning 40 countries (Gao et al., 2010). However, the Brewer is an expensive instrument with involved measurement procedures (Karhu, 2016). In contrast, the SolarSIM infers the total ozone column from a channel at 610 nm, which is spectrally situated near the peak ozone absorption in the Chappius band (Tatsiankou et al., 2016). Because ozone absorption at 610 nm is weak, less than 6% at AM1.5D conditions, it is of interest to assess the accuracy of the SolarSIM-derived ozone data against the Brewer spectrophotometer.

During the IPC-XII, the Brewer MkIII #163 spectrophotometer was

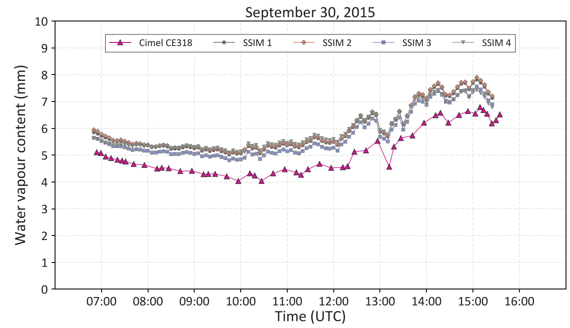

Fig. 6. Daily water vapor content profile as measured by the SolarSIMs and the Cimel CE318 sun photometer on September 30, 2015.

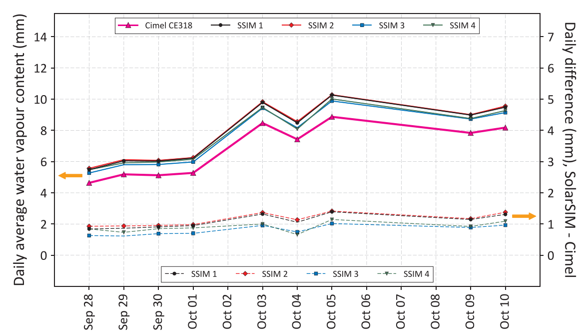

Fig. 7. Daily average water vapor content (left axis) and the difference in the daily water vapor content (right axis) as measured by the SolarSIMs and the Cimel CE318 sun photometer.

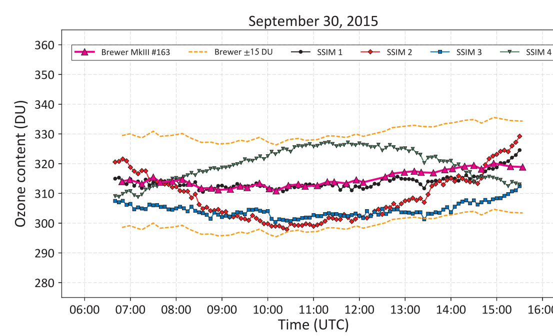

Fig. 8. The daily profile of the total ozone column amount as measured by the SolarSIMs and the Brewer MkIII spectrophotometer #163 on 30 September 2015.

in continuous operation at the WRC. The daily atmospheric ozone profiles as measured by the Brewer spectrophotometer and the SolarSIMs were compared, with data from 30 September 2015 shown in Fig. 8. The SolarSIMs' ozone measurements are all within ± 15DU (or ± 5%) of the reference Brewer measurements. Further assessment was made over the course of two weeks, with 236 matching data points collected between all instruments, over 70% of them occurring between 28 September and 2 October 2015. SolarSIM data with AOD values at 500 nm above 0.12 were discarded, in compliance with the IPC criteria for determining adequate stability under cloudless conditions. For each day of testing, the daily ozone averages were computed for each device; comparisons with the Brewer spectrophotometer data are shown Fig. 9. The average of the daily differences between the SolarSIMs' and the Brewer and their standard deviations across the assessment period were −1 ± 5 DU, −4 ± 7 DU, −10 ± 8 DU, and 8 ± 7 DU for the SSIM 1, SSIM 2, SSIM 3, and SSIM 4, respectively; the average Brewer's total

[4] The SolarSIM AOD performance may be further improved with Langley plot calibrations in suitable locations.

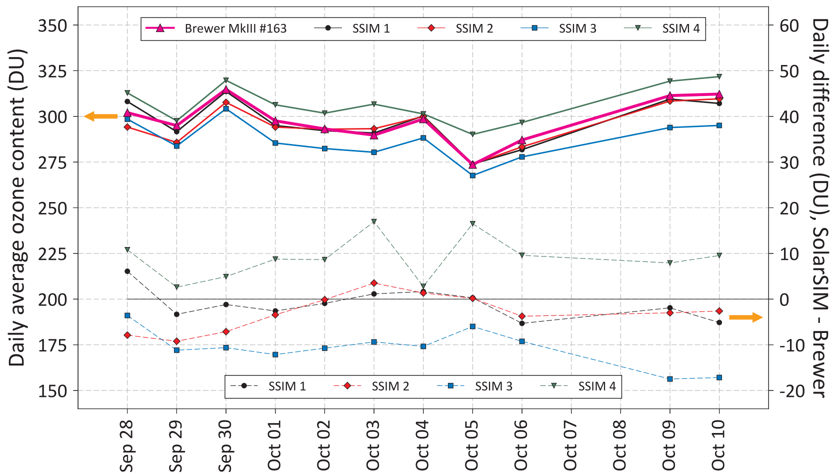

Fig. 9. A comparison of the daily average ozone content (left axis) and the daily average ozone difference (right axis) as measured by the SolarSIMs and the Brewer MkIII spectrophotometer 163 from 28 September 2015 to 10 October 2015.

ozone column was 300 DU. Multi-day measurements by the SolarSIMs apparently provide good quality ozone column data with much better performance than the estimated ozone retrieval uncertainty of 64 DU, as calculated in Section 4.7. However, the SolarSIM ozone measurements are very sensitive to small signal changes at 610 nm, which can occur due to misalignment or soiling. Since these data constitute "best-case" scenario, future research will include a long term study between SolarSIMs and Brewer spectrophotometers to gain further insights into the capability of SolarSIM to retrieve accurate total column ozone.

6. Conclusion

Measurements of direct sunlight are critical for numerous applications, including solar research, atmospheric science, and weather forecasting. Many commercial instruments, such as pyrheliometers, spectroradiometers, and sun photometers, exist for such purposes. Unlike these traditional instruments, the SolarSIM uses ground-based measurements in conjunction with a radiative transfer model to resolve in real-time broadband and spectral DNI, AOD, PWV and atmospheric total column ozone. We assessed the ability of the SolarSIM to resolve these parameters by first performing an extensive uncertainty analysis. These findings were then used to evaluate the measurements of four SolarSIMs deployed from 28 September to 10 October 2015 at the WRC. The availability of numerous, high-quality scientific instruments enabled further insight into the SolarSIM's ability to resolve DNI, spectral DNI and AOD, atmospheric PWV content, and total column ozone.

The SolarSIMs' DNI data were compared against the PMO2 absolute cavity radiometer from the WSG and the SolarSIMs were assigned the WRR factors ranging from 0.999674 to 0.994610. The mean difference in the spectral DNI between SolarSIMs and reference spectroradiometers was found to be < 5% for wavelengths above 400 nm. The median AOD differences and their standard deviations between the four SolarSIMs and the PFR triad averaged 0.0046 ± 0.0044, 0.0016 ± 0.0034, 0.0018 ± 0.0026, and 0.0041 ± 0.0022 for 368 nm, 412 nm, 500 nm, and 865 nm, respectively. The mean difference in total column PWV and the corresponding standard deviation, as compared to a Cimel CE318 sun photometer, averaged 1 ± 0.2 mm for the four SolarSIMs. The difference in mean total column ozone and the corresponding standard deviation between the SolarSIMs and Brewer MkIII spectrophotometer averaged 6 ± 7 DU. The reported results were all within the estimated measurement uncertainties, albeit for the AOD and total column ozone the calculated uncertainties appear to be rather conservative. Therefore, further comparative studies are needed to refine some of the uncertainties associated with the SolarSIM's ability to resolve various atmospheric parameters.

Based on the presented data, we have shown that the SolarSIM-D2 is capable of performing accurate and precise measurements of broadband and spectral DNI, AOD, PWV, and total ozone column. Its compact size, low cost, and rugged design positions the SolarSIM-D2 as a potential alternative for routine and dependable monitoring of direct sunlight and atmospheric constituents. Further SolarSIM deployments and additional comparative studies against reference instruments will help determine the primary role of this promising device within the solar research and atmospheric science communities.

Acknowledgment

The authors would like to acknowledge support from the National Sciences and Engineering Research Council of Canada, the Ontario Research Fund - Research Excellence program, the Ontario Centres of Excellence, the Canada Research Chairs program, the Canadian Foundation for Innovation, and the National Research Council's Industry Research Assistance Program.

We would like to thank Roberto Galleano from the Joint Research Center and Lionel Doppler from the German Meteorological Service for providing the spectral data, and Luca Egli from the World Radiation Center for sharing the ozone data. We also would like to acknowledge the NREL's Solar Radiation Research Laboratory for providing the spectral and irradiance data sets used in our uncertainty analysis.

References

AlYahya, S., Irfan, M.A., 2016. Analysis from the new solar radiation atlas for Saudi Arabia. Solar Energy 130, 116–127.
Andreas, A., 2016. WISER Calibration Certificate at NREL < http://www.nrel.gov/aim/Calibrations/Spectral/MS7XX/7XX_2016_09.rpt.zip > .
Andreas, A., Stoffel, T., 1981. NREL Solar Radiation Research Laboratory (SRRL): Baseline Measurement System (BMS). Golden, Colorado (Data); NREL Report No. DA-5500-56488.
Araki, K., Yamaguchi, M., 2003. Influences of spectrum change to 3-junction concentrator cells. Solar Energy Mater. Solar Cells 75, 707–714.
Caballero, J.A., Fernández, E.F., Theristis, M., Almonacid, F., Nofuentes, G., 2018. Spectral corrections based on air mass, aerosol optical depth, and precipitable water for PV performance modeling. IEEE J. Photovolt. 8 (2), 552–558.
Cebecauer, T., Suri, M., 2016. Site-adaptation of satellite-based DNI and GHI time series: Overview and SolarGIS approach. In: AIP Conference Proceedings. AIP Publishing, pp. 150002.
Fernández, E.F., Soria-Moya, A., Almonacid, F., Aguilera, J., 2016. Comparative assessment of the spectral impact on the energy yield of high concentrator and conventional photovoltaic technology. Solar Energy Mater. Solar Cells 147, 185–197.
Finsterle, W., 2016. WMO International Pyrheliometer Comparison IPC-XII Final Report.

WMO/IOM 124.
Gao, W., Schmoldt, D., Slusser, J.R., 2010. UV Radiation in Global Climate Change: Chapter 6. Springer.
Gröbner, J., Kouremeti, N., Nevas, S., Blattner, P., 2014. Characterisation Studies of Precision Solar Spectroradiometer. Technical Report. WRC/PMOD.
Gueymard, C., 1995. SMARTS2: A Simple Model of the Atmospheric Radiative Transfer of Sunshine: Algorithms and Performance Assessment. Florida Solar Energy Center Cocoa, FL.
Gueymard, C.A., 2004. The sun's total and spectral irradiance for solar energy applications and solar radiation models. Solar Energy 76, 423–453.
Gueymard, C.A., 2006. SMARTS2 code, Version 2.9.5, User's Manual, Technical Report. Solar Consulting Services.
Gueymard, C.A., 2008. Prediction and validation of cloudless shortwave solar spectra incident on horizontal, tilted, or tracking surfaces. Solar Energy 82, 260–271.
Halthore, R.N., Eck, T.F., Holben, B.N., Markham, B.L., 1997. Sun photometric measurements of atmospheric water vapor column abundance in the 940 nm band. J. Geophys. Res. 102, 4343–4352.
Holben, B., Eck, T., Slutsker, I., Tanre, D., 1998. AERONET - a federated instrument network and data archive for aerosol characterization. Rem. Sens. Environ. 66, 1–16.
Holben, B., Tanre, D., Smirnov, A., Eck, T., 2001. An emerging ground-based aerosol climatology: aerosol optical depth from AERONET. J. Geophys. Res.: Atmos. 106, 12067–12097.
JCGM, 2008. Evaluation of Measurement Data - Guide to the Expression of Uncertainty in Measurement. Bureau International des Poids et Mesures.
Karabatić, A., Weber, R., Haiden, T., 2011. Near real-time estimation of tropospheric water vapour content from ground based GNSS data and its potential contribution to weather now-casting in Austria. Adv. Space Res. 47, 1691–1703.
Karhu, J.M., 2016. Brewer spectrometer total ozone column measurements in Sodankylä. Geoscient. Instrumen., Meth. Data Syst. 5, 229.
Kazadzis, S., Kouremeti, N., Gröbner, J., 2016. Fourth WMO Filter Radiometer Comparison (FRC-IV).
Kazadzis, S., Kouremeti, N., Nyeki, S., Gröbner, J., Wehrli, C., 2017. The World aerosol Optical depth Research and Calibration Center (WORCC), Quality assurance and quality control of GAW-PFR AOD measurements. Geoscient. Instrumen., Meth. Data Syst. Disc. 2017, 1–19.
Liang, H., Cao, Y., Wan, X., Xu, Z., Wang, H., Hu, H., 2015. Meteorological applications of precipitable water vapor measurements retrieved by the national GNSS network of China. Geod. Geodynam. 6, 135–142.
Majumdar, Z.K., Cunningham, D.W., 2017. Performance metrics and testing of micro-concentrated and hybrid photovoltaic systems for ARPA-E MOSAIC. In: Optics for Solar Energy. Optical Society of America, p. RW3B-2.
Núñez, R., Domínguez, C., Askins, S., Victoria, M., Herrero, R., Antón, I., Sala, G., 2016. Determination of spectral variations by means of component cells useful for CPV rating and design. Prog. Photovolt.: Res. Appl. 24, 663–679.
Reda, I., Andreas, A., 2008. Solar Position Algorithm for Solar Radiation Applications. Technical Report. NREL.
Rodrigo, P.M., Fernández, E.F., Theristis, M., Cruz, F.A., 2017. Characterization of the spectral matching ratio and the z-parameter from atmospheric variables for CPV spectral evaluation. IEEE J. Photovolt. 7, 1802–1809.
Schmutz, W., Finsterle, W., Kazadzis, S., Kouremeti, N., Gröbner, J., Thomann, C., 2016. PMOD Annual Report 2015.
Schneider, M., Romero, P., Hase, F., Blumenstock, T., Cuevas, E., Ramos, R., 2010. Continuous quality assessment of atmospheric water vapour measurement techniques: FTIR, Cimel, MFRSR, GPS, and Vaisala RS92. Atmos. Measur. Techniq. 3, 323–338.
Tatsiankou, V., Hinzer, K., Muron, A., Mohammed, J., Wilkins, M., Haysom, J., Schriemer, H., Myrskog, S., 2013. Reconstruction of the solar spectral resource using limited spectral sampling for concentrating photovoltaic systems. In: Photonics North. International Society for Optics and Photonics.
Tatsiankou, V., Hinzer, K., Schriemer, H., Haysom, J.E., Beal, R., 2016. Design principles and field performance of a solar spectral irradiance meter. Solar Energy 133, 94–102.
Theristis, M., Fernández, E.F., Almonacid, F., Pérez-Higueras, P., 2016. Spectral corrections based on air mass, aerosol optical depth, and precipitable water for CPV performance modeling. IEEE J. Photovolt. 6, 1598–1604.
WHO, 1994. Ultraviolet Radiation, vol. 160. World Health Organization.
WMO, 2005. Experts Workshop on a Global Surface Based Network for Long Term Observations of Column Aerosol Optical Properties, Technical Report. GAW Report 162.
WMO, 2008. Guide to Meterological Instruments and Methods of Observation.

3.2 Global SolarSIM

3.2.1 Design Principles and Field Performance

3.2.1.1 Scope and Impact

The following article describes the basic design principles, calibration procedure, and field of performance of two SolarSIM-Gs for resolving the spectral and broadband global irradiances in the 280–4000 nm range. The instrument's optics were optimized to couple global irradiance within a 180° field of view, with a directional response surpassing that of ISO 9060:2018 Class A pyranometer. As compared to the direct SolarSIM, the SolarSIM-G makes three additional irradiance measurements; one channel in the ultraviolet and two channels in the infrared ranges. The extra measurements are necessary to resolve the effects of diffuse irradiance and cloud scattering based on my novel, all-sky parametrized transmittance model. In addition, the paper describes the calibration procedure and field performance of two SolarSIM-Gs at NREL's Solar Radiation Research Laboratory. A statistical analysis is presented on the data obtained between the SolarSIM-Gs and reference instrumentation, namely secondary standard spectroradiometers and pyranometers. The results indicate the SolarSIM-Gs' derived spectral and broadband GHI are within the measurement uncertainty of the NREL's reference instruments.

The SolarSIM-G is a novel instrument capable of accurately resolving real-time broadband and spectral global irradiance in the 280–4000 nm range using ground-based measurements coupled with an all-sky parameterized transmittance model. The innovation behind this instrument is encapsulated in two US patents (10,209,132 B2 and 10,359,314 B2), with the most recent patent attached in Appendix to provide more context surrounding the SolarSIM-G's optical and mechanical designs. For reasons pertaining to the intellectual property protection, I chose to publish this work as a conference proceeding instead of a journal paper. One of the most important uses for the SolarSIM-G is in the general solar industry, where the knowledge of spectral irradiance improves the accuracy of module characterization and reduces the performance uncertainty of photovoltaic power plants, which can subsequently make solar technologies a more attractive investment. The SolarSIM-G is positioned to become the default spectral sensor in the solar industry.

3.2.1.2 Author Contributions

Viktar Tatsiankou: All research and scientific contributions in this article are my own but were sometimes guided and supported by other co-authors. The primary contribution of this work is the development of an all-sky parameterized transmittance model capable of deriving the full range spectral and broadband global irradiances from nine optical measurements. The supporting contribution was the electrical, optical and mechanical designs of the SolarSIM-G's hardware, enabling it to measure the global irradiance with a satisfactory directional response within a hemispherical field of view. Two commercially packaged instruments were built and characterized, then calibrated and validated at the NREL against reference instrumentation.

Dr. Karin Hinzer: As my supervisor and the director of the SUNLAB at the University of Ottawa, Karin oversaw my research and assisted with preparing the final manuscript.

Dr. Henry Schriemer: As the associate director of the SUNLAB at the University of Ottawa, Henry oversaw my research and helped to review and edit the manuscript.

Patrick McVey-White: As a research engineer at Spectrafy, Patrick helped to characterize the SolarSIM-Gs' directional response.

Dr. Richard Beal: As a collaborator from Spectrafy, Richard guided my research and aided in reviewing the final manuscript.

3.2.1.3 Publication

The publication follows on next page.

V. Tatsiankou, K. Hinzer, H. Schriemer, P. McVey-White, and R. Beal, "Efficient, real-time global spectral and broadband irradiance acquisition". *45th IEEE Photovoltaic Specialists Conference (PVSC)*, 2018.

The following patent describes in detail the inner-working of the SolarSIM-G, but because it is not laid out in pedagogically effective manner, it is included in the Appendix.

V. Tatsiankou, R. Beal, "Global solar spectrum devices and methods". US Patent 10,359,314 B2 issued July 23, 2019.

Efficient, Real-Time Global Spectral and Broadband Irradiance Acquisition

Viktar Tatsiankou[1,2], Karin Hinzer[1], Henry Schriemer[1], Patrick McVey-White[2], and Richard Beal[2]

***Abstract* — Two global solar spectral irradiance meters (SolarSIM-Gs) were deployed and tested at the National Renewable Energy Laboratory in Golden, USA from 18 September to 6 October 2017. The instruments were installed in the global horizontal orientation at the Solar Radiation Research Laboratory and their measurements were compared against co-located secondary reference spectroradiometers and secondary standard pyranometers. The SolarSIM-Gs' spectral global horizontal irradiance (GHI) accuracy was shown to be < 5% on average per wavelength in the 290-1650 nm range for over 1,900 analyzed spectra. The broadband GHI measurement accuracy for two instruments was shown to have mean bias and standard deviation of 0.97, 1.23 W/m^2 and 5.27, 5.65 W/m^2, respectively, for over 10,000 analyzed data points.**

***Index Terms* — global solar spectral irradiance meter, SolarSIM-G, solar spectrum, GHI, global horizontal spectral irradiance, spectral irradiance, solar sensors, solar instrumentation**

I. Introduction

Photovoltaic (PV) module performance is specified for Standard Testing Conditions (STC) under the ASTM G-173 reference solar spectrum with integrated irradiance of 1000 W/m^2 and an air mass of 1.5 [1]. During field operation, the air mass, aerosols, precipitable water vapour and pollutants modify the spectral distribution as seen by solar panels, hence their performance deviates from the STC. For example, in the continental USA depending on the PV module technology and location, the spectral irradiance variation cause anywhere between -0.6% to +2.6% change in predicted annual energy yield with and without spectral correction [2]. In other locations, such as India and China, the solar spectrum fluctuations are expected to affect PV performance even more [3]. Unarguably, the knowledge of the local global horizontal or plane of array spectral irradiance as opposed to just the broadband irradiance improves the accuracy of instantaneous characterization and reduces the long-term performance uncertainty of PV power plants.

Historically, field spectroradiometers have been the only way to acquire the local solar spectrum, but, due to high instrument costs, the routine spectral measurements are almost non-existent, except for a few, well-funded national labs, such as the Solar Radiation Research Facility (SRRL) at the National Renewable Energy Laboratory (NREL) in the USA [4]. With this challenge in mind, the global solar spectral irradiance meter (SolarSIM-G) was designed as a cost-effective alternative to a spectroradiometer with the added function of providing the broadband global horizontal or tilted irradiance, as typically acquired by a pyranometer. This novel instrument was made to provide PV community with an affordable tool for solar resource assessment, module characterization and power plant performance monitoring.

In this abstract, we describe SolarSIM-G's general design and then assess the instrument's ability of resolving the spectral and broadband global horizontal irradiances (GHI). To do so, we perform a comparative analysis from the datas gathered by two SolarSIM-Gs deployed at the SRRL during 18 September to 6 October 2017 against co-located secondary reference spectroradiometers and secondary standard pyranometers.

II. Design and Operation

The SolarSIM-G measures the global spectral irradiance with seven silicon and two indium gallium arsenide photodetectors combined with nine hard-coated narrow bandpass filters; the instrument also senses ambient pressure, relative humidity, air temperature, as well as device's internal humidity and temperature. These parameters are fed into a radiative transfer model to derive in real-time the spectral and broadband GHIs. The software and hardware of the SolarSIM-G is partially based on the SolarSIM-D2, our six-channel sensor which resolves the spectral and broadband direct normal irradiance, spectral aerosol optical depth, precipitable water vapour and total ozone column amount in the 280-4000 nm range [5,6]. However, compared to the direct beam irradiance, the reconstruction of global sunlight is more involved because one must also consider the diffuse irradiance, arising mainly from the atmospheric scattering, clouds, and ground albedo. Hence, the SolarSIM-G has three additional channels as compared to the D2, which aids in the reconstruction of the diffuse irradiance – one channel is in the ultraviolet and two channels are in the infrared ranges.

The SolarSIM-G couples sunlight with a 180º field of view through a bulk diffuser into a cylindrical integrating cavity, which is coated with a near-Lambertian, high-reflectance coating. The integrating cavity and diffuser combination have been designed to optimize the cosine

978-1-5386-8529-7/18/$31.00 ©2018 IEEE

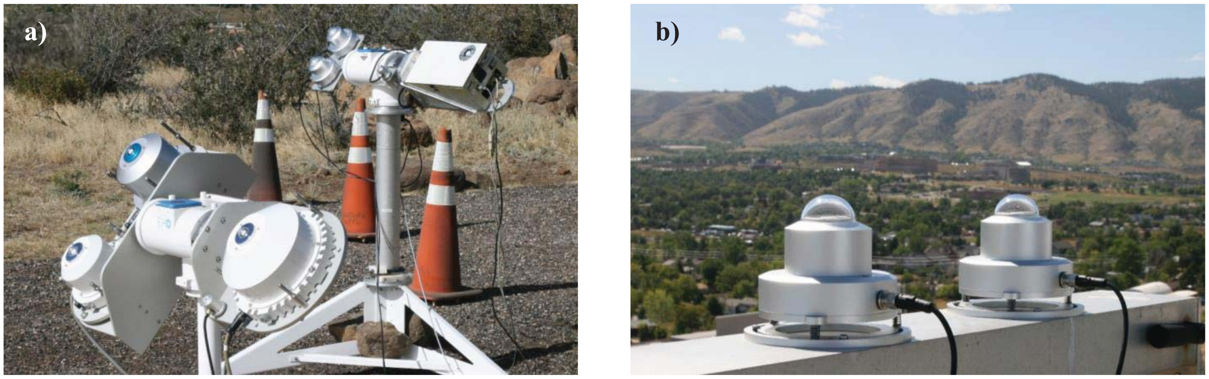

Fig 1. a) Two SolarSIM-Gs were calibrated against the EKO WISER and LICOR Li-1800 spectroradiometers in the global normal orientation at the Solar Radiation Research Laboratory (SRRL). b) Two SolarSIM-Gs were deployed in the global horizontal orientation post-calibration at the SRRL to assess their broadband and spectral performance against NREL's pyranometers and spectroradiometers, respectively.

response which complies with a secondary standard for a pyranometer (±10 W/m^2 as per ISO-9060). The diffuse light then exits the cavity via nine collimation tubes, with each having a bandpass filter and a photodiode below it. The aperture and field stop geometries of the collimation tubes ensure that the light passing through bandpass filters has angular divergence of less than 10º to maintain their stated performance.

Analogous to the D2, the SolarSIM-G data acquisition printed circuit board is housed inside the anodized aluminum enclosure. The electronics sequentially measure the current from each photodiode and digitizes it with a 22-bit analog-to-digital converter. The converted values, along with meteorological measurands are sent via a RS-485 communication protocol to a computer, where a graphical user interface reconstructs in real-time the spectra and broadband GHI in the 280-4000 nm range with a frequency of up to 1 Hz.

III. Calibration

Two SolarSIM-Gs with serial numbers SN1010 and SN1011, manufactured by Spectrafy Inc., were calibrated at the SRRL (39.74º N, 105.18ºW) against a LICOR LI-1800 and EKO MS711/MS712 (WISER) secondary reference spectroradiometers in the global normal orientation, as shown in Fig. 2. The SolarSIM-Gs were mounted on EKOs STR-22G solar tracker alongside the LI-1800, while the WISER was mounted within proximity on a separate STR-22G tracker. The SolarSIM-Gs were connected to as laptop inside the SRRL office, where a computer application acquired and processed raw data from both devices every 5 seconds. On the other hand, the data acquisition of spectroradiometers was handled through SRRL's Baseline Measurement System [4].

The calibration procedure was performed on 18-19 September – it ensured the SolarSIM-G's spectral irradiance in its nine optical channels matched the irradiance from the

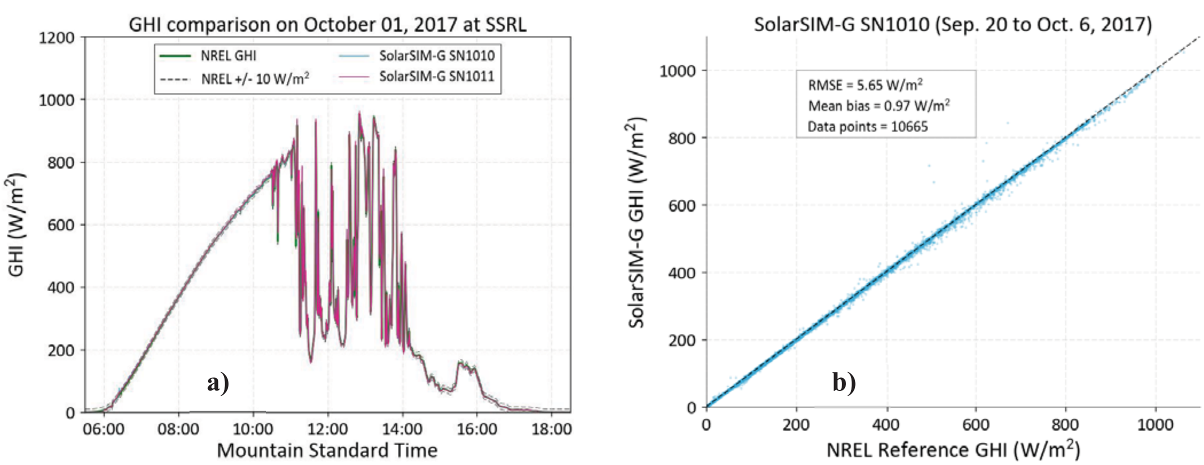

Fig. 2. a) GHI data from the SolarSIM-Gs, as compared to NREL's reference GHI data on 1 October 2017. The dashed black lines represent the ±10 W/m^2 limits from the reference GHI. b) Scatter plot of the GHI data from SolarSIM-G SN1010 versus NREL's reference GHI data from 20 September to 6 October 2017. The mean bias and RMSE of the dataset are 0.97 W/m^2 and 5.65 W/m^2, respectively.

reference spectroradiometers in the corresponding wavelength bands. The data for sun elevation angles below 45º was discarded to avoid ground albedo from affecting the measurements. Upon completion, nine calibration factors were generated for each SolarSIM-G, which compensate for the diffuser absorption, manufacturer's filter transmittances, and photodiode responsivities assumed in our model.

III. Performance

The SolarSIM-Gs were installed in the global horizontal orientation to assess their spectral and broadband GHI performance against NREL's reference instruments, as shown in Fig. 1b. The integral of the SolarSIM-G's spectrum in the 280-4000 nm range yields the broadband GHI, which was compared against NREL's calculated reference GHI. The reference values are computed from the direct normal irradiance, as measured by first class pyrheliometers (average of the two Kipp & Zonen CHP-1s), CMP-22s, one Huksenflux SR-25, and one Eppley-848). This method of obtaining the GHI values has less uncertainty than the data measured by the unshaded pyranometer alone, because the cosine errors are minimized. Fig. 2 shows the daily GHI profile as measured by two SolarSIM-Gs on 1 October 2017 with a one-minute resolution. This day presents a mix of atmospheric conditions, varying from clear sky in the morning to heavy cloudy in the afternoon. The SolarSIM-Gs' data stays within ±10 W/m^2 of the reference NREL GHI throughout this day. We then aggregate the GHI data for the SolarSIM-G SN1010 and SN1011 from 20 September to October 6 into a scatter plot, as presented for SN1010 in Fig. 3. The mean bias and the root mean square error (RMSE) of the SN1010 data set was found to be 0.97 W/m^2 and 5.65 W/m^2, respectively, for over 10,000 data points analyzed. Similarly, for the SN1011 data set, the mean bias and RMSE were 1.23 W/m^2 and 5.27 W/m^2, respectively. Note, the scatter plot for SN1011 is not shown because it's near identical to SN1010's one.

We then compared the spectral measurement performance of the SolarSIM-Gs against the NREL's WISER spectroradiometer in the global horizontal orientation. Fig. 4a shows the mean spectral GHI of the aforementioned instruments from 20 to 24 September 2017, during which 1,929 spectra per instrument were gathered. Note, the spectra with integrated total irradiance of less than 50 W/m^2 were excluded from the analysis. The plot suggests that the mean spectral irradiance of the SolarSIM-Gs is well within the combined uncertainty of the WISER spectroradiometer. For more detail, Fig. 4b shows the mean difference and the standard deviation between the SolarSIM-G SN1010 and WISER's spectral GHI data sets is mainly within 5%, except for areas with oxygen and water vapour absorption bands (vertical gray bands). Increased standard deviation is observed below 350 nm and above 1600 nm, which can be partially attributed to higher temperature dependence and/or stray light limitation of the WISER spectroradiometers.

IV. Conclusion

Two SolarSIM-Gs SN1010 and SN1011 were deployed and validated at the SRRL against NREL's reference instrumentation. The SolarSIM-Gs' broadband and spectral performances in the global horizontal orientation were assessed against co-located secondary standard pyranometers and secondary reference spectroradiometers, respectively, from 20 September to 6 October 2017. Over this period, the mean bias and the RMSE of the SolarSIM-Gs' as compared to reference GHI data sets were 0.97 W/m^2 and 5.65 W/m^2 for SN1010, respectively, and 1.23 W/m^2 and 5.27 W/m^2, for

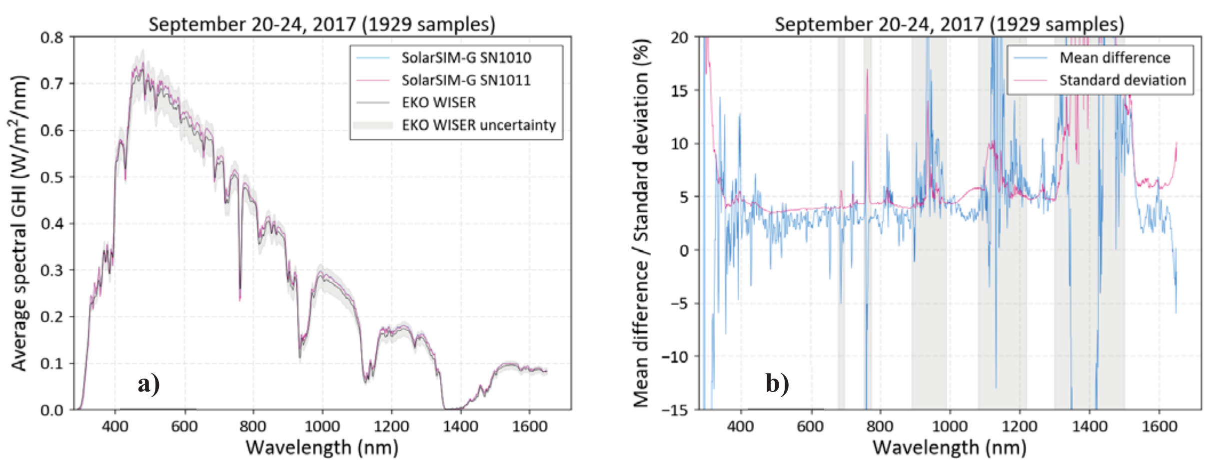

Fig. 3. a) The mean spectral GHI as measured by the SolarSIM-G SN1010 and SN1011 versus the spectral GHI from the WISER spectroradiometer. The mean spectra were calculated from 1,929 measurements, per instrument during the period of 20 to 24 September 2017. The gray band represents the estimated combined uncertainty of the WISER. Note, the SolarSIM-G spectra was smoothed with 5 nm central averaging to approximate the lower measurement resolution of the spectroradiometer. b) The mean difference and standard deviation between the SolarSIM-G's (SN1010) and WISER's spectral GHI data sets. The vertical gray bands are areas with oxygen and water vapour absorption.

SN1011, respectively. Over 10,000 data points per instrument were used in our GHI comparative analysis. Furthermore, the mean difference and the standard deviation of the spectral GHI data set between the SolarSIM-Gs and the WISER spectroradiometer were mainly within ±5%, not including the oxygen and water vapour absorption bands. Over 1,900 spectra per instrument was gathered from 20 to 24 September 2017 and used in our spectral GHI performance analysis. These results indicate the SolarSIM-G can perform very accurate spectral and broadband GHI measurements. In addition, its compact size, low cost, and rugged design makes the SolarSIM-G a capable instrument for performing solar resource assessment, module characterization studies, certification, operation and maintenance of PV power plants.

REFERENCES

[1] IEC 60904-3: Photovoltaic devices - Part 3: Measurement principles for terrestrial photovoltaic (PV) solar devices with reference spectral irradiance data (2009).

[2] K. Passow and M. Lee. "Effect of spectral shift on solar PV performance." *Technologies for Sustainability (SusTech) Conference* (2016).

[3] D. B. Magare, et al. "Effect of seasonal spectral variations on performance of three different photovoltaic technologies in India." *International Journal of Energy and Environmental Engineering* 7.1 (2016):93-103.

[4] T. Stoffel, A. Andreas, I. Reda, et al. "Solar Radiation Research Laboratory". SunShot Grand Challenge Summit and Technology Forum. (2012)

[5] V. Tatsiankou, K. Hinzer, H. Schriemer, K. Emery, and R. Beal "Design principles and field performance of a solar spectral irradiance meter" *Solar Energy* 133 (2016): 94-102.

[6] V. Tatsiankou, K. Hinzer, H. Schriemer, S. Kazadzis, N. Kouremeti, J. Gröbner, and R. Beal. "Extensive validation of solar spectral irradiance meters at the World Radiation Center." *Solar Energy* 166 (2018): 80-89.

3.3 Characterization Methods

Reliable and repeatable characterization methods are critical for improved confidence and higher accuracy in solar radiometric measurements. For example, in this work the thermal calibration setup is used to reduce the temperature dependence uncertainty of SolarSIM's photodiodes through an automated correction. On the other hand, the directional response setup aids in verifying the SolarSIM-G's compliance to an international standard for global irradiance radiometers. Finally, proper optical calibration ensures the measurement uncertainty of a SolarSIM under test remains as close as possible to a reference instrument. This chapter describes the aforementioned characterization methods in detail.

3.3.1 Thermal Test

The spectral responsivity of photodiodes varies as a function of temperature, which depends on the material type, manufacturing processes, and packaging. While in operation outdoors, the SolarSIM channels must be temperature corrected to ensure the highest measurement accuracy. This correction requires prior knowledge of the temperature coefficients for each channel, which are determined using the thermal calibration setup, as shown in Figures 3.1a. I determine these coefficients by monitoring photodiode outputs, during a temperature sweep under a 250 W quartz tungsten light source (3a)[1]. The spectral stability of the lamp is also monitored by external photodiodes with bandpass filters (5a), whose centre wavelength and full-width at half-maxima are matched to the SolarSIM channels. The lamp's output is collimated by a plano-convex lens (6a), which is critical for the SolarSIM-D2 as it only measures the irradiance in a narrow 5° field if view. The SolarSIM under test (7a), either direct or global sensor version, is placed onto the thermo-electric cooler (TEC) stage (8a), which is controlled by the Keithley 2510 TEC sourcemeter (3a). The SolarSIM's internal temperature is first cooled to 20 °C, following which I gradually raise the temperature set point of the stage to 60 °C. As the SolarSIM's internal temperature increases, the specialized software on the computer (1a) communicates with the SolarSIM and records the photodiode current versus the internal temperature. Once the internal temperature reaches 40 °C, the test is stopped and the software computes the best line of fit slopes for each SolarSIM channel, thus yielding the temperature coefficients. The uncertainty in determining the temperature coefficients for each channel was detailed in the journal article in Section 3.1.2.

3.3.2 Directional Response

Solar radiometers measuring global irradiance are often prone to cosine or directional errors, in other words, their response deviates from the Lambertian when the sun's angle of incidence varies relative to the instrument's normal [32], [33]. The directional response error is one of the main sources of measurement uncertainty for pyranometers and spectroradiometers. Through its recently updated ISO 9060:2018 standard,"Solar energy –

[1] refers to item 3 in Figure 3.1a, hence the label "3a"

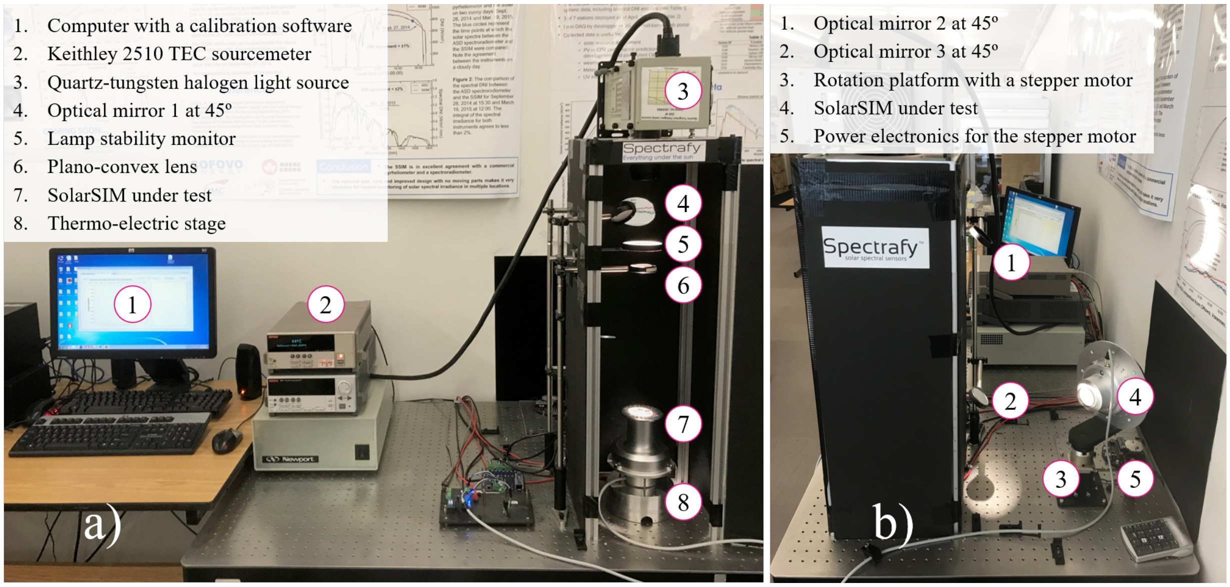

Figure 3.1: a) Thermal calibration setup used to determine the temperature coefficients of a SolarSIM. b) The test setup used to characterize the directional response of a SolarSIM-G. Both setups are located on the same optical table.

Specification and classification of instruments for measuring hemispherical solar and direct solar radiation", the International Organization for Standardization defines three classes of accuracy for radiometers: A, B, and C, with A being the most accurate [34]. As per this standard, the directional response error for class A instruments must be within ± 10 W/m^2 for incidence angles of up to 80°, when at 0° (the sun is directly overhead) such instruments would measure 1000 W/m^2. For example, at the incidence angle of 60° (horizontal beam irradiance of 500 W/m^2) the directional error of 10 W/m^2 is equivalent to a 2% error.

I have designed the setup to automatically characterize the directional response of the SolarSIM-G, as shown in Figure 3.1b. The light from the quartz tungsten lamp (3a) is guided via the three optical mirrors at 45° (4a, 1b[2], 2b) to the SolarSIM-G under test (4b). The SolarSIM-G is mounted vertically on the rotational platform (3b), such that the axis of rotation passes through the origin of its bulk diffuser. The device can be manually mounted onto the platform in azimuthal increments of 30° from 0° to 330°. A control board (5b) drives the stepper motor to move the stage in 0.9° increments in the $-91.8°$ to $+91.8°$ incident angle range, such that at 0° the light beam is co-linear with the normal of the SolarSIM-G. Meanwhile, the software on the computer (1a) acquires the channel data from the SolarSIM-G at every step. For repeatability, the control software performs three subsequent directional response tests. Another script then takes the collected data from multiple tests and generates a performance report. Figure 3.2 shows the SolarSIM-G's directional responses across the $-90°$ to $+90°$ incidence angle range for two azimuth angles: 0° and 90°. Each curve is generated by averaging the responses from the SolarSIM-G's nine channels. As depicted, the directional response error for a SolarSIM-G exceeds the ISO 9060:2018 class A requirement.

[2] refers to item 1 in Figure 3.1b, hence the label "1b"

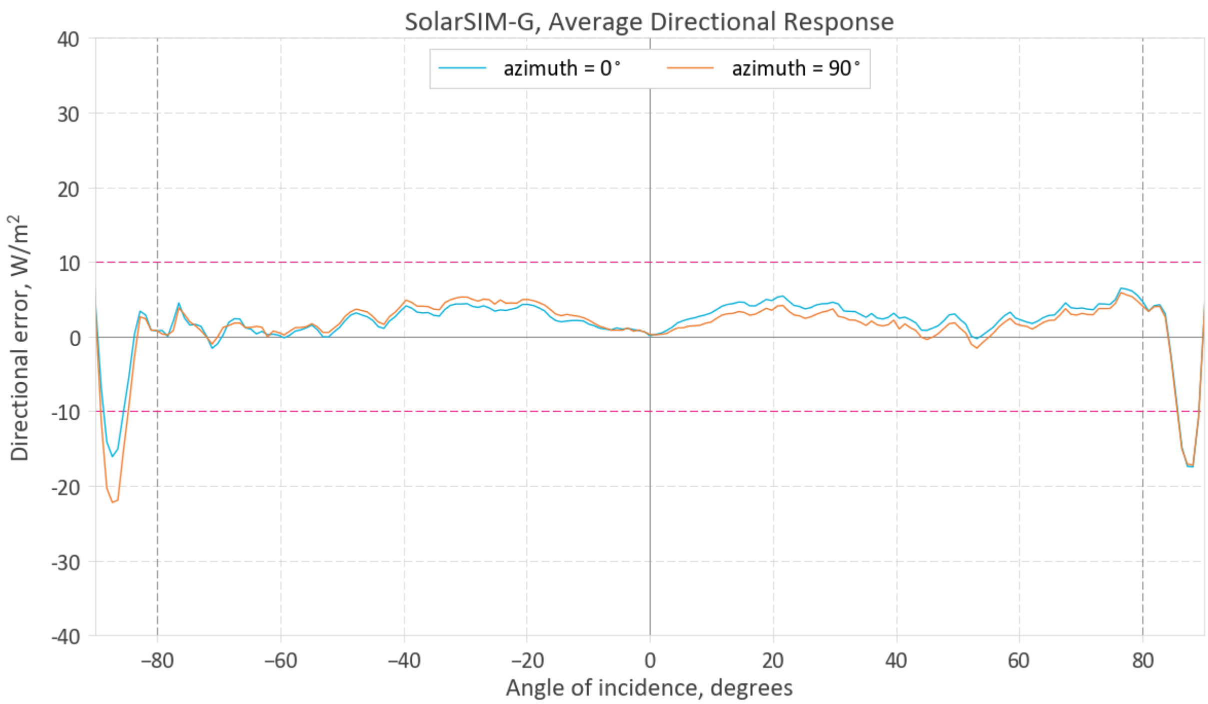

Figure 3.2: An example of the directional response of the SolarSIM-G across the $-90°$ to $+90°$ incidence angle range for two azimuth angles: 0° and 90°. Each curve represents the average of the responses from the SolarSIM-G's nine channels.

3.3.3 Optical Calibration

Proper optical calibration of solar radiometers depends on traceability to an internationally recognized standard. For example, the World Radiometric Reference (WRR) is the primary standard for broadband DNI, which is physically manifested through a group of absolute cavity radiometers, known as the World Standard Group. WRR traceable calibrations are used for pyranometers and pyrheliometers. On the other hand, spectral instruments, such as spectroradiometers, are calibrated indoors against a National Institute of Standards Technology (NIST) traceable lamp. None of these calibration methods can be applied to a SolarSIM, because its hardware neither directly measures the broadband irradiance nor the continuous spectrum. Instead, the reference SolarSIMs are calibrated through a side-by-side on-sun comparison at the National Renewable Energy Laboratory against secondary standard spectroradiometers with a traceability to a NIST Spectral Irradiance Lamp Standard. Uncalibrated SolarSIMs are then subsequently calibrated on-sun at the Ottawa test site, in a similar fashion, against the reference SolarSIMs. This in-house calibration procedure ensures NIST-traceability, without the need to use expensive spectroradiometers. Figure 3.3 shows the optical calibration setup at the Ottawa test site, where the solar tracker (1) is used to orient the reference (2) and device under test (3) SolarSIM-D2s normal to the sun. Specialized software on a laptop acquires and records the photodiode current data from each instrument once every second. The test is considered complete when over 100 measurements are gathered from each SolarSIM under clear-sky

Figure 3.3: Optical calibration setup for either the SolarSIM-D2 (as shown) or the SolarSIM-G.

conditions. Upon completion, an automated script calculates six optical calibration factors, one for each channel, in order to compensate for differences in the manufacturer's photodiode responsivities and filter transmittances. A similar procedure is performed for the SolarSIM-G, except nine calibration factors are obtained and the mounting plate has a 10° tilt from the normal(4), as shown in Figure 3.3, to minimize spectral albedo effects during the calibration procedure.

Chapter 4

Data Acquisition and Applications

4.1 CanSIM Network

4.1.1 Scope and Impact

The following publication describes the commissioning and measurement capabilities of the first three stations that were deployed as part of the wider Canadian Solar Spectral Irradiance Meter (CanSIM) network. Each CanSIM station is equipped with a datalogger, a solar tracker, a pyranometer, a SolarSIM-D2 and a SolarSIM-G, which cumulatively generate an exceptional quantity of solar and atmospheric data, including the air temperature, the ambient pressure, the broadband and spectral direct normal, global horizontal, and diffuse horizontal irradiances within the 280–4000 nm range, spectral aerosol optical depth, total column ozone and precipitable water vapour amount. The paper details deployment and data retrieval from three Ontario stations, situated in Ottawa, Egbert, and Varennes.

The CanSIM network sets a new standard for advanced solar and atmospheric data monitoring by enabling many applications in solar energy research, weather forecasting, and climate studies. To date, CanSIM data has been used by researchers from Natural Resources Canada to improve models of spectral mismatch correction for PV modules [35], while in Section 4.2, I have used Ottawa's station data to demonstrate the use of the spectrally corrected DNI as a metric to encapsulate annual, local atmospheric effects on a hypothetical CPV mono-module's energy yield. In addition, in Section 4.3, I have utilized the equivalent of seven years' worth of station data from four CanSIM stations to develop, calibrate, and validate a novel global irradiance decomposition algorithm to derive the DNI and DHI from spectral GHI measurements with significantly lower uncertainty as compared to state-of-the-art decomposition methods. These few examples demonstrate that the CanSIM data can be used in diverse applications. Long term measurements from the CanSIM network will be used to optimize Canada's solar energy generation potential through solar spectral resource assessment and through performance prediction studies of PV modules using different solar cell technologies.

4.1.2 Author Contributions

Viktar Tatsiankou: All research and scientific contributions in this article are my own but were at times guided and supported by other co-authors. The primary contribution of this work is the development of data acquisition scripts capable of analyzing raw data from each CanSIM station and then automatically generating processed data, which include spectral and broadband irradiances for all three sunshine components, atmospheric constituents and ambient parameters. The supplementary contribution is the installation of equipment at each station and then performing self-consistency checks for all instruments to ensure a proper setup.

Dr. Karin Hinzer: As my supervisor and the director of the SUNLAB at the University of Ottawa, Karin oversaw my research and assisted with preparing the final manuscript.

Dr. Henry Schriemer: As the associate director of the SUNLAB at the University of Ottawa, Henry oversaw my research and helped to review and edit the manuscript. .

Patrick McVey-White: As a research engineer at Spectrafy, Patrick assisted with the installation of CanSIM stations. He also has set up the server application to acquire raw data from each station's datalogger over the cellular network, and to store this information in the database.

Dr. Richard Beal: As a collaborator from Spectrafy, Richard guided my research and aided in reviewing the final manuscript.

4.1.3 Publication

The publication is attached on next page.

V. Tatsiankou, K. Hinzer, H. Schriemer, P. McVey-White, and R. Beal, "Deployment and early results from the CanSIM network". *AIP Conference Proceedings (CPV-13)*, 2017.

Deployment and Early Results from the CanSIM (Canadian Solar Spectral Irradiance Meter) Network

Viktar Tatsiankou[1, 2 a)], Karin Hinzer[1, b)], Henry Schriemer[1, c)], Patrick McVey-White[2, d)], and Richard Beal[2, d)]

[redacted]

[redacted]

Abstract. Three of seven stations have been deployed as part of the Canadian Solar Spectral Irradiance (CanSIM) network situated in Ottawa, Varennes and Egbert to measure long term spectral variation of the direct normal (DNI) and global horizontal irradiances (GHI) across the country. Every station is equipped with a solar tracker, SolarSIM-D2+, SolarSIM-G+, and SR20 pyranometer, reporting the spectral DNI, GHI, diffuse horizontal irradiance (DHI) and aerosol optical depth in the 280–4000 nm range, broadband DNI, GHI, and DHI, atmospheric total column ozone and water vapour amounts. The spectral GHI as measured by the SolarSIM-G+ was within 5% as compared to EKO MS-700 spectroradiometer in 350–1050 nm range on 17 March 2017. The difference in the GHI as reported by SolarSIM-G+ and SR20 pyranometer from all stations was within 2% on 14 April 2017. Furthermore, on this day, the daily GHI sum for the Ottawa, Varennes, and Egbert stations was 7.01, 6.95, and 7.11 kWh/m^2, respectively, while the daily DNI sum was 10.65, 10.86, 10.04 kWh/m^2, respectively.

INTRODUCTION

The solar irradiance reaching the ground level is a dynamic resource fluctuating temporally in spectrum and intensity mainly due to air mass, aerosols, and atmospheric gases. Every photovoltaic (PV) device is affected by spectral changes in sunlight, but a concentrating photovoltaic system (CPV) is impacted the most due to the fundamental structure of its multi-junction solar cells (MJSC). MJSCs consist of several series-connected subcells, so the lowest performing one dictates the overall operation of the device [1]–[3]. Typically, MJSCs are designed to be current matched for the AM1.5D from the ASTM G173 standard. Under field conditions, spectral variations cause MJSCs and consequently the CPV system to deviate from the desired operating point. Thus the knowledge of local solar spectrum is paramount to comprehensively characterize the performance of any PV or CPV system.

Historically, spectral field measurements were challenging to perform due to high instrumentation costs, involved setup and data acquisition protocols. As a result, there are only a few well funded institutions in the world today that continuously measure the solar spectrum, such as the Solar Radiation Research Facility at the National Renewable Energy Laboratory in Golden, Colorado, USA [4] and King Abdullah City for Atomic and Renewable Energy in Saudi Arabia [5]. Recently, the development of a Solar Spectral Irradiance Meter (SolarSIM) models D2+ and G+ by Spectrafy have led to a breakthrough in accuracy, ease of use, and affordability in acquiring direct normal and global horizontal spectral irradiances in the 280–4000 nm range, respectively. The SolarSIM-D2+ uses ground-based measurements to inform software algorithms for real-time resolution of the direct normal solar spectrum, total irradiance and various atmospheric constituents. The SolarSIM-D2+ works by measuring the solar spectral irradiance in

13th International Conference on Concentrator Photovoltaic Systems (CPV-13)
AIP Conf. Proc. 1881, 090002-1–090002-6; doi: 10.1063/1.5001451
Published by AIP Publishing. 978-0-7354-1561-4/$30.00

FIGURE 1. The location of seven stations belonging to the Canadian Solar Spectral Irradiance Meter network

six narrow wavelength bands, using silicon photodiodes with hard coated bandpass filters. These measurements are then used in spectral reconstruction through parametrization of the major atmospheric processes, including aerosol extinction, ozone and water vapour absorptions [6]. Overall, the SolarSIM-D2+ allows the user to infer the total direct normal irradiance (DNI), spectral DNI and the aerosol optical depth (AOD) in the 280–4000 nm range, in addition to the atmospheric total column ozone amount and the precipitable water vapour content. Much like the D2+, the SolarSIM-G+ uses low-cost silicon photodiodes and hard coated bandpass filters to make the accurate measurements of the solar spectrum in several narrow wavelength bands. However, it utilizes an innovative optical design to detect the global sunlight in a 180° field of view, coupled with a software algorithm optimized to spectrally resolve the global horizontal irradiance (GHI) in the 280–4000 nm range and the total GHI. In addition to the aforementioned measurement capabilities, the deployment of both the SolarSIM-D2+ and SolarSIM-G+ allows one to also infer the spectral and broadband diffuse horizontal irradiance (DHI).

In 2016 the Canadian government through the Build in Canada Innovation Program awarded Spectrafy the contract to commission the Canadian Solar Spectral Irradiance Meter (CanSIM) network. This network will help to quantify the long term spectral variation of the DNI and GHI across the country, which is useful for both the PV and CPV applications. The CanSIM network consists of seven stations across Canada, as shown in Fig. 1, equipped with a solar tracker, a SolarSIM-D2+, a SolarSIM-G+, and a pyranometer. In this paper, we describe the CanSIM network and present the early results from three deployed stations thus far. We compare the daily GHI profiles between the SolarSIM-G+ and the SR20 pyranometer from Huksenflux at the Ottawa, Varennes, and Egbert stations. Furthermore, we examine the measurements of the spectral GHI from the EKO MS-700 spectroradiometer and the SolarSIM-G+ at the Ottawa station.

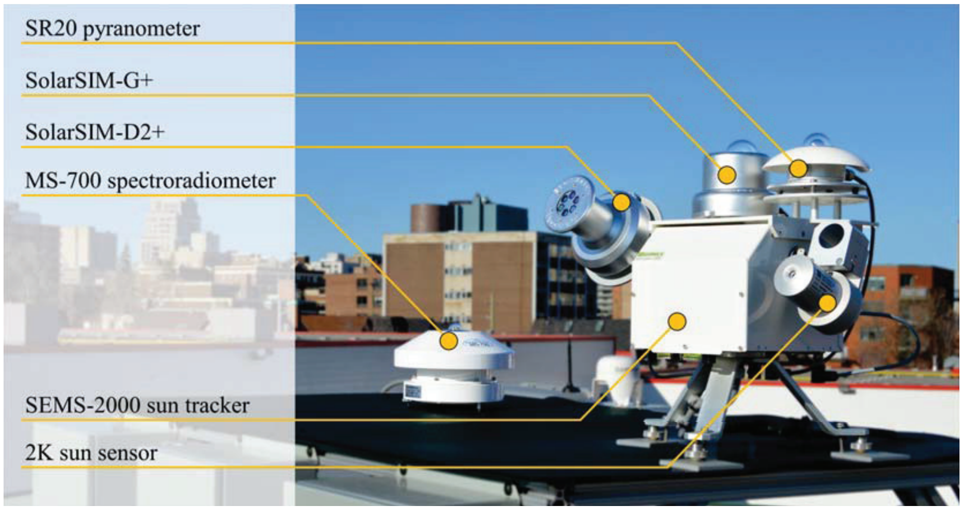

FIGURE 2. CanSIM station 3242 in Ottawa consisting of a SEMS-2000 sun tracker with a 2K sun sensor, a SolarSIM-D2+, a SolarSIM-G+, SR20 pyranometer, and a MS-700 spectroradiometer.

CANSIM NETWORK

The Canadian Solar Spectral Irradiance Meter (CanSIM) network consists of seven stations across six provinces situated in Ottawa and Egbert in Ontario (ON), Varennes in Quebec (QC), Charlottetown in Prince Edward Island (PE), Devon in Alberta (AB), Saturna Island in British Columbia (BC) and Cambridge Bay in Nunavut (NU), as illustrated by Fig. 1. The geographical coordinates of each station are presented in Table 1. The typical CanSIM station consists of a SEMS-2000 solar tracker with a 2K sun sensor (for close loop tracking) from Geonica, a SolarSIM-D2+ and a SolarSIM-G+ from Spectrafy, and a SR20 pyranometer from Huksenflux. The data are acquired in one minute intervals. In addition, the Ottawa station has a MS-700 spectroradiometer from EKO, as shown in Fig. 2. The data from each instrument is collected by Geonica's Meteodata 3000C datalogger every minute and is remotely transmitted to a central server for storage and analysis. The CanSIM station provides a vast amount of atmospheric and solar data, including the ambient temperature, pressure and humidity, the DNI and GHI, the spectral DNI, GHI and AOD in the 280–4000 nm range, the atmospheric total column ozone, and the precipitable water vapour content, as summarized in Table 2. Furthermore, the spectral diffuse horizontal irradiance (DHI) and the total DHI can be readily computed from the spectral DNI and GHI, as derived by the SolarSIM-D2+ and the SolarSIM-G+, respectively.

The first CanSIM station was deployed in Ottawa on 12 December 2016, with subsequent deployments at Varennes and Egbert on 15 December 2016 and 21 February 2017, respectively. The rest of stations are scheduled to be deployed during the summer of 2017.

TABLE 1. CanSIM stations' geographical coordinates.

Station ID	Location	Coordinates	Deployment
3242	Ottawa, ON	75.7° W, 45.4° N	12 Dec. 2016
3240	Varennes, QC	73.4° W, 45.6° N	15 Dec. 2016
3246	Egbert, ON	79.8° W, 44.2° N	21 Feb. 2017
3248	Devon, AB	113.7° W, 53.4° N	1 Jun. 2017*
3250	Saturna Island, BC	123.2° W, 48.8° N	20 Jun. 2017*
3252	Charlottetown, PE	63.1° W, 46.3° N	15 Jul. 2017*
3254	Cambridge Bay, NU	105.1° W, 69.1° N	15 Aug. 2017*

* scheduled to be deployed

TABLE 2. CanSIM station measurement capabilities

Measured parameter	Instrument			
	SolarSIM-D2+	SolarSIM-G+	SR20	MS-700*
DNI	✓			
Spectral DNI	✓[1]			
Spectral AOD	✓[1]			
Ozone content	✓			
Water vapour content	✓			
GHI		✓	✓	
Spectral GHI		✓[1]		✓[2]
Ambient temperature	✓	✓		
Ambient pressure	✓	✓		
Ambient humidity		✓		

∗ installed only at the Ottawa station
[1] 280–4000 nm spectral range
[2] 350–1050 nm spectral range

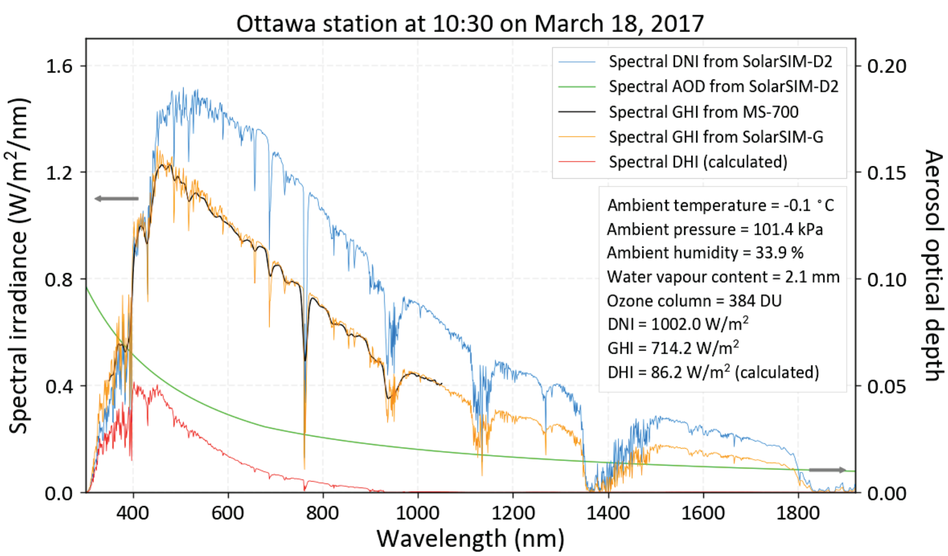

FIGURE 3. A complete parameter data set as produced by the Ottawa CanSIM station at 10:30 am on March 18, 2017.

EARLY RESULTS

The CanSIM network is first of its kind in Canada, providing an unparalleled quality and quantity of solar and atmospheric data. Fig. 3 shows a complete, instantaneous parameter data set gathered at the Ottawa CanSIM station on 18 March 2017 at 10:30 am, including the spectral DNI, GHI, DHI and AOD, broadband DNI, GHI, and DHI, ambient temperature, pressure and humidity, the total column ozone and water vapour amounts. A high DNI of over 1000 W/m^2 was observed on this day, which was mainly due to low AOD (less than 0.05 at 500 nm) and low water vapour column of 2.1 mm. For reference, the ASTM G173 standard DNI spectrum has the AOD at 500 nm of 0.084 and water vapour column of 14.2 mm. Fig. 3 also shows the spectral GHI comparison between the SolarSIM-G+ and EKO MS-700 spectroradiometer in the latter's 350–1050 nm measured range. A good agreement is observed between both instruments, whose spectral GHI is within of 5% of each other.

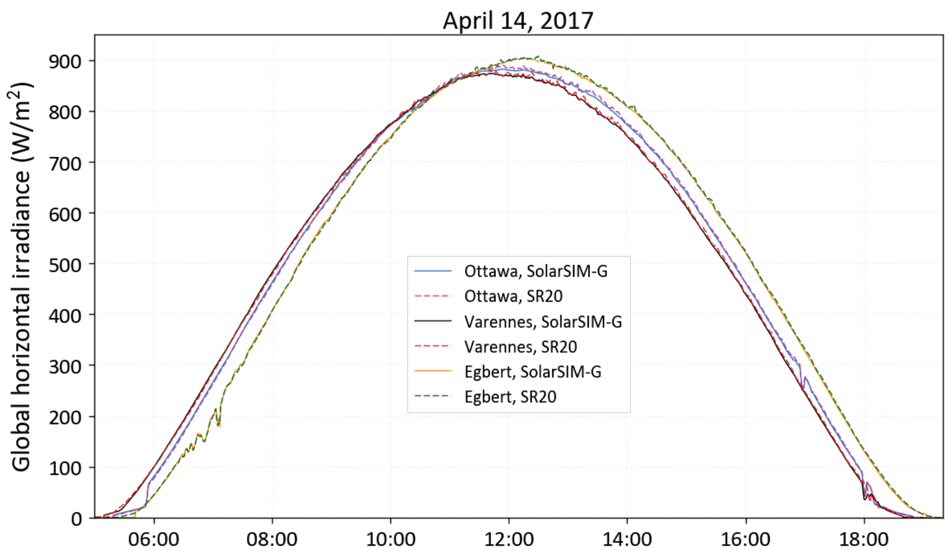

FIGURE 4. The daily GHI comparison between the CanSIM stations in Ottawa, Varennes, and Egbert as measured by the SolarSIM-G+ and SR20 pyranometer on April 14, 2017.

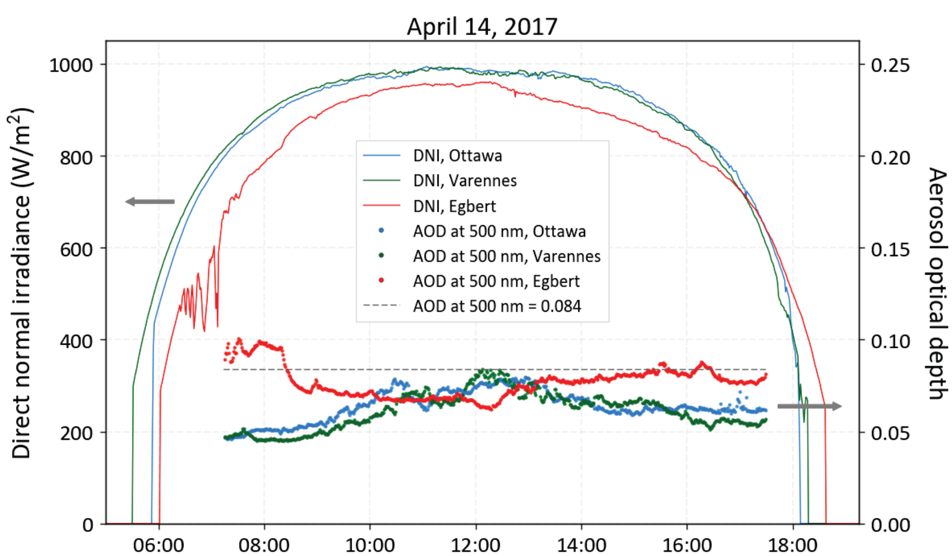

FIGURE 5. The daily DNI and the AOD at 500 nm from the CanSIM stations in Ottawa, Varennes, and Egbert as measured by the SolarSIM-D2+ on April 14, 2017.

The solar spectra from both the SolarSIM-D2+ and SolarSIM-G+ can be integrated for each timestamp throughout the day to obtain the broadband DNI and GHI profiles. Fig. 4 shows the daily GHI comparison from the Ottawa, Varennes, and Egbert stations between the SolarSIM-G+ and SR20 pyranometer on 14 April 2017. For all stations, the difference in the GHI between the SolarSIM-G+ and SR20 pyranometer was within 2% throughout the day. As expected, the GHI profiles are shifted in time – with the east-most, Varennes, and west-most stations, Egbert, having the earliest sunrise and the latest sunset, respectively. The daily GHI sum for the Ottawa, Varennes, and Egbert stations was 7.01, 6.95 and 7.11 kWh/m^2, respectively, with the minimum and maximum daily GHI sum differing by 2.3%. Fig. 5 shows the daily DNI profiles from the aforementioned stations on 14 April 2017. As it can be seen, there is more variability in the DNI between the stations, as compared to the GHI. The daily DNI sum for the Ottawa, Varennes, and Egbert stations was 10.65, 10.86, and 10.04 kWh/m^2, respectively, with the minimum and maximum daily DNI sums differing by 7.5%. All stations are located at near equal latitudes, hence, one expects near identical daily DNI sums if the atmospheric conditions were similar at all locations. However, the Egbert station had the lowest DNI sum due to a few clouds in the morning, higher aerosol optical depth and total water vapour column amount throughout the day. On the other hand, the Ottawa and Varennes stations had near identical DNI profiles due to similar atmospheric conditions. The current data set suggest that the temporal variations of the atmosphere have a more profound impact on the DNI more as opposed to the GHI.

CONCLUSION

The CanSIM network is a bold step forward in measuring the spectral variations of the DNI and GHI across Canada, which is paramount for solar applications. Once completed, this network will provide an unprecedented quality and quantity of solar and atmospheric data, including the spectral DNI, GHI, DHI, and AOD in the 280–4000 nm range, broadband DNI, GHI, and DHI, total column ozone and water vapour atmospheric amounts. Three stations have been deployed so far in Ottawa, Varennes and Egbert. Early results show the SolarSIM-G+ spectral irradiance is within 5% as compared to the EKO spectroradiometer in its 350–1050 nm range as measured at the Ottawa station on 18 March 2017. Furthermore, the difference in the broadband GHI as measured from all stations by the SolarSIM-G+ and SR20 pyranometer was within 2% throughout the day on 14 April 2017.

The data gathered on 14 April 2017 was a rare case when all three stations had a near perfectly clear conditions throughout the day. On this day, the daily GHI sum for the Ottawa, Varennes, and Egbert stations was 7.01, 6.95, and 7.11 kWh/m^2, respectively, while the daily DNI sum was 10.65, 10.86, 10.04 kWh/m^2, respectively. As expected, the GHI was less sensitive to variations in the atmospheric conditions, as compared to the DNI. Further deployments and data analysis will aid in quantifying the spectral GHI and DNI fluctuations across the country, and how they will impact prospective PV or CPV installations.

ACKNOWLEDGMENTS

The authors would like to acknowledge the support from Public Works and Government Services Canada, the Natural Resources Canada, the Environment and Climate Change Canada, the National Science and Engineering Research Council of Canada, the Ontario Centres of Excellence, and the Industry Research Assistance Program.

REFERENCES

[1] E. F. Fernández, A. Soria-Moya, F. Almonacid, *et al.*, "Comparative assessment of the spectral impact on the energy yield of high concentrator and conventional photovoltaic technology," *Solar Energy Materials and Solar Cells*, vol. 147, pp. 185–197, 2016.

[2] B. García-Domingo, J. Aguilera, J. de la Casa, *et al.*, "Modelling the influence of atmospheric conditions on the outdoor real performance of a cpv (concentrated photovoltaic) module," *Energy*, vol. 70, pp. 239–250, 2014.

[3] N. L. A. Chan, H. E. Brindley, and N. J. Ekins-Daukes, "Impact of individual atmospheric parameters on CPV system power, energy yield and cost of energy," *Progress in Photovoltaics: Research and Applications*, vol. 22, no. 10, pp. 1080–1095, 2014.

[4] T. Stoffel, A. Andreas, I. Reda, *et al.*, "Solar radiation research laboratory," in *SunShot Grand Challenge Summit and Technology Forum*, 2012.

[5] E. Zell, S. Gasim, S. Wilcox, *et al.*, "Assessment of solar radiation resources in Saudi Arabia," *Solar Energy*, vol. 119, pp. 422–438, 2015.

[6] V. Tatsiankou, K. Hinzer, H. Schriemer, *et al.*, "Design principles and field performance of a solar spectral irradiance meter," *Solar Energy*, vol. 133, pp. 94–102, 2016.

4.2 Spectral Correction for CPV Systems

4.2.1 Scope and Impact

The following paper demonstrates the use of CanSIM network data to derive the spectrally corrected DNI, which is a product of the measured broadband DNI and a spectral correction factor, for a specific CPV module. The SolarSIM-D2 data from Ottawa's CanSIM station is used to compute a one-year time series of spectrally corrected DNI for a hypothetical CPV monomodule consisting of a standard triple-junction solar cell. The yearly sum of spectrally corrected and measured DNIs differed by 3%, representing the magnitude of spectral effects on an annual basis for the CPV module in question. These results are significant in the context of utility-scale CPV power plants.

This work highlights the versatility and multi-functionality of the SolarSIM-D2, whose measurements are used to obtain spectrally corrected DNI data, which encapsulates the effects of local atmospheric conditions on the performance of a specific CPV system. This valuable data set can be handily generated by a single sensor without the need for sophisticated data analysis and multiple, expensive instruments, such as spectroradiometers, spectroheliometers, or pyrheliometers. More importantly, the spectrally corrected DNI data can be directly substituted into existing CPV performance prediction models in place of measured DNI, thus eliminating the complexity of working with large spectral datasets.

4.2.2 Author contributions

Viktar Tatsiankou: All research and scientific contributions in this article are my own but were at times guided and supported by other co-authors. The primary contribution of this work is the methodology development to derive spectrally corrected DNI time series from the SolarSIM-D2's measurements for a hypothetical CPV monomodule consisting of a silicon on glass Fresnel lens and a standard triple-junction solar cell. The supporting contribution is the application of the developed methodology to quantify the cumulative impact of local spectral effects on the simulated CPV monomodule in Ottawa over the course of a year.

Dr. Karin Hinzer: As my supervisor and the director of the SUNLAB at the University of Ottawa, Karin oversaw my research and assisted with preparing the final manuscript.

Dr. Henry Schriemer: As the associate director of the SUNLAB at the University of Ottawa, Henry oversaw my research and helped to review and edit the manuscript.

Dr. Richard Beal: As a collaborator from Spectrafy, Richard guided my research and aided in reviewing the final manuscript.

4.2.3 Publication

The publication is attached on next page.

V. Tatsiankou, K. Hinzer, H. Schriemer, and R. Beal, "Toward routine measurement and calculation of spectrally corrected DNI for CPV systems". *AIP Conference Proceedings (CPV-15)*, 2019.

Toward Routine Measurement and Calculation of Spectrally Corrected DNI for CPV Systems

Viktar Tatsiankou[1, a)], Karin Hinzer[1, b)], Henry Schriemer[1, c)] and Richard Beal[2, d)]

[redacted]

[redacted]

Abstract. In this work, we demonstrate the capabilities of the SolarSIM-D2 in deriving the spectrally corrected DNI for a hypothetical concentrating photovoltaic (CPV) mono-module consisting of Azur Space's 3C42 triple-junction solar cell with a silicone on glass Fresnel lens. The annual spectrally corrected and measured DNI sums in Ottawa, Canada were 1114.7 kWh/m^2 and 1145.6 kWh/m^2, respectively, representing a difference of 2.8% - which is significant in the context of developing a CPV powerplant.

INTRODUCTION

It is well known that concentrating photovoltaic (CPV) systems utilizing multi-junction solar cells (MJSC) are much more sensitive to changes in the solar spectrum than traditional single-junction, silicon or cadmium-telluride flat panels. It is therefore desirable to quantify these spectral effects within CPV performance prediction models, with a view to improve the bankability of CPV power plants [1]. Arguably the most accurate method is to use measured spectral DNI data within a CPV performance model built from fundamental physical principles. Yet, while spectral DNI over the wavelength range relevant to CPV can be measured using a collection of field spectroradiometers, these instruments are still far too expensive and impractical for routine industrial deployment, and are only deployed by well-funded institutions and research laboratories [2, 3]. In lieu of measured spectral data, one can model the local solar spectra, using a radiative transfer model, such as SMARTS, with ground-based measurements of aerosol optical depth (AOD) at 500nm and atmospheric precipitable water vapour (PWV) as inputs [4]. This approach is limited by the accuracy of the spectral model and by the fact that AOD and PWV parameters are often not available for a given location of interest. An alternative to working directly with spectral data is to use a spectroheliometer – a sensor based on triple-junction isotype reference cells [5]. While spectroheliometers can be more affordable and reliable than spectroradiometers, they are also less flexible, being restricted to a particular MJSC architecture.

In 2012 the authors began work on an alternative technology for solar spectral measurement that consists of a multi-filter radiometer coupled to a proprietary radiative transfer software that enables accurate reconstruction of full-range (280-4000nm) spectral and broadband DNI, as well as various atmospheric parameters [6, 7]. This approach combines the flexibility and accuracy of full-range spectral data within a single, reliable, and affordable sensor. This technology was first commercialized in 2015 as the SolarSIM-D2, of which more than 50 units are now deployed around the world. However, the next challenge in quantifying the spectral effects on a CPV module became the usability of the

15th International Conference on Concentrator Photovoltaic Systems (CPV-15)
AIP Conf. Proc. 2149, 080009-1–080009-5; https://doi.org/10.1063/1.5124219
Published by AIP Publishing. 978-0-7354-1894-3/$30.00

FIGURE 1. Solar test site in Ottawa consisting of Spectrafy's spectral instruments: the SolarSIM-D2 (3), the SolarSIM-G (4), and the SolarSIM-E (1), Huksenflux's SR20 pyranometer (5), Geonica's datalogger (2) and SEMS-2000 solar tracker (6).

vast spectral DNI data set that the instrument provides within the existing CPV performance models. As such, in this work we demonstrate the capabilities of the SolarSIM-D2 in deriving the spectral correction factors and by extension the spectrally corrected DNI for a hypothetical CPV mono-module. The aforementioned metric incapsulates the effects of local spectral conditions on the performance of a specific CPV module as time series and can be easily substituted into existing performance prediction models in place of measured DNI.

METHODOLOGY

We first define the spectral correction factor, C_{SCF}, for a hypothetical CPV module consisting of a multi-junction solar cell with x number of subcells:

$$C_{\mathrm{SCF}} = \frac{D_{\mathrm{AM1.5D}}}{D_{\mathrm{meas}}} \cdot \frac{min\left[\int_{280}^{4000} (S_{\mathrm{meas}}(\lambda) \cdot T_{\mathrm{OTF}}(\lambda) \cdot R_x(\lambda) \cdot d\lambda)\right]}{min\left[\int_{280}^{4000} (S_{\mathrm{AM1.5D}}(\lambda) \cdot T_{\mathrm{OTF}}(\lambda) \cdot R_x(\lambda) \cdot d\lambda)\right]} \tag{1}$$

where D_{meas} and $D_{\mathrm{AM1.5D}}$ are the measured and reference broadband DNI, respectively, $S_{\mathrm{meas}}(\lambda)$ and $S_{\mathrm{AM1.5D}}(\lambda)$ are the measured and reference spectral DNI, respectively, $T_{\mathrm{OTF}}(\lambda)$ is the optical transfer function (OTF) of a given CPV module and $R_x(\lambda)$ is the spectral response of subcell x for the MJSC within that module. Eq. 1 can be re-arranged to define the spectrally corrected DNI, D_{corr}, as:

$$D_{\mathrm{corr}} = C_{\mathrm{SCF}} \cdot D_{\mathrm{meas}} = D_{\mathrm{AM1.5D}} \cdot \frac{min\left[\int_{280}^{4000} (S_{\mathrm{meas}}(\lambda) \cdot T_{\mathrm{OTF}}(\lambda) \cdot R_x(\lambda) \cdot d\lambda)\right]}{min\left[\int_{280}^{4000} (S_{\mathrm{AM1.5D}}(\lambda) \cdot T_{\mathrm{OTF}}(\lambda) \cdot R_x(\lambda) \cdot d\lambda)\right]} \tag{2}$$

For this work, we defined a hypothetical CPV mono-module to consist of a silicon on glass (SOG) Fresnel lens and Azur Space's 3C42 MJSC. The SOG transmission profile from [8] is assumed to be the OTF and the spectral response for each subcell is taken from [9]. For simplicity, the effects of temperature on the MJSC's spectral response and OTF curves were not considered. The spectral DNI data was obtained from the SolarSIM-D2 radiometer at Spectrafy's solar test site in Ottawa, as shown in Fig. 1, which is one of seven stations comprising the Canadian Solar Spectral Irradiance Meter (CanSIM) network [10]. A typical CanSIM station includes of a SEMS-2000 solar tracker from Geonica, a SolarSIM-D2 and a SolarSIM-G [11] (for resolving global horizontal spectral irradiance in the 280-4000 nm range) from Spectrafy, and a SR20 pyranometer from Huksenflux. In addition, the Ottawa station has the

SolarSIM-E, an automated shadow band accessory for the SolarSIM-G, which allows to resolve the diffuse horizontal, global horizontal and consequently direct normal spectral irradiances in the 280-4000 nm range. The data from each instrument is collected by Geonica's Meteodata 3000C datalogger every minute and is remotely transmitted to a central server for storage and analysis. At this stage, a specialized software processes the raw SolarSIM-D2 data to reconstruct the spectral and broadband DNI in the 280-4000 nm range. For this work, we have modified the standard SolarSIM-D2 software to allow the real-time calculation of the spectrally corrected DNI as per Eq. 2 by using the dataset from the Ottawa CanSIM station spanning from August 1, 2017 to August 1, 2018.

RESULTS

We first examine the diurnal differences between the measured and spectrally corrected DNI for our hypothetical CPV module on August 1, 2017, as presented in Fig. 2. Also shown are the spectrally corrected DNI for each subcell of the 3C42 MJSC and how the overall spectrally corrected DNI varied throughout the day. The red-rich morning and evening spectra make the device top-subcell-limiting, while later in the day the blue-rich spectrum results in the device being middle-subcell-limiting. It is evident that the spectrally corrected DNI can vary substantially from the measured DNI over the course of a day. We extend this analysis to a yearly basis by comparing the measured DNI sum to that of the spectrally corrected DNI sum from August 1, 2017 to August 1, 2018, as shown in Fig. 3. The annual spectrally corrected and measured DNI sums amount to 1114.7 kWh/m^2 and 1145.6 kWh/m^2, respectively, representing a difference of 2.8%. As expected, this analysis demonstrates that spectral conditions in Ottawa during the selected time period do not significantly variate from the atmospheric conditions found under the reference AM1.5D spectrum.

CONCLUSION

Historically, there were two main challenges impeding one from quantifying spectral effects on the CPV system performance - the first was the difficulty obtaining spectral DNI data in the full wavelength range, and the second one was the lack of spectral data inputs into the CPV performance prediction models. With the advent of the SolarSIM-D2, one can now cost-effectively and accurately obtain the local solar spectrum, but the usability challenge of this data set within the existing performance models was still present. Therefore, in this work we have demonstrated the capability of the SolarSIM-D2 in deriving the spectrally corrected DNI for a hypothetical CPV module consisting of a SOG Fresnel lens and Azure Space's 3C42 MJSC. This metric encapsulates the effects of local spectral conditions on the performance of a specific CPV system and is expressed in simple time series. We showed that for the first time this valuable data set can be readily generated by a single sensor without the need for sophisticated data analysis and multiple, expensive instruments, such as spectroradiometers, spectroheliometer, and/or pyrheliometer. More importantly, the spectrally corrected DNI data can be directly substituted into existing CPV performance prediction models in place of measured DNI, thus eliminating the complexity of working with the large spectral data sets.

ACKNOWLEDGMENTS

The authors would like to acknowledge the support from Public Works and Government Services Canada, the Natural Resources Canada, the Environment and Climate Change Canada, the National Science and Engineering Research Council of Canada, and the Ontario Centres of Excellence.

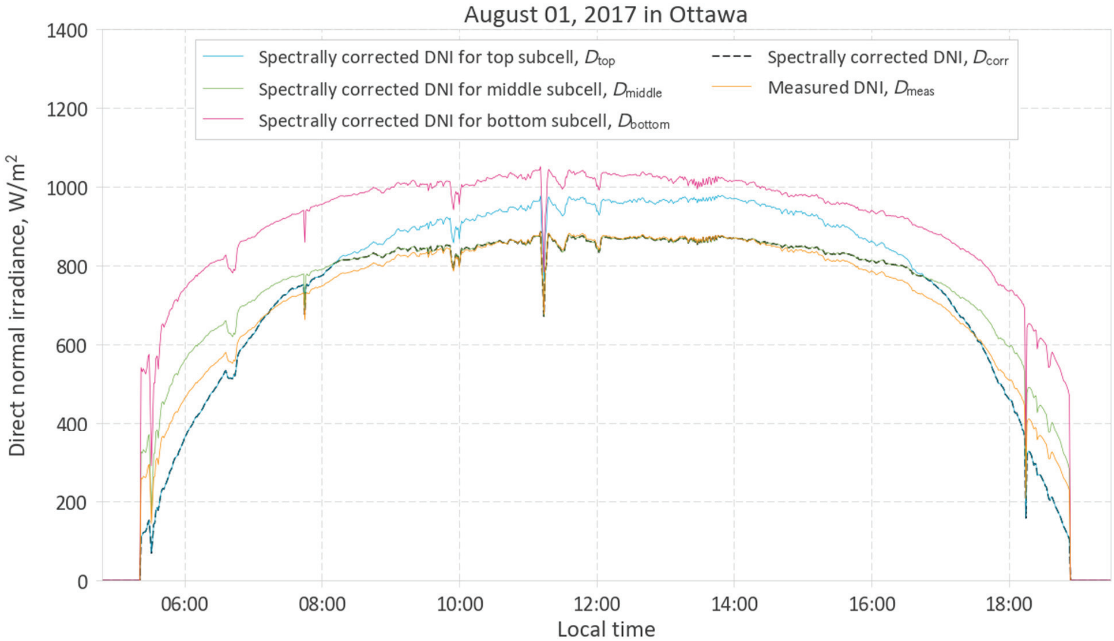

FIGURE 2. Daily profile of the measured DNI, along with spectrally corrected DNI for each subcell and the overall mono-module, based on Azur Space's 3C42 triple junction solar cell with a silicone on glass primary optic. The spectral DNI data was obtained by the SolarSIM-D2.

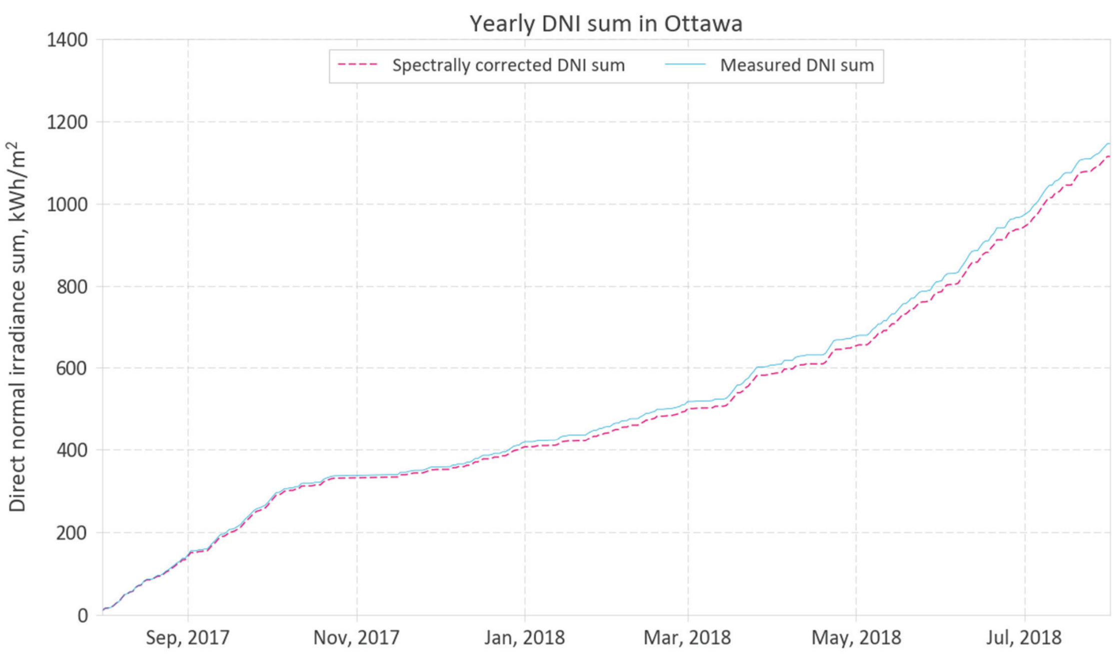

FIGURE 3. Yearly comparison of the measured and spectrally corrected DNI sums for Ottawa, based on a CPV mono-module using Azur Space's 3C42 triple junction solar cell with a silicone on glass primary optic. The spectrally corrected DNI sum is 2.8% lower than the measured DNI sum. The spectral DNI data was obtained by the SolarSIM-D2.

REFERENCES

1. Chan, N. L. A., Brindley, H. E., & Ekins-Daukes, N. J. "Impact of individual atmospheric parameters on CPV system power, energy yield and cost of energy." *Progress in Photovoltaics: Research and Applications* (2014): 1080-1095.
2. Zell, E., et al. "Assessment of solar radiation resources in Saudi Arabia." *Solar Energy* 119 (2015): 422-438.
3. Andreas, A., Stoffel, T. "NREL Solar Radiation Research Laboratory (SRRL): Baseline Measurement System (BMS)". NREL Report No. DA-5500-56488 (1981).
4. Núñez, R., et al. "Spectral impact on multijunction solar cells obtained by means of component cells of a different technology." *IEEE Journal of Photovoltaics* 8.2 (2018): 646-653.
5. Antón, I., et al. "Power rating of CPV systems based on spectrally corrected DNI." *AIP conference proceedings* (2012).
6. Tatsiankou, V., et al. "Design principles and field performance of a solar spectral irradiance meter." *Solar Energy* (2016).
7. Tatsiankou, V., et al. "Extensive validation of solar spectral irradiance meters at the World Radiation Center." *Solar Energy* (2018).
8. Shanks, K., Sundaram S., and Tapas K. M. "Optics for concentrating photovoltaics: Trends, limits and opportunities for materials and design." *Renewable and Sustainable Energy Reviews* 60 (2016): 394-407.
9. Azur Space, "Concentrating triple junction solar cell – 3C42", datasheet (2014). URL: http://www.azurspace.com/images/pdfs/DB_3879-00-00_3C42_AzurDesign_3x3_20140226.pdf.
10. Tatsiankou, V., et al. "Deployment and early results from the CanSIM (Canadian Solar Spectral Irradiance Meter) network". *AIP conference proceedings* (2017).
11. Tatsiankou, V, et al. "Efficient, Real-Time Global Spectral and Broadband Irradiance Acquisition." *2018 IEEE 7th World Conference on Photovoltaic Energy Conversion* (2018).

4.3 Global Irradiance Decomposition

4.3.1 Scope and Impact

The following article presents a global irradiance decomposition methodology for retrieving broadband DNI and DHI from the SolarSIM-G's spectral GHI measurements in real-time. The manuscript presents a more quantitative approach to classifying sky conditions via measured spectral clearness indices, which are also used as predictors in the algorithm. The one-minute resolution data from five measurement stations, which cumulatively represent a seven-year data set, is used to calibrate and validate the decomposition algorithm against co-located reference instruments. The evaluation of the algorithm is performed through calculation of various statistical estimators related to the difference between the modelled and reference DNI and DHI time series for each station.

The described global irradiance decomposition algorithm leverages the insights from the SolarSIM-G's measurements of spectral irradiance to classify sky conditions through enhanced metrics of an atmosphere's clearness, i.e. the spectral clearness indices. The results show that the proposed method has a factor of two to three improvement in the root-mean-square error for the DNI retrieval as compared to existing state-of-the-art decomposition algorithms. This methodology is an interesting alternative to other measurement and modelling techniques for obtaining all three sunshine components, as it is performed with a rugged, compact, and low-power instrument with no moving parts. Without doubt, the SolarSIM-G based decomposition algorithm can be further improved as more measurements become available from existing and future installations.

4.3.2 Author contributions

Viktar Tatsiankou: All research and scientific contributions in this article are my own but were sometimes guided and supported by other co-authors. The primary contribution of this work is the development of the global irradiance decomposition algorithm based on measured spectral clearness indices to retrieve DNI and DHI with significantly lower uncertainty over traditional modelling methods and comparable uncertainty to non-tracking, instrumentation-based techniques. A critical supporting contribution is a novel sky condition classification method which is based on the realization that similar atmospheric conditions correlate with sky conditions.

Dr. Karin Hinzer: As my supervisor and the director of the SUNLAB at the University of Ottawa, Karin guided my research and assisted with preparing the final manuscript.

Dr. Henry Schriemer: As the associate director of the SUNLAB at the University of Ottawa, Henry guided my research and helped to review and edit the manuscript.

Dr. Richard Beal: As a collaborator from Spectrafy, Richard guided my research and aided in reviewing the final manuscript.

4.3.3 Publications

The publication follows on next page.

V. Tatsiankou, K. Hinzer, H. Schriemer, and R. Beal, “Improved global irradiance decomposition by sky condition classification from measured spectral clearness indices”. *47th IEEE Photovoltaic Specialists Conference (PVSC)*, 2020.

Improved Global Irradiance Decomposition by Sky Condition Classification from Measured Spectral Clearness Indices

Viktar Tatsiankou
[redacted]

Dr. Karin Hinzer
[redacted]

Dr. Henry Schriemer
[redacted]

Dr. Richard Beal
[redacted]

***Abstract*—This manuscript describes a decomposition algorithm for deriving the broadband direct normal (DNI) and diffuse horizontal (DHI) irradiances from one-minute spectral global horizontal irradiance measurements performed by the SolarSIM-G. The algorithm was calibrated and validated at four stations across Canada (Ottawa, Varennes, Egbert, and Devon) and at one station in China (Xianghe), which cumulatively represent a seven-year data set. For the DNI estimation, the root mean square error (RMSE) ranged from 26 W/m^2 to 48 W/m^2, while the largest mean bias error (MBE) was 4 W/m^2. For the DHI estimation, the RMSE ranged from 14 W/m^2 to 27 W/m^2, while the largest MBE was 3 W/m^2. In addition, the integrated DNI and DHI errors for each station were less than 1% and 2%, respectively. The described method is an alternative to other measurement techniques for obtaining all three irradiance components.**

Keywords—Global horizontal irradiance, direct normal irradiance, diffuse horizontal irradiance, irradiance decomposition algorithm, SolarSIM-G, spectral clearness index, GHI, DNI, DHI

I. Introduction

Sunlight at the earth's surface is typically represented by global horizontal, direct normal, and diffuse horizontal irradiances, known as GHI, DNI, and DHI, respectively. Knowledge of these quantities is essential for many applications, such as climate research, solar resource assessment, photovoltaic system monitoring, and many more [1]. Of the three, GHI measurements are by far the most common, mainly because they only require a relatively inexpensive, low maintenance pyranometer statically mounted on a flat surface. In contrast, to obtain measurements of DNI and DHI one requires a pyrheliometer and a pyranometer (with a shadow ball assembly), respectively, both mounted on a solar tracker. The measurement methods described in [2] are the most accurate way to obtain all three sunshine components. For more cost-sensitive applications, one can use "tracker-less" options to derive the GHI, DNI and DHI with a single instrument, such as a rotating shadowband radiometer or a shadow-mask pyranometer but the resultant measurements have a higher uncertainty than the aforementioned methods [3]. Another convenient option is to solely measure the GHI and then use one of many available irradiance decomposition algorithms to derive the DNI and/or DHI, such as Erbs, Skartveit, Reindl, DirInt, DISC, and others. These models vary in complexity, but generally have a relatively high uncertainty, with the root mean square errors for DNI retrieval of ~85 W/m^2 at hourly resolution [4].

Most decomposition algorithms are based on a clearness index, which is a unitless measure of the atmosphere's clearness, derived from the product of the local GHI and the airmass divided by the extraterrestrial irradiance [5]. Some models have improved the decomposition results by also including the atmospheric turbidity and total column water vapor (i.e. the precipitable water vapor) in their calculations [6,7]. The additional insight from local atmospheric parameters translates to improved model performance.

A comprehensive way to assess the atmospheric conditions is to use local spectral irradiance data, which historically has been very difficult to obtain, as it requires several co-located field spectroradiometers. With the advent of a spectral pyranometer – the SolarSIM-G – it is now possible to obtain full-range spectral and broadband GHI data from a single, compact, low power instrument with no moving parts [8]. In this manuscript we use one-minute spectral measurements made by the SolarSIM-G to derive spectral clearness indices at several wavelengths. We then use these predictors in our decomposition algorithm. We apply data from five test stations to calibrate our algorithm, then validate it by comparing the derived DNI and DHI data at each station against the corresponding measurements from co-located reference instruments. The methodology and the summary of results are presented here.

II. Spectral Pyranometer

The SolarSIM-G is a unique instrument that combines a multi-filter radiometer with an advanced radiative transfer model to derive in real-time full-range spectral and broadband global irradiances under all sky conditions. The instrument's mechanical and optical design have been described elsewhere [8]. In brief, the SolarSIM-G measures the global spectral irradiance using hard-coated narrow bandpass filters paired with seven silicone and two indium gallium arsenide calibrated detectors. The center wavelengths are shown in Table I, along with the atmospheric parameters or conditions targeted. The instrument also senses the ambient temperature, humidity and atmospheric pressure. The irradiance and environmental measurements are fed into our radiative transfer model to derive the spectral and broadband GHI in the 280-4000 nm range. The spectral reconstruction algorithm is as follows:

1. Calibrate the instrument:
   a. Determine the temperature coefficients for each channel, similar to [9];
   b. Optimize the cosine response of the instrument to comply with class A pyranometer requirements from ISO9060:2018 standard;
   c. Perform on-sun calibration against a reference SolarSIM-G or a reference spectroradiometer [8].
2. Acquire currents from the nine optical channels, the ambient temperature and atmospheric pressure, and the internal temperature of the device.
3. Use our radiative transfer model to derive the spectral global irradiance in the 280-4000 nm range, based on [10]:
   a. Compute the zenith angle and the sun-earth distance using a solar position algorithm;
   b. Apply the sun earth-distance correction on the extraterrestrial solar spectrum;
   c. Calculate Rayleigh scattering and the transmittances from various atmospheric gases (CO_2, CH_4, O_2, NO_2);
   d. Determine the spectral AOD and its transmittance from all channels except the ozone channel at 610 nm and the water vapor channel at 940 nm, similar to [10], but now with three extra channels;
   e. Compute the total column ozone and its spectral transmittance from the 610 nm channel;
   f. Calculate the precipitable water vapor content and its spectral transmittance from the 940 nm channel;
   g. Determine the spectral irradiance by applying the derived transmittance functions from steps c-f to the extraterrestrial solar spectrum;
   h. Calculate the cloud transmittance based on the irradiance at channels 8 and 9 and apply a spectral cloud correction to the spectrum from step "g" in the 1000 to 4000 nm range;
   i. Calculate the diffuse irradiance correction based on the irradiance at channel 1 and adjust the spectrum from step "h" in the 280 to 360 nm range;
   j. Integrate the spectral irradiance obtained in step "i" to obtain the GHI.

The correction functions in steps "h" and "i" extend the radiative transfer model described in [10] and are proprietary.

TABLE I. LIST OF SOLARSIM-G CHANNELS

Optical channel	Center wavelength (nm)	Resolves
1	< 420[a]	Aerosols, diffuse
2	420	Aerosols, diffuse
3	500	Aerosols, diffuse
4	610	Ozone
5	675	Aerosols, diffuse
6	880	Aerosols, diffuse
7	940	Water vapor
8	> 1000[a]	Aerosols, clouds
9	> 1000[a]	Aerosols, clouds

[a.] proprietary

III. DATA SET

Spectral and broadband irradiance data are obtained from five stations across a range of environments, as summarized in Table II. Four stations are a part of the Canadian Spectral Irradiance Network operated by Spectrafy [11], while the fifth is operated by the Institute of Atmospheric Physics in the People's Republic of China. Each station is equipped with the SolarSIM-D2 and the SolarSIM-G, with raw data acquired at one-minute resolution by a datalogger, and subsequently sent to a central server for processing and storage. The SolarSIM-D2 provides the spectral and broadband DNI in the 280-4000 nm range, spectral aerosol optical depth in the 280-4000 nm range, the total column ozone, and the precipitable water vapor [9,10]; the SolarSIM-G delivers the spectral and broadband GHI in the 280-4000nm range. By combining the measurements from both instruments, we have computed the spectral and broadband DHI in the 280-4000 nm range.

The data sets from each location end by 1 December 2019 and vary in length from 9 to 24 months, in aggregate the equivalent of almost seven station-years. The data sets were carefully screened and validated. Data for solar elevation angles less than 10° were excluded to minimize horizon perturbations, and to avoid shadowing. Data taken during periods of snow, rain, or maintenance were likewise excluded. Three stations – Egbert, Ottawa, and Varennes – operate under similar atmospheric conditions. Their mean AODs at 500 nm (AOD_{500}) are shown in Table II as near or at 0.1. The other two stations show greater diversity in atmospheric conditions. Devon station has slightly heavier AOD_{500} loading at 0.14, while the Xianghe station in China has a mean AOD_{500} of 0.48. The combined data set represents a diverse range of environmental conditions that is representative of many locations around the world.

IV. GLOBAL IRRADIANCE DECOMPOSITION

DNI and DHI data may be extracted from the SolarSIM-G's GHI data. The algorithm for its extraction is given below, followed by a more comprehensive discussion of the spectral clearness index, its application as a predictor of sky conditions,

TABLE II. LIST OF MEASUREMENT STATIONS

Station	Latitude	Longitude	Altitude	AOD_{500}	Range
Devon	53.4°	113.7°	800 m	0.14	9 months
Egbert	44.2°	79.8°	98 m	0.10	21 months
Ottawa	45.4°	75.7°	70 m	0.11	23 months
Varennes	45.6°	73.4°	60 m	0.11	21 months
Xianghe	39.8°	-117.0°	36 m	0.48	9 months

and subsequent employment in the computation of the DNI and the DHI.

A. *Decomposition algorithm*

The decomposition algorithm is as follows:

1. Acquire spectral and broadband GHI data from the SolarSIM-G;
2. Compute the "clear-sky" spectral GHI from (1);
3. Calculate spectral clearness indices for central wavelengths of all SolarSIM-G's channels using (2);
4. Determine the sky condition as per Table III;
5. Compute the modelled DNI and DHI from (3) and (4), respectively.

B. *Spectral clearness index*

We start by defining the "clear-sky" spectral global horizontal irradiance as:

$$S_{\mathrm{GHI,clr}}(\lambda) = S_{\mathrm{DNI,clr}}(\lambda) \cdot m^{-1} + S_{\mathrm{DHI,clr}}(\lambda) \tag{1}$$

where $S_{\mathrm{DNI,clr}}(\lambda)$ and $S_{\mathrm{DHI,clr}}(\lambda)$ are the modelled "clear-sky" spectral DNI and spectral DHI, respectively, in the 280-4000 nm range, and m is the optical air mass. The DNI is obtained through a parameterized direct beam transmittance model, similar to our previous work [10], except the aerosol transmittance is generated by fixing the AOD at 500 nm to 0.05 with its spectral dependence defined by two Ångström exponents, 0.98 and 1.22 for wavelengths before and after 500 nm, respectively. The spectral ozone and water vapor transmittance functions are generated from the total column ozone and precipitable water vapor content obtained by the SolarSIM-G measurements. Finally, the modelled "clear-sky" spectral DHI in the 280-4000 nm is based on [12]. As a more comprehensive measure of the atmosphere's clearness, we may then define

$$\kappa(\lambda) = \frac{S_{\mathrm{GHI}}(\lambda)}{S_{\mathrm{GHI,clr}}(\lambda)} \tag{2}$$

as a spectral clearness index, where $S_{\mathrm{GHI}}(\lambda)$ is the measured spectral GHI as derived by the SolarSIM-G, and $S_{\mathrm{GHI,clr}}(\lambda)$ is the modelled "clear-sky" spectral GHI, computed from (1).

C. *Classifcation of sky conditions*

The crucial insight leveraged in our decomposition algorithm is the realization that similar atmospheric conditions correlate with sky conditions. The classification is presented in Table III. We categorize sky conditions into seven classes based on the values of the spectral clearness indices $\kappa(\lambda_1)$ and $\kappa(\lambda_9)$, using optical channels 1 and 9 of the SolarSIM-G, respectively. These two channels are chosen because the spectral clearness indices at these wavelengths shows the strongest sensitivity to sky conditions. Channel 1 was chosen because it is the most sensitive to small changes in the diffuse irradiance, while channel 9 was chosen because it is the least sensitive to the clear-sky diffuse irradiance and to the aerosol absorption of the direct beam. As a result, channel 9 is the most sensitive channel to cloud absorption and scattering, and therefore is a good estimator of the clouds' optical depth that obscure the sun.

Sky clarity is quantified by index ranges, as shown in Table III. Based on the AOD_{500} data from all stations, we found that values for $\kappa(\lambda_9)$ of 0.75 and above correlate with an unobstructed sun disk for over 95% of the data. When the sky is free of clouds, the values of $\kappa(\lambda_1)$ can be used to further characterize the sky as either "very clear", "clear", or "hazy". When the sky is cloudy, but the sun disk is not obscured, the GHI in some cases can exceed the solar constant. This is the special case of lensing, where $\kappa(\lambda_9)$ is found to exceed 1.05. Values of $\kappa(\lambda_9)$ below 0.75 correlate with a sun obstructed by the clouds for over 90% of the data, as determined by the SolarSIM-D2's AOD_{500} measurements at each station. Decreasing values of $\kappa(\lambda_9)$ correlate well with cloud optical depth, allowing "thin" clouds, "thick" clouds, and completely overcast conditions to be identified by their $\kappa(\lambda_9)$ ranges.

D. *Computation of DNI and DHI*

For a specific sky condition x, the decomposition of the modelled DNI may be parameterized as

$$I_{\mathrm{DNI,mod}} = \alpha_{1,x} \cdot I_{\mathrm{GHI}} \cdot m + \alpha_{2,x} \cdot I_{\mathrm{DNI,clr}} + \\ + \sum_{i=1,i\neq 7}^{9} \beta_{i,x} \cdot \kappa(\lambda_i) \tag{3}$$

where I_{GHI} is the measured broadband GHI; $I_{\mathrm{DNI,clr}}$ is the integral of the modeled "clear-sky" spectral DNI, $S_{\mathrm{DNI,clr}}(\lambda)$, in the 280-4000 nm range; $\alpha_{1,x}$and $\alpha_{2,x}$, are unitless coefficients for the broadband predictors, I_{GHI} and $I_{\mathrm{DNI,clr}}$, respectively; $\beta_{i,x}$ is a set of eight coefficients for spectral clearness indices at the center wavelengths of all SolarSIM-G's optical channels, except for the water vapor channel, i.e. channel 7. This channel is

TABLE III. CLASSIFICATION OF SKY CONDITIONS BASED ON CLEARNESS INDICES AT SOLARSIM-G'S CHANNELS 1 AND 9

Sky condition	x	$\kappa(\lambda_1)$		$\kappa(\lambda_9)$	
		Min	*Max*	*Min*	*Max*
Very clear	1	1.0	-	0.75	1.05
Clear	2	0.8	1.0	0.75	1.05
Hazy	3	-	0.8	0.75	1.05
Thin clouds	4	-	-	0.5	0.75
Thick clouds	5	-	-	0.25	0.5
Overcast	6	-	-	-	0.25
Lensing	7	-	-	1.05	-

TABLE IV. THE DERIVED COEFFICIENTS FOR THE DNI ESTIMATION FOR A SPECIFIC SKY CONDITION

Sky condition	x	Coefficients									
		$\alpha_{1,x}$	$\alpha_{2,x}$	$\beta_{1,x}$	$\beta_{2,x}$	$\beta_{3,x}$	$\beta_{4,x}$	$\beta_{5,x}$	$\beta_{6,x}$	$\beta_{8,x}$	$\beta_{9,x}$
Very clear	1	1.104	-0.357	-812.1	557.9	1345.6	-2828.2	3796.9	-3898.7	-179.4	2070.9
Clear	2	0.447	-0.368	-1042.6	1362.2	3039.6	-5446.7	5138.8	-2897.2	-1228.3	1949.9
Hazy	3	0.707	-0.806	-174.2	779.4	1672.6	-6004.2	8345.3	-4876.0	360.0	888.5
Cloudy	4	0.850	-0.647	-287.1	-123.7	1766.2	-4047.3	4234.6	-2205.3	698.5	387.0
Very cloudy	5	0.086	-0.097	242.0	-490.8	660.8	-970.3	741.7	-404.2	436.7	-51.0
Overcast	6	-	-	-	-	-	-	-	-	-	-
Lensing	7	0.475	0.501	-1473.6	1453.1	1682.9	1303.6	-2802.0	262.0	-1151.1	629.1

excluded because variation in the total column water vapor is already captured within the I_{GHI} and $I_{\text{DNI,clr}}$ variables. The α and β coefficients for each sky condition x were determined using a multivariate ordinary least squares linear regression algorithm that minimized the difference between the modelled DNI and the measured DNI time series from *all* stations at the same time. These coefficients are presented in Table IV for all sky conditions, except when it is overcast, in which case the modeled DNI is set to zero.

The DHI can be computed from the GHI and the DNI as

$$I_{\text{DHI}} = I_{\text{GHI}} - I_{\text{DNI}} \cdot m^{-1}. \quad (4)$$

V. RESULTS AND DISCUSSION

We assess the performance of our decomposition algorithm by comparing modeled DNI and DHI time series at each station against their corresponding references values. The reference DNI was determined from the SolarSIM-D2 measurements, while the reference DHI was computed from (4) using the reference DNI and GHI, as derived by the SolarSIM-D2 and the SolarSIM-G, respectively, at each station. We assume that any differences between reference instruments and derived DNI and DHI values are dominated by the limitations of the decomposition algorithm. Therefore, reference instrument measurement uncertainties were not included in the comparative analysis (i.e. reference DNI and DHI data were assumed to be true).

We evaluate the decomposition algorithm by calculating various statistical estimators from the difference between the modeled and reference DNI and DHI time series for each station. Fig. 1a and Fig. 1b show boxplot diagrams of the error distributions of the modeled DNI and modeled DHI, respectively, as compared to their corresponding reference measurements at each station. The Interquartile Range (IQR) is defined as the difference between the 75$^{\text{th}}$ and 25$^{\text{th}}$ percentiles of the data set, while the extended range represents the errors within the 5$^{\text{th}}$ and 95$^{\text{th}}$ percentiles, which corresponds to approximately ±1.8σ or 90% coverage, if assuming a normal distribution. The mean bias error (MBE) assesses the average bias in the prediction, while the root mean square error (RMSE) is the standard deviation of the prediction error.

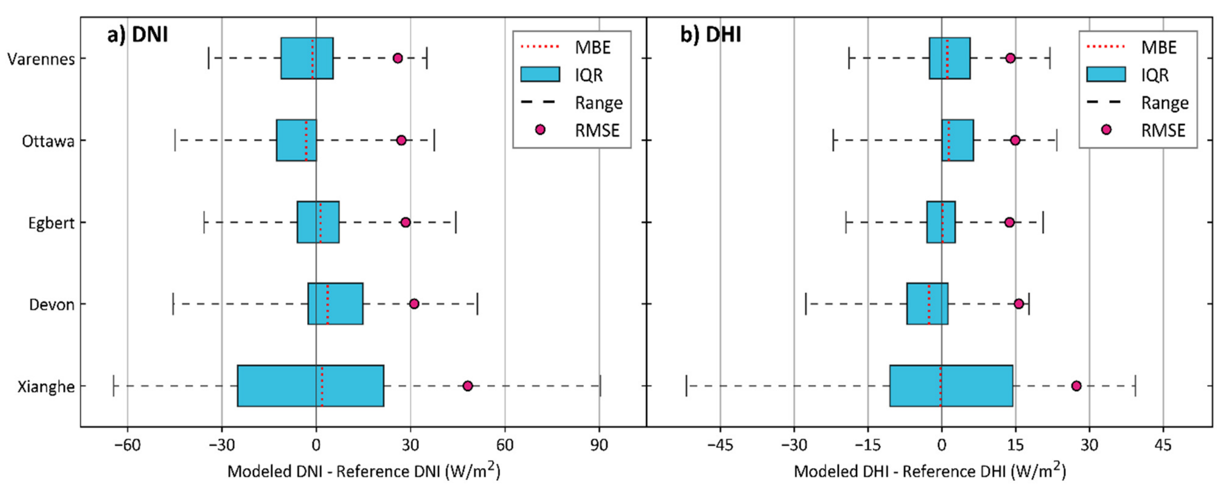

Fig. 1. Boxplot diagram of the error distributions between the a) modeled direct normal irradiance (DNI), b) modeled diffuse horizontal irradiance (DHI) from our decomposition algorithm and the corresponding DNI, DHI measurements made by the reference instruments. The plots show the mean bias error (MBE), interquartile range (IQR), defined as the values within the 25$^{\text{th}}$ and 75$^{\text{th}}$ percentiles, the extended error range, defined as the values within 5$^{\text{th}}$ and 95$^{\text{th}}$ percentiles, and the root mean square error (RMSE) for each station.

As can be seen from Fig. 1a, the extended error ranges for DNI retrieval are very similar for Ottawa, Varennes and Egbert stations, about ±40 W/m^2, while the MBE is around - 1 W/m^2 and the RMSE is about 27 W/m^2. This is expected since these stations are relatively close to each other and are subjected to similar environmental conditions. For Devon station, which has a slightly higher mean AOD_{500} than the aforementioned stations, the extended error range is a bit wider at about ±48 W/m^2, while the RMSE is very similar. For Xianghe station, which experiences large variations in aerosol conditions due to changes in pollution, the extended error range for the DNI is relatively high, ranging from -64 W/m^2 to +90 W/m^2, while the RMSE is 48 W/m^2. This is due to numerous periods at Xianghe when the reduction of GHI irradiance due to aerosol absorption of the direct beam is partially compensated for by the gain in the GHI from the diffuse irradiance due to aerosol scattering. In such cases our algorithm has a difficult time differentiating between the "clear", "hazy", and "thin clouds" sky conditions, which leads to increased uncertainty for the DNI retrieval. Nonetheless, the MBE for the DNI estimation for all stations is less than 4 W/m^2.

The modeled DHI propagates the errors from the modeled DNI, as per (4). The extended error range for Varennes, Ottawa, Egbert stations is about ±21 W/m^2, while the MBE and the RMSE are at +1 W/m^2 and 14 W/m^2, respectively. For Devon station the MBE was approximately -3 W/m^2 with the extended error range stretching from -28 W/m^2 to 17 W/m^2, while the RMSE was 15 W/m^2. Similar to the DNI retrieval, the Xianghe station saw the highest error spread with the extended error range varying from - 52 W/m^2 to 39 W/m^2, with negligible MBE and the RMSE of 27 W/m^2.

We also computed the integrated energy per unit surface area errors for the entire DNI and DHI datasets at each station and compared them against the corresponding reference values. The DNI and DHI integrated energy errors are less than 1% and 2%, respectively, at each station. This is an important result as it suggests that even in high aerosol environments such as Xianghe, the decomposition algorithm can accurately provide the estimate of the DNI and DHI solar resource potential.

VI. Conclusion

We have described a decomposition algorithm that uses spectral GHI measurements made by the SolarSIM-G to derive broadband DNI and DHI. We have proposed a more quantitative approach to the classification of atmospheric conditions via spectral clearness indices, which are also used as predictors to estimate DNI, and consequently to compute DHI. We used one-minute resolution measurement data from five stations (equivalent to seven station-years) to calibrate and validate our decomposition algorithm. For the DNI estimation, the RMSE ranged from 26 W/m^2 to 48 W/m^2, while for the DHI estimation - from 14 W/m^2 to 27 W/m^2. The largest absolute MBE for both cases was less than 4 W/m^2. In addition, the integrated DNI and DHI errors for each station were less than 1% and 2%, respectively.

These results show that the described decomposition algorithm has a factor of 2 to 3 improvement in the RMSE over existing, state-of-the-art decomposition algorithms, even with a one-minute resolution data set. Furthermore, based on [3], the proposed method is a comparable alternative to other tracker-less methods for obtaining all three components of sunlight, such as rotating shadowband radiometer and shadow-mask pyranometer. Undoubtedly, the SolarSIM-G based decomposition algorithm can be further improved as more data becomes available from the existing measurement stations and future installations worldwide.

References

[1] C. A. Gueymard and D. R. Myers, "Evaluation of conventional and high-performance routine solar radiation measurements for improved solar resource, climatological trends, and radiative modeling," Solar Energy, vol. 83, no. 2, pp. 171–185, 2009.

[2] A. Ohmura, et al., "Baseline Surface Radiation Network (BSRN/WCRP): New precision radiometry for climate research," Bulletin of the American Meteorological Society, vol. 79, pp. 2115-2136, 1998.

[3] L. Vuilleumier, et al., "Performance evaluation of radiation sensors for the solar energy sector," Meteorologische Zeitschrift, vol. 26, pp. 485-505, 2017.

[4] P. Ineichen, "Comparison and validation of three global-to-beam irradiance models against ground measurements," Solar Energy, vol. 82, pp. 501-512, 2008.

[5] D. G. Erbs, S. A. Klein, and J.A.Duffie, "Estimation of the diffuse radiation fraction for hourly, daily and monthly-average global radiation", Solar Energy, vol. 28, pp. 293-302, 1982.

[6] P. Ineichen, et al., "Dynamic global-to-direct irradiance conversion models," Ashrae Transaction, vol. 98, pp. 354-369, 1992.

[7] R. R Perez, et. al, "A new operational model for satellite-derived irradiances: description and validation," Solar Energy, vol. 73, pp. 307-317, 2002.

[8] V. Tatsiankou, K. Hinzer, H. Schriemer, and R. Beal, "Efficient, Real-Time Global Spectral and Broadband Irradiance Acquisition," 7th World Conference on Photovoltaic Energy Conversion, 2018

[9] V. Tatsiankou, et al., "Extensive validation of solar spectral irradiance meters at the World Radiation Center," Solar Energy, vol. 166, pp. 80-89, 2018.

[10] V. Tatsiankou, K. Hinzer, H. Schriemer, K. Emery, and R. Beal, "Design principles and field performance of a solar spectral irradiance meter," Solar Energy, vol. 133, pg. 94-102, 2016.

[11] V. Tatsiankou, K. Hinzer, H. Schriemer, P McVey-White, and R. Beal, "Deployment and early results from the CanSIM (Canadian Solar Spectral Irradiance Meter) network," AIP Conference Proceedings, vol. 1881, 2017.

[12] R.E. Bird and C. Riordan, "Simple solar spectral model for direct and diffuse irradiance on horizontal and tilted planes at the earth's surface for cloudless atmospheres," Journal of Climate and Applied Meteorology, vol. 25, pp. 87-97, 1986.

4.4 Research Impact of SolarSIM Technology

This section lists the articles published by third-party researchers that were enabled by the SolarSIM technology. At the time of writing, there were twelve such manuscripts, the majority of which have been published in prestigious scientific journals, such as the IEEE Journal of Photovoltaics and the Journal of Solar Energy. The research findings in the articles listed below were enabled by local spectral measurements obtained from SolarSIM sensors.

1. P. Pelland, *et al.*, "Development and benchmarking of a simple model of photovoltaic spectral mismatch factor". *47th IEEE Photovoltaic Specialists Conference (PVSC)*, 2020.

2. J. A. Caballero, *et al.*, "Annual energy harvesting of passively cooled hybrid thermoelectric generator-concentrator photovoltaic modules". *IEEE Journal of Photovoltaics*, vol. 9, no. 6, pp. 1652-1660, 2019.

3. E. F. Fernández, *et al.*, "Spectral nature of soiling and its impact on multi-junction based concentrator systems". *Solar Energy*, vol. 201, pp. 110-118, 2019

4. J. A. Caballero, *et al.*, "Spectral corrections based on air mass, aerosol optical depth, and precipitable water for PV performance modeling". *IEEE Journal of Photovoltaics*, vol. 8, no. 2, pp. 552-558, 2018.

5. F. Almonacid, *et al.*, "Spectral-matching-ratio modelling based on ANNs and atmospheric parameters for the electrical characterization of multi-junction concentrator PV systems". *Solar Energy*, vol. 156, pp. 409-417, 2018.

6. M. Yandt, *et al.*, "Representative atmospheric parameters in multijunction solar cell design". *IEEE Journal of Photovoltaics*, vol. 8, no. 3, pp. 409-417, 2018.

7. V. Paraskeva, *et al.*, "Investigation of solar spectral irradiance measurements using the spectral matching ratio". *IEEE 7th World Conference on Photovoltaic Energy Conversion*, pp. 2331-2336, 2018.

8. M. Benhammane, *et al.*, "Output power simulation for CPV receivers based on experimental spectral matching ratio modeling". *AIP Conference Proceedings*, vol. 2012(1), 2018.

9. F. Ghani, *et al.*, "The numerical computation of lumped parameter values using the multi-dimensional Newton-Raphson method for the characterisation of a multi-junction CPV module using the five-parameter approach". *Solar Energy*, vol. 149, pp. 302-313, 2017.

10. P. M. Rodrigo, *et al.*, "Characterization of the spectral matching ratio and the Z-Parameter from atmospheric variables for CPV spectral evaluation". *IEEE Journal of Photovoltaics*, vol. 7, no. 6, pp. 1802-1809, 2017.

11. J. A. Caballero, *et al.*, "Analytical transfer equations for the spectral modelling of III–V multi-junction concentrator solar cells". *IEEE Spanish Conference on Electron Devices*, pp. 1-4, 2017.

12. M. Theristis, *et al.*, "Spectral corrections based on air mass, aerosol optical depth, and precipitable water for CPV performance modeling". *IEEE Journal of Photovoltaics*, vol. 6, no. 6, pp. 1598-1604, 2016.

Chapter 5

Conclusion

In an era of unpredictable weather and hundreds of gigawatts of deployed solar energy power plants, it is arguably more important than ever to perform detailed spectral irradiance and atmospheric measurements. This valuable information allows one to completely understand the local atmospheric effects and consequently to quantify the solar spectral resource. These datasets are desired in a range of applications from solar energy research to weather prediction. Prior to this work, performing the measurements of spectral irradiance required several expensive scientific instruments, accessible to only well-funded research groups. As such, my thesis work has addressed this problem by designing, validating and then commercializing two software-augmented, multi-functional state-of-the-art sensors, the SolarSIM-D2 and the SolarSIM-G, that are capable of resolving the solar spectral irradiance and atmospheric constituents. All findings in this dissertation are presented via published, stand-alone manuscripts, the main results of which are contextualized below.

In Section 3.1.1, the journal article entitled "Design principles and field performance of a solar spectral irradiance meter" describes the parameterized transmittance model and the methodology used to derive the spectral and broadband DNI from six irradiance measurements made by the SolarSIM-D2. The paper also describes the calibration procedure and field performance of two commercially packaged SolarSIMs as compared to state-of-the-art reference instruments. The publication demonstrated that for the first time the spectral and broadband DNI in the 280–4000 nm range could be obtained with a single, rugged device with no moving parts, with accuracies comparable to field spectroradiometers and pyrheliometers, at a fraction of the cost.

In Section 3.1.2, the journal article entitled "Extensive validation of solar spectral irradiance meters at the World Radiation Center" presents a comprehensive uncertainty analysis which validates SolarSIM-D2's ability to not only accurately resolve the spectral and broadband DNI, but also atmospheric parameters, such as the spectral aerosol optical depth, total column ozone and precipitable water vapour. The uncertainty analysis was complimented with field trials of multiple SolarSIMs, deployed at World Radiation Center, where their measurements were compared to state-of-the-art reference instrumentation, including spectroradiometers, sun photometers, pyrheliometers and spectrophotometers. The publication demonstrates that the SolarSIM-D2 can accurately resolve the spectral aerosol optical depth, total column ozone and precipitable water vapour, and ultimately to obtain the spectral and broadband DNI - thus providing data that typically requires five to seven commercial instruments. Furthermore, the ability to simultaneously obtain the aforementioned detailed solar and atmospheric data from a single device avoids the complexity of multiple data acquisition protocols and setup requirements, thus positioning the SolarSIM-D2 as the preferred instrument for solar energy research and atmospheric sciences applications.

The aforementioned papers illustrate that with proper packaging, careful characterization, and precise measurements, an optimized spectral sampling technique can achieve a high level of accuracy and robustness for deriving the spectral and broadband DNI, and the atmospheric constituents. This research was a required stepping stone in extending the said technique to derive the global spectral irradiance.

In Section 3.2.1, the paper entitled "Efficient, Real-Time Global Spectral and Broadband Irradiance Acquisition" describes the design principles, optical calibration and field performance of two commercially packaged SolarSIM-Gs for resolving the spectral and broadband global irradiance in the 280–4000 nm range. This feat is achieved by a compact, rugged, and low cost instrument with no moving parts. The field trials at the National Renewable Energy Laboratory against the state-of-the-art spectroradiometers and pyranometers demonstrated the SolarSIM-Gs' high accuracy and precision, with a measurement uncertainty comparable to the state-of-the-art reference instruments. These characteristics position the SolarSIM-G to be become the default sensor in the solar industry for providing spectral and broadband global irradiance as part of module characterization studies, certification, resource assessment, operation and maintenance of PV power plants.

The development of the SolarSIM-G represents a breakthrough in solar measurements, as, at the time of writing, no other sensor can simultaneously obtain the spectral and broadband global irradiance data under all-sky conditions across the full spectral range. The path toward instrument's commercialization involved incremental advancements of engineering principles, as the inner-workings of the SolarSIM-G are much more complex, compared to the SolarSIM-D2. Two major innovations were realized. First, the SolarSIM-G's optics were designed to couple the global irradiance within a hemispherical field of view and this design was optimized to ensure the directional response of the instrument complies with the highest accuracy of radiometer classification, i.e. class A as per the ISO 9060:2018 standard. Secondly, an all-sky parameterized transmittance model was developed, capable of deriving the spectral and broadband global irradiance from the SolarSIM-G's nine optical measurements under clear and cloudy conditions. This model uses radiative transfer algorithms to resolve in real-time the combined contribution of the direct and diffuse irradiances components, including the effects of atmospheric and cloud scattering. The novelty underpinning the SolarSIM-G technology is encapsulated in two U.S. patents.

The SolarSIM sensors represent a significant advance in the field of solar measurements by providing an unparallelled quality and quantity of detailed spectral and atmospheric data at a fraction of the cost as compared to traditional alternatives. A notable result of this work is the commissioning and ongoing operation of the CanSIM network, consisting of seven stations across Canada, each containing the SolarSIM-D2 and the SolarSIM-G, as described in Section 4.1. The CanSIM network is the world's first real-time solar spectral irradiance network enabling many applications in solar energy research, atmospheric sciences and solar power forecasting. Section 4.2 details one such use of CanSIM data to calculate spectral correction factors to quantify local spectral effects as simple time series data. Furthermore, in Section 4.3 CanSIM data is used to develop and validate a novel global irradiance decomposition algorithm, capable of deriving broadband DNI and DHI from SolarSIM-G measurements. The proposed algorithm leverages the insight provided by spectral irradiance data to classify sky conditions through the spectral clearness indices. The results show that the described method has a factor of two to three improvement in the root-mean-square error for the DNI retrieval as compared to existing state-of-the-art decomposition algorithms, and is a viable alternative to other tracker-less methods for obtaining all three components of sunlight.

One natural extension of the thesis work would be to investigate the applicability of the spectral sampling technique for resolving the spectral albedo, which is critical for bifacial PV performance characterization and modelling. This work would explore the limitations of the SolarSIM-G in resolving the reflected spectral irradiance from various surfaces. Another possible avenue for future work would be to exploit the spectral clearness indices and sky classification methodology developed for the decomposition algorithm in Section 4.3 to improve very short-term forecasting or nowcasting of GHI. The current limitations of PV forecasting techniques represent a key challenge to achieving high penetration rates of solar systems worldwide.

Appendix

The innovations underpinning the SolarSIM-G are described by two US patents 10,209,132 B2 and 10,359,314 B2 granted on 19 February 2019 and 23 July 2019, respectively. The latter is a continuation patent which includes additional claims to the embodiments presented in the earlier patent. Both patents claim the benefit of priority from the U.S. provisional patent application filed on 20 October 2015. For intellectual property reasons, the earlier SolarSIM-G publications, including the one in Section 3.2.1, did not discuss some of the instrument's more sensitive technical details. As such, the latest patent is included in this section to provide additional insight into sensor's optical, mechanical and software designs. More specifically, it presents two earlier SolarSIM-G's embodiments - a six channel version with a Teflon bulk diffuser and a seven channel version with an integrating sphere. The third SolarSIM-G embodiment presented in this thesis has nine optical channels and captures global irradiance via the combination of a bulk diffuser and an integrating cavity. As such, the inclusion of the patent in this thesis highlights the incremental advancement of engineering principles that was achieved through my continuous research and development.

The patent publication follows on next page.

V. Tatsiankou, R. Beal, "Global solar spectrum devices and methods". U.S. Patent 10,359,314 B2 issued July 23, 2019.

US010359314B2

(12) **United States Patent**
Tatsiankou et al.

(10) **Patent No.: US 10,359,314 B2**
(45) **Date of Patent: Jul. 23, 2019**

(54) **GLOBAL SOLAR SPECTRUM DEVICES AND METHODS**

(71) Applicant: **SPECTRAFY INC.**, Ottawa (CA)

(72) Inventors: **Viktar Tatsiankou**, Ottawa (CA); **Richard Beal**, Ottawa (CA)

(73) Assignee: **Spectrafy Inc.**, Ottawa (CA)

(*) Notice: Subject to any disclaimer, the term of this patent is extended or adjusted under 35 U.S.C. 154(b) by 0 days.

(21) Appl. No.: **16/237,942**

(22) Filed: **Jan. 2, 2019**

(65) **Prior Publication Data**

US 2019/0137336 A1 May 9, 2019

Related U.S. Application Data

(63) Continuation of application No. 15/769,601, filed as application No. PCT/CA2016/000264 on Oct. 20, 2016, now Pat. No. 10,209,132.

(Continued)

(51) **Int. Cl.**
G01N 21/25 (2006.01)
G01J 3/36 (2006.01)

(Continued)

(52) **U.S. Cl.**
CPC ***G01J 3/36*** (2013.01); ***G01J 1/0403*** (2013.01); ***G01J 1/0411*** (2013.01); ***G01J 1/0474*** (2013.01); ***G01J 1/0492*** (2013.01); ***G01J 1/06*** (2013.01); ***G01J 3/0202*** (2013.01); ***G01J 3/0205*** (2013.01); ***G01J 3/0208*** (2013.01); ***G01J 3/0262*** (2013.01); ***G01N 21/31*** (2013.01); ***G01N 21/538*** (2013.01); *G01J 2001/061* (2013.01); *G01J 2001/4266* (2013.01); *G01J 2003/1213* (2013.01); *G01N 2201/065* (2013.01); *G01N 2201/0616* (2013.01)

(58) **Field of Classification Search**
CPC G01J 3/02; G01J 3/36; G01J 1/06; G01J 1/04; G01N 21/33; G01N 21/25; H01L 31/00; H01L 31/055; H01L 27/146; G01S 17/93; G01S 17/89
See application file for complete search history.

(56) **References Cited**

U.S. PATENT DOCUMENTS

2009/0272424 A1 * 11/2009 Ortabasi H01L 31/0543 136/246

* cited by examiner

Primary Examiner — Abdullahi Nur
(74) *Attorney, Agent, or Firm* — Rosenberg, Klein & Lee

(57) **ABSTRACT**

Solar spectral irradiance (SSI) measurements are important for solar collector/photovoltaic panel efficiency and solar energy resource assessment as well as being important for scientific meteorological/climate observations and material testing research. To date such measurements have exploited modified diffraction grating based scientific instruments which are bulky, expensive, and with low mechanical integrity for generalized deployment. A compact and cost-effective tool for accurately determining the global solar spectra as well as the global horizontal or tilted irradiances as part of on-site solar resource assessments and module performance characterization studies would be beneficial. An instrument with no moving parts for mechanical and environment stability in open field, non-controlled deployments could exploit software to resolve the global, direct and diffuse solar spectra from its measurements within the 280-4000 nm spectral range, in addition to major atmospheric processes, such as air mass, Rayleigh scattering, aerosol extinction, ozone and water vapor absorptions.

21 Claims, 20 Drawing Sheets

100A

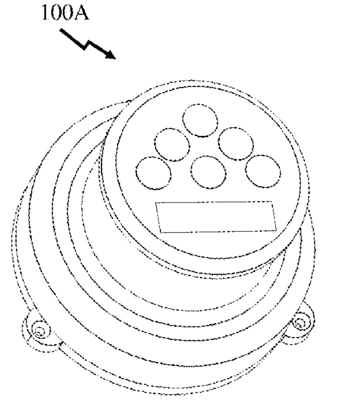

100B

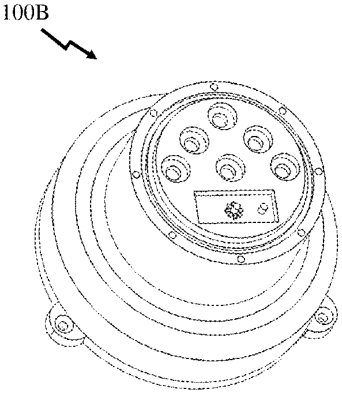

Related U.S. Application Data

(60) Provisional application No. 62/243,706, filed on Oct. 20, 2015.

(51) **Int. Cl.**

G01N 21/31	(2006.01)
G01J 3/02	(2006.01)
G01J 1/04	(2006.01)
G01J 1/06	(2006.01)
G01N 21/53	(2006.01)
G01J 1/42	(2006.01)
G01J 3/12	(2006.01)

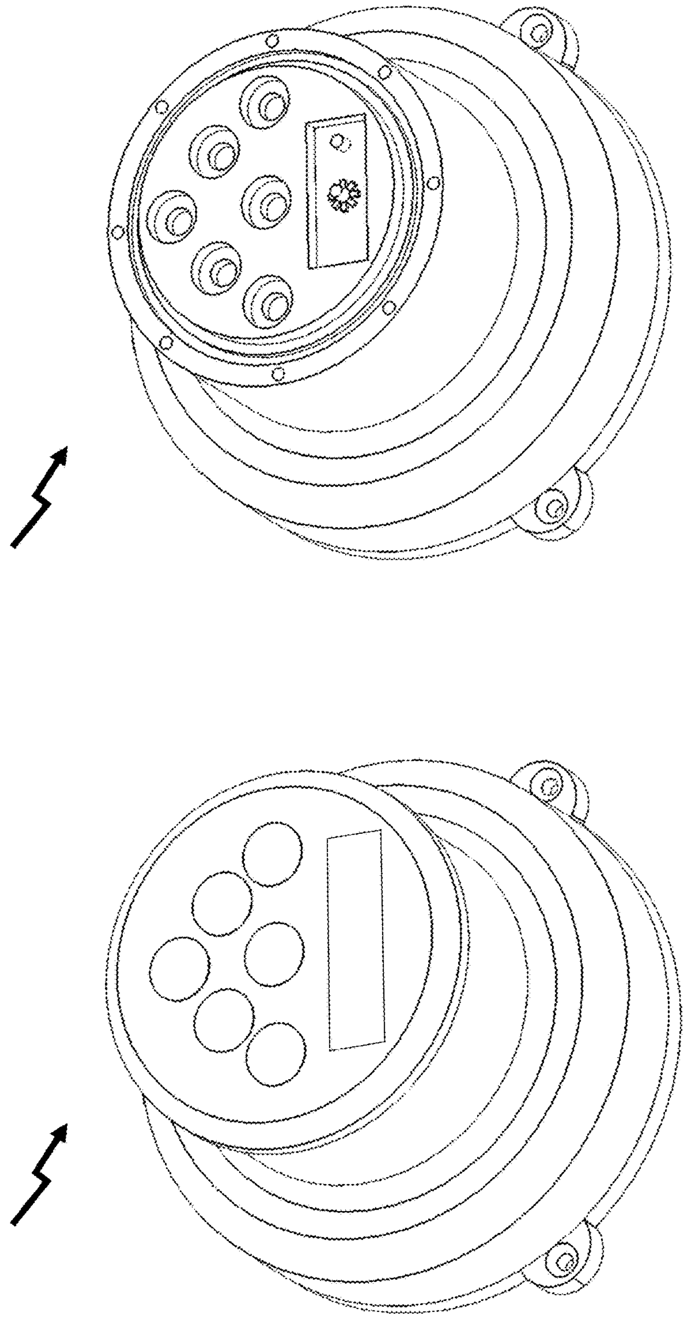

Figure 1

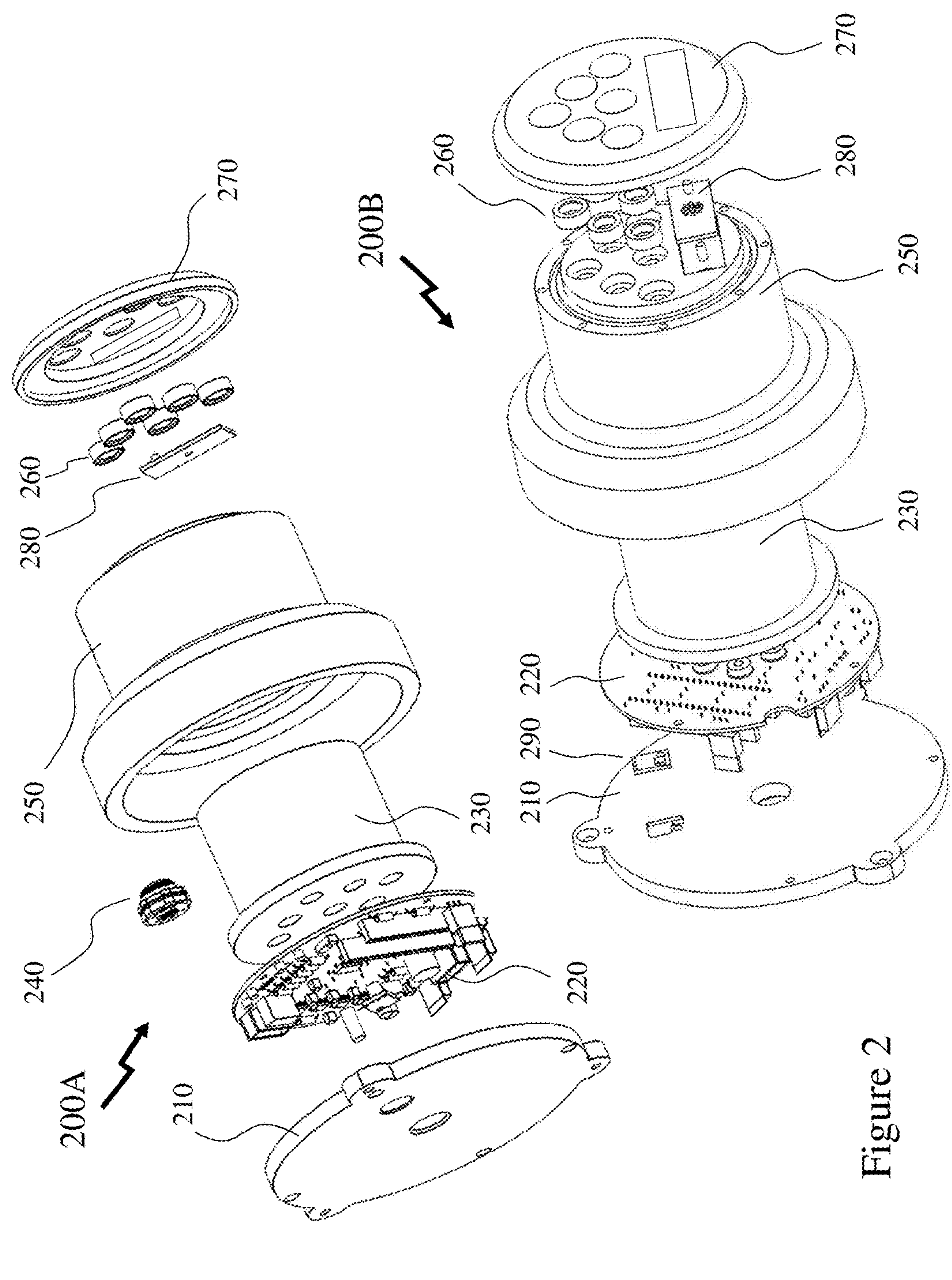
200A
200B
210
220
230
240
250
260
270
280
290
210
220
230
250
260
270
280

Figure 2

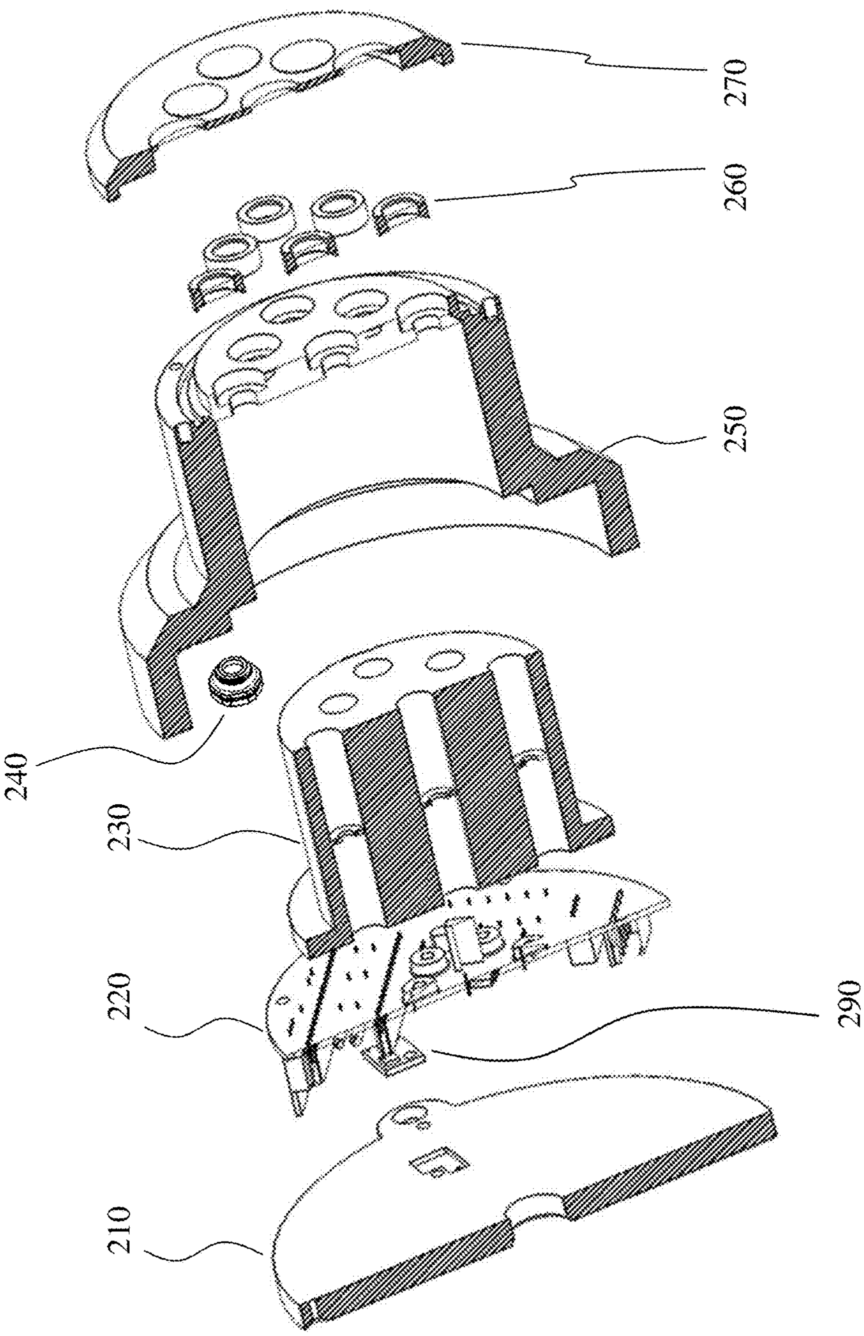

Figure 3

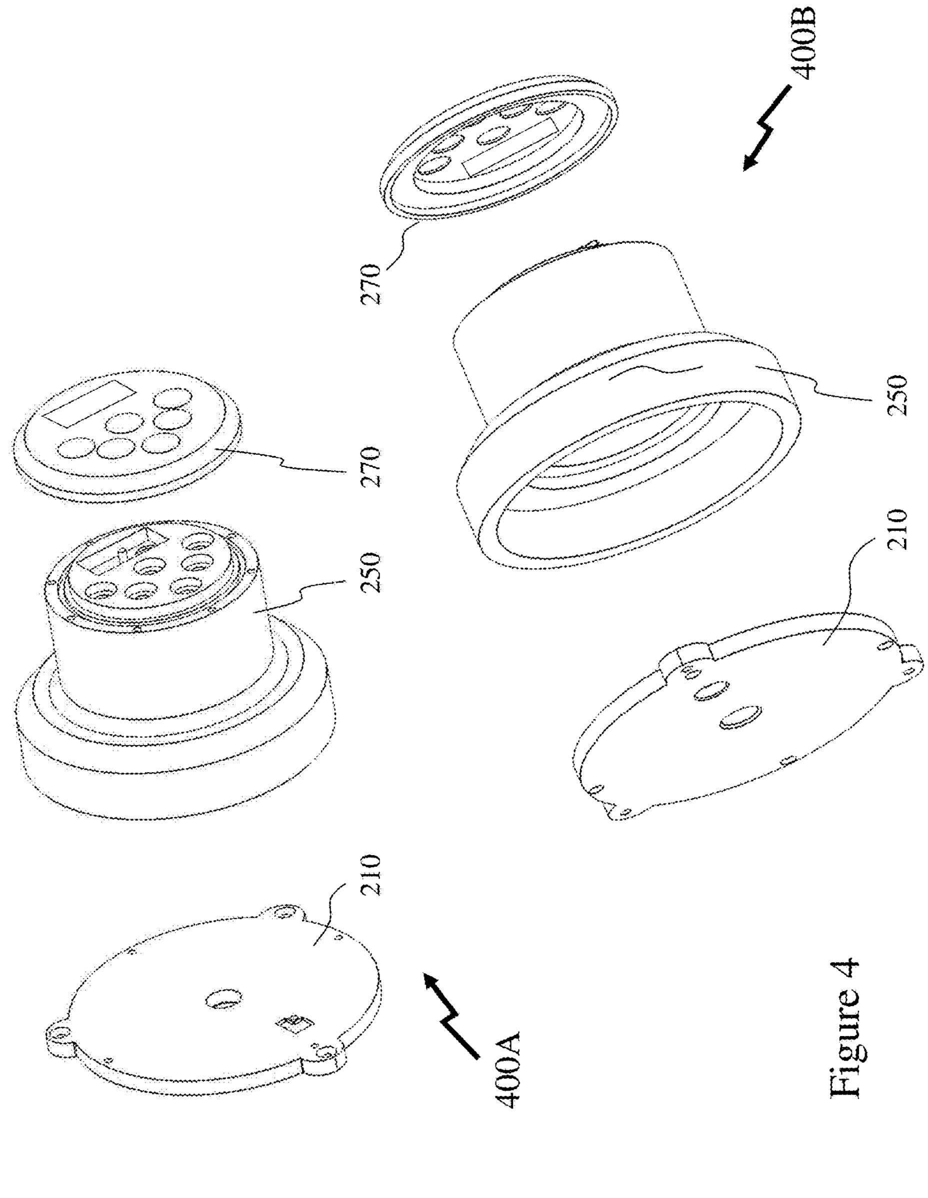

Figure 4

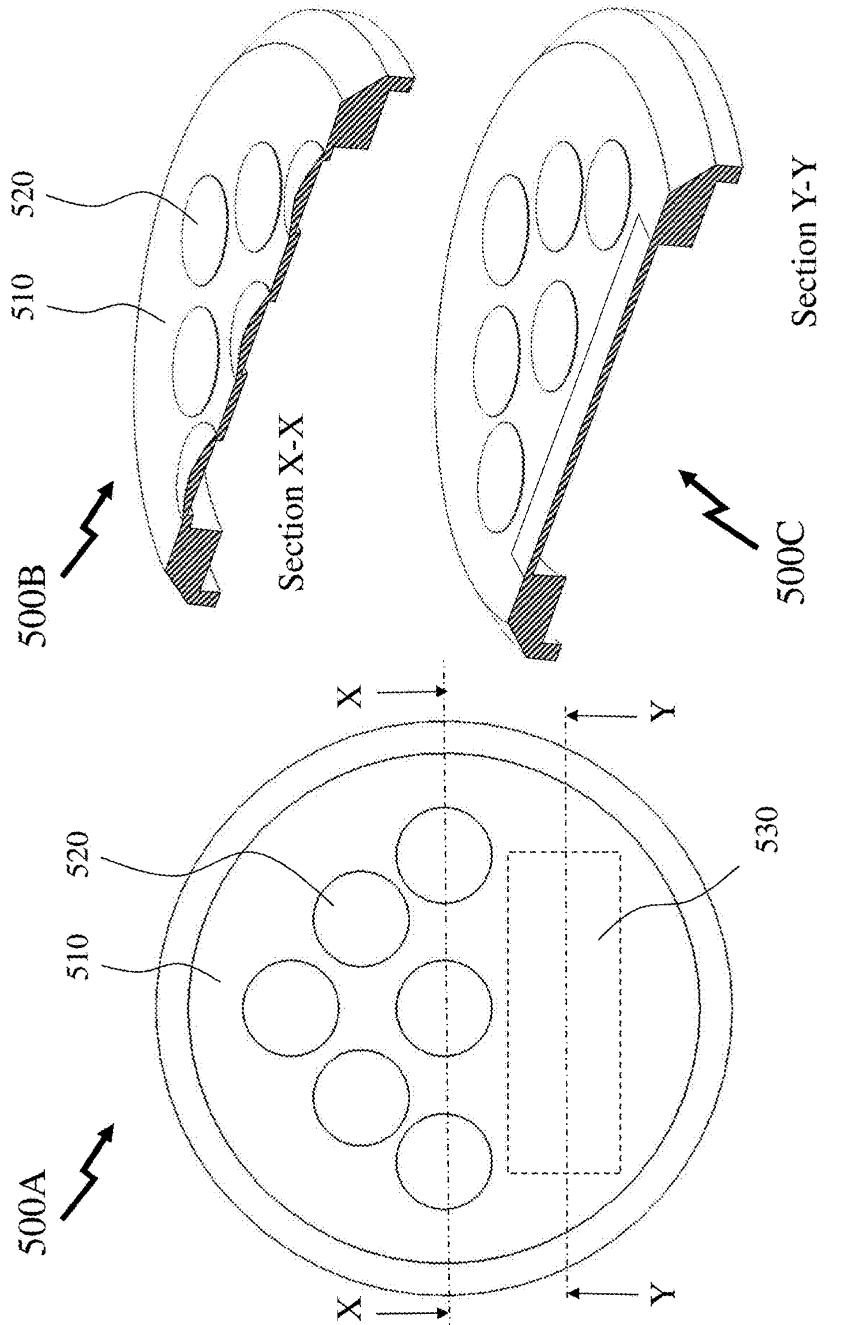

Figure 5

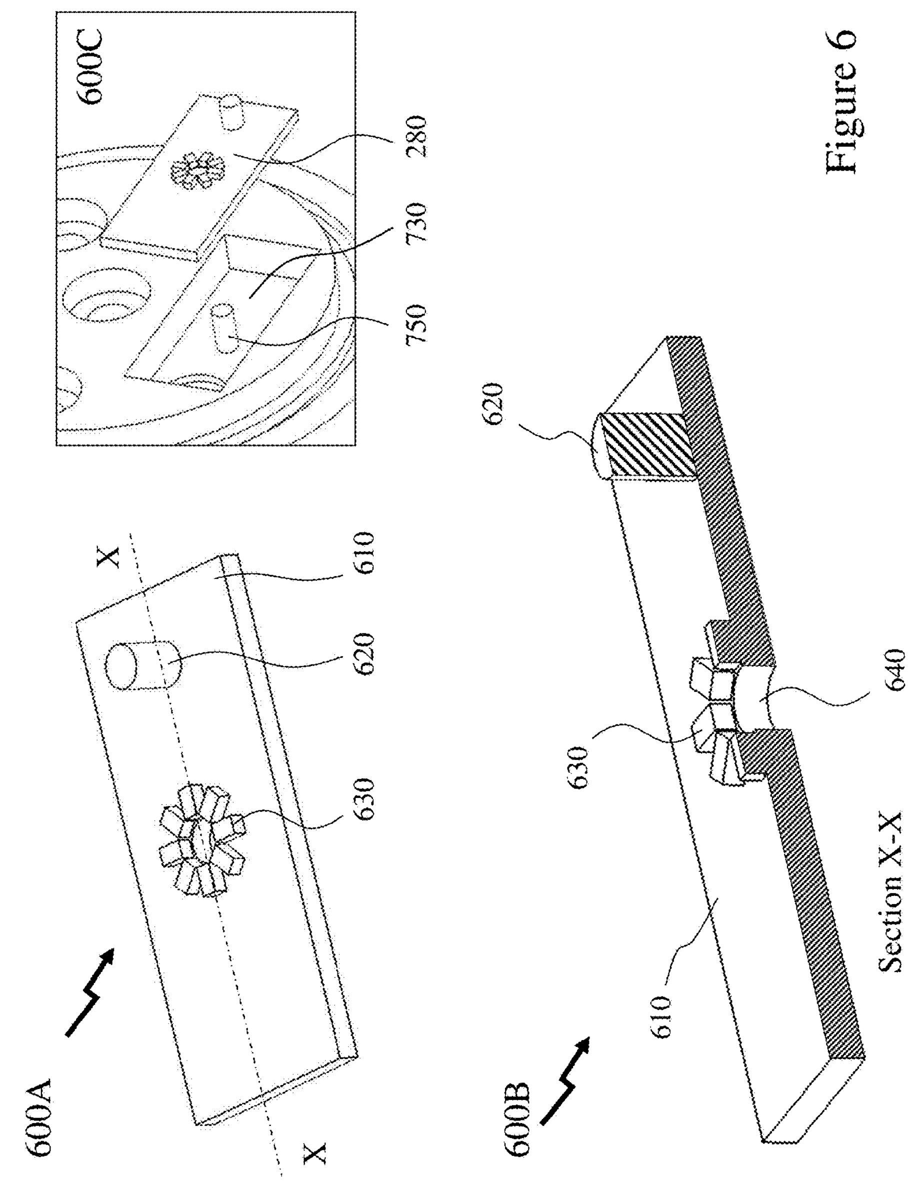
600C
280
730
750
600A
X
X
610
620
630
600B
620
630
640
610
Section X-X

Figure 6

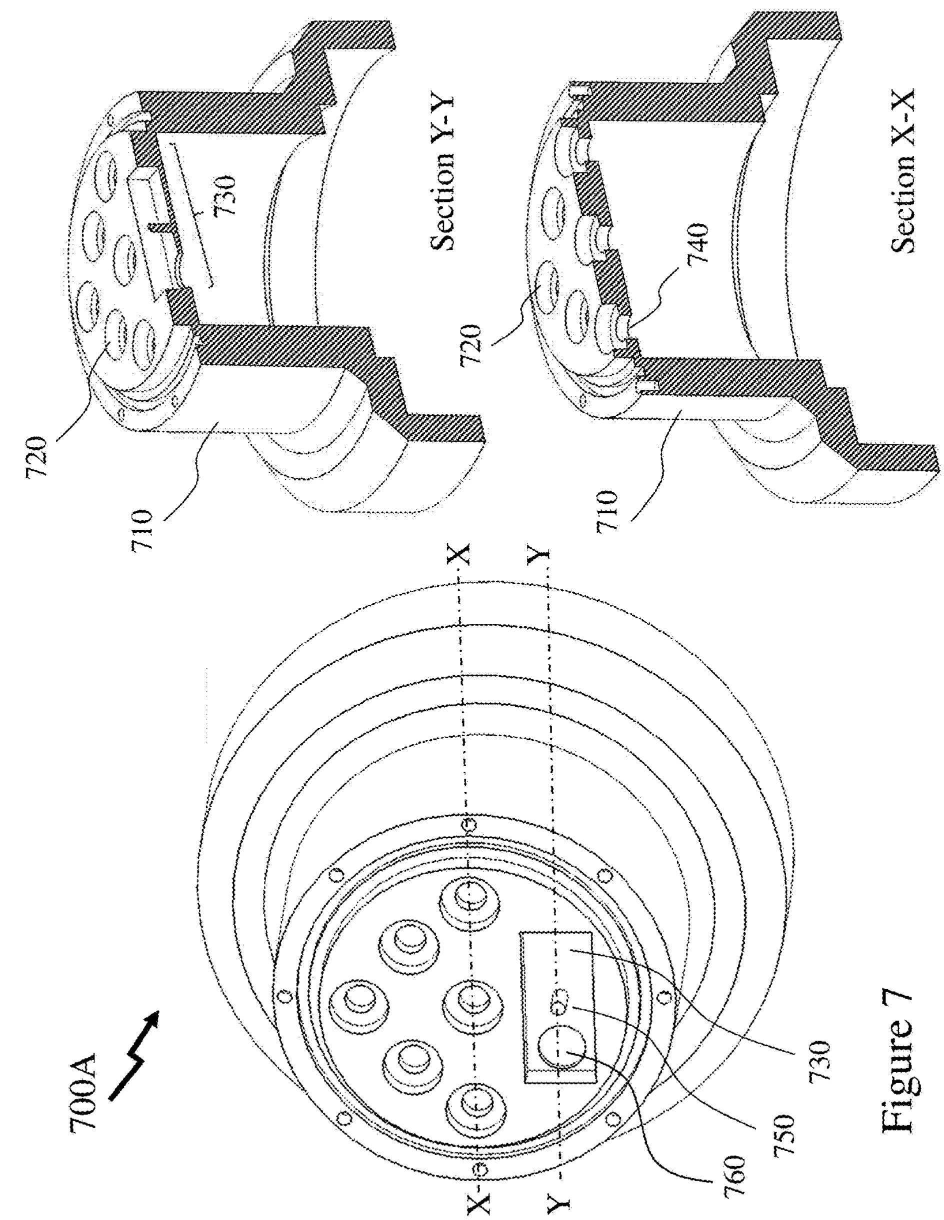
720
710
730
Section Y-Y
720
740
710
Section X-X
X
Y
700A
X
Y
730
750
760

Figure 7

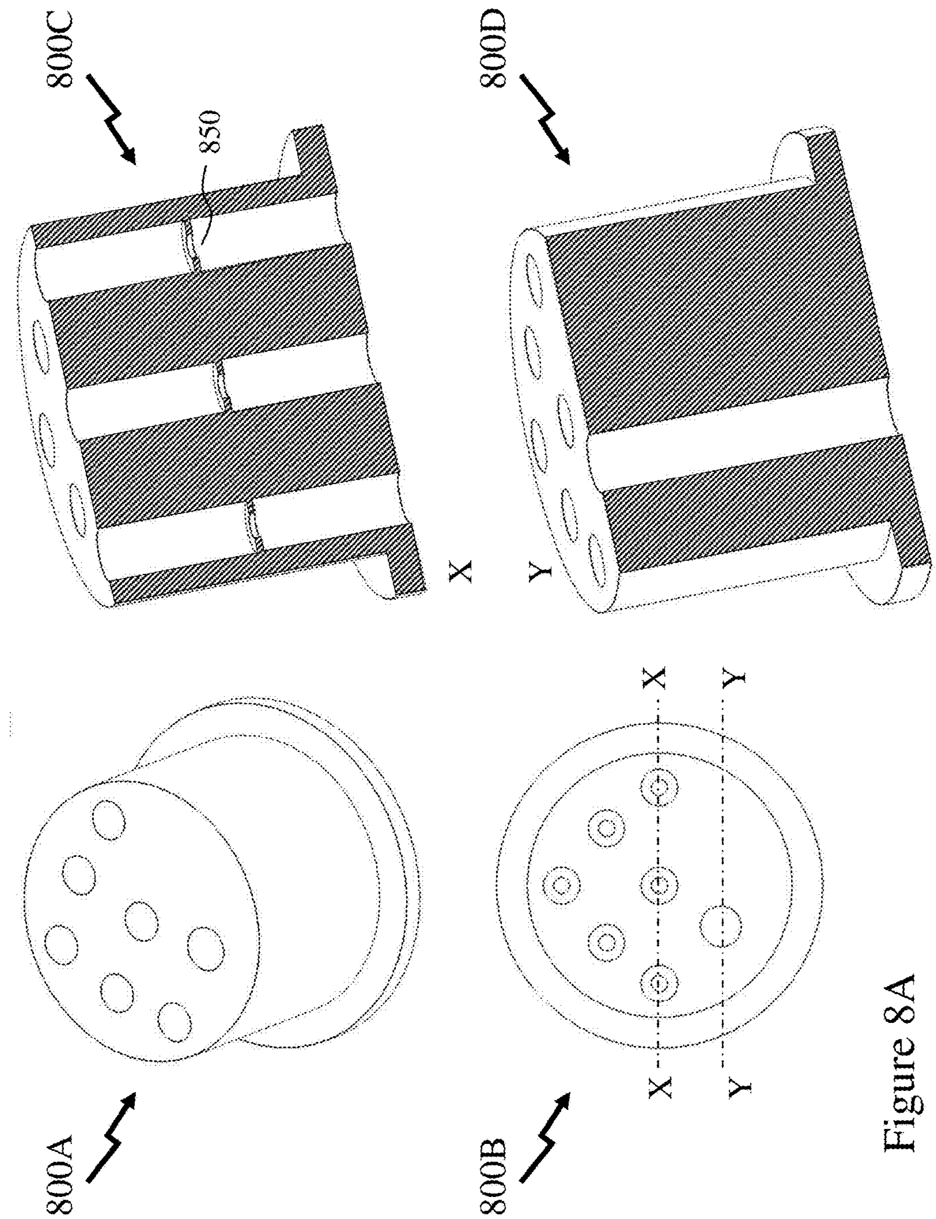

Figure 8A

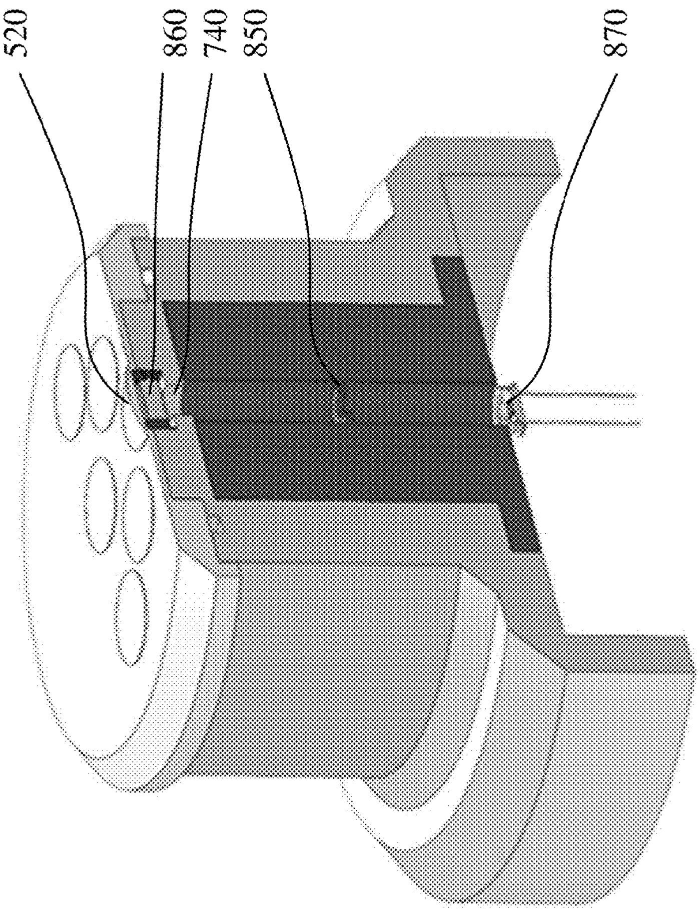

Figure 8B

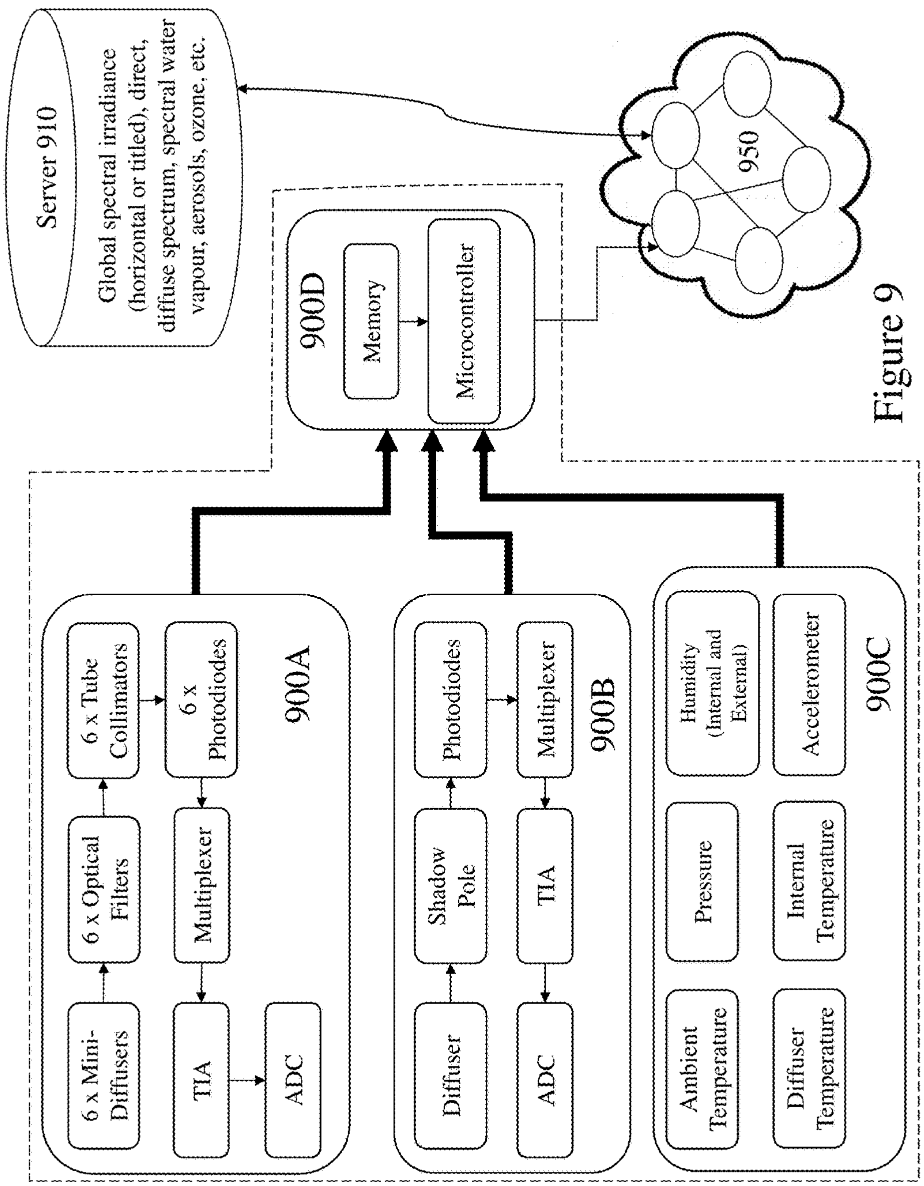
Server 910
Global spectral irradiance (horizontal or titled), direct, diffuse spectrum, spectral water vapour, aerosols, ozone, etc.
950
900D
Memory
Microcontroller
6 x Mini-Diffusers
6 x Optical Filters
6 x Tube Collimators
6 x Photodiodes
Multiplexer
TIA
ADC
900A
Diffuser
Shadow Pole
Photodiodes
Multiplexer
TIA
ADC
900B
Ambient Temperature
Pressure
Humidity (Internal and External)
Diffuser Temperature
Internal Temperature
Accelerometer
900C

Figure 9

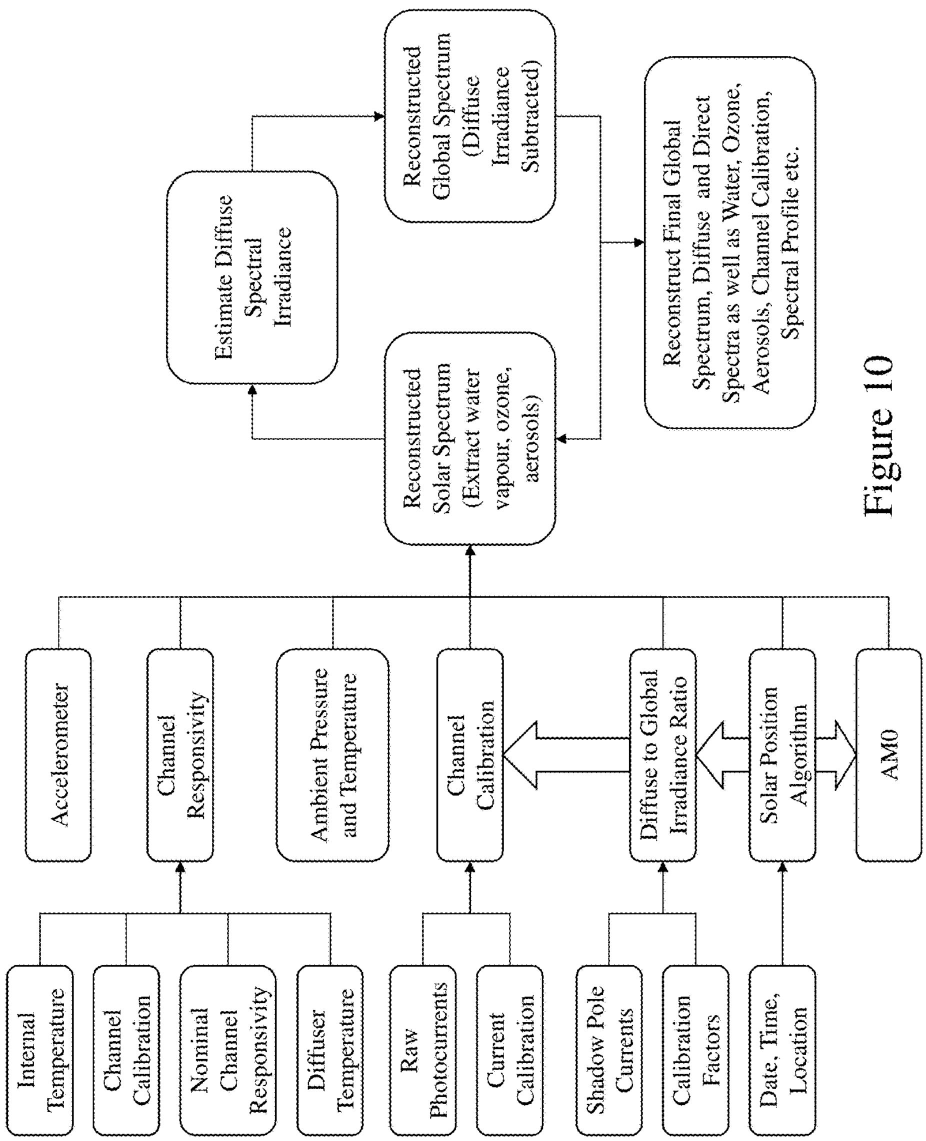
Internal Temperature
Channel Calibration
Nominal Channel Responsivity
Diffuser Temperature
Raw Photocurrents
Current Calibration
Shadow Pole Currents
Calibration Factors
Date, Time, Location
Accelerometer
Channel Responsivity
Ambient Pressure and Temperature
Channel Calibration
Diffuse to Global Irradiance Ratio
Solar Position Algorithm
AM0
Reconstructed Solar Spectrum (Extract water vapour, ozone, aerosols)
Estimate Diffuse Spectral Irradiance
Reconstructed Global Spectrum (Diffuse Irradiance Subtracted)
Reconstruct Final Global Spectrum, Diffuse and Direct Spectra as well as Water, Ozone, Aerosols, Channel Calibration, Spectral Profile etc.

Figure 10

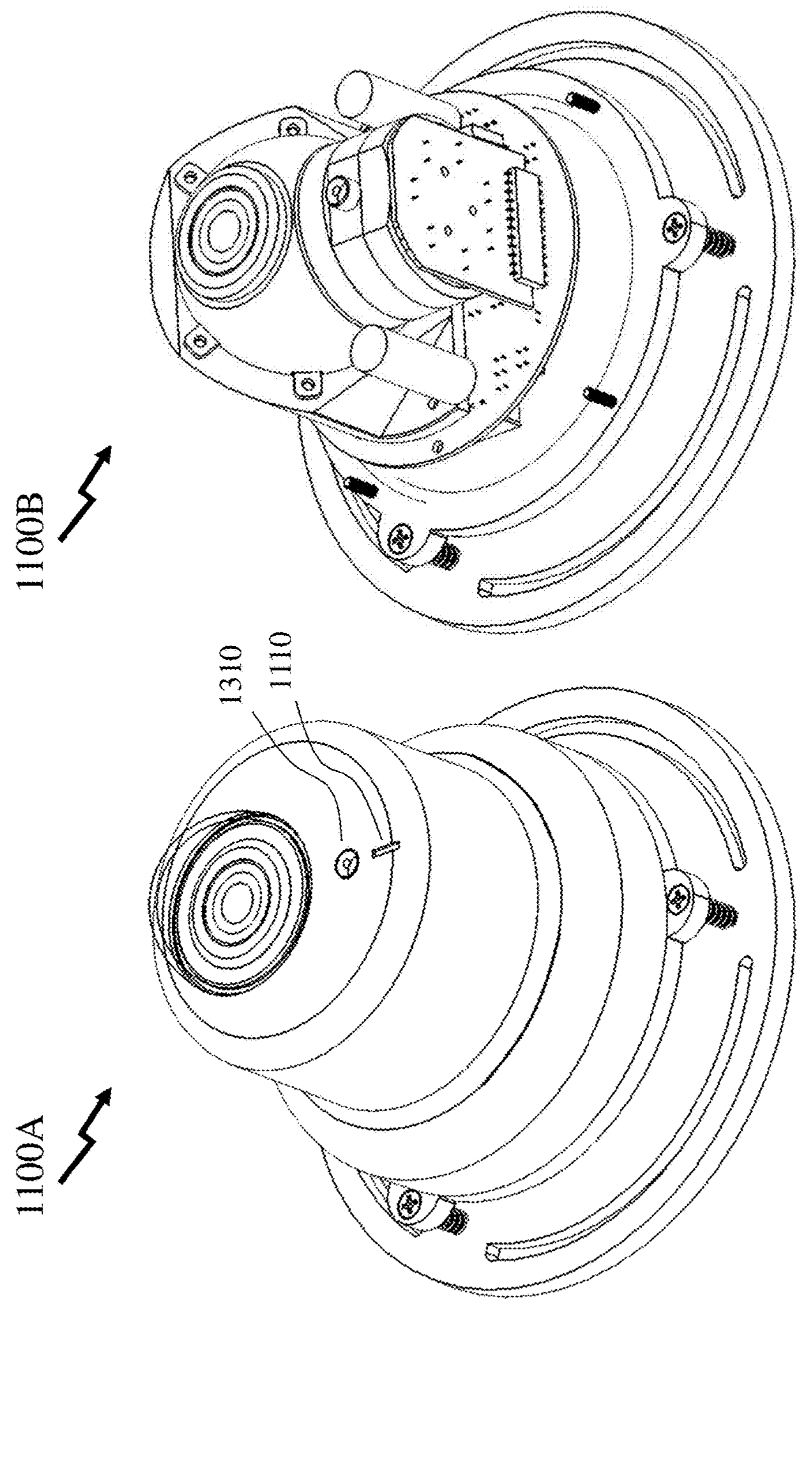

Figure 11

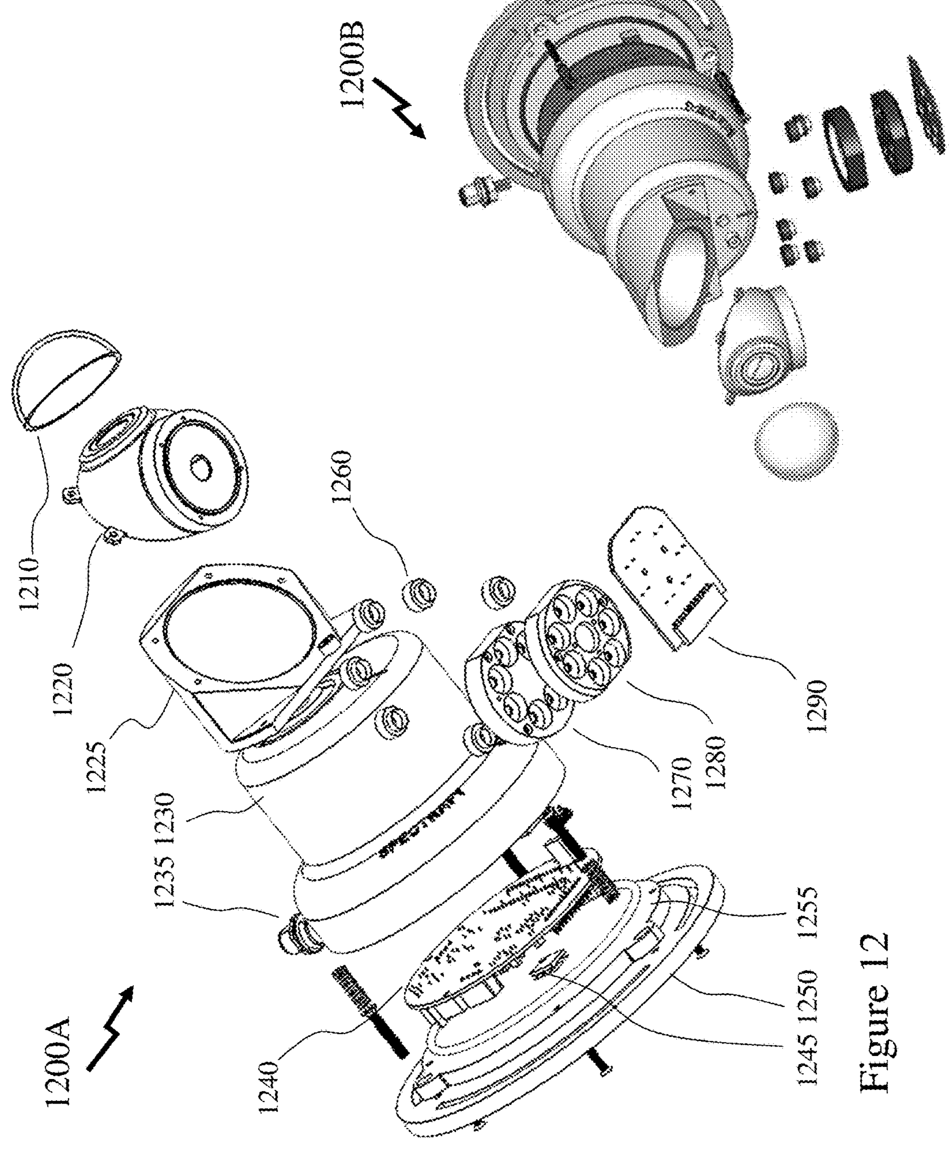
1200B
1210
1220
1225
1235 1230
1260
1270
1280
1290
1255
1245 1250
1240
1200A

Figure 12

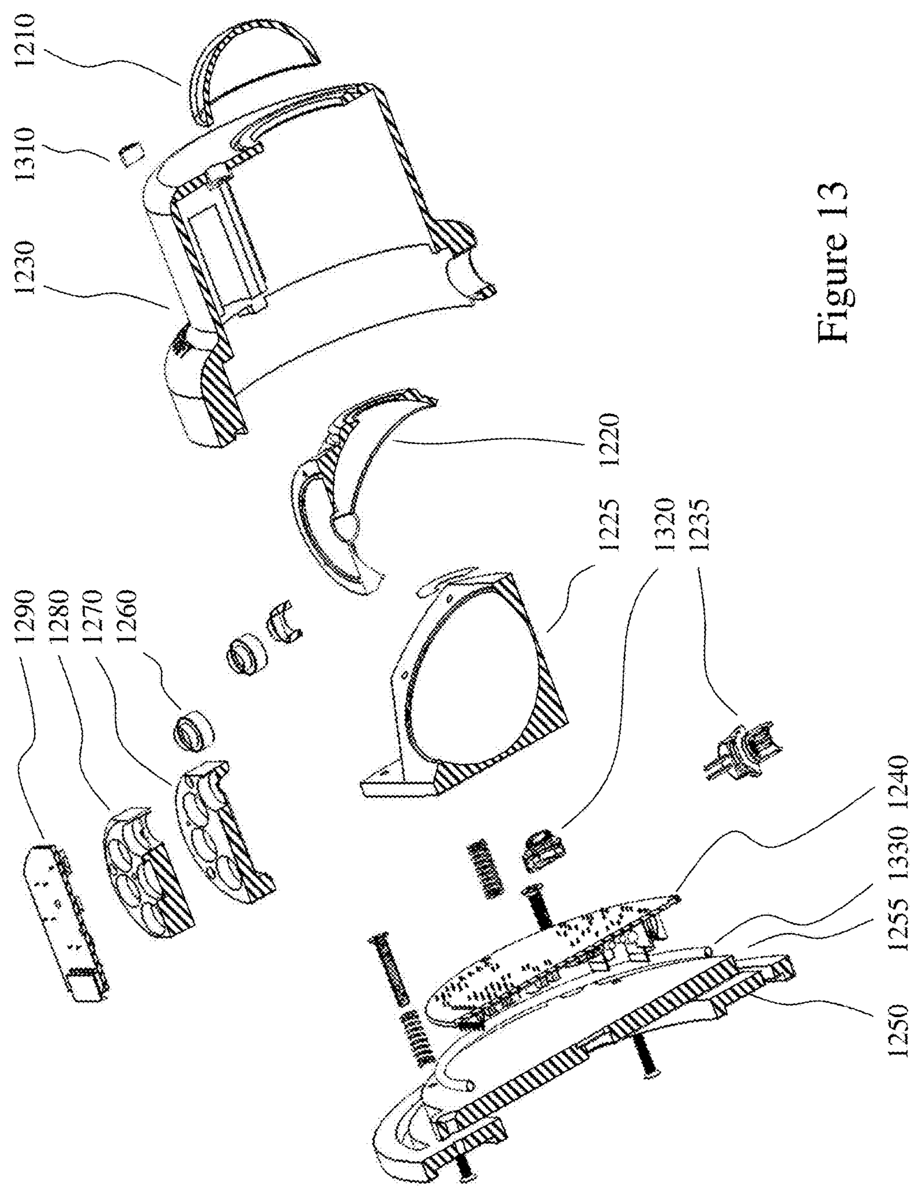
1210
1310
1230
1220
1225
1320
1235
1290
1280
1270
1260
1240
1330
1255
1250

Figure 13

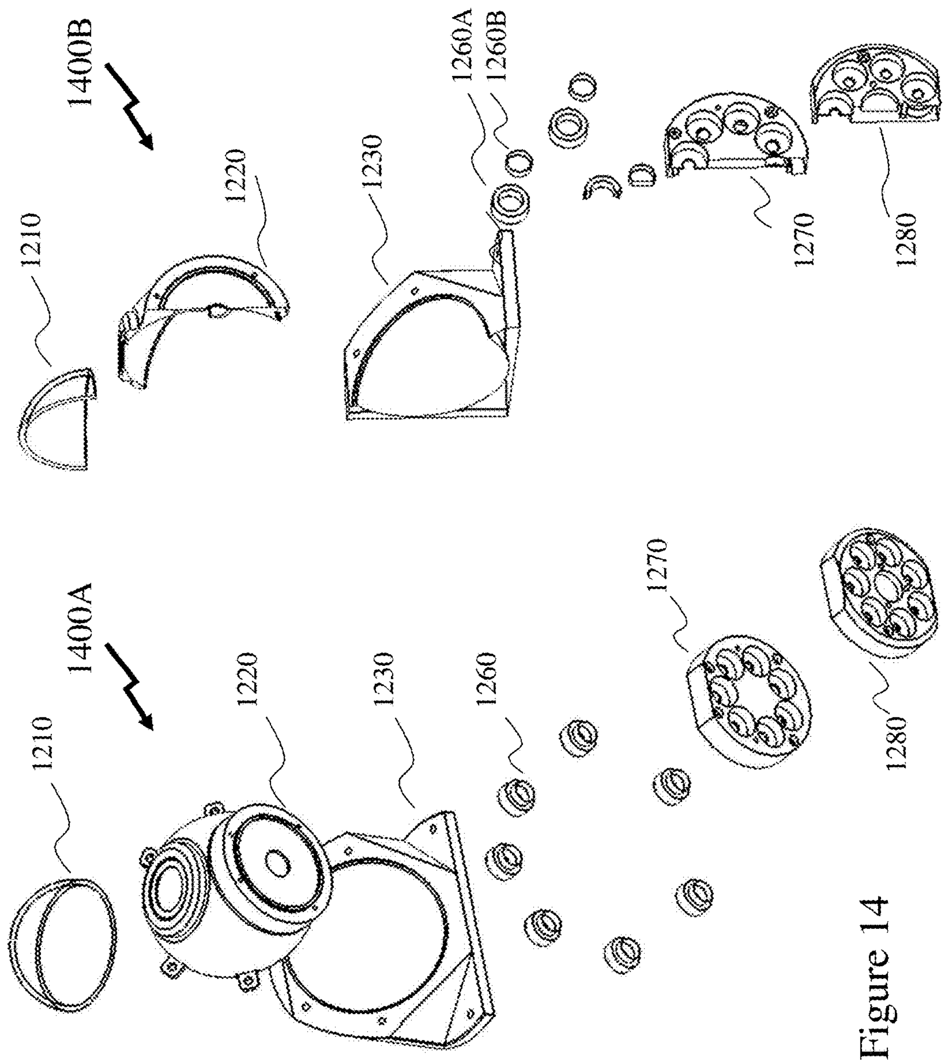
1400A
1210
1220
1230
1260
1270
1280
1400B
1210
1220
1230
1260A
1260B
1270
1280

Figure 14

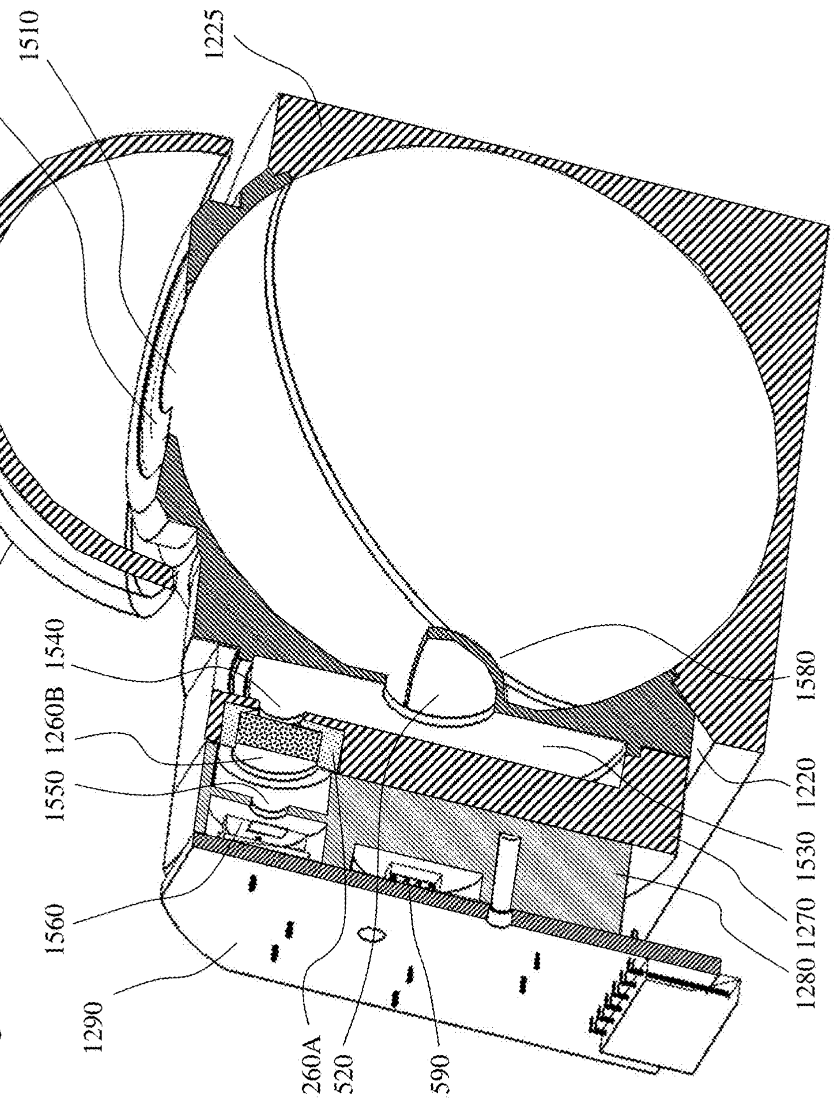
1570
1510
1225
1210
1540
1260B
1550
1560
1290
1260A
1520
1590
1580
1220
1530
1270
1280

Figure 15A

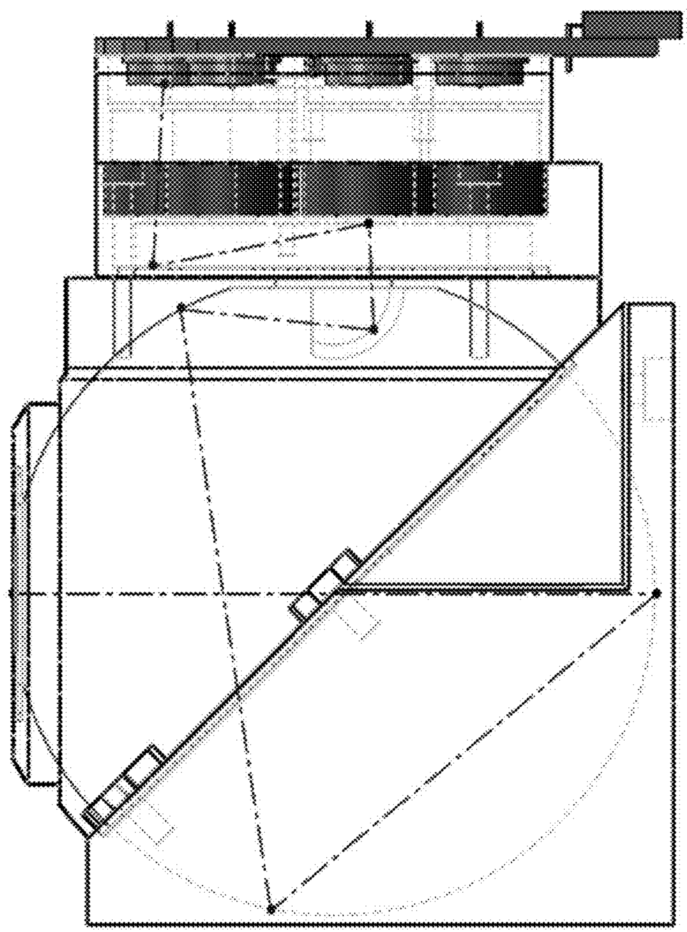

Figure 15B

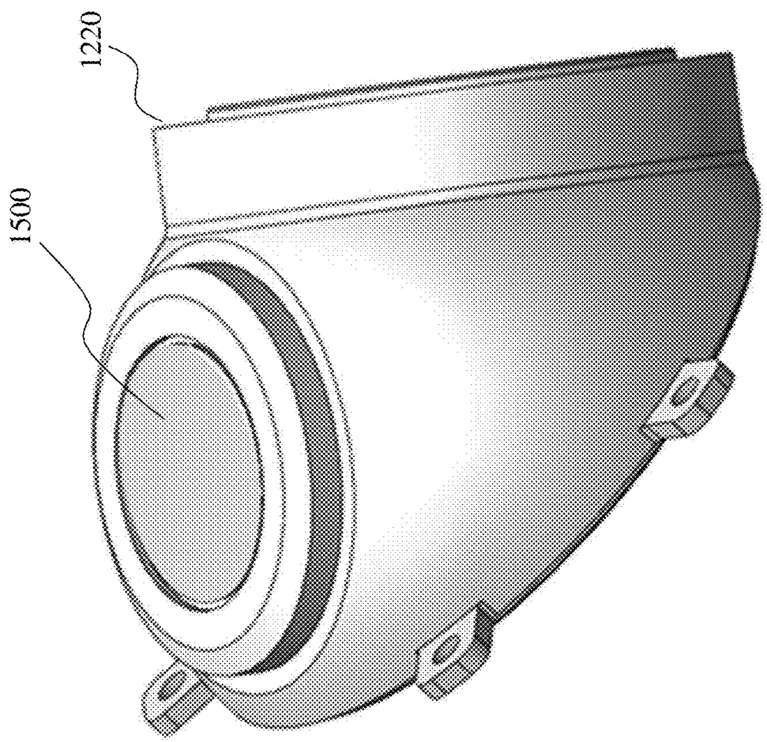

Figure 15C

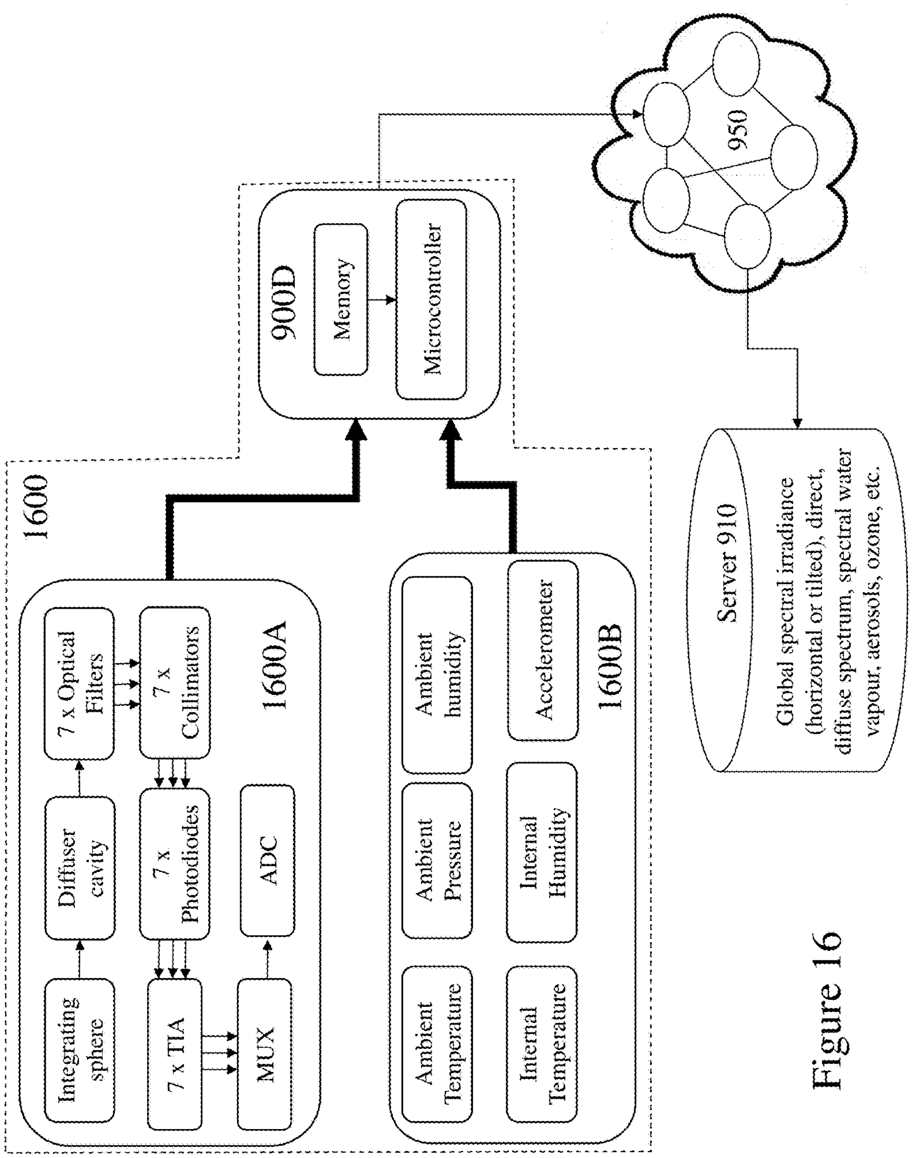
1600
Integrating sphere
Diffuser cavity
7 x Optical Filters
7 x Collimators
7 x Photodiodes
7 x TIA
MUX
ADC
1600A
Ambient Temperature
Ambient Pressure
Ambient humidity
Internal Temperature
Internal Humidity
Accelerometer
1600B
900D
Memory
Microcontroller
950
Server 910
Global spectral irradiance (horizontal or tilted), direct, diffuse spectrum, spectral water vapour, aerosols, ozone, etc.

Figure 16

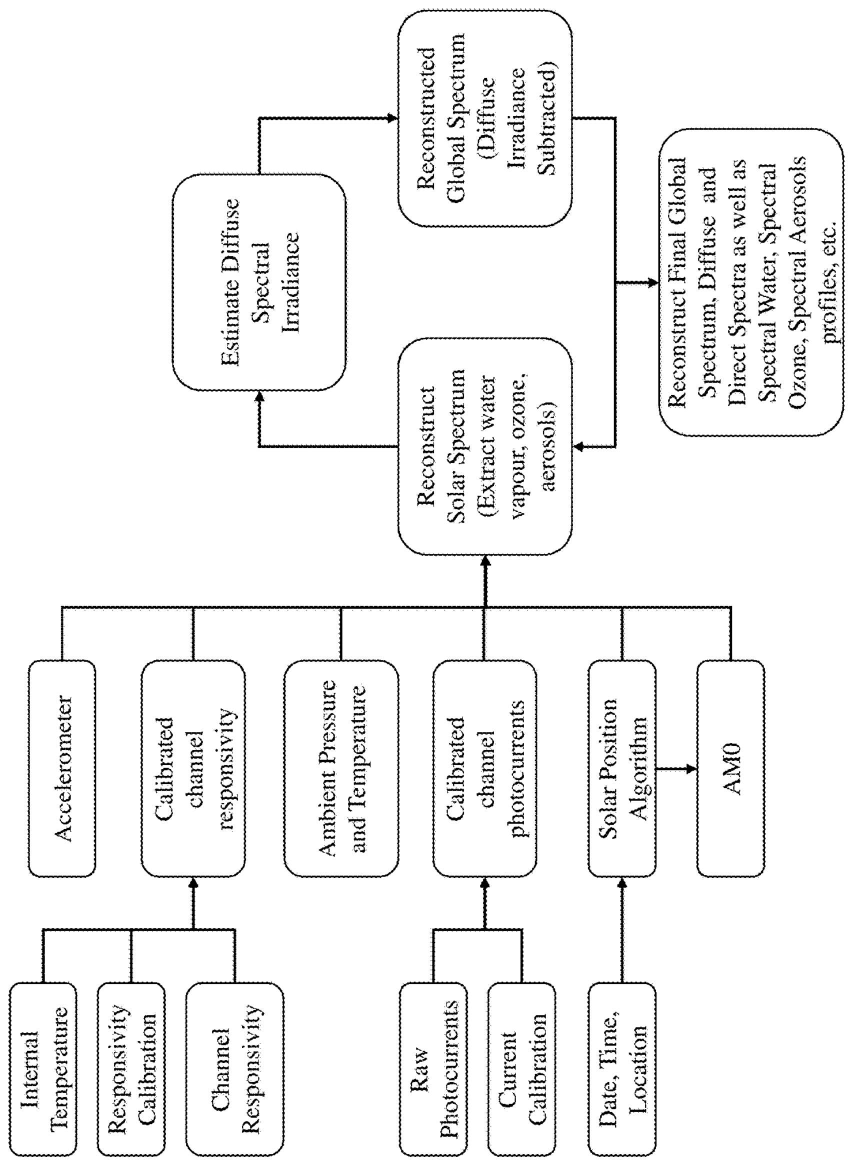
Internal Temperature
Responsivity Calibration
Channel Responsivity
Raw Photocurrents
Current Calibration
Date, Time, Location
Accelerometer
Calibrated channel responsivity
Ambient Pressure and Temperature
Calibrated channel photocurrents
Solar Position Algorithm
AM0
Reconstruct Solar Spectrum (Extract water vapour, ozone, aerosols)
Estimate Diffuse Spectral Irradiance
Reconstructed Global Spectrum (Diffuse Irradiance Subtracted)
Reconstruct Final Global Spectrum, Diffuse and Direct Spectra as well as Spectral Water, Spectral Ozone, Spectral Aerosols profiles, etc.

Figure 17

GLOBAL SOLAR SPECTRUM DEVICES AND METHODS

CROSS-REFERENCE TO RELATED APPLICATIONS

This specification claims the benefit of priority as a continuation patent application of U.S. patent application Ser. No. 15/769,601 filed Apr. 19, 2018 entitled "Global Solar Spectrum Devices and Methods" which itself claims priority as a 371 National Phase Entry application of PCT/CA2016/000,264 entitled "Global Solar Spectrum Devices and Methods" filed Oct. 20, 2016, which itself claims the benefit of priority from U.S. Provisional Patent Application 62/243,706 filed Oct. 20, 2015 entitled "Global Solar Spectrum Devices and Methods", the entire contents of each being incorporated herein by reference.

FIELD OF THE INVENTION

This invention relates to global solar spectral irradiance and more particularly to compact, no-moving part field deployable devices and methods of measuring and resolving global, direct and diffuse solar spectral irradiance, direct normal irradiance together with aerosol, water vapour and ozone spectral absorption profiles.

BACKGROUND OF THE INVENTION

Solar energy is the radiant light and heat from the Sun harnessed using a range of ever-evolving technologies such as solar heating, photovoltaics, solar thermal energy, solar architecture and artificial photosynthesis. It is an important source of renewable energy and its technologies are broadly characterized as either passive solar or active solar depending on the way they capture and distribute solar energy or convert it into solar power. Active solar techniques include the use of photovoltaic systems, concentrated solar power and solar water heating to harness the energy. Passive solar techniques include orienting a building to the Sun, selecting materials with favorable thermal mass or light dispersing properties, and designing spaces that naturally circulate air.

Photovoltaic cells, commonly referred to as solar cells, are electrical devices that convert incident light within their wavelength range of operation into electricity for immediate use or subsequent use through storage within a battery. Historically, two time-of-day dependent factors have complicated both the characterization of photovoltaic module and array performance and projected power generation in different deployment locations. These factors are the changes in the solar spectrum over the day and optical effects arising from solar angle-of-incidence. Accordingly, solar spectral irradiance (SSI) measurements are important for solar collector/photovoltaic panel efficiency and solar energy resource assessment. However, they are also important for scientific meteorological/climate observations and material testing research.

To date SSI measurements exploit modified scientific instruments based upon diffraction gratings and accordingly are generally defined by being bulky, expensive, and with low mechanical integrity for generalized deployment. Accordingly, it would be beneficial to provide a compact and cost-effective tool for accurately determining the global solar spectra as well as the global horizontal or tilted irradiances as part of on-site solar resource assessments and module performance characterization studies. It would be further beneficial for the tool to have no moving parts for

mechanical and environment stability in open field, non-controlled deployments and to exploit software to resolve the global, direct and diffuse solar spectra from its measurements within the 280-4000 nm spectral range, in addition to major atmospheric processes, such as air mass, Rayleigh scattering, aerosol extinction, ozone and water vapour absorptions.

Other aspects and features of the present invention will become apparent to those ordinarily skilled in the art upon review of the following description of specific embodiments of the invention in conjunction with the accompanying figures.

SUMMARY OF THE INVENTION

It is an object of the present invention to mitigate limitations within the prior art relating to global solar spectral irradiance and more particularly to compact, no-moving part field deployable devices and methods of measuring and resolving global, direct and diffuse solar spectral irradiance, together with aerosol, water vapour and ozone spectral absorption profiles.

In accordance with an embodiment of the invention there is provided a device comprising

a spherical diffuser comprising a spherical cavity within an outer body, the spherical cavity coated with a first near Lambertian material;

a first aperture of a first predetermined diameter formed in a first predetermined position on the spherical diffuser;

a second aperture of a second predetermined diameter formed in a second predetermined position on the spherical diffuser;

a baffle disposed in a predetermined relationship relative to the first aperture and the second aperture, the baffle having a predetermined thickness, is coated with a second near Lambertian material and is disposed on the inner surface of the spherical diffuser and having a geometry defining a predetermined portion of a sphere;

a plurality of optical collimators coupled to the second aperture and defining a maximum angular acceptance angle for each photodetector of a plurality of photodetectors disposed at the distal end of an optical collimator from that coupled to the second aperture; and

a plurality of optical filters, each filter having a passband of predetermined optical wavelengths and disposed in combination with an optical collimator of the plurality of collimators to filter optical signals exiting the second aperture.

In accordance with an embodiment of the invention there is provided a device comprising

a plurality of first photodetectors, each first photodetector receiving a predetermined wavelength range of the ambient optical environment via an optical path comprising a diffuser element, a bandpass filter, and an optical collimator to limit the angle of incident ambient light within a predetermined field of view;

a plurality of second photodetectors arranged radially around a post projecting above the upper surface of the plurality of second photodetectors; and

an electronic circuit comprising a first portion for digitizing a photocurrent for each first photodetector of the plurality of first photodetectors, a second portion for digitizing a photocurrent for each second photodetector of the plurality of second photodetectors, and a third portion for generating a reconstructed solar spectrum in dependence upon at least the digitized photocurrents of the plurality of first photodetectors, the digitized photocurrents of the plurality of second photodetectors, and a model of the solar spectrum with no atmosphere.

In accordance with an embodiment of the invention there is provided a device comprising:

a plurality of wavelength filtered photodetectors each receiving light from the ambient environment within a predetermined wavelength range and within a predetermined angle of incidence to the normal of the photodetector;

a plurality of second photodetectors each receiving light from the ambient environment;

a shadow pole disposed with respect to the plurality of second photodetectors; and

an optical element disposed on a front face of the device comprising:

a first uniform transparent region disposed in front of the plurality of second photodetectors and a second diffuser region comprising a plurality of features, each feature designed in dependence upon a predetermined wavelength associated with a wavelength filtered photodetector and the material from which the optical element is formed.

a transparent dome that sits above the front surface of the device and protects the diffuser, shadow pole and second plurality of photodiodes from the elements.

Other aspects and features of the present invention will become apparent to those ordinarily skilled in the art upon review of the following description of specific embodiments of the invention in conjunction with the accompanying figures.

BRIEF DESCRIPTION OF THE DRAWINGS

Embodiments of the present invention will now be described, by way of example only, with reference to the attached Figures, wherein:

FIG. **1** depicts a global solar spectral irradiance meter (SolarSIM-G) according to an embodiment of the invention with diffuser attached and removed;

FIG. **2** depicts exploded assembly views of the SolarSIM-G according to an embodiment of the invention depicted in FIG. **1**;

FIG. **3** depicts an exploded cross-sectional assembly view of the SolarSIM-G according to an embodiment of the invention depicted in FIG. **1**;

FIG. **4** depicts exploded views of the SolarSIM-G housing according to an embodiment of the invention depicted in FIG. **1**;

FIG. **5** depicts a plan view and cross-sectional perspective views of a diffuser plate according to an embodiment of the invention as employed within the SolarSIM-G according to an embodiment of the invention depicted in FIG. **1**;

FIG. **6** depicts a perspective view and cross-sectional perspective views of a shadow pole and photodetector element according to an embodiment of the invention as employed within the SolarSIM-G according to an embodiment of the invention depicted in FIG. **1**;

FIG. **7** depicts a perspective view and cross-sectional perspective views of a filter and enclosure according to an embodiment of the invention as employed within the SolarSIM-G according to an embodiment of the invention depicted in FIG. **1**;

FIG. **8**A depicts a perspective view and cross-sectional perspective views of a tube collimator according to an embodiment of the invention as employed within the SolarSIM-G according to an embodiment of the invention depicted in FIG. **1**;

FIG. **8**B depicts the optical path within an embodiment of the invention as employed within the SolarSIM-G according to an embodiment of the invention depicted in FIG. **1**;

FIG. **9** depicts an assembly structure and data flow for a SolarSIM-G according to an embodiment of the invention depicted in FIG. **1**;

FIG. **10** depicts a processing flow for result generation for a SolarSIM-G according to an embodiment of the invention depicted in FIG. **1**;

FIG. **11** depicts a global solar spectral irradiance meter (SolarSIM-G) according to an embodiment of the invention with protective dome and outer mechanical housing attached and removed;

FIG. **12** depicts exploded views of the SolarSIM-G housing according to an embodiment of the invention depicted in FIG. **11**;

FIG. **13** depicts an exploded cross-sectional assembly view of the SolarSIM-G according to an embodiment of the invention depicted in FIGS. **11** to **12**;

FIG. **14** depicts exploded and exploded cross-section assembly views of the optical diffuser-filter-optical collimator elements within the SolarSIM-G according to an embodiment of the invention depicted in FIGS. **11** to **13**;

FIG. **15**A depicts a cross-section assembly view of the optical sub-assembly comprising optical diffuser-filter-optical collimator-and photodetector elements within the SolarSIM-G according to an embodiment of the invention depicted in FIGS. **11** to **14**;

FIG. **15**B depicts a single ray tracing within a SolarSIM-G according to an embodiment of the invention depicted in FIGS. **11** to **14**;

FIG. **15**C depicts a SolarSIM-G according to an embodiment of the invention.

FIG. **16** depicts an assembly structure and data flow for a SolarSIM-G according to an embodiment of the invention depicted in FIG. **11**; and

FIG. **17** depicts a processing flow for result generation for a SolarSIM-G according to an embodiment of the invention depicted in FIG. **11**.

DETAILED DESCRIPTION

The present invention is directed to global solar spectral irradiance and more particularly to compact, no-moving part field deployable devices and methods of measuring and resolving global, direct and diffuse solar spectral irradiance, together with aerosol, water vapour and ozone spectral absorption profiles.

The ensuing description provides representative embodiment(s) only, and is not intended to limit the scope, applicability or configuration of the disclosure. Rather, the ensuing description of the embodiment(s) will provide those skilled in the art with an enabling description for implementing an embodiment or embodiments of the invention. It being understood that various changes can be made in the function and arrangement of elements without departing from the spirit and scope as set forth in the appended claims. Accordingly, an embodiment is an example or implementation of the inventions and not the sole implementation. Various appearances of "one embodiment," "an embodiment" or "some embodiments" do not necessarily all refer to the same embodiments. Although various features of the invention may be described in the context of a single embodiment, the features may also be provided separately or in any suitable combination. Conversely, although the invention may be described herein in the context of separate embodiments for clarity, the invention can also be implemented in a single embodiment or any combination of embodiments.

Reference in the specification to "one embodiment", "an embodiment", "some embodiments" or "other embodiments" means that a particular feature, structure, or characteristic described in connection with the embodiments is included in at least one embodiment, but not necessarily all embodiments, of the inventions. The phraseology and terminology employed herein is not to be construed as limiting but is for descriptive purpose only. It is to be understood that where the claims or specification refer to "a" or "an" element, such reference is not to be construed as there being only one of that element. It is to be understood that where the specification states that a component feature, structure, or characteristic "may", "might", "can" or "could" be included, that particular component, feature, structure, or characteristic is not required to be included.

Reference to terms such as "left", "right", "top", "bottom", "front" and "back" are intended for use in respect to the orientation of the particular feature, structure, or element within the figures depicting embodiments of the invention. It would be evident that such directional terminology with respect to the actual use of a device has no specific meaning as the device can be employed in a multiplicity of orientations by the user or users. Reference to terms "including", "comprising", "consisting" and grammatical variants thereof do not preclude the addition of one or more components, features, steps, integers or groups thereof and that the terms are not to be construed as specifying components, features, steps or integers. Likewise, the phrase "consisting essentially of", and grammatical variants thereof, when used herein is not to be construed as excluding additional components, steps, features integers or groups thereof but rather that the additional features, integers, steps, components or groups thereof do not materially alter the basic and novel characteristics of the claimed composition, device or method. If the specification or claims refer to "an additional" element, that does not preclude there being more than one of the additional element.

A "portable electronic device" (PED) as used herein and throughout this disclosure, refers to a wireless device used for communications and other applications that requires a battery or other independent form of energy for power. This includes devices, but is not limited to, such as a cellular telephone, smartphone, personal digital assistant (PDA), portable computer, pager, portable multimedia player, portable gaming console, laptop computer, tablet computer, a wearable device and an electronic reader.

A "fixed electronic device" (FED) as used herein and throughout this disclosure, refers to a wireless and/or wired device used for communications and other applications that requires connection to a fixed interface to obtain power. This includes, but is not limited to, a laptop computer, a personal computer, a computer server, a kiosk, a gaming console, a digital set-top box, an analog set-top box, an Internet enabled appliance, an Internet enabled television, and a multimedia player.

A "server" as used herein, and throughout this disclosure, refers to one or more physical computers co-located and/or geographically distributed running one or more services as a host to users of other computers, PEDs, FEDs, etc. to serve the client needs of these other users. This includes, but is not limited to, a database server, file server, mail server, print server, web server, gaming server, or virtual environment server.

An "application" (commonly referred to as an "app") as used herein may refer to, but is not limited to, a "software application", an element of a "software suite", a computer program designed to allow an individual to perform an activity, a computer program designed to allow an electronic device to perform an activity, and a computer program designed to communicate with local and/or remote electronic devices. An application thus differs from an operating system (which runs a computer), a utility (which performs maintenance or general-purpose chores), and programming tool (with which computer programs are created). Generally, within the following description with respect to embodiments of the invention an application is generally presented in respect of software permanently and/or temporarily installed upon a PED and/or FED.

"Electronic content" (also referred to as "content" or "digital content") as used herein may refer to, but is not limited to, any type of content that exists in the form of digital data as stored, transmitted, received and/or converted wherein one or more of these steps may be analog although generally these steps will be digital. Forms of digital content include, but are not limited to, information that is digitally broadcast, streamed or contained in discrete files. Viewed narrowly, types of digital content include popular media types such as MP3, JPG, AVI, TIFF, AAC, TXT, RTF, HTML, XHTML, PDF, XLS, SVG, WMA, MP4, FLV, and PPT, for example, as well as others, see for example http://en.wikipedia.org/wiki/List_of_file_formats. Within a broader approach digital content mat include any type of digital information, e.g. digitally updated weather forecast, a GPS map, an eBook, a photograph, a video, a Vine™, a blog posting, a Facebook™ posting, a Twitter™ tweet, online TV, etc. The digital content may be any digital data that is at least one of generated, selected, created, modified, and transmitted in response to a user request, said request may be a query, a search, a trigger, an alarm, and a message for example.

A "scaffold" or "scaffolds" as used herein, and throughout this disclosure, refers to a structure that is used to hold up, interface with, or support another material or element(s). This includes, but is not limited to, such two-dimensional (2D) structures such as substrates and films, three-dimensional (3D) structures such as geometrical objects, non-geometrical objects, combinations of geometrical and non-geometrical objects, naturally occurring structural configurations, and manmade structural configurations. A scaffold may be solid, hollow, and porous or a combination thereof. A scaffold may contain recesses, pores, openings, holes, vias, and channels or a combination thereof. A scaffold may be smooth, textured, have predetermined surface profiles and/or features. A scaffold may be intended to support one or more other materials, one or more films, a multilayer film, one type of particle, multiple types of particles etc. A scaffold may include, but not be limited to, a spine of a device and/or a framework, for example, which also supports a shell and/or a casing.

A "shell" as used herein, and throughout this disclosure, refers to a structure that is used to contain and/or surround at least partially and/or fully a number of elements within a device according to embodiments of the invention. A shell may include, but not limited to, a part or parts that are mounted to a scaffold or scaffolds that support elements within a device according to an embodiment of the invention.

A "casing" as used herein, and throughout this disclosure, refers to a structure surrounding a scaffold and/or shell. This includes structures typically formed from an elastomer and/

or silicone to provide a desired combination of properties to the device it forms part of and other properties including, but not limited to, hermeticity, liquid ingress barrier, solid particulate ingress barrier, surface sheen, physical tactile surface, and colour. A casing may include, but not limited to, a part or parts that are mounted to a scaffold or scaffolds and/or a casing or casings forming part of a device according to an embodiment of the invention.

A "polyester" as used herein, and throughout this disclosure, refers to a category of polymers that contain the ester functional group in their main chain. This includes, but is not limited to polyesters which are naturally occurring chemicals as well as synthetics through step-growth polymerization, for example. Polyesters may be biodegradable or not. Polyesters may be a thermoplastic or thermoset or resins cured by hardeners. Polyesters may be aliphatic, semi-aromatic or aromatic. Polyesters may include, but not be limited to, those exploiting polyglycolide, polylactic acid (PLA), polycaprolactone (PCL), polyhydroxyalkanoate (PHA), polyhydroxybutyrate (PHB), polyethylene adipate (PEA), polybutylene succinate (PBS), polyethylene terephthalate (PET), polybutylene terephthalate (PBT), polytrimethylene terephthalate (PTT), and polyethylene naphthalate (PEN).

A "thermoplastic" or "thermosoftening plastic" as used herein and throughout this disclosure, refers to a category of polymers that become pliable or moldable above a specific temperature and solidify upon cooling. Thermoplastics may include, but not be limited, polycarbonate (PC), polyether sulfone (PES), polyether ether ketone (PEEK), polyethylene (PE), polypropylene (PP), poly vinyl chloride (PVC), polytetrafluoroethylene (PTFE), polyimide (PI), polyphenylsulfone (PPSU), polychlorotrifluoroethene (PCTFE or PTFCE), florinated ethylene propylene (FEP), and perfluoroalkoxy alkane (PFA).

A "metal" as used herein, and throughout this disclosure, refers to a material that has good electrical and thermal conductivity. Such materials may be malleable and/or fusible and/or ductile. Metals may include, but not be limited to, aluminum, nickel, copper, cobalt, chromium, silver, gold, platinum, iron, zinc, titanium, and alloys thereof such as bronze, stainless steel, brass, and phosphor bronze.

A "silicone" as used herein, and throughout this disclosure, refers to a polymer that includes any inert, synthetic compound made up of repeating units of siloxane.

An "elastomeric" material or "elastomer" as used herein, and throughout this disclosure, refers to a material, generally a polymer, with viscoelasticity. Elastomers may include, but not be limited to, unsaturated rubbers such as polyisoprene, butyl rubber, ethylene propylene rubber, silicone rubber, fluorosilicone rubber, fluoroelastomers, perfluoroelastomers, and thermoplastic elastomers.

A global spectral irradiance meter (SolarSIM-G) is an instrument for resolving the global, direct and diffuse solar spectral irradiance together with aerosol, water vapour and ozone spectral absorption profiles over a predetermined wavelength range, for example 280 nm≤λ≤4000 nm as described below with respect to the embodiment of the invention depicted in FIGS. **1** to **10**. Accordingly, the SolarSIM-G according to embodiments of the invention combines capabilities from multiple instruments such as a spectroradiometer, pyranometer, sun photometer, pyheliometer and a weather station all in one single compact housing. As described below in respect of an embodiment of the invention in FIGS. **1** to **10** the SolarSIM-G provides six spectral channels although it would be evident that more or less spectral channels can be implanted although, typically, reductions will result in corresponding performance and/or feature reduction. Accordingly, a SolarSIM-G according to an embodiment of the invention comprises:

a plurality of spectral channels in conjunction with custom shaped mini-diffusers for each spectral channel to optimize its cosine response;

a diffuse light sensor;

other ambient environmental sensors as measure inputs; and

software algorithm that resolves the global, direct, and diffuse solar spectra, along with spectral, atmospheric aerosol, water vapour and ozone transmission profiles.

As will become evident from the description below in respect of FIGS. **1** to **9** each spectral channel comprises a photodiode-collimation tube-band pass filter combination which limits the field of view that each photodiode senses from the filter. This eliminates high incident angle light from hitting the photodiodes which eliminates the central wavelength shift that the band-pass filters exhibit with high incident angle light.

As will become evident from the description below in respect of FIGS. **1** to **9** the diffuse irradiance sensor consists of a shadow pole surrounded by several small photodiodes that enable the device to estimate the ratio of diffuse/global light and estimate the diffuse irradiance. The knowledge of diffuse to global ratio allows the SolarSIM-G to actively correct for the cosine response of the instrument and aids the software algorithm in resolving the global, direct and diffuse solar spectra.

Referring to FIG. **1** there are depicted first and second three-dimensional (3D) perspective views **100**A and **100**B respectively of a SolarSIM-G according to an embodiment of the invention with and without the front diffuser plate attached. In FIG. **2** first and second 3D perspective views **200**A and **200**B respectively are depicted of the SolarSIM-G as an exploded assembly. The SolarSIM-G depicted in FIGS. **1** to **3** being a 6 channel design operating over a predetermined wavelength range, e.g. 280 nm≤λ≤4000 nm. Accordingly, the descriptions in respect of FIGS. **2-9** reflect this 6 channel design but it would be evident to one of skill in the art that alternate embodiments with varying channel counts may be implemented. Similarly, it would be evident that elements such as the diffuse light sensor may be omitted. As depicted the elements include

Diffuser plate **270**;

Optical bandpass interference filters **260**;

Diffuse Light and Temperature Sensor (DILITS) **280**;

Enclosure **250**

Collimation tube **230**;

Main PCB **220**;

Ambient environment sensor **290**;

Backplate **210**, and

Waterproof membrane vent **240**.

Now referring to FIG. **4** there are depicted first and second 3D perspective views **400**A and **400**B respectively of the SolarSIM-G external housing elements which provide the exterior surfaces of the SolarSIM-G and the barriers to direct ingress etc. both directly and at their interfaces. These external housing elements comprising baseplate **210**, enclosure **250**, and diffuser plate **270**. As depicted the enclosure **250** forms the majority of the external housing to which the diffuser plate **270** mounts on the top and the baseplate **210** to the bottom.

The diffuser plate **270** receives the light from an entire hemisphere and scatters it an all directions (forward and backward). For the optical wavelength range of 280 nm≤λ≤4000 nm, for this embodiment of the invention, PTFE or Teflon™ are examples of materials for forming the diffuser. The diffuser plate **270** scatters the light incident on the upper face of the SolarSIM-G and is required to scatter independently of incident angle such that the light to a photodetector is coupled at all incident angles in order to achieve a good cosine response. Without a diffuser plate **270**, at large incident angles the light would be mostly reflected and would not be detected, and a cosine response is not achieved. The SolarSIM-G diffuser plate **270**, as pictured in FIG. **5** in first to third views **500**A to **550**C provides a dual functionality. It acts as a front cover for the shadow pole and photodetectors and a diffuser for the wavelength selective photodetectors at the same time. The six protruding areas **520** of the diffuser body **510** are diffusers for each wavelength filter within the SolarSIM-G. The geometry of these six mini-diffusers is optimized to achieve the best cosine response for its corresponding wavelength range of interest. Each filter therefore has a specific diffuser **520** design in the embodiment depicted. However, in other embodiments of the invention depending upon the design of the diffuser and the optical properties of the different diffuser designs may be required or in some embodiments may not be required for one, two or more of the wavelength channels. The window **530** within the diffuser plate **270** is transparent and provides a cover to the shadow pole and its associated photodetectors.

Within embodiments of the invention the diffuser plate **270** may be formed from an optically transparent material over the wavelength range of interest and the protruding areas **520** are made diffusing through processing of the material, e.g. sandblasting, etching etc. leaving the window **530** transparent. Alternatively, the body of the diffuser element may be formed from a diffusing but optically transparent material over the wavelength range of interest and the window **530** is formed from a separate material which is clear and optically transparent material over the wavelength range of interest.

Within other embodiments of the invention the SolarSIM-G diffuser plate **270** may be formed from other materials transparent over the wavelength range of interest such as a glass for example. Optionally, the SolarSIM-G diffuser plate **270** may be formed from two or more elements rather than a single piece or even different diffuser elements per channel. In other embodiments the diffuser may be transparent and may be frosted and/or translucent.

As depicted in FIGS. **1** to **9** the SolarSIM-G employs six channels with center wavelengths (CWLs) at approximately 410-430 nm, 480-505 nm, 600-620 nm, 670-690 nm, 860-880 nm, and 930-960 nm. Further, the region of the diffuser body **510** above the DILITS **280**, depicted as area **530**, may be flat, as depicted, or alternatively employ a surface profile. As evident in second view **500**B with cross-section X-X the inner surface of the diffuser body **510** there is a recess to align each filter with its respective mini-diffuser. Further, as evident in third view **500**C with cross-section Y-Y the region of the diffuser body **510** above the DILITS **280** is also recessed.

The DILITS **280** within the SolarSIm-Gas depicted in FIGS. **1** to **4** allows the G-SolarSIM to determine the ratio of the global incident irradiance versus the diffuse irradiance. As depicted in FIG. **6** with 3D perspective view **600**A and cross-sectional 3D perspective view **600**B this is accomplished through the use of a shadow pole **750** (protruding metallic piece) formed within the upper surface of the external enclosure together with a recess **730** into which the DILITS **280** sits. The shadow pole **750** projects through an opening **640** within the DILITS **280** and is surrounded by several small photodetectors **630** which are mounted to a PCB **610** which forms the bulk of the DILITS **280**. Optionally, the small photodetectors **630** may be replaced by one or more detector arrays. Throughout the day, the sun's apparent motion in the sky causes the shadow pole **750** to cast its shadow onto different photodiodes **630**. This blocks the direct beam of sunlight from those photodiodes **630** that are shadowed, and we can effectively estimate the diffuse irradiance in relative terms. Optionally, the region of the diffuser body **510** over the DILITS **280** may be transparent rather than diffusing or translucent. The photodetectors **630** that are not covered by the shadow report the global irradiance (diffuse+direct beam irradiance) whilst those that are covered report the diffuse beam irradiance. The ratio of the two provides information about the magnitude of the diffuse irradiance and the atmospheric conditions. For example, on a very cloudy day, we can expect the readings from each photodetector to be approximately the same. On a clear day, the shadowed photodetectors will report low irradiance, whilst the others will report relatively high irradiance.

The knowledge of the diffuse to direct beam ratio is important for several reasons. The active cosine response correction can be performed on the instrument if this ratio is known. Under laboratory conditions, the instruments cosine response is determined by having a nearly collimated light source shine light onto the instrument at various angles. The response of the instrument is compared against an ideal cosine response and a correction is obtained. However, under outdoor conditions, the instrument does not "know" how much light is coming directly at some angles versus the other angles. By establishing the direct to diffuse ratio we can accurately determine how much light is coming from the direct beam irradiance as we know the position of the sun at all times throughout the day.

The shadow pole is positioned "behind" the filters to eliminate the shadowing of the filters at low solar elevations angles. Within an embodiment of the invention, the shadow pole is oriented due north, while the arrow like arrangement of the filters points to the south. The DILITS **280** also includes a temperature sensor **620** for adjusting the transmission of the diffuser for temperature. It is conveniently positioned on the diffuse light sensor PCB **610**, which is connected to the main PCB **220**.

The enclosure **250** provides the means to hold everything together and protects components from the weather elements. The enclosure **250** as depicted in FIGS. **1** to **4** is depicted in 3D perspective view **700**A and first and second cross-section 3D perspective views **700**B and **700**C respectively in FIG. **7**. As depicted the upper outer surface comprises the recess **730** within which is shadow pole **750** as well as opening **760**. Also depicted are the six filter recesses **720** within each of which is an aperture **740**. The upper surface also contains an O-ring slot for the insertion/placement of an O-ring between the enclosure and the diffuser which allows the diffuser to seal the enclosure against moisture and debris ingress. The enclosure also has a cavity for desiccant to regulate the humidity inside the device.

Each of the bandpass interference filters pass a narrow band of light to the photodiode around their CWL. For the embodiment described in respect of FIGS. **1** to **9** these CWLs are at approximately 410-430 nm, 480-505 nm, 600-620 nm, 670-690 nm, 860-880 nm, and 930-960 nm respectively. These can be off-the-shelf hard-coated and rugged filters capable of withstanding outdoor environments. Within the embodiment of the invention described with respect to FIGS. **1** to **9** the filters are circular and may be discrete or within a housing wherein the geometry and depth of the recesses on the enclosure and diffuser adapt to suit.

Within the enclosure as depicted in FIGS. **2** to **3** sits a collimation tube **230** as depicted by 3D perspective view **800**A, end-view **800**B, and first and second cross-sections **800**C and **800**D representing cross-sections X-X and Y-Y respectively. The function of the collimation tube **230** is to limit the photodiodes view to light within a specific range of angular incidence. The bandpass interference filters are designed to operate at normal incidence. The center wavelength blue-shifts (approaches UV spectral range) as the incidence angle increases. However, most bandpass interference filters exhibit negligible shift up at angles of incidence of 0°-10°. Therefore, the purpose of the collimation tube is to "filter out" the light for angles greater than near optimal angle of acceptance (which depends on the filter specifications).

The collimation tube **230** is coated to minimize absorption across the wavelengths of interest, namely 280 nm≤λ≤4000 nm. For example, an aluminium baffle with black anodizing provides one physical embodiment. Each collimation tube comprises a tube within which are baffles in order to prevent light reflecting off the walls and onto the detectors. The walls may also be threaded or have their surfaces modified to minimize specular reflections. Since the collimation tube **230** is a separate component to the enclosure, the latter doesn't have to be black anodized or treated in the same manner to absorb light.

The optical path is shown in FIG. **8**B where the incoming light undergoes the following transformation:

- the diffuser **520** scatters the light in all directions
- the scattered light passes through the filter **860**
- the filtered scattered light is limited by the front aperture **740**;
- the remaining light that has the right incidence angle passes through the baffle **850** and hits the active area of the associated photodiode **870**.

The photodetectors **870** are electrically coupled to a main PCB **220** which is positioned at the bottom of the collimation tube **230** and retained together with the collimation tube **230** by the enclosure **250** and back plate **210**. The enclosure **250** and back plate may be similarly designed with an O-ring seal and screw/bolt mounting as the diffuser plate **270** is attached to the enclosure **250** although other liquid and particle barriers may be employed within other embodiments of the invention such as soldering the back plate **210** onto the enclosure **250** or employing a gasket between the enclosure **250** and the back plate **210**. The main PCB **220** provides all of the analog data acquisition and passes this information through a communications protocol to a host. For example, an RS-485 communication protocol may be employed from the SolarSIM-G to a host computer. However, it would be evident that the SolarSIM-G and host computer may be linked by other wired and wireless protocols including but not limited to IEEE 802.11, IEEE 802.15, IEEE 802.16, IEEE 802.20, UMTS, GSM 850, GSM 900, GSM 1800, GSM 1900, GPRS, ITU-R 5.138, ITU-R 5.150, ITU-R 5.280, IMT-1000, DSL, Dial-Up, DOCSIS, Ethernet, G.hn, ISDN, MoCA, PON, and Power line communication (PLC). Optionally, the host computer may be associated with an installation, for example, of which the SolarSIM-G forms part. In other embodiments of the invention the host may be remote and, in some instances, may be a remote server rather than a remote computer.

Also connected to the main PCB **220** are the diffuse light sensor PCB **610** and ambient environment PCB **290**, the latter of which senses ambient temperature, pressure and humidity. The later, in order to accomplish the desired measurement is connected to a waterproof membrane vent **240** that allows ambient air to pass through but not water. The ambient PCB **220** monitoring the environment is sealed with silicone or O-ring to the waterproof membrane vent **240** which may also provide for pressure equalization between the inner environment of the SolarSIM-G and ambient external environment.

Within embodiments of the invention an outer protective cover, e.g. dome, may be deployed to protect the diffuser element from the ambient environment. This outer protective cover being designed such that it allows the sunlight to impinge upon the shadow pole and the plurality of detectors around the shadow pole in addition to the collimator tubes for the wavelength filtered channels. Within embodiments of the invention with a dome it would be evident that the diffuser element may be designed according to different design guidelines as the diffuser element is now not providing environmental protection. Accordingly, the window (e.g. window **530** in FIG. **5**) may be omitted such that no other element is disposed between the shadow pole and the dome. In this instance the diffuser element (e.g. diffuser element **510**) may be disposed to only cover part of the upper surface of the SolarSIM-G. Optionally, the diffuser structures, e.g. protruding areas **520**, may be disposed only within the collimator tube openings or within and around the collimator tubes.

Optionally, a fan may be disposed to blow periodically and/or continuously across the outside of the outer protective cover in order to mitigate soiling.

Now referring to FIG. **9** there is depicted an exemplary system block diagram of a SolarSIM-G according to an embodiment of the invention as depicted in FIGS. **1** to **8** respectively comprising first to fourth functional blocks **900**A to **900**D respectively. As depicted first functional block **900**A relates to the multiple wavelength channels and consists for each wavelength a mini-diffuser, optical filter, optical collimator (tube) collimator, photodiode and multiplexer. The output of the multiplexer is coupled to a transimpedance amplifier (TIA) and converted to digital form via an analog-to-digital converter (ADC). The output of the ADC is coupled to the electronic functional block **900**D. Within another embodiment of the invention each photodetector has an associated TIA and the multiple TIA outputs are multiplexed for the ADC or multiple ADCs.

Second functional block **900**B relates to diffuse/direct irradiance and comprises the diffuser, shadow pole, photodetectors around the shadow pole, wherein the photodetector outputs are multiplexed and coupled to the TIA and converted to digital form via an analog-to-digital converter (ADC). Optionally, the photodetector outputs are coupled to TIAs and then multiplexed to one or more ADCs. The output of the ADC is coupled to the electronic functional block **900**D. Third functional block **900**C relates to the other sensors including, but not limited to, ambient temperature, pressure, humidity, diffuser temperature, internal temperature, and accelerometer. The outputs of these being also coupled to the electronic functional block **900**D.

The electronic functional block **900**D therefore receives multiplexed digital data relating to the multiple wavelength channels, multiplexed data relating the photodiodes around the shadow pole, and digital data from multiple environmental sensors. These are processed by a microcontroller within the electronic functional block **900**D via a software algorithm or software algorithms stored in memory associated with the microcontroller. The electronic functional block **900**D also implements one or more communication protocols such that the raw and/or processed data are pushed to or pulled to a host computer, in this instance a remote server **910** via a network **950**. The remote server **910** processes the data from the SolarSIM-G or stores processed data from the SolarSIM-G. This data may include, but is not limited to, global spectral irradiance (horizontal or titled), direct spectrum, diffuse spectrum, spectral water vapour, aerosols, and ozone absorption profiles.

A software block diagram for the software algorithm of a SolarSIM-G is depicted in FIG. **10**. As indicated all of the inputs on the left are fed to a series of initial processing algorithms and subsequent reconstruction algorithms in order to resolve the global, direct and diffuse solar spectrum. Accordingly, as indicated the channel responsivity is derived in dependence upon the internal SolarSIM-G temperature, the channel calibration, the nominal channel responsivity and the diffuser temperature. The raw digitized photocurrents and current calibration data are used, with or without the diffuse to global irradiance ratio to generate (final) calibrated channel data. This diffuse to global irradiance ratio being generated in dependence upon the shadow pole photodetector currents, their calibration data, and solar position data derived from a solar position algorithm exploiting date, time, and location data. This solar position data also defines the air mass zero (AM0) spectrum which is that of the sun with no intervening atmosphere. These outputs are combined with accelerometer, ambient pressure and ambient temperature in an initial algorithm to derive a reconstructed solar spectrum with extracted water vapour, aerosols, and ozone as a result of the wavelengths selected for the six channels.

Next the diffuse spectral irradiance is estimated and then employed to generate a refined reconstructed solar spectrum which is then employed to reconstruct the final global spectrum, diffuse and direct spectra as well as the atmospheric absorption profiles for water, ozone, and aerosols.

As the global spectrum is a combination of the direct and the diffuse spectral irradiances, the first reconstruction will not be perfect, as we are not taking the diffuse irradiance into account. However, the reconstructed proxy spectrum allows estimating the aerosols, water vapour and ozone content in the atmosphere, which in turn allow a better approximation of the diffuse irradiance (which is further enhanced by the global to diffuse ratio as determined by the shadow pole photodiodes). The approximated diffuse irradiance is then subtracted from the proxy global solar spectrum and reconstruction is performed once again, which gives the direct component of the global spectral irradiance. Addition of the estimated diffuse spectral irradiance to the direct component yields the global spectral irradiance.

The embodiment of the invention described and depicted in respect of FIG. **9** exploits six wavelength channels at CWLs of 410-430 nm, 480-505 nm, 600-620 nm, 670-690 nm, 860-880 nm, and 930-960 nm. Referring to Table 1 the association of these wavelengths to atmospheric components are listed.

TABLE 1

Bandpass Filter CWL Association to Atmospheric Components

Channel CWL (nm)	Atmospheric Component
410-430	Aerosols
480-505	Aerosols
600-620	Ozone

TABLE 1-continued

Bandpass Filter CWL Association to Atmospheric Components

Channel CWL (nm)	Atmospheric Component
670-690	Aerosols
860-880	Aerosols
820-850, 930-960	Water vapour

For aerosols, other wavelengths may be considered including, for example, CWLs of 770-790 nm, 1040-1060 nm, 1240-1260 nm, and 1640-160 nm. Beneficially, wavelengths below approximately 1100 nm can be detected with silicon photodetectors whereas longer wavelengths require germanium (Ge) or indium gallium arsenide (InGaS) photodetectors.

Now referring to FIG. **11** there are depicted first and second three-dimensional (3D) perspective views **1100**A and **1110**B respectively of a SolarSIM-G according to an embodiment of the invention with and without a protective dome and outer mechanical housing attached. Disposed within the top surface of the SolarSIM-G depicted in first and second 3D perspective views **1100**A and **1110**B respectively are tilt bubble **1310** and solar noon indicator **1110**. The solar noon indicator **1110** must be positioned so that it points toward the solar noon at the location of the SolarSIM-G installation, for example due south in the northern hemisphere. It would be evident from FIG. **12** that the optical train from the integrating sphere (spherical diffuser) lies along this line such that the optical collimators are aligned north-south.

In FIG. **12** first and second 3D perspective views **1200**A and **1200**B respectively are depicted of the SolarSIM-G of FIG. **11** as an exploded assembly from two different perspective viewpoints. The SolarSIM-G depicted in FIGS. **11** and **12** being a 7 channel design operating over a predetermined wavelength range, e.g. 280 nm≤λ≤4000 nm. Accordingly, the descriptions in respect of FIGS. **13** to **17** reflect this 7 channel design but it would be evident to one of skill in the art that alternate embodiments with varying channel counts may be implemented. Accordingly, as depicted within FIG. **12** and first perspective view **1200**A the elements include

Protective dome **1210**;
Upper diffuser body **1220**;
Lower diffuser body **1225**;
Outer mechanical housing **1230**;
Electrical connector **1235**;
Electrical circuit board **1240**;
Ambient environment sensor(s) **1245**;
Mounting plate **1250**;
SolarSIM-G base plate **1255**;
Optical filter assembly **1260**;
First optical collimator element **1270**;
Second optical collimator element **1280**; and
Photodetector circuit board **1290**.

FIG. **13** depicts an exploded cross-sectional assembly view of the SolarSIM-G according to an embodiment of the invention depicted in FIGS. **11** and **12** where the outer mechanical housing **1230** and protective dome **1210** are depicted in correct physical relationship rather than for compact presentation in FIG. **12**. Accordingly, as depicted these elements are:

Protective dome **1210**;
Tilt bubble **1310**;
Outer mechanical housing **1230**;
Upper diffuser body **1220**;

Lower diffuser body **1225**;
Electrical connector **1235**;
Electrical circuit board **1240**;
Gore™ vent **1320**;
O-ring **1330**;
SolarSIM-G base plate **1255**;
Mounting plate **1250**;
Optical filter assembly **1260**;
First optical collimator element **1270**;
Second optical collimator element **1280**; and
Photodetector circuit board **1290**.

FIG. **14** depicts exploded cross-section assembly views of the optical diffuser-filter-optical collimator elements within the SolarSIM-G according to an embodiment of the invention depicted in FIG. **11** wherein each optical filter assembly **1260** comprises an optical filter **1260**B within a housing **1260**A. In contrast FIG. **15**A depicts a cross-section assembly view of the optical sub-assembly comprising optical diffuser-filter-optical collimator-and photodetector elements within the SolarSIM-G according to an embodiment of the invention depicted in FIGS. **11** to **14** respectively allowing the optical path from external ambient environment to each of the photodetectors **1560** on the photodetector circuit board **1290**. Also depicted is the internal temperature sensor **1590**.

Now referring to FIG. **15**B a single normal incident axial ray is traced within the optical assembly. Accordingly, light from the ambient environment passes through the protective dome **1210** and a portion of this light will pass through the precision aperture **1510** formed from aperture ring **1570** fitted to the upper diffuser body **1220**. Accordingly, this light therefore reflects and diffuses within the integrating sphere (spherical diffuser) formed from the mating of upper diffuser body **1220** and lower diffuser body **1225** before exiting through outlet aperture **1520** formed in the lateral wall of the upper diffuser body **1220** into diffuser cavity **1530** formed by the first optical collimator element **1270** and the outer wall of the upper diffuser body **1220**.

Disposed within the region around the lower half of the outlet aperture **1520** is diffuser baffle **1580** which prevents direct reflective paths from the precision aperture **1510** to the outlet aperture. The inner surfaces of the integrating sphere (spherical diffuser) formed by the mating of upper diffuser body **1220** and lower diffuser body **1225** are within an embodiment of the invention coated with a paint providing broad spectral Lambertian-like light diffusion across the wavelength range of interest, e.g. a white paint. Within other embodiments of the invention these inner surfaces may be roughened via sand blasting, for example, rather than as machined.

The light within the diffuser cavity **1530**, which may be similarly coated and treated as the inner surfaces of the integrating sphere (spherical diffuser), is then coupled via the optical collimator formed by the first and second optical collimator elements **1270** and **1280** respectively to each photodetector **1560** and their associated electronics on photodetector circuit board **1290**. Disposed within each optical collimator formed by the first and second optical collimator elements **1270** and **1280** respectively is an optical filter **1260**B within its housing **1260**A. Within the first and second optical collimator elements **1270** and **1280** respectively are first and second collimator apertures **1540** and **1550**. Accordingly, the overall combination of optical elements provides the desired cosine response in respect of the performance of the SolarSIM-G.

Now referring to FIG. **15**C there is depicted a variant of the SolarSIM-G depicted in FIGS. **11** to **15**B wherein the precision optical aperture and protective dome on the top of integrating sphere (spherical diffuser) **1220** are replaced with a diffuser element **1500**, such as one formed from PTFE for example. This diffuser element **1500** may provide an improved cosine response relative to the precision aperture within the thin sheet.

Now referring to FIG. **16** there is depicted an exemplary system block diagram of a SolarSIM-G **1600** according to an embodiment of the invention as depicted in FIGS. **11** to **15** respectively comprising first to third functional blocks **1600**A, **1600**B and **900**D of the SolarSIM-G **1600**. As depicted first functional block **1600**A relates to the multiple wavelength channels and consists of integrating sphere (spherical diffuser) and diffuser cavity **1530** which are common to all channels and then for each wavelength an optical filter and optical collimator assembly coupled to a photodiode and then the outputs from the multiple photodetectors are coupled via an array of transimpedance amplifiers (TIAs) to an electrical multiplexer. The output of the multiplexer is converted to digital form via an analog-to-digital converter (ADC). The output of the ADC is coupled to the electronic functional block **900**D. Within another embodiment of the invention each photodetector has an associated TIA and the multiple TIA outputs are multiplexed for the ADC or even multiple ADCs may be employed. Optionally, the outputs from the photodetectors are multiplexed prior to being amplified by a TIA and digitized.

Second functional block **1600**C relates to the other sensors within the SolarSIM-G **1600** including, but not limited to, ambient temperature, ambient pressure, ambient humidity, internal temperature, internal humidity and accelerometer. The outputs of these being also coupled to the electronic functional block **900**D.

The electronic functional block **900**D therefore receives multiplexed digital data relating to the multiple wavelength channels and digital data from multiple environmental sensors. These are processed by a microcontroller within the electronic functional block **900**D via a software algorithm or software algorithms stored in memory associated with the microcontroller. The electronic functional block **900**D also implements one or more communication protocols such that the raw and/or processed data are pushed to or pulled to a host computer, in this instance a remote server **910** via a network **950**. The remote server **910** processes the data from the SolarSIM-G or stores processed data from the SolarSIM-G. This data may include, but is not limited to, global spectral irradiance (horizontal or titled), direct spectrum, diffuse spectrum, spectral water vapour, aerosols, and ozone absorption profiles. Optionally, the data acquired by the SolarSIM-G is processed directly onboard the SolarSIM-G prior to be transmitted to the remote server **910** or another device via the network **950**.

The SolarSIM-G may employ one or more wireless interfaces to communicate with the network **950** selected from the group comprising, but not limited to, IEEE 802.11, IEEE 802.15, IEEE 802.16, IEEE 802.20, UMTS, GSM 850, GSM 900, GSM 1800, GSM 1900, GPRS, ITU-R 5.138, ITU-R 5.150, ITU-R 5.280, and IMT-1000. Alternatively, the SolarSIM-G may employ one or more wired interfaces to communicate with the network **950** selected from the group comprising, but not limited to, DSL, Dial-Up, DOCSIS, Ethernet, G.hn, ISDN, MoCA, PON, and Power line communication (PLC).

A software block diagram for the software algorithm of a SolarSIM-G is depicted in FIG. **17**. As indicated all of the inputs on the left are fed to a series of initial processing algorithms and subsequent reconstruction algorithms in order to resolve the global, direct and diffuse solar spectrum. Accordingly, as indicated the channel responsivity is derived in dependence upon the internal SolarSIM-G temperature, the channel responsivity calibration and the channel responsivity. The raw digitized photocurrents and current calibration data are used to generate calibrated channel photocurrents. The date, time, and location information are employed within a solar position algorithm which is employed in generating the air mass zero (AM0) spectrum which is that of the sun with no intervening atmosphere. These outputs are combined with accelerometer, ambient pressure and ambient temperature in an initial algorithm to derive a reconstructed solar spectrum with extracted water vapour, aerosols, and ozone as a result of the wavelengths selected for the seven channels of the SolarSIM-G.

Next the diffuse spectral irradiance is estimated and then employed to generate a refined reconstructed solar spectrum which is then employed to reconstruct the final global spectrum, diffuse and direct spectra as well as the atmospheric absorption profiles for water, ozone, and aerosols. As the global spectrum is a combination of the direct and the diffuse spectral irradiances, the first reconstruction will not be perfect, as we are not taking the diffuse irradiance into account. However, the reconstructed proxy spectrum allows estimating the aerosols, water vapour and ozone content in the atmosphere, which in turn allow a better approximation of the diffuse irradiance (which is further enhanced by the global to diffuse ratio as determined by the shadow pole photodiodes). The approximated diffuse irradiance is then subtracted from the proxy global solar spectrum and reconstruction is performed once again, which gives the direct component of the global spectral irradiance. Addition of the estimated diffuse spectral irradiance to the direct component yields the global spectral irradiance.

The SolarSIM-G depicted in FIGS. **11** to **15**A is mounted to a surface via the mounting plate **1250** which permits rotation of the SolarSIM-G prior to locking it down. The SolarSIM-G itself is mounted via its baseplate **1255** to the mounting plate **1250** by 3 screws with springs allowing the SolarSIM-G to be leveled via adjustment of these screws and the tilt bubble **1310**. The outer mechanical housing **1230** is attached to the baseplate **1255** via a series of screws and disposed within the baseplate **1255** is a vent **1320** which allows pressure equalization for the outdoor environment sensor to measure ambient pressure, temperature and humidity. Vent **1320** provides for pressure equalization of the internal environment of the SolarSIM-G with the ambient environment whilst acting as a barrier to liquids such as water and particulates such as dust.

On the upper side of the SolarSIM-G depicted in FIGS. **11** to **15**A the protective dome **1210** fits within a groove formed in the upper surface of the outer mechanical housing **1230** and is adhered in position by a material such as a silicone or an epoxy for example. The precision aperture **1510** is formed by the inner opening within the aperture ring **1570** which is formed from a very thin piece of material, e.g. 80 μm high purity nickel sheet, as this ideally should be zero thickness and perfectly reflective, the former to avoid cosine losses and the latter to aid light diffusion within the integrating sphere (spherical diffuser). This aperture ring **1570** is similarly sealed against the precision aperture **1510** via silicone although a mechanical attachment may also be employed.

The upper and lower diffuser bodies **1220** and **1225** form an integrating sphere (spherical diffuser) that creates, ideally, a perfect cosine response and the inner surfaces are coated with a highly Lambertian material to provide a

Lambertian reflectance which is an “ideal” matte or diffusively reflecting surface with apparent brightness constant with observation angle. Within the embodiment depicted the upper and lower diffuser bodies **1220** and **1225** are joined via screws with a lipped joint between although within other embodiments of the invention an O-ring or other seal may be employed as may other means of joining the upper and lower diffuser bodies **1220** and **1225** together. The diffuser is then mounted to the baseplate **1255** via screws.

Within the upper diffuser body **1220** is the output aperture **1520** which has formed around its lower half the diffuser baffle **1580** which is used to prevent a first reflection from the integrating sphere (spherical diffuser) at near normal incidence illumination. The diffuser baffle **1580** is spherical to allow for azimuthal symmetry, which improves the cosine response. The output aperture **1520** allows light to enter the diffusing cavity **1530** which allows the rays to undergo multiple reflections for optimal diffusion. This diffusing cavity **1530** being formed from the upper diffuser body **1220** and first optical collimator element **1270**.

Within the first optical collimator element **1270** are first collimator apertures **1540** for each wavelength channel. Mounted to the first optical collimator element **1270** is second optical collimator element **1280** which has wells machined within to house the optical filters **1260**B and their housings **1260**A. Also formed within second optical collimator element **1280** are second collimator apertures **1550** which in conjunction with the first collimator apertures **1540** define the angular distribution of light rays allowed to strike each detector. This being necessary as the performance of bandpass filters degrades as the incidence angle increases and accordingly only near collimated light, in reality an approximately 10-degree half angle, is allowed to pass to the photodetectors **1560**.

Within embodiments of the invention the diffuser may be formed from one or more thermoplastics, polyesters, and glasses according to the wavelength range, cost, diffuser performance etc. required from the diffuser. For example, the diffuser may be BK7 glass. Optionally, the enclosure, baseplate and tube collimator may be formed from a plastic, thermoplastic, polyester, or a metal or formed from different plastics, thermoplastics, polyesters, or metals. Optionally, in embodiments of the invention the mechanical structure may be encased partially or fully within a casing such as a silicone for example. Optionally, the enclosure and tube collimators may be formed as a single piece-part or two or more piece-parts.

Specific details are given in the above description to provide a thorough understanding of the embodiments. However, it is understood that the embodiments may be practiced without these specific details. For example, circuits may be shown in block diagrams in order not to obscure the embodiments in unnecessary detail. In other instances, well-known circuits, processes, algorithms, structures, and techniques may be shown without unnecessary detail in order to avoid obscuring the embodiments.

Implementation of the techniques, blocks, steps and means described above may be done in various ways. For example, these techniques, blocks, steps and means may be implemented in hardware, software, or a combination thereof. For a hardware implementation, the processing units may be implemented within one or more application specific integrated circuits (ASICs), digital signal processors (DSPs), digital signal processing devices (DSPDs), programmable logic devices (PLDs), field programmable gate arrays (FPGAs), processors, controllers, micro-controllers, microprocessors, other electronic units designed to perform the functions described above and/or a combination thereof.

Also, it is noted that the embodiments may be described as a process which is depicted as a flowchart, a flow diagram, a data flow diagram, a structure diagram, or a block diagram. Although a flowchart may describe the operations as a sequential process, many of the operations can be performed in parallel or concurrently. In addition, the order of the operations may be rearranged. A process is terminated when its operations are completed, but could have additional steps not included in the figure. A process may correspond to a method, a function, a procedure, a subroutine, a subprogram, etc. When a process corresponds to a function, its termination corresponds to a return of the function to the calling function or the main function.

Furthermore, embodiments may be implemented by hardware, software, scripting languages, firmware, middleware, microcode, hardware description languages and/or any combination thereof. When implemented in software, firmware, middleware, scripting language and/or microcode, the program code or code segments to perform the necessary tasks may be stored in a machine readable medium, such as a storage medium. A code segment or machine-executable instruction may represent a procedure, a function, a subprogram, a program, a routine, a subroutine, a module, a software package, a script, a class, or any combination of instructions, data structures and/or program statements. A code segment may be coupled to another code segment or a hardware circuit by passing and/or receiving information, data, arguments, parameters and/or memory content. Information, arguments, parameters, data, etc. may be passed, forwarded, or transmitted via any suitable means including memory sharing, message passing, token passing, network transmission, etc.

For a firmware and/or software implementation, the methodologies may be implemented with modules (e.g., procedures, functions, and so on) that perform the functions described herein. Any machine-readable medium tangibly embodying instructions may be used in implementing the methodologies described herein. For example, software codes may be stored in a memory. Memory may be implemented within the processor or external to the processor and may vary in implementation where the memory is employed in storing software codes for subsequent execution to that when the memory is employed in executing the software codes. As used herein the term "memory" refers to any type of long term, short term, volatile, nonvolatile, or other storage medium and is not to be limited to any particular type of memory or number of memories, or type of media upon which memory is stored.

Moreover, as disclosed herein, the term "storage medium" may represent one or more devices for storing data, including read only memory (ROM), random access memory (RAM), magnetic RAM, core memory, magnetic disk storage mediums, optical storage mediums, flash memory devices and/or other machine readable mediums for storing information. The term "machine-readable medium" includes, but is not limited to portable or fixed storage devices, optical storage devices, wireless channels and/or various other mediums capable of storing, containing or carrying instruction(s) and/or data.

The methodologies described herein are, in one or more embodiments, performable by a machine which includes one or more processors that accept code segments containing instructions. For any of the methods described herein, when the instructions are executed by the machine, the machine performs the method. Any machine capable of executing a set of instructions (sequential or otherwise) that specify actions to be taken by that machine are included. Thus, a typical machine may be exemplified by a typical processing system that includes one or more processors. Each processor may include one or more of a CPU, a graphics-processing unit, and a programmable DSP unit. The processing system further may include a memory subsystem including main RAM and/or a static RAM, and/or ROM. A bus subsystem may be included for communicating between the components. If the processing system requires a display, such a display may be included, e.g., a liquid crystal display (LCD). If manual data entry is required, the processing system also includes an input device such as one or more of an alphanumeric input unit such as a keyboard, a pointing control device such as a mouse, and so forth.

The memory includes machine-readable code segments (e.g. software or software code) including instructions for performing, when executed by the processing system, one of more of the methods described herein. The software may reside entirely in the memory, or may also reside, completely or at least partially, within the RAM and/or within the processor during execution thereof by the computer system. Thus, the memory and the processor also constitute a system comprising machine-readable code.

In alternative embodiments, the machine operates as a standalone device or may be connected, e.g., networked to other machines, in a networked deployment, the machine may operate in the capacity of a server or a client machine in server-client network environment, or as a peer machine in a peer-to-peer or distributed network environment. The machine may be, for example, a computer, a server, a cluster of servers, a cluster of computers, a web appliance, a distributed computing environment, a cloud computing environment, or any machine capable of executing a set of instructions (sequential or otherwise) that specify actions to be taken by that machine. The term "machine" may also be taken to include any collection of machines that individually or jointly execute a set (or multiple sets) of instructions to perform any one or more of the methodologies discussed herein.

The foregoing disclosure of the exemplary embodiments of the present invention has been presented for purposes of illustration and description. It is not intended to be exhaustive or to limit the invention to the precise forms disclosed. Many variations and modifications of the embodiments described herein will be apparent to one of ordinary skill in the art in light of the above disclosure. The scope of the invention is to be defined only by the claims appended hereto, and by their equivalents.

Further, in describing representative embodiments of the present invention, the specification may have presented the method and/or process of the present invention as a particular sequence of steps. However, to the extent that the method or process does not rely on the particular order of steps set forth herein, the method or process should not be limited to the particular sequence of steps described. As one of ordinary skill in the art would appreciate, other sequences of steps may be possible. Therefore, the particular order of the steps set forth in the specification should not be construed as limitations on the claims. In addition, the claims directed to the method and/or process of the present invention should not be limited to the performance of their steps in the order written, and one skilled in the art can readily appreciate that the sequences may be varied and still remain within the spirit and scope of the present invention.

What is claimed is:

1. A device comprising:

a diffuser disposed in front of a first aperture of a cavity;

a first body portion comprising the first aperture having a first predetermined diameter positioned in a first predetermined position on the first body portion and forming a first predetermined portion of the cavity;

a second body portion comprising a plurality of second apertures, each second aperture having a second predetermined diameter and positioned in a second predetermined position on the second body portion and forming a second predetermined portion of the cavity;

a plurality of optical collimators, each optical collimator coupled to a predetermined second aperture of the plurality of second apertures and defining a maximum angular acceptance angle for each photodetector of a plurality of photodetectors disposed at the distal end of an optical collimator from that coupled to the predetermined second aperture of the plurality of second apertures; and

a plurality of optical filters, each filter having a passband of predetermined optical wavelengths and disposed in combination with a predetermined optical collimator of the plurality of collimators to filter optical signals exiting the second aperture.

2. The device according to claim 1, wherein

at least one of the first predetermined portion of the cavity and the second predetermined portion of the cavity are coated with a near Lambertian material.

3. The device according to claim 1, wherein

each optical collimator of the plurality of optical collimators comprises a third aperture having a predetermined third diameter disposed at a predetermined position between the end of the optical collimator coupled to the second body portion and the distal end of the optical collimator from that coupled to the predetermined second aperture of the plurality of second apertures.

4. The device according to claim 1, wherein

the device when deployed is attached to a baseplate mounted to a structure and the device is orientated such that the optical collimators are aligned north-south and point towards the solar noon at the location of the installation.

5. The device according to claim 1, further comprising

a first electronic circuit for digitizing a photocurrent generated by each photodetector of the plurality of photodetectors; and

a second electronic circuit for generating a reconstructed solar spectrum in dependence upon at least the digitized photocurrents of the plurality of photodetectors and model of the solar spectrum with no atmosphere.

6. The device according to claim 5, wherein

the reconstructed solar spectrum is at least one of a final global spectrum, a diffuse solar spectrum, and a direct solar spectrum.

7. The device according to claim 1, further comprising

a first electronic circuit for digitizing a photocurrent generated by each photodetector of the plurality of photodetectors; and

a second electronic circuit for generating an absorption profile relating to one of atmospheric precipitable water vapour, atmospheric ozone, and atmospheric aerosols; wherein

at least one filter of the plurality of filters has its passband of predetermined optical wavelengths established in dependence upon the one of precipitable water vapour, ozone, and atmospheric aerosols.

8. The device according to claim 1, wherein

each collimator comprises a first portion with a first diameter and a second portion with a second diameter and the associated filter of the plurality of filters is disposed between the first portion and the second portion.

9. The device according to claim 1, further comprising

a cover plate for mounting atop the first body portion having an upper surface, a central opening within the upper surface within which the diffuser is disposed, and an outer raised lip of a predetermined height relative to the upper surface of the diffuser when it is disposed within the central opening.

10. The device according to claim 9, wherein

at least one of:

the height of the outer raised lip is level with the upper surface of the diffuser;

the central opening restrains lateral movement of the diffuser; and

a first predetermined portion of the diffuser projects above the upper surface of the cover plate and a second predetermined portion of the diffuser is disposed below the upper surface of the cover plate.

11. The device according to claim 9, further comprising

at least one of:

one or more spacers disposed between the cover plate and the first body portion, the one or more spacers each comprising an opening within which the diffuser is disposed and adjusting the height of the outer raised lip of the cover plate relative to the diffuser; and

a transparent protective element disposed to cover the cover plate, diffuser, and a predetermined portion of the first body portion, the transparent protective element protecting the cover plate, diffuser, and a predetermined portion of the first body portion from the ambient environment and allow sunlight to impinge directly on the diffuser.

12. The device according to claim 1, wherein

each optical collimator of the plurality of optical collimators comprises sequentially away from the second body portion:

a first portion having a predetermined first length and predetermined third diameter;

a second portion having a predetermined second length and predetermined fourth diameter; and

a third portion having a predetermined third length and predetermined fifth diameter.

13. The device according to claim 12, wherein

at least one of:

the predetermined third diameter is greater than the predetermined second diameter; and

the predetermined fourth diameter is less than both the predetermined third diameter and the predetermined fifth diameter.

14. A device comprising:

a plurality of photodetectors, each photodetector receiving a predetermined wavelength range of the ambient optical environment via an optical path comprising a diffuser element, an optical cavity, a bandpass filter, and an optical collimator to limit the angle of incident ambient light to within a predetermined range; and

an electronic circuit comprising a first portion for digitizing a photocurrent for each photodetector of the plurality of first photodetectors and a second portion for at least one of generating a reconstructed solar spectrum in dependence upon at least the digitized photocurrents of the plurality of photodetectors and a model of the solar spectrum with no atmosphere; wherein

the plurality of detectors are disposed radially around a first portion of the optical cavity disposed opposite an aperture within a second portion of the optical cavity covered by the diffuser element;

the optical cavity for each photodetector of the plurality photodetectors is a cavity common to all of the plurality of photodetectors;

the diffuser element for each photodetector of the plurality photodetectors is a diffuser common to all of the plurality of photodetectors.

15. The device according to claim **14**, wherein

the reconstructed solar spectrum is at least one of a final global spectrum, a diffuse solar spectrum, and a direct solar spectrum.

16. The device according to claim **14**, further comprising

generating an atmospheric absorption profile relating to at least one of precipitable water vapour, ozone, an atmospheric aerosol and atmospheric aerosols.

17. The device according to claim **14**, wherein

in deployment the plurality of detectors are disposed towards the north.

18. The device according to claim **14**, wherein

the diffuser element is designed in dependence upon the predetermined wavelength ranges for the plurality of photodetectors and the material from which the diffuser element is formed.

19. The device according to claim **14**, further comprising

an environmental sensing circuit comprising at least one of a humidity sensor, a pressure sensor and a temperature sensor disposed within the device and coupled to the external environment of the device by a vent, the vent allowing passage of air but not water.

20. The device according to claim **14**, further comprising

an outer raised lip of predetermined radius and predetermined height; wherein

the diffuser element for each photodetector of the plurality photodetectors is a diffuser common to all of the plurality of photodetectors; and

the top of the outer raised lip is established in dependence upon the upper surface of the diffuser.

21. The device according to claim **14**, wherein

a predetermined portion of the optical cavity is coated with a near Lambertian material.

* * * * *

References

[1] SolarPower Europe, "Global market outlook 2018–2020", SolarPower Europe, Tech. Rep., 2018.

[2] DNV GL, "Energy transition outlook – a global and regional forecast to 2050", DNV GL, Tech. Rep., 2017.

[3] K. Passow and M. Lee, "Effect of spectral shift on solar PV performance", in *2016 IEEE Conference on Technologies for Sustainability (SusTech)*, IEEE, 2016, pp. 246–250.

[4] D. Magare, O. Sastry, R. Gupta, *et al.*, "Effect of seasonal spectral variations on performance of three different photovoltaic technologies in India", *International Journal of Energy and Environmental Engineering*, vol. 7, no. 1, pp. 93–103, 2016.

[5] G. Nofuentes, B. García-Domingo, J. Muñoz, *et al.*, "Analysis of the dependence of the spectral factor of some PV technologies on the solar spectrum distribution", *Applied energy*, vol. 113, pp. 302–309, 2014.

[6] R. Núñez, M. Victoria, S. Askins, *et al.*, "Spectral impact on multijunction solar cells obtained by means of component cells of a different technology", *IEEE Journal of Photovoltaics*, vol. 8, no. 2, pp. 646–653, 2018.

[7] R. Núñez, C. Dominguez, S. Askins, *et al.*, "Determination of spectral variations by means of component cells useful for CPV rating and design", *Progress in Photovoltaics: Research and Applications*, vol. 24, no. 5, pp. 663–679, 2016.

[8] E. F. Fernández, A. Soria-Moya, F. Almonacid, *et al.*, "Comparative assessment of the spectral impact on the energy yield of high concentrator and conventional photovoltaic technology", *Solar Energy Materials and Solar Cells*, vol. 147, pp. 185–197, 2016.

[9] N. L. A. Chan, H. E. Brindley, and N. J. Ekins-Daukes, "Impact of individual atmospheric parameters on CPV system power, energy yield and cost of energy", *Progress in Photovoltaics: Research and Applications*, vol. 22, no. 10, pp. 1080–1095, 2014.

[10] S. AlYahya and M. A. Irfan, "Analysis from the new solar radiation atlas for Saudi Arabia", *Solar Energy*, vol. 130, pp. 116–127, 2016.

[11] T. Cebecauer and M. Suri, "Site-adaptation of satellite-based DNI and GHI time series: Overview and SolarGIS approach", in *AIP Conference Proceedings*, AIP Publishing, vol. 1734, 2016.

[12] T. Stoffel, A. Andreas, I. Reda, *et al.*, “Solar radiation research laboratory”, in *SunShot Grand Challenge Summit and Technology Forum*, 2012.

[13] I. Antón, M. Martinez, F. Rubio, *et al.*, “Power rating of CPV systems based on spectrally corrected DNI”, in *AIP conference proceedings*, American Institute of Physics, vol. 1477, 2012, pp. 331–335.

[14] V. Tatsiankou, “Instrumentation development for site-specific prediction of spectral effects on concentrated photovoltaic system performance”, Master’s thesis, University of Ottawa, 2014.

[15] B. Holben, T. Eck, I. Slutsker, *et al.*, “AERONET - a federated instrument network and data archive for aerosol characterization”, *Remote Sensing of Environment*, vol. 66, no. 1, pp. 1–16, 1998.

[16] B. Holben, D. Tanre, A. Smirnov, *et al.*, “An emerging ground-based aerosol climatology: Aerosol optical depth from AERONET”, *Journal of Geophysical Research: Atmospheres*, vol. 106, no. D11, pp. 12 067–12 097, 2001.

[17] N. L. A. Chan, T. B. Young, H. E. Brindley, *et al.*, “Validation of energy prediction method for a concentrator photovoltaic module in Toyohashi, Japan”, *Progress in Photovoltaics: Research and Applications*, vol. 21, no. 8, pp. 1598–1610, 2013.

[18] J. Michalsky, “Estimation of continuous solar spectral distributions from discrete filter measurements: Ii. a demonstration of practicability”, *Solar energy*, vol. 34, no. 6, pp. 439–445, 1985.

[19] J. Michalsky and E. Kleckner, “Estimation of continuous solar spectral distributions from discrete filter measurements”, *Solar Energy*, vol. 33, no. 1, pp. 57–64, 1984.

[20] C. Osterwald, K. Emery, D. Myers, *et al.*, “Extending the spectral range of silicon-based direct-beam solar spectral radiometric measurements”, in *Photovoltaic Specialists Conference, 1988., Conference Record of the Twentieth IEEE*, IEEE, 1988, pp. 1246–1250.

[21] T. Cannon and R. Hulstrom, “Atmospheric optical calibration system for outdoor testing of photovoltaic devices”, *Metrologia*, vol. 30, no. 4, p. 409, 1993.

[22] C. A. Gueymard, “The sun’s total and spectral irradiance for solar energy applications and solar radiation models”, *Solar Energy*, vol. 76, pp. 423–453, 2004.

[23] WMO, *Guide to meterological instruments and methods of observation*, 2008.

[24] G. Kopp and J. L. Lean, “A new, lower value of total solar irradiance: Evidence and climate significance”, *Geophysical Research Letters*, vol. 38, no. 1, 2011.

[25] I. Reda and A. Andreas, “Solar position algorithm for solar radiation applications”, NREL, Tech. Rep., 2008. [Online]. Available: `https://midcdmz.nrel.gov/spa/`.

[26] R. E. Bird and C. Riordan, “Simple solar spectral model for direct and diffuse irradiance on horizontal and tilted planes at the earth’s surface for cloudless atmospheres”, *Journal of Climate and Applied Meteorology*, vol. 25, no. 1, pp. 87–97, 1986.

[27] C. Gueymard, *SMARTS2: a simple model of the atmospheric radiative transfer of sunshine: algorithms and performance assessment*. Florida Solar Energy Center Cocoa, FL, 1995.

[28] C. A. Gueymard, "SMARTS2 code, version 2.9.5, user's manual", Solar Consulting Services, Tech. Rep., 2006.

[29] P. Tzoumanikas, E. Nikitidou, A. Bais, *et al.*, "The effect of clouds on surface solar irradiance, based on data from an all-sky imaging system", *Renewable energy*, vol. 95, pp. 314–322, 2016.

[30] J. S. Bartlett, Á. M. Ciotti, R. F. Davis, *et al.*, "The spectral effects of clouds on solar irradiance", *Journal of Geophysical Research: Oceans*, vol. 103, no. C13, pp. 31 017–31 031, 1998.

[31] C. Emde, R. Buras-Schnell, A. Kylling, *et al.*, "The libRadtran software package for radiative transfer calculations (version 2.0.1)", 2016.

[32] J. Michalsky, L. Harrison, and W. Berkheiser III, "Cosine response characteristics of some radiometric and photometric sensors", *Solar Energy*, vol. 54, no. 6, pp. 397–402, 1995.

[33] D. R. Myers, I. Reda, S. Wilcox, *et al.*, "Optical radiation measurements for photovoltaic applications: Instrumentation uncertainty and performance", in *Organic Photovoltaics V*, International Society for Optics and Photonics, vol. 5520, 2004, pp. 142–154.

[34] International Organization for Standardization, *ISO 9060:2018, Solar energy – Specification and classification of instruments for measuring hemispherical solar and direct solar radiation*, 2018.

[35] S. Pelland, C. Beswick, D. Thevenard, *et al.*, "Development and benchmarking of a simple model of photovoltaic spectral mismatch factor", in *47th IEEE Photovoltaic Specialists Conference (PVSC)*, 2020.